TECHNICAL REPORT DOCUMENTATION PAGE

TR0003 (REV 10/98)

1. REPORT NUMBER	2. GOVERNMENT ASSOCIATION NUMBER	3. RECIPIENT'S CATALOG NUMBER
CA18-2994		

4. TITLE AND SUBTITLE	5. REPORT DATE
Seismic behavior of grade 80 RC Bridge Columns – Phase 1 and critical bending strain of longitudinal reinforcement	June 2018
	6. PERFORMING ORGANIZATION CODE RD-18-02

7. AUTHOR	8. PERFORMING ORGANIZATION REPORT NO.
Leo Barcley, Mervyn Kowalsky	

9. PERFORMING ORGANIZATION NAME AND ADDRESS	10. WORK UNIT NUMBER
North Carolina State University, Department of Civil Construction and Environmental Engineering, Mann Hall, 208 Stinson Drive, Raleigh, NC 27695	11. CONTRACT OR GRANT NUMBER 65A0600

12. SPONSORING AGENCY AND ADDRESS	13. TYPE OF REPORT AND PERIOD COVERED
California Department of Transportation Division of Engineering Services 1801 30th Street, MS #9-2/5i Sacramento, CA 95816	Final
	14. SPONSORING AGENCY CODE

15. SUPPLEMENTARY NOTES

16. ABSTRACT

Modern seismic design relies on the principles of capacity design wherein certain structural members are chosen as plastic hinge members. In reinforced concrete, the choice of reinforcement is crucial for desirable performance of plastic hinge members. Current design codes specify a maximum yield strength of 60 ksi (Grade 60) for reinforcement used in plastic hinge members. However, using higher strength reinforcement (Grade 80) would reduce rebar congestion, construction cost, and building environmental footprint. Due to a lack of experimental evidence, engineers are hesitant to prescribe this rebar for use in plastic hinge members. A research program was developed to test concrete columns reinforced with A706-80 rebar.

Four columns were designed as scaled models of bridge columns with varying axial load and transverse steel ratios; each had a comparison Grade 60 column. The goal of this project was to evaluate the seismic performance of the Grade 80 columns and to compare multiple design variables to current values used for Grade 60 columns. A unique optical measurement system was employed to measure strains in the longitudinal and transverse reinforcement well past the capacity of typical strain gages.

Results of the Grade 80 column tests indicated that the plastic hinge length, bond slip, strain-based limit states, and equivalent viscous damping were not significantly different to typical Grade 60 columns. Based off the results of these four column tests, Grade 80 rebar could be specified in place of Grade 60 rebar without major changes in design practice. However, the Grade 80 columns had slightly lower displacement capacities than the Grade 60 columns. This was due to differences in the critical bending strain, which were found to cause bar fracture after buckling.

A method to predict the tensile strain prior to longitudinal bar fracture was developed from the relationship between uniaxial tension strain demand, the degree of longitudinal bar buckling and the newly identified critical bending strain. In addition, a simplified material test was developed to quantify the critical bending strain for any rebar. Rebar rib radius and manufacture process influenced the critical bending strain.

17. KEY WORDS	18. DISTRIBUTION STATEMENT
Grade 80, reinforcing steel, seismic, column	No Restrictions

19. SECURITY CLASSIFICATION *(of this report)*	*20. NUMBER OF PAGES*	*21. COST OF REPORT CHARGED*
None	202	

Disclaimer

This document is disseminated in the interest of information exchange. The contents of this report reflect the views of the authors who are responsible for the facts and accuracy of the data presented herein. The contents do not necessarily reflect the official views or policies of the State of California or the Federal Highway Administration. This publication does not constitute a standard, specification or regulation. This report does not constitute an endorsement by the Department of any product described herein.

For individuals with sensory disabilities, this document is available in Braille, large print, audiocassette, or compact disk. To obtain a copy of this document in one of the alternate formats, please contact: the Division of Research and Innovation MS-83, California Department of Transportation, P.O. Box 942873, Sacramento, CA 94273-0001.

Constructed Facilities Laboratory

Department of Civil, Construction, and Environmental Engineering

Research Report

No. RD-18-02

Seismic Behavior of Grade 80 RC Bridge Columns – Phase 1 and Critical Bending Strain of Longitudinal Reinforcement

Prepared by:

Leo Barcley, *Graduate Research Assistant*
Dr. Mervyn Kowalsky, *Principle Investigator*

Prepared for:

California Department of Transportation
Sacramento, California

May 2018

Constructed Facilities Laboratory
2414 Campus Shore Drive
North Carolina State University
Raleigh, NC 27695-7533
Tel: (919) 513-1733
Fax: (919) 513-1765
Email: cfl@ncsu.edu
Web Site: www.cfl.ncsu.edu

STATE OF CALIFORNIA • DEPARTMENT OF TRANSPORTATION

SEISMIC BEHAVIOR OF GRADE 80 RC BRIDGE COLUMNS – PHASE 1 AND CRITICAL BENDING STRAIN OF LONGITUDINAL REINFORCEMENT

Final Report

September 25, 2018

The research described in this report is supported by the California Department of Transportation under agreement #65A0600. Their support is gratefully acknowledged. The conclusions are those of the authors alone and should not be construed as to imply endorsement by Caltrans.

Acknowledgments

Funding for this research, which was provided by the California Department of Transportation under Agreement #65A0600, is gratefully acknowledged. Additionally, the authors would like to thank the three producing mills (Nucor, Gerdau, and CMC) for their generous donation of the reinforcing steel used in the project, as well as for their technical expertise regarding metallurgy. We would like to thank MS Student Robyn Manhard who conducted all of the energy dissipation calculations in Chapter 5. Lastly, the assistance of the entire staff of the Constructed Facilities Laboratory is greatly appreciated.

Abstract

Modern seismic design relies on the principles of capacity design wherein certain structural members are chosen as plastic hinge members. In reinforced concrete, the choice of reinforcement is crucial for desirable performance of plastic hinge members. Current design codes specify a maximum yield strength of 60 ksi (Grade 60) for reinforcement used in plastic hinge members. However, using higher strength reinforcement (Grade 80) would reduce rebar congestion, construction cost, and building environmental footprint. Due to a lack of experimental evidence, engineers are hesitant to prescribe this rebar for use in plastic hinge members. A research program was developed to test concrete columns reinforced with A706-80 rebar.

Four columns were designed as scaled models of bridge columns with varying axial load and transverse steel ratios; each had a comparison Grade 60 column. The goal of this project was to evaluate the seismic performance of the Grade 80 columns and to compare multiple design variables to current values used for Grade 60 columns. A unique optical measurement system was employed to measure strains in the longitudinal and transverse reinforcement well past the capacity of typical strain gages.

Results of the Grade 80 column tests indicated that the plastic hinge length, bond slip, strain-based limit states, and equivalent viscous damping were not significantly different to typical Grade 60 columns. Based off the results of these four column tests, Grade 80 rebar could be specified in place of Grade 60 rebar without major changes in design practice. However, the Grade 80 columns had slightly lower displacement capacities than the Grade 60 columns. This was due to differences in the critical bending strain, which were found to cause bar fracture after buckling.

A method to predict the tensile strain prior to longitudinal bar fracture was developed from the relationship between uniaxial tension strain demand, the degree of longitudinal bar buckling and the newly identified critical bending strain. In addition, a simplified material test was developed to quantify the critical bending strain for any rebar. Rebar rib radius and manufacture process influenced the critical bending strain.

Notation and Definitions

A_g	Gross area of column cross-section
A_{st}	Total area of longitudinal steel
A_1	Area inside hysteretic loop
A_2	Area inside rectangle encompassing maximum and minimum force and displacement for each hysteretic loop
CF	Correction factor for Jacobsen hysteretic damping
D	Column diameter
d_{bl}	Diameter of longitudinal reinforcement
Δ	Column displacement
Δ_p	Plastic column displacement
Δ_y	Equivalent yield displacement
Δ'_y	First yield displacement
E_s	Elastic modulus of steel
ε_{ap}	Strain amplitude for fatigue test
ε_b	Bending strain on rebar
$\varepsilon_{c\,yield}^{spiral}$	Compressive strain at yielding of transverse steel
ε_{cr}	Critical bending strain for rebar
ε_{rate}	Dynamic strain rate for tensile loading
$\varepsilon_{s\,buckling}^{bar}$	Previous tension strain in longitudinal reinforcement prior to bar buckling
f'_{ce}	Expected concrete compressive strength
f_y	Steel yield strength
f_{yd}	Steel yield strength under dynamic loading
f_{yhe}	Expected yield strength of transverse steel
f_{ye}	Expected yield strength of longitudinal steel
κ	Elastic damping correction factor
L	Clear length of column
L_{eff}	Effective column length
L_p	Plastic hinge length
λ	Secant stiffness correction factor
M_N	Nominal moment capacity
M'_y	First yield moment
μ	Displacement ductility
N_f	Number of cycles to failure for fatigue test
P	Column axial load
φ	Column curvature
φ_{bl}	Curvature on cross-section of rebar

φ_p	Plastic column curvature
φ_y	Equivalent yield curvature
ρ_s	Longitudinal steel ratio
ρ_v	Transverse volumetric steel ratio
ξ_{el}	Elastic damping
ξ_{eq}	Equivalent viscous damping
ξ_{hyst}	Hysteretic damping
ξ_{jac}	Jacobsen hysteretic damping
$w(x)$	Position function of rebar deformation

TABLE OF CONTENTS

LIST OF TABLES

LIST OF FIGURES

CHAPTER 1. INTRODUCTION

1.1. Background

Seismic design presents a unique challenge for structural engineers. Engineers can estimate most loads a structure will undergo to a reasonable level of precision, but earthquake loading is highly variable. However, the design of buildings for seismic hazards has evolved tremendously over the last 100 years. A noteworthy evolution is the development of performance-based earthquake engineering, wherein structures are designed to achieve prescribed performance limit states under defined levels of seismic hazard. Successful implementation of performance-based design must include reliable definitions of performance limit states, such as levels of damage or structural stability, consistent with measurable parameters, such as strain, drift, or ductility limits. In addition, designers must have accurate definitions of seismic hazards. Furthermore, the analysis and design procedures must directly consider non-linear behavior. Lastly, capacity design principles must be applied to ensure that the chosen locations of damage are suitably detailed for their deformation demands while all other modes of failure are avoided (Paulay and Priestley, 1992).

In capacity design, structural damage is designed to occur in the "plastic hinge regions," dissipating energy from a seismic event, protecting other members from sustaining large amounts of damage, and preventing undesirable failure modes. In reinforced concrete (RC) members designed as plastic hinges, the choice of reinforcement is crucial to yield desirable performance. The tensile reinforcement must have a large inelastic strain capacity to ensure that the member can sustain large displacements prior to failure. In addition, engineers must know the material properties of the reinforcement to a high degree of accuracy in order to guarantee correct force demands to the surrounding capacity protected members. In the United States, reinforcing steel (rebar) is most commonly manufactured with either the ASTM A615 or the ASTM A706 designation. A615 rebar has less restrictive requirements on chemical composition and stress/strain parameters, while A706 rebar has much tighter requirements on chemical composition and limits on minimum and maximum yield and tensile strengths. For these reasons, A706 rebar is typically specified for structures in higher seismic regions.

Until 2009, the A706 standard only included reinforcing steel with a yield strength of 60 ksi (Grade 60), but now the standard includes rebar with a nominal yield strength of 80 ksi (Grade 80). A member reinforced with A706 Grade 80 rebar would require less reinforcing steel to achieve the same strength as a member designed with A706 Grade 60 rebar. Using A706-80 rebar has the potential to decrease rebar congestion, which could decrease the cost and time of construction. Reducing congestion could also simplify the design of cap beams and connection details. Grade 80 transverse steel would also provide more confinement to column core concrete, increasing the load-carrying capacity of the member and restraint against longitudinal bar buckling.

However, past research (Overby et al., 2015) has shown that increasing rebar strength results in a decrease in the strain at ultimate stress (also referred to as the "uniform elongation") and length of yield plateau, which could lead to undesirable seismic performance. The loss of ductile behavior is one of the main reasons engineers have been hesitant to use high strength rebar in seismic design. In addition, very little experimental data exists on A706-80 reinforcing steel. A report by Overby et al. (2015) presented a statistically defensible stress vs. strain relationship for A706-80 rebar by performing almost 800 tensile tests. After correctly characterizing the tensile behavior of A706-80 rebar, the next logical step is to examine the seismic performance of members reinforced with A706-80 rebar by conducting tests on RC members.

1.2. Research Objective

This report seeks to add to the current literature concerning the seismic behavior of Grade 80 RC columns in order to determine the suitability of the rebar in plastic hinge members. To accomplish this goal, four circular columns reinforced with A706-80 rebar were constructed at North Carolina State University (NCSU). These columns were subjected to reverse cyclic loading to simulate the effects of a seismic event. Within the column test matrix, variables include axial load ratio, aspect ratio, longitudinal steel ratio, and transverse steel ratio. The primary purpose of these column tests was to examine plastic hinge lengths, bond slip performance, and nonlinear strain limit states for A706-80 rebar. In addition, the behavior of the A706-80 RC columns was compared to columns reinforced with A706-60 rebar (Goodnight et al., 2015) with similar geometry and reinforcement content.

1.3. Scope

In order to determine the suitability of A706-80 rebar for use in plastic hinge members, RC columns reinforced with A706-80 rebar were tested. Results of these column tests are included in this report. However, after examining the results of the four column tests, a trend between the bending strain demand on the buckled longitudinal reinforcing bars and their fracture was observed. This performance was replicated in a simple bar test and the results of these bar tests are also included in this report.

1.3.1. Column Tests

Four circular, reinforced concrete columns were constructed and tested at the Constructed Facilities Laboratory (CFL) on the campus of NCSU. These column tests used an optical non-contact measuring system, the Optotrak Certus (Northern Digital, Inc., 2011), to measure strain in the longitudinal and transverse steel. Results included bar strains at various column limit states, extent of plasticity over the height of the column, and longitudinal bar slip into the footing. The optical measurement system also enabled the evaluation of column curvature profiles that were then integrated over the height of the column to determine flexural deformation. Area-based hysteretic energy dissipation was also calculated for all columns. Each of these parameters was compared to results of similar Grade 60 columns in order to determine relative column performance.

1.3.2. Cyclic Rebar Tests

The displacement capacity of the Grade 80 columns was slightly lower than comparison Grade 60 columns. However, it was observed that longitudinal bar buckling occurred at approximately the same level of displacement for each column. Using Optotrak data to measure the curvature of a buckled bar, a trend was observed between strain from bending and bar fracture. When a rebar buckled to a certain critical curvature, and corresponding bending strain demand, the bar fractured upon the subsequent tensile load cycle. A simple test was developed to find the critical bending strain resulting in bar fracture.

1.4. Overview of Report Contents

Chapter 1 introduces the topic of A706 Grade 80 reinforcement and the motivation for performing this research. In addition, the chapter introduces the two major parts of this report: column test results and cyclic rebar test results.

Chapter 2 summarizes other experimental work on high strength steel reinforcement in RC members. Current literature contains very few tests on columns reinforced with A706-80 rebar, so the chapter presents various examples of reinforced concrete members built with high strength rebar ($f_y \geq 80$ ksi) to consider performance relative to normal strength reinforcement. First, the chapter includes previous research on the mechanical properties of A706-80 rebar. Next, a review of experimental tests on reinforced concrete members constructed with A706-80 rebar is included. Third, the chapter briefly summarizes other experimental tests on RC members with other high strength reinforcing steel. Finally, this chapter includes a review of the literature concerning cyclic behavior of rebar, as well as evidence of compressive stresses affecting the tensile capacity of rebar.

Chapter 3 discusses the design and construction of the four A706-80 columns tested at NCSU. Each column was built on-site at the CFL by undergraduate and graduate students assisted by lab technical staff to ensure accurate detailing and construction. This chapter also describes the optical measurement system employed in this project, as well as other instrumentation used in the research. Lastly, the chapter includes a description of the test setup and footing reinforcement.

Chapter 4 includes the results of each column test, beginning with a description of the column test matrix and the three cycle set load history. A tabular summary is included at the beginning of each column test with displacements and strains at various performance limit states. The summary of each column test includes analysis of the strain data from the optical measurement system, different components of column displacement, hysteretic energy dissipation, and a comparison to similar Grade 60 columns.

Chapter 5 discusses different design parameters of the Grade 80 columns and analyzes how they compare to Grade 60 columns. This includes strains at the following performance limit states:

core crushing (serviceability), transverse steel yielding, longitudinal bar buckling (damage control), and bar fracture. In addition, evaluation of current models for plastic hinge length, equivalent viscous damping, and bond slip are included.

Chapter 6 describes the process used to determine the strain demand from bending on bucked longitudinal bars. As previously noted, a trend between bending strain demand and bar fracture capacity was observed and hypothesized to be related to a critical bending strain.

Chapter 7 discusses a material test developed to assess the critical bending strain of rebar, called the "Buckled Bar Tension Test" (BBT Test). The test was developed to quantify the post-buckling performance of rebar. As will be described later, and as supported by test data collected in this research, rebar buckling is described as a continuum process, as opposed to binary behavior. Analysis of the results of this test also indicated how rebar rib geometry and chemical composition influenced this performance.

CHAPTER 2. LITERATURE REVIEW

This chapter presents a review of current literature relevant to this project, specifically the performance of Grade 80 reinforced concrete columns compared to columns reinforced with typical Grade 60 rebar. The current literature contains very few tests conducted on A706-80 reinforced columns, so the report presents various examples of reinforced concrete members built with high strength rebar to consider the performance relative to normal strength steel reinforcement. First, the chapter includes mechanical properties of A706 Grade 80 rebar. Next, a review of experimental tests on reinforced concrete members constructed with A706-80 rebar is included. Finally, the chapter briefly summarizes other experimental tests with reinforced concrete members constructed with other high strength rebar ($f_y \geq 80$ ksi). In addition to reviewing current research on high strength rebar, this chapter also examines relevant literature concerning cyclic rebar behavior and bar fracture induced by buckling.

2.1. ASTM A706 Grade 80 Reinforcement

2.1.1. Overby, Kowalsky, and Seracino (2015)

Overby et al. (2015) conducted 788 tensile tests on ASTM A706 Grade 80 rebar in order to develop a statistically defendable stress-strain curve for A706-80 rebar. Prior to their project, very few tensile test results were found in the literature with data on the stress-strain relationship of A706-80 rebar. For the tensile tests, rebar of sizes 4 through 18 were obtained from three different rebar production mills, with three different heats from each mill, in order to develop a statistically significant dataset for future design values. An extensometer recorded strain data, while an optical non-contact optical positioning system enabled the measurement of strain over the length of the rebar. Researchers found that the strain increased uniformly over the length of the bar until the rebar began necking.

The report presented several mechanical properties that are important for material modeling: elastic modulus, yield stress, yield strain, strain at the onset of strain hardening, ultimate tensile stress, and strain at ultimate tensile stress. The elastic modulus was found by evaluating the slope of the stress-strain curve between 20% and 80% of the yield stress. The yield stress was

measured three ways: the Autographic Diagram Method (ADM) or "top of knee," the 0.2% offset method, and the 0.0035 Extension under Load (EUL) method. The "top of knee" method was found to be the most accurate. Yield strain was found for each calculation of yield stress, but the strain at the "top of knee" stress was used for parameter recommendations. The strain at the onset of strain hardening was found as the strain at the intersection of the horizontal line intersecting with the 0.2% offset yield stress and the line tangent to the stress-strain curve at the onset of strain hardening. Ultimate stress was the maximum tensile stress in the member and the corresponding strain as the ultimate strain, which is sometimes referenced as uniform elongation.

One of the major restrictions on using A706-80 rebar in new design is the relative recent introduction into the ASTM standard (December 2009). The final deliverable of their project increased the available material data on A706-80 rebar to provide a statistically reliable dataset to use in design.

Due to the large dataset, statistical analysis was provided for each design parameter. They found little variation in the material properties of the A706-80 rebar between bar sizes and between reinforcing mills. They recommended that any "off the shelf" batch of A706-80 rebar should have similar material properties.

The researchers also performed strain-aging tests over multiple lengths of time and multiple environmental conditions. These tests concluded that A706-80 rebar did not experience strain-aging similar to A706-60 rebar, likely due to the higher vanadium content in the A706-80 rebar.

Table 2-1 includes the final design recommendations from this report.

Table 2-1. A706-80 design parameters (Overby et al., 2015)

	Notation	Value	Units	St. Dev.	CV
Modulus of elasticity	E_s	29000	ksi	--	--
Specified minimum yield strength	f_y	80	ksi	--	--
Expected yield strength	$f_{ye\ (mean)}$	85	ksi	3.03	3.56%
Nominal yield strain	ε_y	0.0028		--	--
Expected yield strain	$\varepsilon_{ye\ (mean)}$	0.0033		0.0003	9.03%
Specified minimum tensile strength	f_u	100	ksi	--	--
Expected tensile strength	$f_{ue\ (mean)}$	112	ksi	3.65	3.24%
95th percentile tensile strength	$f_{ue\ (95\%)}$	119	ksi	--	--
Ultimate tensile strain	$\varepsilon_{su\ (mean)}$	0.0954		0.0055	5.8%
5th percentile ultimate tensile strain	$\varepsilon_{su\ (5\%)}$	0.0845		--	--
Onset of strain hardening	$\varepsilon_{sh\ (mean)}$	0.0074		0.0019	26.17%

2.1.2. Slavin and Ghannoum (2015)

This project was conducted as the first stage in a series of tests performed at the University of Texas at Austin investigating the use of high strength reinforcement in the design of reinforced concrete structures. Their motivation was to encourage the use of high strength reinforcement in design and to change the design code restrictions on high strength reinforcement.

While current literature contains information about the monotonic stress-strain curve of A706-80 rebar, the authors sought to examine the cyclic fatigue behavior of high strength rebar. In addition, their report gives an overview of the traditional methods used for increasing the strength of rebar: quenching and tempering, and microalloying. They found that process of quenching and self-tempering (QST) results in bars with relatively low tensile to yield (T/Y) strength ratios, but higher strains at fracture. Reinforcement created through a standard microalloying process, however, had relatively high T/Y ratios and high strains at fracture. Currently, A706 Grade 80 bars are produced with the micro-alloying process because this process preserves the ductility and weldability of the bars, and the QST rebar does not meet the 1.25 limit on T/Y in ASTM A706.

Cyclic tests were performed on #5, #8, and #11 rebar from two different mills of A706-60 and A706-80 as well as Grade 100 rebar (for which there was no specification). Manufacturer 1 used microalloying, Manufacturer 2 used a combination of microalloying and QST to produce higher strength rebar. The cyclic loading was bounded by strains of +4% and –1% for all members, but the loading protocol changed for each depending on the specimen size.

Monotonic tensile tests were conducted on three sample coupons from each of the tested bars. Table 2-2 shows the results of these tests. Little variation was seen in material properties for different rebar sizes or manufacturers, and the results are consistent with Overby et al. (2015) test results.

Table 2-2. Rebar stress vs. strain values (Slavin and Ghannoum, 2015)

Bar Size	Manuf-acturer	Grade	Yield Strength (ksi)	Tensile Strength (ksi)	T/Y Ratio (unitless)	Elastic Modulus (ksi)	Uniform Strain (%)	Fracture Strain (%)	Percent Difference in Fracture and Uniform Strains
#11	1	60	67.0	97.1	1.45	28,300	11.9	21.7	82%
		100	103.4	128.8	1.27	28,300	8.3	11.7	42%
	2	60	62.7	91.1	1.45	29,200	11.4	18.1	59%
		100	99.6	118.9	1.19	28,300	6.7	9.9	48%
#8	1	60	63.2	93.7	1.48	26,900	11.6	18.8	73%
		80	80.3	110.0	1.37	27,400	10.0	16.7	67%
		100	101.5	128.5	1.27	30,100	8.1	11.6	42%
	2	60	61.5	103.1	1.68	25,800	9.5	14.5	53%
		100	104.6	123.8	1.18	31,400	6.2	9.8	58%
#5	1	60	68.5	95.8	1.40	30,700	10.0	14.4	45%
		80	83.3	107.1	1.28	26,900	9.5	13.7	45%
		100	111.0	134.9	1.22	26,000	8.8	11.6	32%
	2	60	72.4	104.3	1.44	28,300	10.0	15.3	54%
		80	83.6	105.0	1.26	26,900	9.7	13.9	43%
		100	106.8	127.7	1.20	28,100	7.6	10.8	43%

Additionally, reinforcement with a higher yield strength was shown to have decreased deformation capacities and lower strains at ultimate strength, as seen in Figure 2-1.

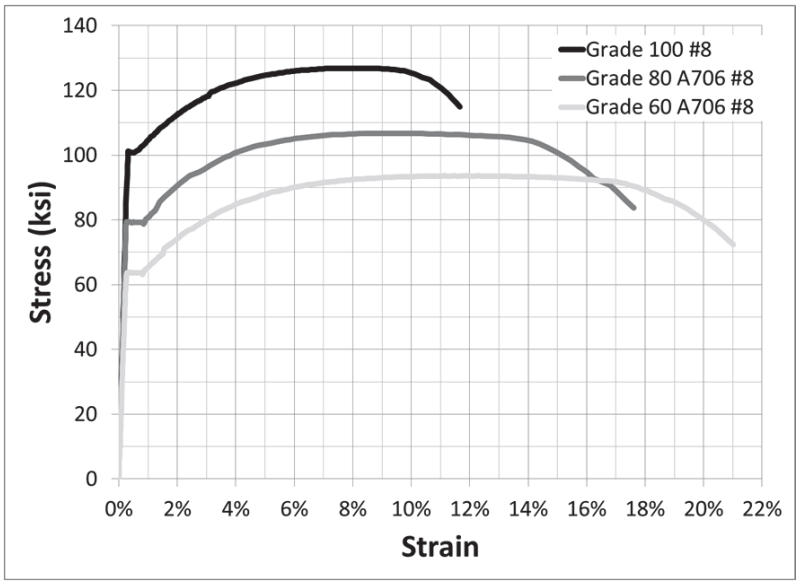

Figure 2-1. Comparison of stress-strain curves (Slavin and Ghannoum, 2015)

The researchers also performed many low-cycle fatigue tests. Rebar with higher clear spans had lower fatigue life, which was measured by the amount of cycles to fracture at the loading protocol. This was likely because rebar is more prone to buckle with longer clear lengths. Buckling introduces a combination of axial and bending loads, which likely result in decreased performance. They observed that fatigue life of the A706-80 bars from Manufacturer 2 (QST) exhibited much better fatigue performance than those from Manufacturer 1. No definitive conclusions were derived from the capacity of A706-80 bars to resist cyclic loading due to the insufficient amount of test specimens. The authors recommended a reduction of the clear span limit from $6d_b$ to $4d_b$ for high strength reinforcement to increase cyclic capacity.

2.2. ASTM A706 Grade 80 Reinforced Concrete Columns

2.2.1. Trejo, Barbosa, and Link (2014)

Trejo et al. (2014) conducted six lateral cyclic load tests on circular reinforced concrete columns at Oregon State University. The motivation for the experiments came from a desire to use high strength rebar in plastic hinge members. The Oregon Department of Transportation's (ODOT) Bridge Design and Drafting Manual allows the use of A706 Grade 80 rebar in bridge decks, drilled shafts, crossbeams, and end beams but not in members designed to form plastic hinges. In addition, ODOT does not allow spiral reinforcement with yield strengths higher than 60 ksi. Table 2-3 shows

the test matrix for each of the six columns. All of the columns had a diameter of 24 inches and #3 bar spiral reinforcement with a spacing of 2.5 inches. The columns had 1.25-inch concrete cover.

Table 2-3. Test matrix for Trejo et al., (2014)

Tests	Shear span ratio M/VD	Design concrete strength, f'_c	Longitudinal reinforcement	Transverse reinforcement
C1	6	4 ksi (30 MPa)	ASTM A706 Grade 60 ksi (420 MPa) 16 #5 (#16M) ρ_l = 1.11%	ASTM A706 Grade 60 ksi (420 MPa)
C2	6	4 ksi (30 MPa)	ASTM A706 Grade 80 ksi (550 MPa) 12 #5 (#16M) ρ_l = 0.83%*	ASTM A706 Grade 80 ksi (550 MPa)
C3	6	4 ksi (30 MPa)	ASTM A706 Grade 60 ksi (420 MPa) 22 #6 (#19M) ρ_l = 2.19 %	ASTM A706 Grade 60 ksi (420 MPa)
C4	6	4 ksi (30 MPa)	ASTM A706 Grade 80 ksi (550 MPa) 16 #6 (#19M) ρ_l = 1.58%	ASTM A706 Grade 80 ksi (550 MPa)
C5	3	4 ksi (30 MPa)	ASTM A706 Grade 60 ksi (420 MPa) 22 #6 (#19M) ρ_l = 2.19 %	ASTM A706 Grade 60 ksi (420 MPa)
C6	3	4 ksi (30 MPa)	ASTM A706 Grade 80 ksi (550 MPa) 16 #6 (#19M) ρ_l = 1.58%	ASTM A706 Grade 80 ksi (550 MPa)

Each pair (C1 and C2, C3 and C4, C5 and C6) were designed with comparable nominal moment capacities considering the differences in reinforcement yield strength to compare performance of columns reinforced with Grade 60 rebar to the less congested Grade 80 reinforced columns. Each column was loaded with one cycle at 0.25” increments until 1.25”, then cycles at 1.25” until 10” for columns C1 to C4 and half for C5 and C6. Displacements were measured by string pods on the specimen and strains measured by strain gages placed on reinforcing bars. Each of the columns had an axial load of $0.05*A_g f'_c$.

In comparing the performance of the pairs of columns, column C2 (reinforced with A706-80) performed better than C1 as bar fracture was observed in C2 at a larger displacement than C1. It was also noted that bar fracture occurred at a higher elevation in column C2 than C1, signifying that the plastic hinge zone and/or development length may need to be extended for the high strength rebar. Additionally, the force versus displacement hysteretic loops were similar for each column, but column C1 had more area between the loading and unloading curves than C2, representing the

fact that column C1 dissipated more energy (193 kip-ft versus 150 kip-ft at failure as seen in Figure 2-2). The other column pairs had similar displacements at bar fracture, as well as relative amounts of energy dissipation.

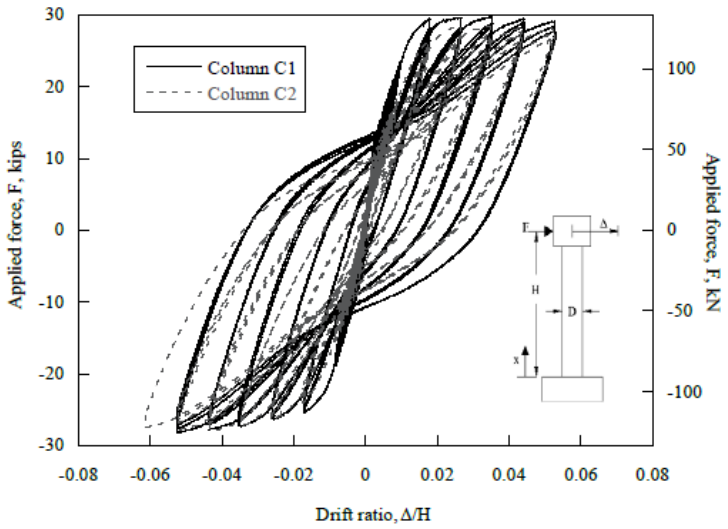

Figure 2-2. Force-displacement response of column C1 of Grade 60) vs. column C2 of Grade 80 (Trejo et al., 2014)

The failure mode of each of the columns was observed to be buckling of longitudinal bars, followed by bar rupture. The yield displacement increased as the yield strength increased, yet the ultimate drift ratio for the columns reinforced with Grade 80 was either equal to or higher than the ultimate drift ratio for columns with Grade 60. The energy dissipation was also found to be less in the Grade 80 columns than in the Grade 60. The authors believed this might be because the columns reinforced with Grade 60 rebar had a higher area of longitudinal steel than the corresponding Grade 80 columns. This resulted in the Grade 60 columns being stiffer, which can increase energy dissipation capacity. This hypothesis was supported by showing that energy dissipation was a function of amount of reinforcement rather than reinforcement grade. Overall, the researchers found that the columns with Grade 80 rebar performed similarly or better than Grade 60 columns. The authors recommended that A706-80 rebar should be considered for use in any reinforced concrete member.

2.2.2. Sokoli and Ghannoum (2016)

Sokoli and Ghannoum (2016) conducted three large-scale column tests on square columns subjected to high shear stresses and relatively high axial loads. The columns were reinforced with rebar of A706-60, A706-80, and an unspecified Grade 100. Their research was motivated by the observation that higher strength rebar signifies an increase of strain at yield. This translates to larger strains at service loads, indicating increased crack widths and deflections. Larger crack widths can weaken the concrete shear transfer mechanisms and reduce the shear strength of the element. In addition, similar compressive and tensile forces in the members would lead to higher forces in the reinforcement due to the concentration of forces on members with smaller diameter or fewer members in number. These relatively higher compressive forces have the potential to increase the bar buckling susceptibility, while the higher tensile forces result in increased bond demands and could increase bond slip.

The research team constructed three large-scale columns with the same reinforcing detail with 12 longitudinal bars and transverse hoops spaced at 5.5 inches (4.5 inches for Grade 100 columns). The columns reinforced with Grade 60 rebar used #10 longitudinal bars and #5 transverse hoops, while the Grade 80 column used #9 longitudinal bars and #4 transverse hoops. The third column used #8 bars for longitudinal reinforcement of Grade 100 and #3 hoops for transverse reinforcement of Grade 120. The expected plastic moment strength of each of the columns was approximately 7500 kip-inches while the peak shear demand was approximately 178 kips. Each column had concrete of 4.5 ksi and an axial load of 370 kips; the design axial load ratio was 27% of $A_g f'_c$.

The columns were subjected to lateral cyclic loads of the following drift ratios: 0.2, 0.3, 0.4, 0.6, 0.8, 1.0, 1.5, 2.0, 3.0, 4.0, 5.5, and 7.0%. Table 2-4 shows the column behavior at various damage limit states. After the columns began to lose axial load carrying capacity, the axial load was reduced, and the columns were laterally loaded to failure. In each column, longitudinal bars did not buckle, but load carrying capacity was lost when severe cracks occurred and concrete cover spalled.

Table 2-4. Column performance at various limit states (Sokoli and Ghannoum, 2016)

	CS60		CS80		CS100	
	V, kip (kN)	Drift ratio, %	*V*, kip (kN)	Drift ratio, %	*V*, kip (kN)	Drift ratio, %
First longitudinal reinforcement yield	164 (730)	1.60	148 (658)	1.00	150 (667)	1.23
First transverse reinforcement yield	159 (707)	3.10	–170 (–756)	–2.00	–98 (–436)	4.00
First flexural crack	–76 (–338)	–0.30	98 (436)	0.40	–85 (–378)	–0.40
First inclined crack	104 (462)	0.60	101 (449)	0.60	103 (458)	0.60
Peak lateral load	176 (782)	2.90	178 (792)	1.90	169 (752)	2.00
Initiation of lateral strength loss	144 (640)*	5.20*	–150 (–667)*	–4.60*	158 (702)†	–3.00†
Initiation of axial failure	135 (601)	5.80	–112 (–498)	–5.50	NA	12.00‡

The columns constructed with Grade 60 and 80 rebar showed stable lateral load carrying capacity up to a drift ratio of 5.5%. A stable response up to a drift ratio of 4% is typically seen as the base performance standard for the maximum considered earthquake. Additionally, there was little difference noted in the different crack widths between the three specimens. In terms of the shear strength of the columns, columns with both Grade 60 and Grade 80 reinforcement sustained large inelastic deformations prior to failure. This signifies that the Grade 80 hoops were effective in preserving the concrete core up to a drift ratio of 5.5%. In addition, the columns did not experience bond failure, which the researchers interpreted as signifying that the development length equations in ACI 318 are overly conservative and may need to be adjusted.

Figure 2-3 shows the lateral load versus lateral drift ratio for the Grade 60 and 80 columns. As observed in the Trejo et al. (2014) tests, the force-displacement response of the columns with Grade 60 rebar was slightly “fatter” than that of the Grade 80 rebar, signifying an increase in the hysteretic energy dissipation capacity for the columns reinforced with a larger amount of lower grade rebar. In conclusion, the authors found that the Grade 80 reinforcement was effective at producing the shear transfer necessary for concrete columns under lateral loads, and Grade 80 performed similarly to Grade 60.

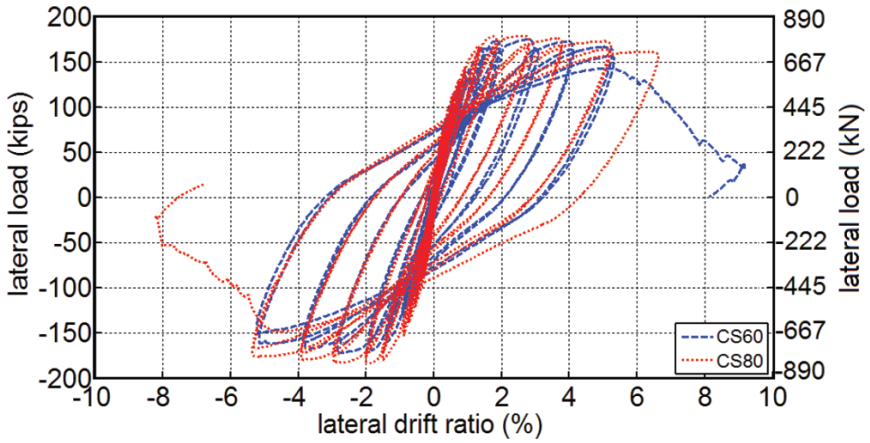

Figure 2-3. Force-displacement response for Grade 60 and 80 columns (Sokoli and Ghannoum, 2016)

2.2.3. Rautenberg, Pujol, Tavallai, and Lepage (2013)

Rautenberg et al. (2013) performed tests on eight square columns with rebar of ASTM A706 Grades 60 and 80 and ASTM A1035 Grade 120. The motivation behind this project was to encourage the use of high strength rebar in reinforced concrete columns.

The failure modes of seven out of the eight columns was buckling in the longitudinal reinforcement in the compression cycle followed by bar fracture. One of the columns had a bar fracture in tension without evidence of bar buckling, which caused a loss in lateral load-carrying capacity. For the bars that buckled, visible buckling occurred when the column was vertical, signifying that the cracks that had formed earlier by the loading cycles entering inelastic regions had not closed and by bringing the column back to zero displacement, the elongated bar buckled. Table 2-5 shows the test matrix for these column tests, and Table 2-6 shows the shear force and drift ratio at first yield and ultimate displacement.

From the data, the columns reinforced with high strength rebar had drift capacities approximately 80% of the columns reinforced with Grade 60 reinforcement. More analysis was done on the columns reinforced with Grade 120 than the Grade 80 columns, but the researchers found that the Grade 120 columns had a much lower amount of energy dissipated than those reinforced with Grade 60 rebar. The authors hypothesized that this was due to the reduction in post-cracking stiffness because of the reduction of longitudinal steel area. Overall, the columns

reinforced with high strength rebar had comparable drift capacities to those reinforced with Grade 60 rebar.

Table 2-5. Test matrix for Rautenberg el al. (2013)

Specimen	Longitudinal reinforcement							f'_c, psi (MPa)	P, kips (kN)	P/f'_cA_g
	ASTM standard	Quantity*	d_b, in. (mm)	ρ_g, %	f_y†, ksi (MPa)	f_u, ksi (MPa)	ε_u (200 mm), %			
CC-3.3-10	A706/A706M Grade 60	6	7/8 (22)	3.3	66 (455)	94 (648)	23.4	5200 (36)	65 (290)	0.11
HC-2.2-10	A706/A706M Grade 80	4	7/8 (22)	2.2	83 (572)	118 (814)	14.0	7750 (53)	84 (375)	0.10
UC-1.6-10	A1035/A1035M Grade 120	4	3/4 (19)	1.6	133 (917)	168 (1160)	8.6	5300 (37)	64 (285)	0.11
CC-3.3-20	A706/A706M Grade 60	6	7/8 (22)	1.6	64 (441)	92 (634)	20.3	7800 (54)	169 (750)	0.20
HC-2.2-20	A706/A706M Grade 80	4	7/8 (22)	2.2	83 (572)	118 (814)	14.0	7850 (54)	170 (755)	0.20
UC-1.6-20	A1035/A1035M Grade 120	4	3/4 (19)	1.6	133 (917)	168 (1160)	8.6	6300 (43)	140 (620)	0.21
CC-2.4-20	A706/A706M Grade 60	6	3/4 (19)	2.4	65 (448)	91 (627)	16.4	5250 (36)	108 (480)	0.19
UC-1.1-20	A1035/A1035M Grade 120	4	5/8 (16)	1.1	134 (924)	165 (1140)	9.0	5350 (37)	116 (515)	0.20

Table 2-6. Column yield and ultimate limit states (Rautenberg et al., 2013)

Specimen	V_y, kips (kN)	θ_y, %	V_u^*, kips (kN)	v_u^*, $\sqrt{f'_c}$ psi (MPa)	θ_u†, %
CC-3.3-10	45.7 (203)	0.9	46.3 (206)	6.0 (0.49)	10.0
HC-2.2-10	43.1 (192)	1.0	45.5 (202)	4.8 (0.40)	7.0
UC-1.6-10	42.3 (188)	1.7	48.0 (214)	6.1 (0.51)	8.0
CC-3.3-20	58.0 (258)	0.9	60.0 (267)	6.3 (0.52)	5.0
HC-2.2-20	52.5‡ (234)	1.0	54.7‡ (243)	5.7 (0.47)	4.0
UC-1.6-20	47.0 (209)	1.5	51.3 (228)	6.0 (0.50)	4.5
CC-2.4-20	41.0 (182)	0.9	41.6 (185)	5.3 (0.44)	8.0
UC-1.1-20	34.1 (152)	1.4	37.0 (165)	4.7 (0.39)	4.0

2.3. High Strength Rebar in Reinforced Concrete Members

This section will examine a few of the topics of interest when examining the current literature for experimental tests performed on reinforced concrete members using high strength

rebar. High strength rebar signifies reinforcing steel with a yield strength equal to or greater than 80 ksi.

2.3.1. Sufficient Displacement Capacity

Throughout the literature, cyclic tests on concrete members reinforced with high strength rebar have returned satisfactory results for application in seismic design. These tests can be divided into columns, beams, and beam-column joints.

Tests performed on square columns comparing reinforcing steel with yield strengths of 52 ksi and 100 ksi by Okamoto et al. (2004) both experienced similar failure mechanisms (longitudinal bar buckling) after three cycle set displacements at similar levels of displacement (3.5% drift ratio). Sun et al. (2013) conducted tests on columns reinforced with 210-ksi reinforcing steel, which sustained cyclic lateral load up to a drift of 5%. Xiao et al. (2008) suggested that using both high strength and normal strength longitudinal bars offers the best option for increasing deformation and strength capacity in column tests. They also found that columns reinforced with high strength bars (145-ksi) produced stable cyclic hysteresis loops. Columns tested by Restrepo et al. (2006) comparing reinforcement with yield strength 60 ksi and 100 ksi found that the behavior of both was ductile, but they used butt-welded hoops for transverse steel in the columns reinforced with high strength rebar. The spirals failed at the heat-affected region causing a loss of load carrying capacity at a much lower level of displacement.

Tests performed by Hassan et al. (2008), found that beams reinforced with Grade 100 rebar performed better than comparable beams with Grade 60 rebar, as the failure mode was more ductile since the specimens with high strength reinforcement experienced higher levels of deformation prior to failure.

The literature also includes high strength rebar in beam-column joints. In tests performed by Chang et al. (2014), rectangular beam-column joints with ASTM A1035 Grade 100 reinforcement achieved a drift ratio greater than 5% before failure, and exceeded the plastic hinge rotation limit imposed by FEMA 356. Brooke el al. (2006) also tested beam-column joints with 72.5-ksi reinforcing steel and found them to fail at 4% drift.

2.3.2. Hysteretic Energy Dissipation

One common theme in the literature regarding cyclic force-displacement responses of normal strength and high strength rebar for reinforced concrete members was the reduction in hysteretic energy dissipation. Similar to the results seen in Trejo et al. (2014), the hysteretic energy dissipation has been calculated by numerical integration of the force-displacement hysteresis at different levels of ductility. In square column tests performed by Okamoto et al. (2004), the researchers noticed a reduction in area under the force-displacement hysteresis for the members reinforced with high strength rebar and proposed that the equivalent viscous damping be adjusted to 75% of the value used for normal strength reinforcement. The normal strength rebar had a yield strength of 52 ksi and the high strength rebar was 100 ksi. In tests conducted by Sun et al. (2013), they also found the hysteresis loops to be very thin on columns constructed with longitudinal steel with a yield strength of 210 ksi. This can also be seen in tests on RC members with rebar having yield strengths of 97 ksi and 120 ksi performed by Lepage et al. (2012). Tests conducted by Wang et al. (2014) found that columns reinforced with 500 MPa (72.5 ksi) rebar had stable hysteresis loops and that the size of the loops (and corresponding hysteretic damping) could be increased by using smaller spacing of transverse steel. This would signify that a smaller transverse steel spacing would result in higher energy dissipation.

2.3.3. Localized Bond Slip

When concrete members incorporate high strength rebar into the design, one of the goals is to reduce the number of longitudinal bars in the section while maintaining the same strength as when a higher area of normal strength reinforcement is used. This reduction of required longitudinal steel area leads to higher stresses on the embedded longitudinal bars. In tests conducted by Hassan et al. (2008), beams reinforced with Grade 100 rebar had larger deformations than those reinforced with Grade 60 rebar. The assumed cause of the higher deformations was higher localized bond slip due to the comparably higher strains in the high strength rebar. Tests performed by Restrepo et al. (2006) found that the expressions for plastic hinge length and spread of plasticity that were presented by Priestley et al. (1996) underestimated the actual plastic hinge length for Grade 100 reinforced members due to the increased strain penetration length of the high

strength rebar. These papers indicate that the development length and strain penetration length may need to be examined and adjusted before the use of high strength rebar becomes standard in design.

2.3.4. Strain Limit States

Numerous strain limits can be evaluated for high strength rebar reinforced concrete. At the lowest level, it is well established that yield curvature is proportional to yield strain (Priestley et al., 2007). As a result, the yield displacement of members with higher strength rebar will be larger than that of members with lower strength rebar. Beyond that, Shahrooz et al. (2014) is the only paper known to the author to suggest a change in the design strain limits for high strength rebar. The authors suggest that the limit to ensure tensile behavior be changed from 0.005 to 0.008 and compressive behavior changed from 0.002 to 0.004.

2.4. Summary of Column Literature

In order to accomplish the goals of performance-based seismic design, accurate evaluation of non-linear behavior is essential. This in turn requires accurate models for spread of plasticity, damage-based strain limit states, and hysteretic energy dissipation. Since Grade 80 rebar was introduced into ASTM A706 standards in 2009, to the knowledge of the authors, there have been three sets of cyclic experimental tests on concrete columns reinforced with A706 Grade 80 rebar. Due to the lack of experimental data, this report examines various experimental studies performed on high strength rebar in order to find possible areas of interest for future experimental study. When compared to normal strength rebar, members reinforced with high strength rebar typically have exhibited slightly reduced levels of hysteretic damping. Additionally, research suggest that the current prediction methods for bond slip may not be accurate when applied to high strength rebar.

After a review of the current available literature, equivalent viscous damping and strain penetration depth will be of particular interest in the experimental portion of the research, in addition to spread of plasticity and damage-based strain limit states. These values will be compared

to the data available from Goodnight et al. (2015) who tested 30 columns reinforced with A706 Grade 60 rebar.

2.5. Buckling Induced Fracture

Cyclic performance of steel reinforcement is a key parameter when considering the seismic performance of a reinforced concrete structure. With the advent of modern detailing practices, plastic hinge members fail by the fracture of previously buckled longitudinal bars under the cyclic loads of a seismic event. Many researchers have often referred to the fracture of previously buckled longitudinal reinforcement as low-cycle fatigue failures (Mander, 1983; Chai, 1991, Haber et al., 2013). Researchers have studied this failure mode for many years and ASTM includes a standard for this type of fatigue testing (ASTM E606).

While fatigue loading does result in crack propagation in the rebar that eventually lead to fracture, buckled longitudinal steel is subjected to axial loads and bending loads. This failure mechanism is more complex than a typical fatigue test. Kunnath et al. (2009), who studied the low-cycle fatigue performance of large diameter bars, noticed a reduction in cyclic performance if the bar buckled. They also observed that when the bar was subjected to high compressive strain demands that resulted in buckling, the bar fractured on the subsequent pull cycle. Ghannoum and Slavin (2016) also observed a reduction in low-cycle fatigue capacity at higher clear span ratios. At higher clear span ratios, rebar experience more buckling, signifying that buckling influences fatigue performance.

Some researchers, however, believe that low-cycle fatigue does not properly characterize the failure mode of longitudinal reinforcement in plastic hinge members. Restrepo-Posada (1992) suggested a buckled bar would fracture on the subsequent tensile cycle if the compressive capacity of material were exceeded. Compressive cracks have been a well-documented occurrence as Gerber and Fuchs (1968) showed evidence of crack formation when specimens were unloaded from high compressive stresses. Cracks were more likely to form at stress concentrations and areas with residual tensile stresses. Jhmab and MacGregor (1974) showed that in reinforcing bars, compressive stresses concentrate at the base of the ribs. Restrepo-Posada (1992) showed evidence of these compressive cracks by photographing the cross-section of a buckled bar with an electron

microscope, as seen in Figure 2-4. The "compression cracks" compromise the tensile capacity of the bar, leading to premature fracture under tensile loads. While Figure 2-4 seems to indicate that the material has cracked under a compressive stress, due to the presence of the rib, the local stress is likely in a state of shear stress at the base of these ribs (Restrepo, 2018, personal communication). High shearing stresses likely weaken the material so that when the compressive load is relaxed, the cracks easily propagate through the affected region.

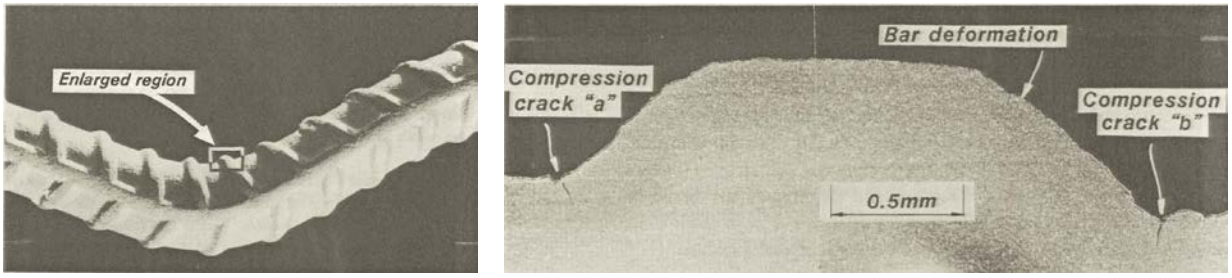

(a) **(b)**

Figure 2-4. (a) Buckled bar; (b) Cracks at base of rebar rib (Restrepo-Posada, 1992)

CHAPTER 3. SPECIMEN DESIGN, TEST SETUP AND INSTRUMENTATION

3.1. Specimen Geometry

Each test specimen was designed as a scaled model of bridge column consisting of a footing, column, and loading cap. Figure 3-1 shows the dimensions of the single degree of freedom specimens. The footing geometry was determined to allow for development length of the column and footing longitudinal steel and to tie down the footing to the strong floor with post-tensioning bars. The loading cap was designed to allow axial load to be applied directly to the top of the specimen and to bolt a hydraulic actuator for lateral loading.

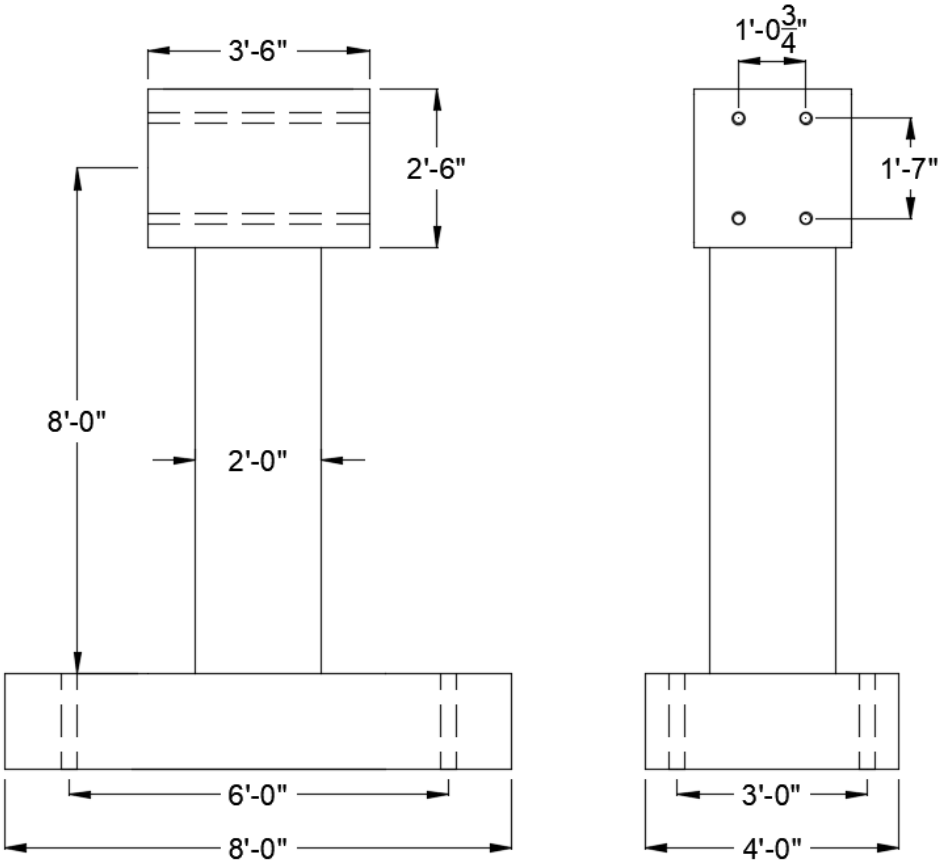

Figure 3-1. Test specimen geometry

The columns were reinforced entirely with A706-80 rebar (both transverse and longitudinal steel). Reinforcement details of the column were varied to represent realistic column details as well as to match columns that had been previously constructed and tested with Grade 60 rebar and are summarized in Table 4.1. The footing and loading cap were designed as capacity protected members using the over-strength shear and moment demands from the column. The longitudinal reinforcement of the footing consisted of six #9 bars and four #6 bars top and bottom. Joint shear forces were resisted using "Z" shaped longitudinal bars and eight #4 external J-hooks. Figure 3-2 shows the reinforcement details.

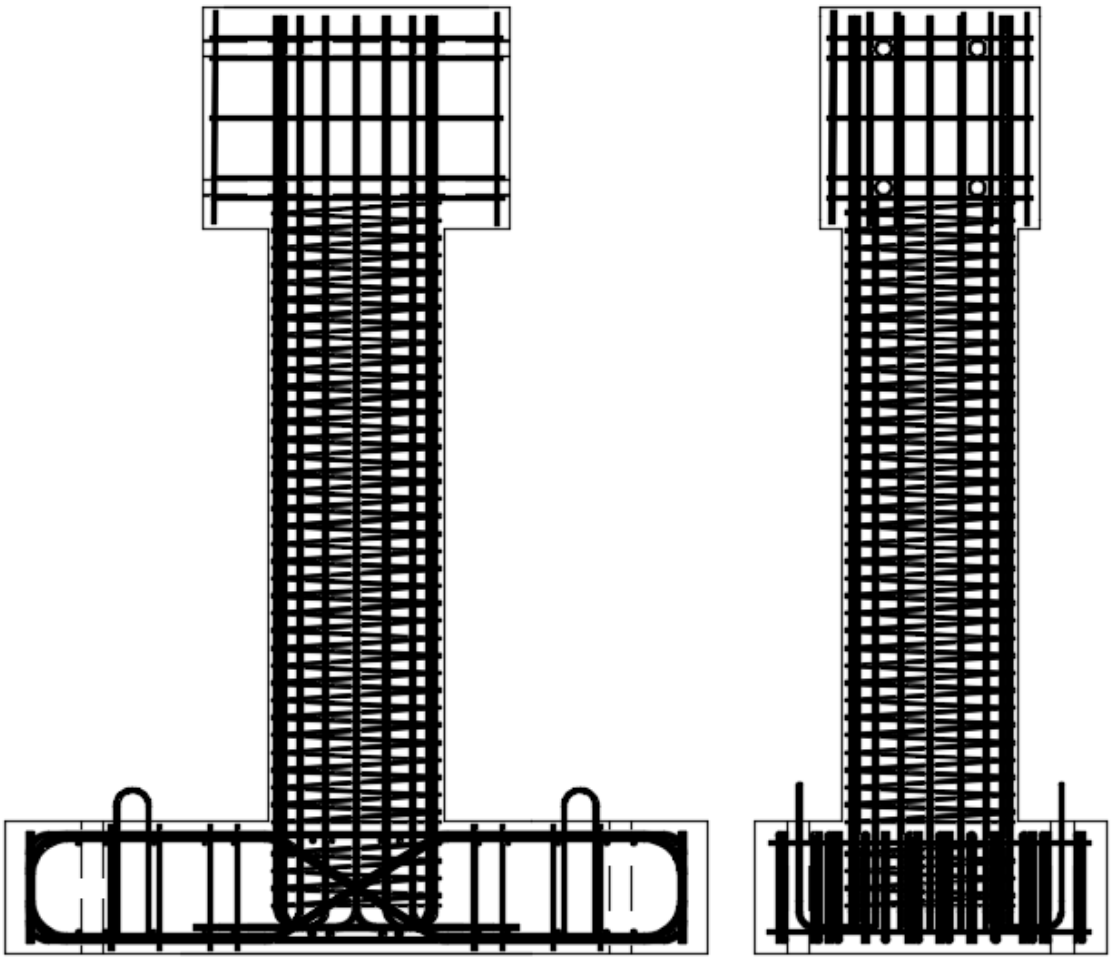

SIDE VIEW FRONT VIEW

(a) **(b)**

Figure 3-2. Reinforcement Plan

3.2. Construction Sequence

The reinforcement cage of the column was constructed in the lab using plywood forms and a crane to ensure accurate longitudinal bar placement and a straight column cage. The transverse reinforcing steel (spirals) was attached to the longitudinal reinforcing steel with loop ties while wood spacers and clamps maintained a consistent spiral spacing, as seen in Figure 3-3.

Figure 3-3. Tying column cage

The column longitudinal bars were bent to 90° to allow for adequate development. The tails of the bars closest to the extreme fibers of the column turned inward in order to enhance joint shear performance, while the other tails turned outward to improve column stability, seen in Figure 3-4(a). Figure 3-4(b) shows footing longitudinal "Z" bars tied to the bottom of the column cage and individual spirals added to the column longitudinal bars inside the footing.

Steel-ply formwork was used for the footing formwork and PVC pipes were added to the formwork in the locations where the specimen would be tied down to the strong floor. In addition, foam block-outs were placed on each side of the column where post-tension bars would be used to apply column axial load. Figure 3-5(a) shows the footing formwork. The column cage was then placed in steel-ply formwork and additional footing rebar was added, as seen in Figure 3-5(b). Figure 3-6(a) shows casting the footing concrete, and Figure 3-6(b) shows the column cage centered and leveled with ratchet straps as the footing concrete sets.

(a) **(b)**

Figure 3-4. (a) Column longitudinal bar tails; (b) Footing "Z" bars and column cage

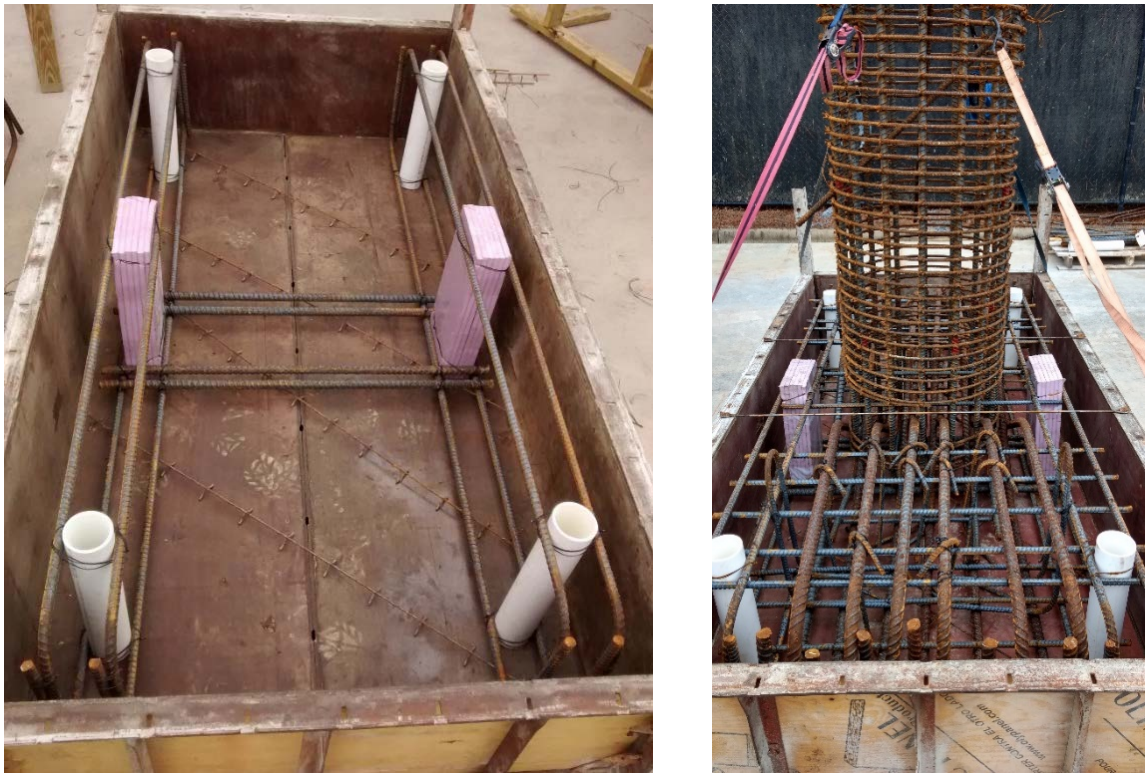

(a) **(b)**

Figure 3-5. (a) Footing formwork with block-outs; (b) Column and footing rebar

(a) **(b)**

Figure 3-6. (a) Pouring footing concrete; (b) Footing concrete setting

After the concrete cured, the footing formwork was removed and foam strips of widths equal to the clear distance between transverse reinforcement were tied to the longitudinal reinforcement between the spirals. These foam strips were wrapped with clear packing tape to prevent concrete from bonding to the strips. The strips blocked out the cover concrete so that the longitudinal and transverse reinforcing steel would be visible after concrete was poured. The foam strips can be seen attached to the column cage in Figure 3-7(a). With the cover concrete blocked out, optical markers (also referred to as LED's) could be placed on longitudinal and transverse reinforcement and an optical measuring system could be used to measure strains and deformations in the rebar throughout the cyclic test. As the inelastic action of the column in single bending would be concentrated near the base, only the lower half of the cover concrete was blocked out. A larger foam sheet covered the foam strips to further block out cover concrete, as seen in Figure 3-7(b).

A sonotube was then placed over the column cage as the column formwork, shown in Figure 3-8(a). A wooden frame was built to support the loading cap, seen Figure 3-8(b). The steel reinforcement for the loading cap and PVC pipes for actuator connection were placed in the formwork. Wood diagonal cross-bracing was used to ensure that the loading cap and specimen were level and square.

(a) **(b)**

Figure 3-7. (a) Cover concrete block-out strips; (b) Cover concrete block-out sheet

(a) **(b)**

Figure 3-8. (a) Sonotube installation; (b) Cap stub formwork and reinforcement

Figure 3-9(a) shows the completed column and loading cap formwork. The Sonotube was wrapped with plastic sheeting to prohibit moisture affecting the concrete and ratchet straps to

prevent the Sonotube from bursting. A forklift lifted a concrete skip to cast concrete in the column and loading cap, seen in Figure 3-9(b).

(a) **(b)**

Figure 3-9. (a) Column formwork; (b) Pouring column concrete

Following column concrete curing, the forms were stripped as seen in Figure 3-10(a). The block-out strips were removed and the concrete that remained on the longitudinal bars was removed with an air needle scaler, shown in Figure 3-10(b).

Next, the column was moved into the lab where it was placed on ½" fiber roofing boards. Gypsum cement was poured into the gap between footing and floor to ensure a level connection and to enhance the coefficient of friction between floor and specimen. Finally, the specimen was painted white and instrumentation was attached, as seen in Figure 3-10(c).

(a) **(b)** **(c)**

Figure 3-10. (a) Column without formwork; (b) Removing concrete from rebar; (c) Completed test specimen

3.3. Specimen Instrumentation

Lateral displacement of the specimen was measured by two string potentiometers attached to the center of the loading cap. The differences in these measurements indicated rotation of the column and torsional loading, which was negligible in each test. Linear potentiometers were attached to the footing to ensure that there was no slip or rotation of the footing under the reverse cyclic loading. Lateral force was measured by the load cell in the 110-kip hydraulic actuator. An MTS Universal Testing Machine regulated axial force with three hydraulic jacks connected in a closed hydraulic loop.

A 3D, non-contact optical position system, the Optotrak Certus developed by Northern Digital, Inc. (Northern Digital, Inc. 2011), was utilized to measure the strain as well as the deformation profile of longitudinal and transverse reinforcement. Figure 3-11 shows that since the cover concrete in the lower half of the column is blocked out, Optotrak markers can be placed directly on the longitudinal and transverse reinforcement. This optical measuring system captures the 3D position of each of these markers throughout the course of the test.

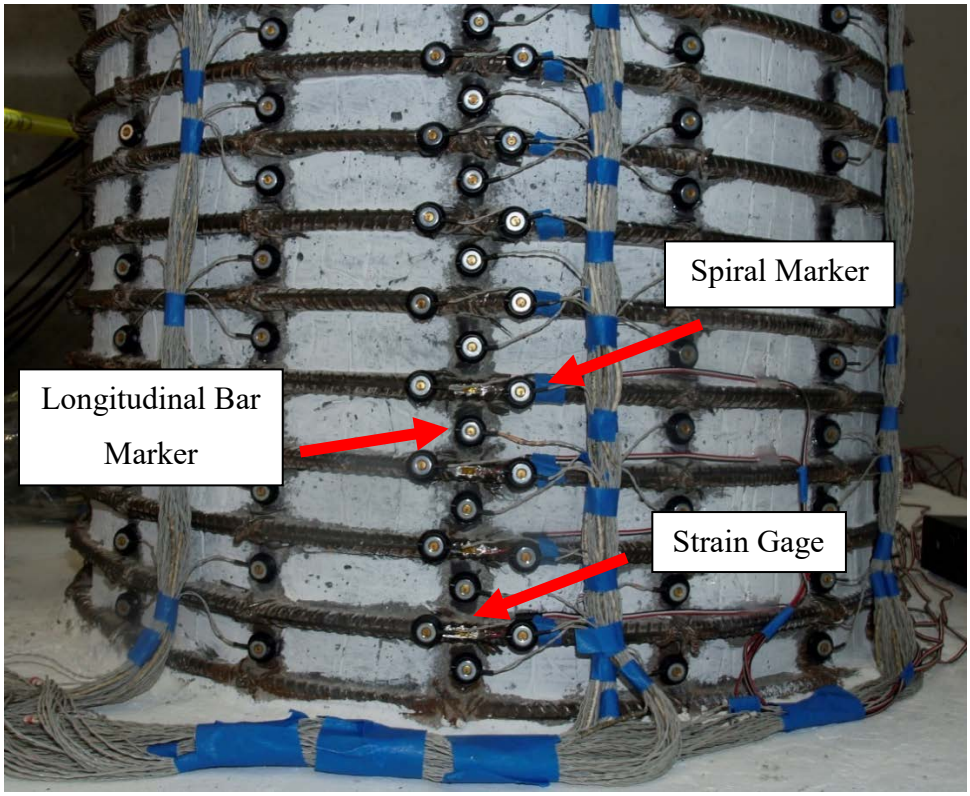

Figure 3-11. Optotrak markers in block-out region

The change in length between each marker can be calculated to find the strains at discrete locations along the longitudinal reinforcing steel. This technique represents a substantial improvement over the use of strain gages (which are unreliable when cast in reinforced concrete and subjected to high strains, especially for longitudinal reinforcing steel), and is superior to the use of external potentiometers which provide only a course representation of strains. Strains in the transverse spirals were also measured with the Optotrak system along with four electronic resistance strain gages attached to the four lowest spirals at the extreme tensile fiber of each side of the column, as seen in Figure 3-11.

3.4. Test Setup

The specimen was designed as a single degree of freedom bridge column in single bending with a fixed base. To ensure a fixed connection, gypsum cement was poured in the ½" space between the footing and laboratory strong floor. Then, four post-tensioning (PT) bars were run through the floor and specimen footing with approximately 80 kips in each bar.

Axial load was applied to the specimen by running two PT bars from the base of the strong floor, through the footing, to a spreader beam at the top of the column. Two 200-kip hydraulic jacks applied force on each PT bar. These two hydraulic jacks were connected in a closed hydraulic loop to a third jack in an MTS Universal Testing machine, as seen in Figure 3-12(a). This system kept the axial load at the desired level ±5 kips throughout the test.

(a) **(b)**

Figure 3-12. (a) 200-kip hydraulic jack in MTS Universal Testing Machine to regulate axial load; (b) Post-tensioning HSS for test setup

A 110-kip hydraulic actuator applied lateral load to the specimen. However, due to laboratory space restraints, the actuator could not be attached directly to the strong wall. Two HSS 12x8x½ tubes were connected to the strong wall with an HSS 4x4x½ and two PT bars, each with approximately 70 kips of force. When the actuator loaded the specimen in the push cycles, it would bear on the strong wall through a 1.5" plate and two smaller HSS tubes. The HSS 12x8 tubes acted as cantilevers when the actuator pulled the specimen and the force was translated to the strong wall with the PT bars. Figure 3-12(b) shows the PT bars holding the HSS tubes in the test setup. Figure 3-13 shows a conceptual render of the test setup, and Figure 3-14 shows a picture of the final test setup. For reference throughout this report, the side of the column closest to the actuator will be referred to as the South, and the opposite as the North, as indicated in Figure 3-14.

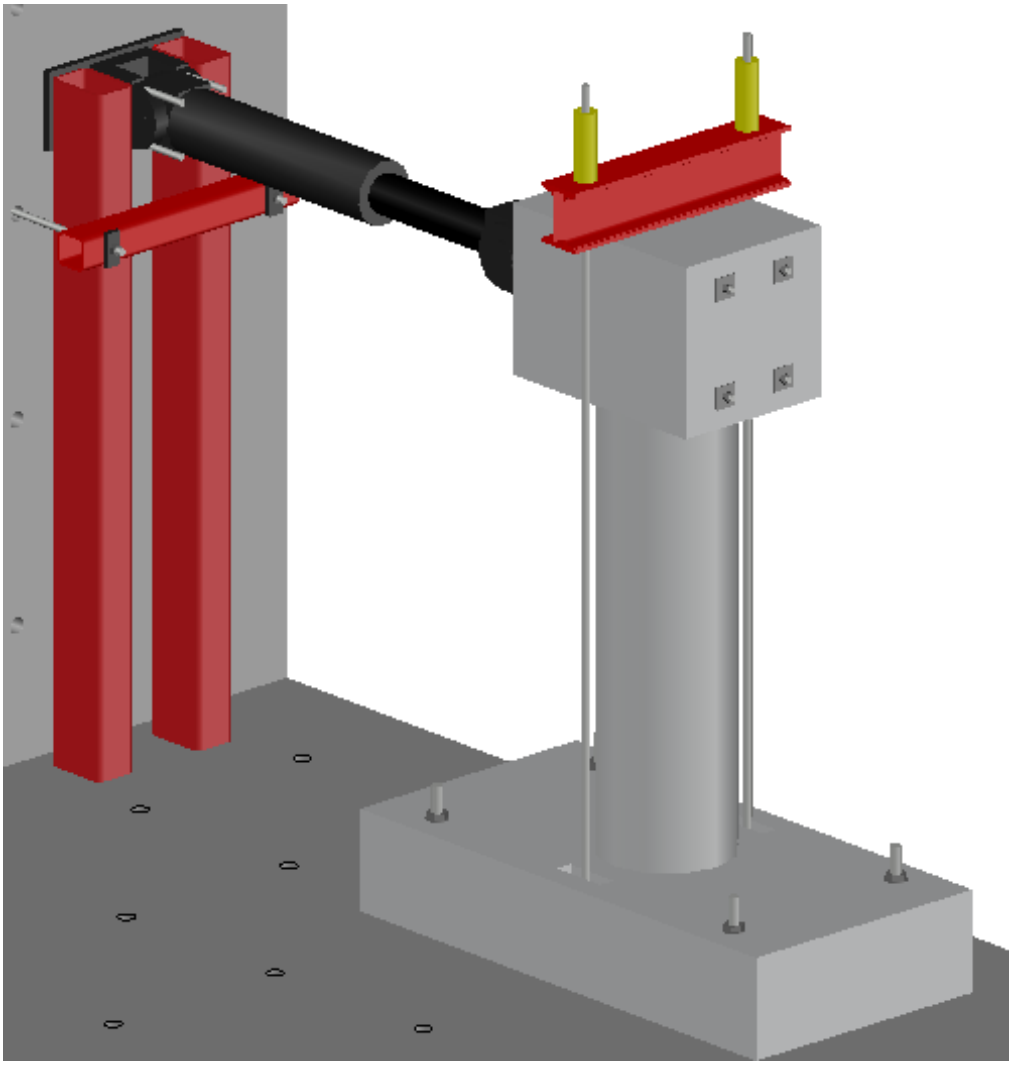

Figure 3-13. Conceptual test setup

Figure 3-14. Actual test setup

3.5. Footing Design

The footing and cap stub were designed as capacity protected members. As the column was loaded in single bending, the cap stub experienced very small moment demands. The footing, on the other hand, was subjected to large moment demands, and was designed for over-strength shear and moment demands to ensure the footing would remain elastic to resist excessive flexural or shear deformation of the footing

The joint shear design of the footing followed the procedure for joint shear design in Priestley et al. (1996). For the design of the footing, the maximum over-strength moment demand using over-strength material properties from the column was determined, and the footing was designed to this demand. Using the over-strength demand, the principle tensile and compressive

stresses in the joint were calculated to ensure they were below design limits. Following the tests, the actual joint shear stresses were calculated using the lateral and axial loads and material properties from the tests. The maximum principle stresses both occurred during column test two. The maximum principle compressive stress in the joint was 995 psi, which was below the limit of $0.3 \times f'_c = 2310$ psi. The maximum principle tensile stress in the joint was 330 psi, which is above the limit requiring special joint reinforcement ($3.5\sqrt{f'_c}$ = 307 psi), but below the maximum principle tensile stress allowed for joint shear ($5\sqrt{f'_c}$ = 439 psi). For special joint reinforcement, eight #4 "J" hooks were placed within 12 inches of the footing-column interface to anchor the joint compression strut. Furthermore, the three extreme fiber column longitudinal bars had their tails facing towards the center of the column to anchor the footing joint compression strut (other column longitudinal bar tails faced away from the center of the column for added stability during construction). The column transverse spirals also extended into the footing for added joint shear reinforcement. These details ensured that the joint was sufficiently protected from shear failure during the column tests.

CHAPTER 4. SUMMARY OF COLUMN TESTS

During phase one of this project, four reverse cyclic tests were performed on circular A706-80 RC columns. These four columns were constructed at the CFL on the campus of NCSU. Each column had different combinations of axial load ratio and transverse reinforcing steel ratio as shown in Table 4-1 below.

Table 4-1. Phase 1 column test matrix

Column Number	Dia.	L/D	Longitudinal Steel	Transverse Steel (Spirals)	Axial Load Ratio
1	24”	4	16 #6 (1.6%)	#3 @ 2” (1%)	5%
2	24”	4	16 #6 (1.6%)	#3 @ 2” (1%)	10%
3	24”	4	16 #6 (1.6%)	#3 @ 2.75” (0.7%)	5%
4	24”	4	16 #6 (1.6%)	#3 @ 1.5” (1.3%)	5%

The effects of each variable on plastic hinge length, bond slip, and nonlinear strain limit states for circular A706-80 RC bridge columns were observed during testing. Other parameters of interest included the spread of plasticity, bond slip and development length, and hysteretic energy dissipation. In addition, experimental results were compared to the prior results of the reverse cyclic tests on columns reinforced with A706-60 rebar. Comparisons were made between the plastic hinge lengths, bond slip and development lengths, hysteretic damping, and strain limit states.

Tensile tests were performed on the longitudinal and transverse reinforcement per ASTM A370. Figure 4-1 shows plots of the stress vs. strain curve for each material and Table 4-2 includes numerical results. The rebar used to construct each specimen came from the same production heat from the same mill; reinforcement properties remained the same in each test. Spiral stress-strain curves in Figure 4-1(b) are slightly different because the spirals were manually straightened in order to conduct materials tests. Cold working affects the material behavior by removing the yield plateau and decreasing strain capacity.

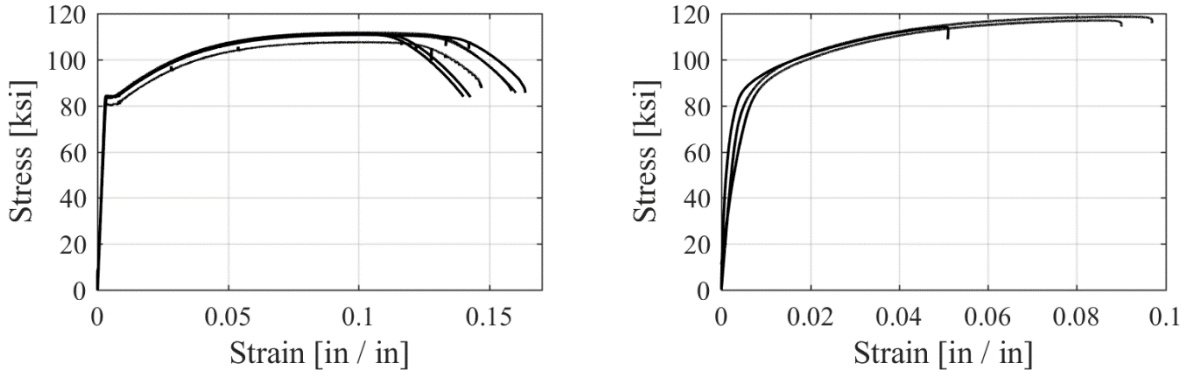

Figure 4-1. (a) Longitudinal steel stress-strain. (b) Transverse steel stress-strain curve

Table 4-2. Tensile test results

Bar	Yield Stress [ksi]	Yield Strain	Maximum Tensile Stress [ksi]	Strain at Max. Stress	T/Y Ratio
#6	83	0.29 %	110	10.4%	1.33
#3	79	0.48 %	117	7.6 %	1.48
Overby Average	85	0.33 %	112	9.5 %	1.32

Each column was subjected to three-cycle set loading. This load history consisted of single positive and negative cycles up to the theoretical force at which the reinforcement first yields (F_y) at levels of 0.25*F_y, 0.5*F_y, 0.75*F_y, F_y. The average of the positive and negative first yield displacement and the ratio of analytical first yield and nominal moments was used to calculate the equivalent yield displacement, as seen in Equation 4-1.

$$\Delta_y = \frac{M_N}{M'_y}\Delta'_y \qquad \text{Equation 4-1}$$

Increments of the equivalent yield displacement were used for the rest of the test, performing three positive and negative cycles at displacement ductility (μ) 1, 1.5, 2, 3, 4, 5, 6, 7, and 8. Displacement ductility is the ratio of current displacement to equivalent yield displacement. The test was completed when the column experienced at least a 20% loss in lateral strength capacity.

4.1. Column Test 1 Summary

Column Test 1 was conducted at the CFL on the campus of NCSU on Tuesday, May 30, 2017 as a part of a larger test matrix to evaluate the suitability of A706-80 rebar for use in seismic regions. The 8' specimen was subjected to a quasi-static three-cycle set loading and a constant 5% axial load ratio.

Table 4-3. Column Test 1 summary information

COLUMN PARAMETERS	
Longitudinal Steel:	(16) #6 A706-80 Bars
Transverse Steel:	#3 Spirals @ 2" Pitch
Longitudinal Steel Yield Strength:	83 ksi
Transverse Steel Yield Strength:	79 ksi
Test Day Concrete Strength:	5.8 ksi
Axial Load:	130 kips
Axial Load Ratio:	5%
Experimental First Yield Displacement:	0.78"
Analytical Nominal Moment Capacity:	546.9 kip*ft
Equivalent Yield Displacement:	1.05"
Maximum Lateral Force:	74.1 kips
Failure Mode:	Rupture of previously buckled reinforcement
DAMAGE OBSERVATIONS	
First Cracking North:	-½ Fy' = -0.33"
First Cracking South:	½ Fy' = 0.33"
Core Concrete Crushing North:	μ_2^{1+} = 2.10"
Core Concrete Crushing South:	μ_2^{1-} = -2.10"
Transverse Steel Yielding North:	At 3.14" during push to μ_3^{1+} = 3.15"
Transverse Steel Yielding South:	At -2.93" during pull to μ_4^{1-} = -4.20"
Longitudinal Bar Buckling North	During reversal from μ_6^{1-} = -6.50"
Longitudinal Bar Buckling South	During reversal from μ_6^{1+} = 6.30"
Longitudinal Bar Fracture North	At 4.06" during pull to μ_6^{2-} = -6.30"
Longitudinal Bar Fracture South	At 0.13" during push to μ_6^{2+-} = 6.30"
Note: μ_6^{1-} signifies the first pull cycle of displacement ductility 6	

Table 4-4. Column Test 1 strain limit states

MATERIAL STRAINS	
Core Concrete Crushing North:	N/A *(too much noise)*
Core Concrete Crushing South:	ε_s = 0.0058 *(rebar compressive strain)*
Transverse Steel Yielding North:	N/A *(too much noise)*
Transverse Steel Yielding South:	ε_s = 0.0129 *(rebar compressive strain)*
Longitudinal Bar Buckling North	ε_s = 0.0441 *(peak tensile strain prior to BB)** N/A *(too much noise)*
Longitudinal Bar Buckling South	ε_s = 0.049 *(peak tensile strain prior to BB)* ε_s = 0.0146 *(rebar comp. strain prior to BB)*
* Peak tensile strain at μ_5, but LED marker on bar N4 was lost	

As mentioned above, the column was subjected to three-cycle set loading. First yield on the extreme fiber tensile reinforcement on the North side was measured at 0.76" and on the South at 0.80", which were averaged to 0.78". The equivalent yield displacement was calculated by multiplying the first yield displacement by the ratio of the analytical first yield and nominal moments (1.35), as seen in Equation 4-1. The equivalent yield displacement of 1.05" was used for the rest of the test, performing three positive and negative cycles at displacement ductility (μ) 1, 1.5, 2, 3, 4, 5, and 6.

On the day of the test, compressive tests were performed on 4" x 8" concrete cylinders that were tested per ASTM C39. Table 4-5 contains the test day results.

Table 4-5. Test day concrete strength for column test 1

Column Concrete			**Footing Concrete**	
Cylinder	**Stress [ksi]**		**Cylinder**	**Stress [ksi]**
1	5.63		1	6.82
2	5.98		2	6.90
3	5.54		3	6.72
4	5.94		4	7.07
Average	**5.77**		**Average**	**6.88**

Figure 4-2 displays a plot of the force-displacement response along with a progression of longitudinal reinforcement fractures. Figure 4-3(a) shows the load history for this test, along with similar markings for rebar fracture and two other damage limit states. Figure 4-3(b) displays the bar-labeling scheme. As seen below, the column experiences failure when the longitudinal bars fracture, significantly reducing the lateral load-carrying capacity. Each bar fractures on the loading cycle subsequent to bar buckling.

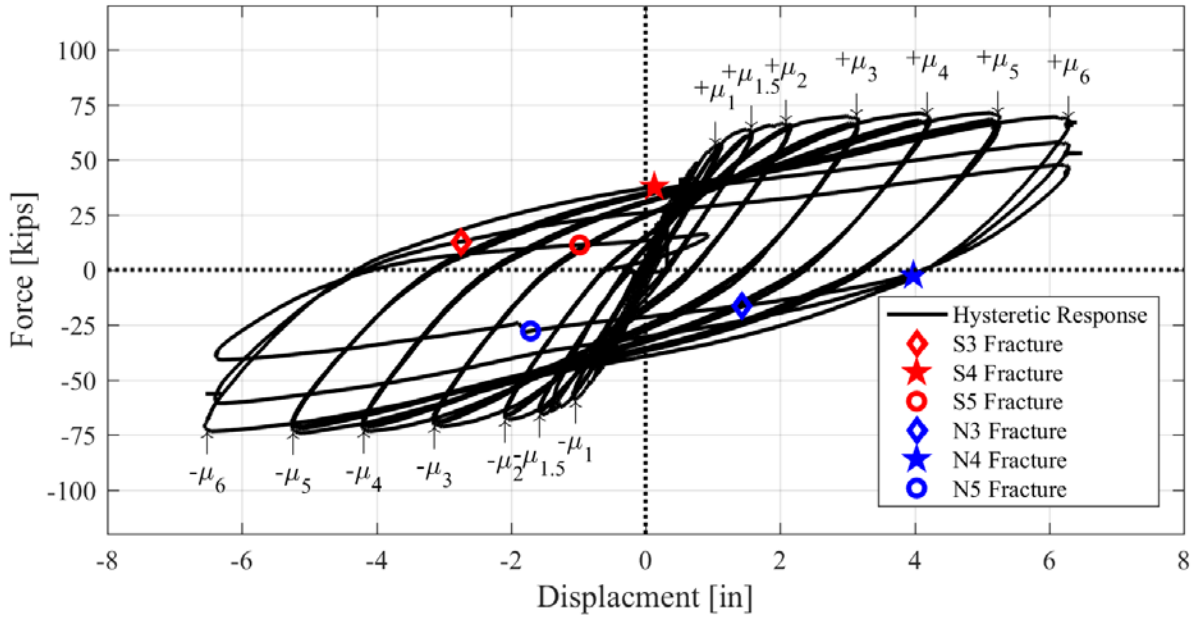

Figure 4-2. Column test 1 force-displacement response with rebar fracture locations

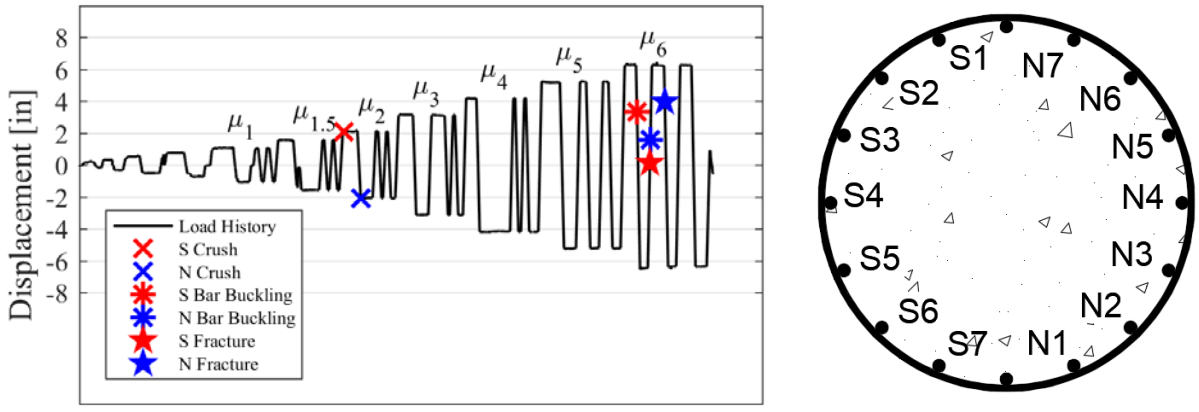

(a) **(b)**

Figure 4-3. (a) Test 1 load history. (b) Test 1 bar labels

4.1.1. Damage Progression

The first cracks were observed in the column concrete at 0.5*F_y (displacement of 0.33 inches). Horizontal cracks continued to develop on each extreme fiber side of the column, while diagonal "fanned" cracks developed on the column East and West column faces. During the first cycle of μ_2 (Δ=2.10"), core concrete scaling was observed, corresponding to the limit state of concrete crushing. The column then maintained a stable hysteretic response through μ_5. At μ_6, buckling was observed in the extreme fiber reinforcement on the South side of the column (S4) during the first pull cycle of ductility 6 (μ_6^{1-}). The peak tensile strain that reinforcement experienced prior to bucking was 0.049 in/in. On the cycle following the buckling of the reinforcement, when the bar was subjected to tensile loads, it fractured. Following the first fracture of reinforcement (S4), other bars fractured on subsequent cycles. The order of fracture was S4-N4-S3-N3-N5-S5.

Several pictures showing the damage progression over the course of the test are included below. Cracks were marked with black and red markers: black represents the cracks that occurred on the push cycles and red the cracks on the pull cycles. Figure 4-4 shows that cracks developed in a fan pattern throughout the plastic hinge region.

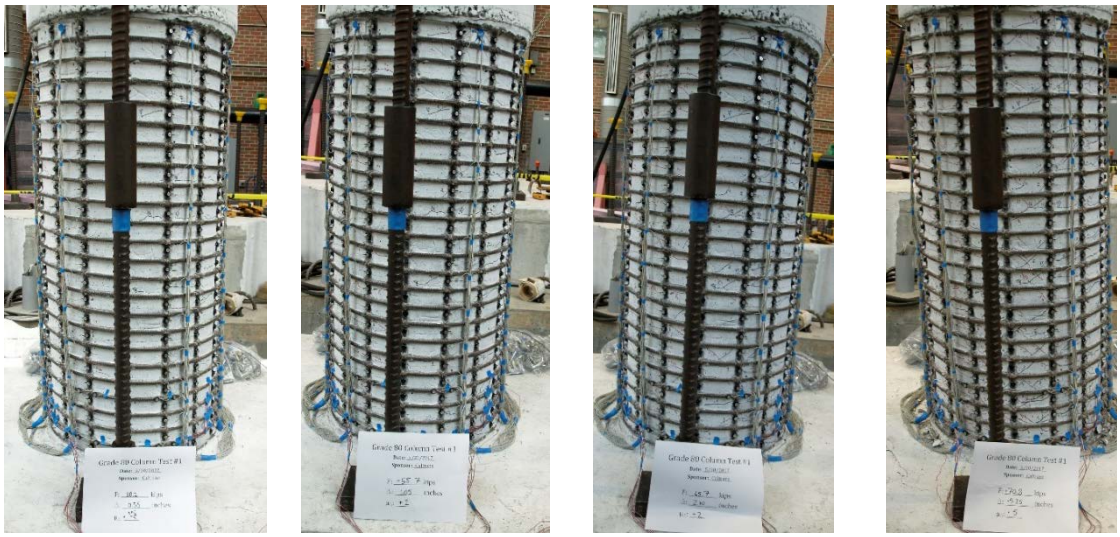

(a) **(b)** **(c)** **(d)**

Figure 4-4. Crack pattern after (a) + ¾ F_y, (b) +μ_1, (c) +μ_2, (d) +μ_5

During the test, the reinforcement fractured in two different ways. Bars S4 and N5 experienced sudden rupture, which generated a large amount of energy (loud "pop") and a relatively flat fracture surface, as seen in Figure 4-5(a). The other bars fractured after several quiet "pops," and the fracture surface was flat on the inside of the buckle and jagged on the other half, as seen in Figure 4-5(b). The cause of this will be discussed later in the report.

(a) **(b)**

Figure 4-5. (a) Flat bar fracture surface (S4); (b) Uneven bar fracture surface (N4)

The two pictures in Figure 4-6 show the ultimate limit state. On the left, bar S4 has fractured, and on the right, three of the bars on the north face have fractured. It is evident from both pictures that the spirals are no longer providing confinement to the longitudinal bars to prevent bar buckling. There is also significant crushing of the core concrete.

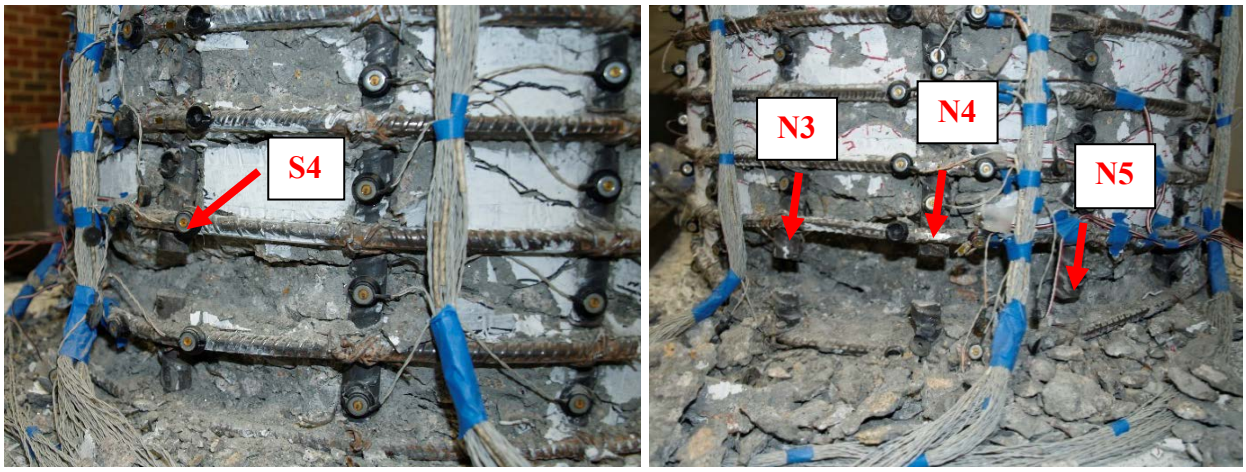

(a) **(b)**

Figure 4-6. Fractured longitudinal bars: (a) S4, (b) N3, N4, and N5

After the test was completed, the loose concrete was chipped away in order to see the damage on the reinforcing steel. Figure 4-7 shows the damage after the crushed concrete has been removed.

(a) **(b)**

Figure 4-7. (a) South side final damage state; (b) North side final damage state

As seen in the pictures above, the majority of the longitudinal reinforcing bars on both extreme faces were either fractured or buckled. The transverse reinforcement experienced significant plastic deformation, and significant portions of the concrete crushed. The cover concrete of the footing on the North side of the column also experienced significant crushing; so much that the footing reinforcing steel was visible after removing the crushed concrete. Footing cover concrete on the South side did not experience the same crushing.

4.1.2. Strain Analysis

Position data from the Optotrak LED markers was analyzed to determine the strains in the longitudinal and transverse reinforcing bars throughout the test. Figure 3-11 shows a picture of the instrumentation setup. Using the distance formula, the change in distance between two markers was compared to the initial length to calculate strain.

Strain data captured on the North side of the column had more “noise” (jumps in strain data) than the data captured on the South side. The Optotrak camera was placed at a greater distance from the test specimen on the North than on the South. The longer focal distance introduced “noise” into the optical position and strain data. In addition, the third LED marker from the bottom of the column on the North extreme fiber bar (N4) came loose after the first cycle of μ_5

and strain data from bar N4 was not analyzed in this test. More care was taken in applying the LED caps in the remaining tests.

Longitudinal bar buckling is a critical design limit state in reinforced concrete columns representing a level of damage that cannot be easily repaired. The optical measuring system provides a way to determine bar buckling. Figure 4-8(a) plots the strain in bar S4 versus the displacement at the top of the column. As the column is pushed from +6 inches to -6 inches, the longitudinal bar should be experiencing a compressive strain (negative). However, the instrumentation shows that the bar has positive strain. This positive strain is evidence of bar buckling, as shown in the animation in Figure 4-8(b), and corroborates the visual evidence of bar buckling.

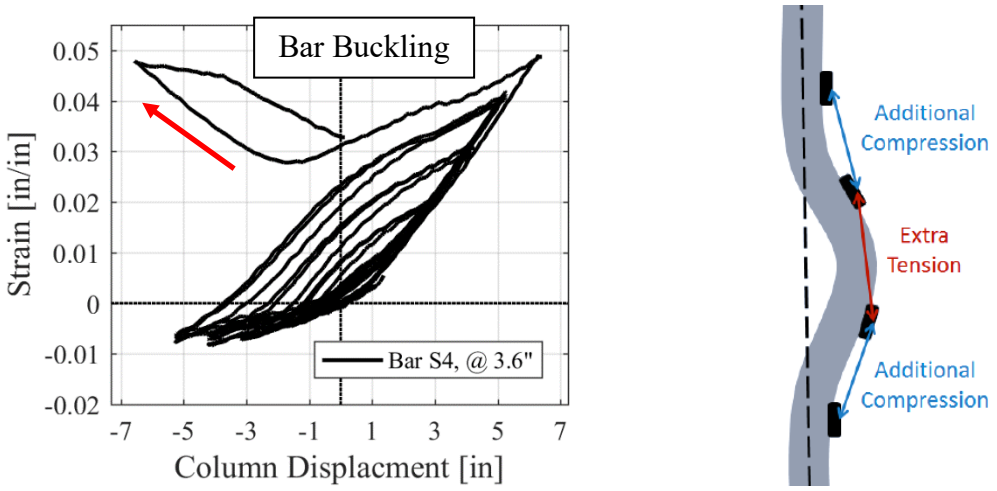

(a) **(b)**

Figure 4-8. (a) Bar S4 strain vs. displacement; (b) Bar buckling animation (Goodnight et al. (2015)

Previous research has shown that the onset of bar buckling is dependent on the peak tensile strain in the bar (Moyer and Kowasky, 2003). The optical measuring system can measure this strain, whereas a typical strain gage would have likely failed due to de-bonding under this high strain. Bar S4 experiences a maximum tensile strain of 0.049.

Figure 4-9(a) shows the strain vs. displacement of bar N4. The LED marker slipped from the bar at ductility 5, rendering the rest of the strain data irrelevant. Bar N3 appears to have buckled at a lower strain than S4, as seen in Figure 4-9(b), but this is most likely because it was not the

extreme fiber reinforcement, so it was subjected to less strain demands. However, when bars S4 and N4 buckled and fractured, much higher demands were placed on this bar, causing buckling and subsequent fracture.

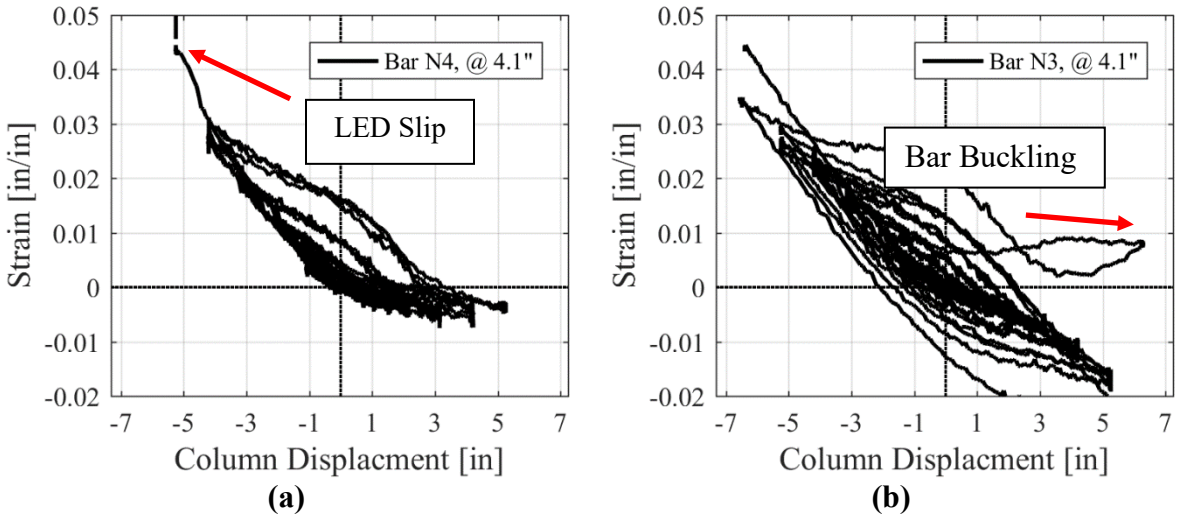

Figure 4-9. (a) Bar N4 strain vs. displacement; (b) N3 strain vs. displacement

Figure 4-10 shows the strains in the spiral that confines the plastic hinge region. These spirals were instrumented with a strain gage and Optotrak LED markers. As seen from the figures, both appear to agree until the spiral experiences a large amount of plastic strain. Strain measured by the strain gage is higher than measured by the optical measurements because the strain gage measures the strain directly at the position at which it is applied, which is over a width of approximately 0.25". The optical measurement system measures average strain over the gage length, which is almost 2". The strain gages on both sides de-bond around tensile strains of 0.017. The spiral on the South face experienced significant plastic deformation following the first push cycle of ductility 6. This is also when bar S4 began to buckle; as the longitudinal bar buckles, it forces the spiral out as well. As the spiral yields prior to longitudinal bar buckling, this lack of stiffness in the transverse reinforcement clearly decreases the restraint against buckling.

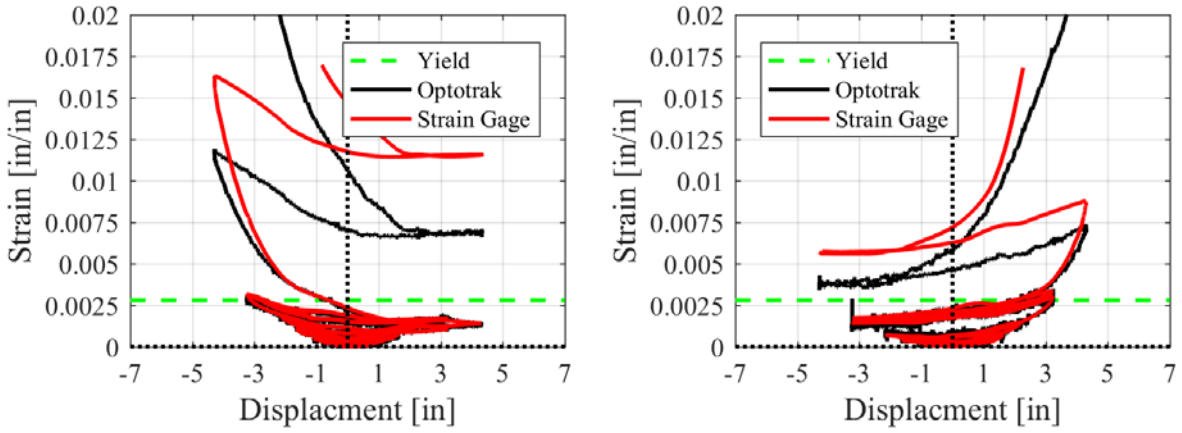

Figure 4-10. (a) South spiral (2nd) strain vs. displacement; (b) North spiral (2nd) strain vs. displacement

In addition, the strain over the height of the column was plotted to show the extent of plasticity over the height of the plastic hinge region. Figure 4-11 shows the graphs of the strain vs. height for bars S4 and N4. Solid lines represent the maximum tensile strains for each gage at the specified cycle and dashed lines show the maximum compressive strains. The spread of plasticity is approximately 37 inches on the South side and 33 inches on the North side.

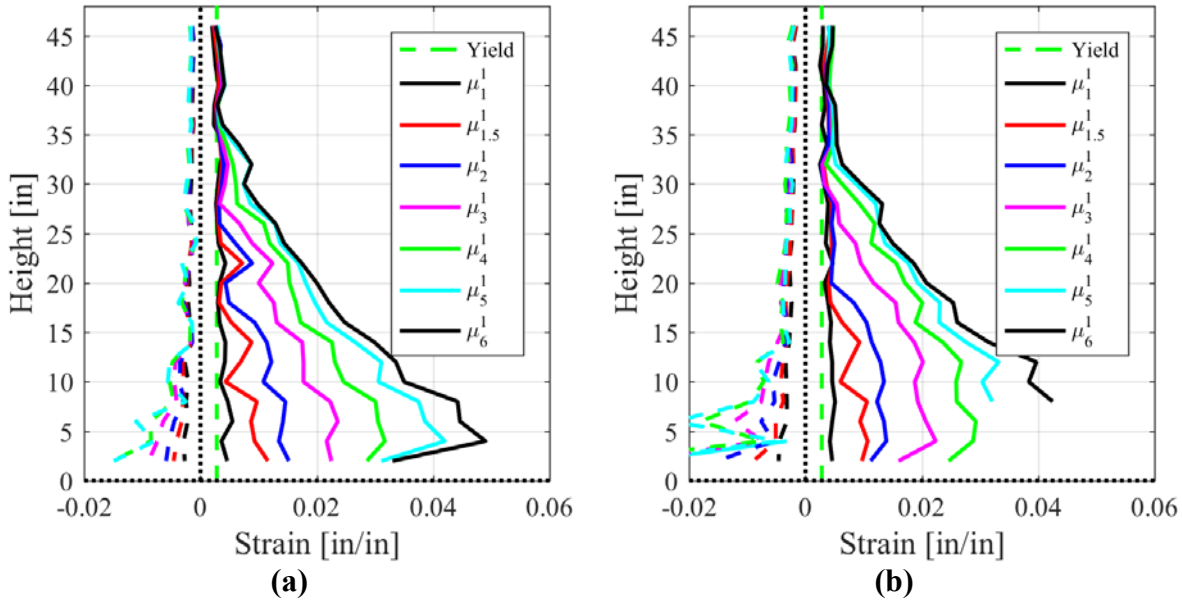

Figure 4-11. (a) Bar S4 strain profile; (b) Bar N4 strain profile

In addition to strain profiles for the longitudinal bars, Figure 4-12 shows the strain profiles for the spirals over the length of the column. The gaps in the graphs are indicators where LED markers malfunctioned during the test.

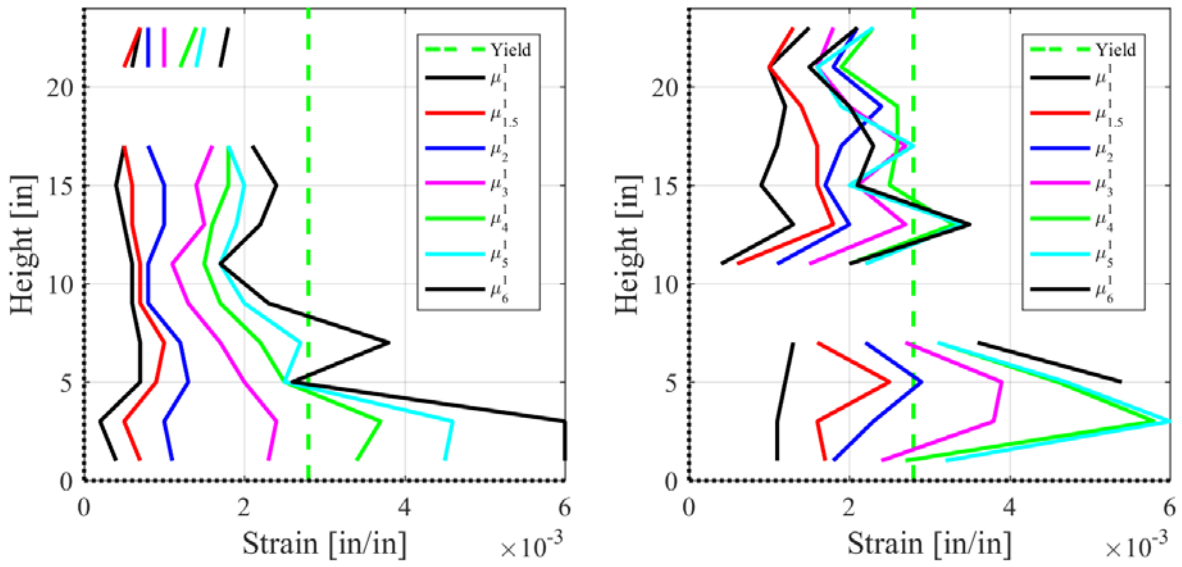

Figure 4-12. (a) South spiral strain profile; (b) North spiral strain profile

4.1.3. Components of Displacement

Previous research has shown that columns designed to modern performance standards experience two components of displacement: rotation due to strain penetration and flexural deformation (Priestley et al., 2007). Some columns also experience substantial shear deformations.

In order to measure the displacement from strain penetration, the position of the bottom optical markers on the extreme fiber longitudinal bars was used. Figure 4-13 shows the position of the bottom sensor of the three extreme fiber bars on each side of the column at the first cycle of each level of ductility. This figure shows the change in height of these sensors and the corresponding elongation of the longitudinal bar. This elongation is due to elastic and plastic elongation of the rebar penetrating into the footing, known as strain penetration or bond slip. By fitting a line through these positions, the best estimate of the total amount of strain penetration was obtained.

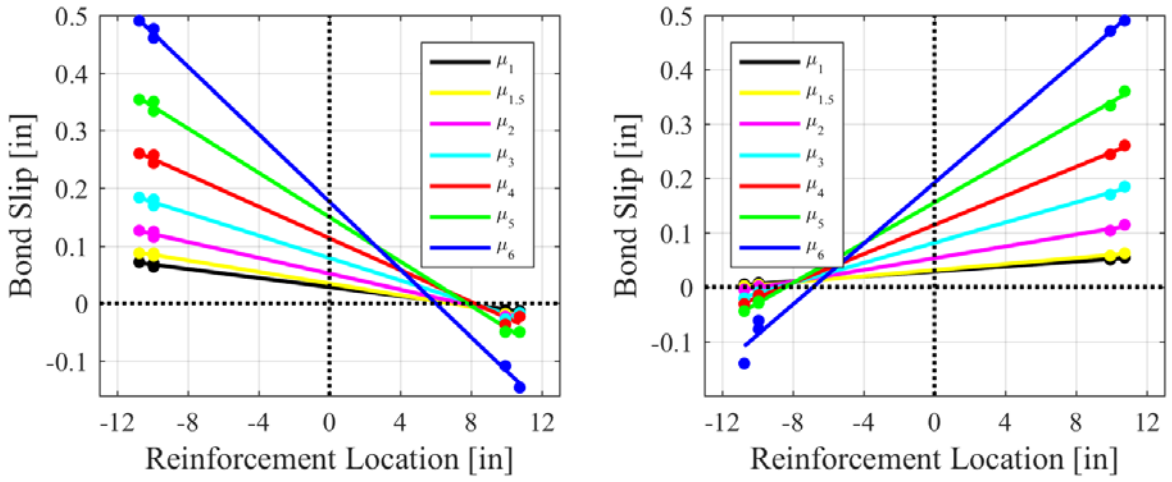

Figure 4-13. (a) Bond slip of south extreme fiber bar under push cycles; (b) Bond slip of north extreme fiber bar under pull cycles

The total amount of column displacement due to strain penetration, or bond slip, was calculated by taking a line equal to the height of the column perpendicular to each bond slip profile in Figure 4-13. This represented the total amount of column displacement due to column base rotation from strain penetration.

In addition to strain penetration, the column also experienced flexural deformation concentrating in the plastic hinge region. In order to calculate the magnitude of these deformations, the curvature of the column was integrated over the height of the column. The actual curvature distribution was calculated using the strain profile provided by the optical measurement system. The optical measurement system provided the strains in multiple longitudinal bars at discrete locations over the lower half of the column. At each discrete height, a linear interpolation was performed through the strain in each bar, as seen in Figure 4-14(a). The slope of this linear fit was used to estimate the curvature at each discrete height. Figure 4-14(b) shows the curvature distribution from the first cycle of each level of ductility. The component of column displacement from flexural deformation was then calculated by integrating the curvature distribution over the height of the column at the first cycle of each level of ductility.

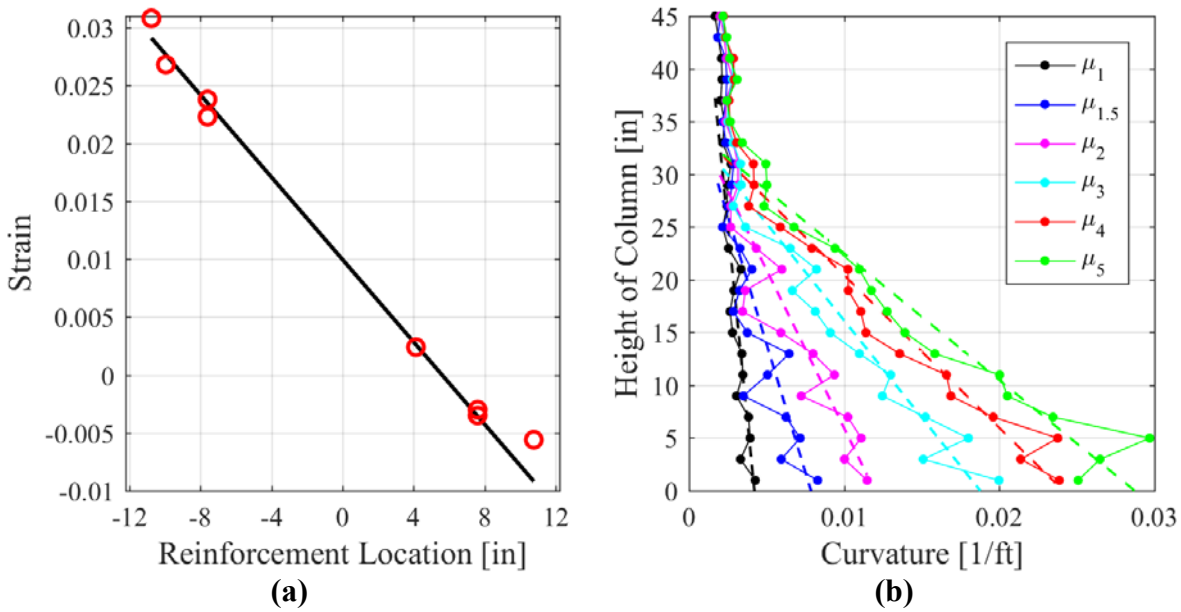

Figure 4-14. (a) Sample of cross-section strains at discrete heights used for curvature calculation; (b) Curvature distribution over height of column

These two components of displacement can be added together in order to visualize the contribution of each component of displacement to the total column displacement. Adding each component also tests the accuracy of the methods used to calculate the components of displacement. Figure 4-15 shows the combination of the components of displacement at the first cycle of each level of ductility from base rotation due to strain penetration and the flexural deformation from integration of the curvature profile. These two components of displacement combine to equal the column displacement at each ductility cycle, validating the assumption that these are the major components of column displacement and that the methods to calculate each were accurate. The small difference in displacement is attributed to errors in the calculation of each displacement component. An important aspect to notice is the large amount of deformation due to base rotation. There were no joint shear cracks in the footing, and as a result, no there was no rigid body rotation of the base due to shear deformation. The measured rotation is due to elongation of the longitudinal reinforcement into the footing, and is accurately predicted by the L_{sp} component of Equation 5-1.

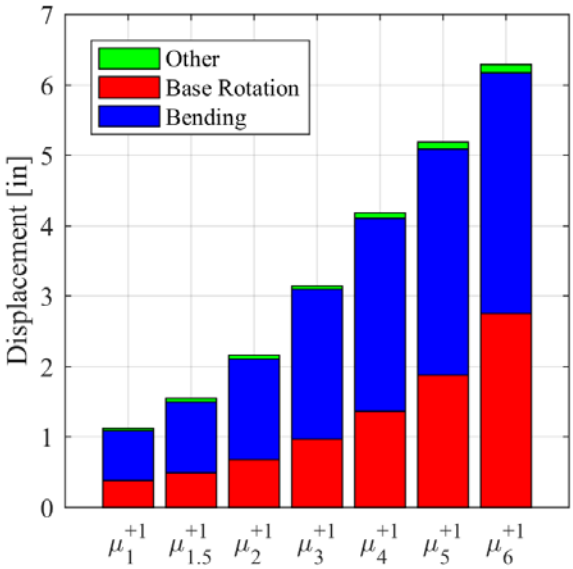

Figure 4-15. Components of displacement

4.1.4. Hysteretic Energy Dissipation

In order to determine the hysteretic damping of the RC column, the area-based hysteretic damping (Jacobsen, 1930) was calculated for the first cycle of each level of ductility. In this method, the area inside each hysteretic loop is determined by numerical integration, labeled "A_1" in Figure 4-16(a). The area of the rectangle with vertices at the maximum and minimum force and displacement for that cycle is labeled "A_2". This ratio is multiplied by $2/\pi$ as seen in Equation 4-2.

$$\xi_{jac} = \frac{2}{\pi}\frac{A_1}{A_2} \qquad \text{Equation 4-2}$$

However, Priestley et al. (2007) performed multiple non-linear time history analyses to show that area-based damping calculations overestimate the hysteretic damping. They proposed a table for correcting the equivalent viscous damping (Priestley et al., 2007), and Montejo et al. (2009) fit an equation to this corrective table, shown in Equation 4-3. Values of damping (ξ_{jac}) are percentages. Thus, Figure 4-16(b) includes the Jacobsen hysteretic damping as well as the corrected hysteretic damping.

$$CF = \left[\left(0.53\mu + 0.8\right)\xi_{jac}\right]^{-\left(\frac{\mu}{40}+40\right)} \qquad \text{Equation 4-3}$$

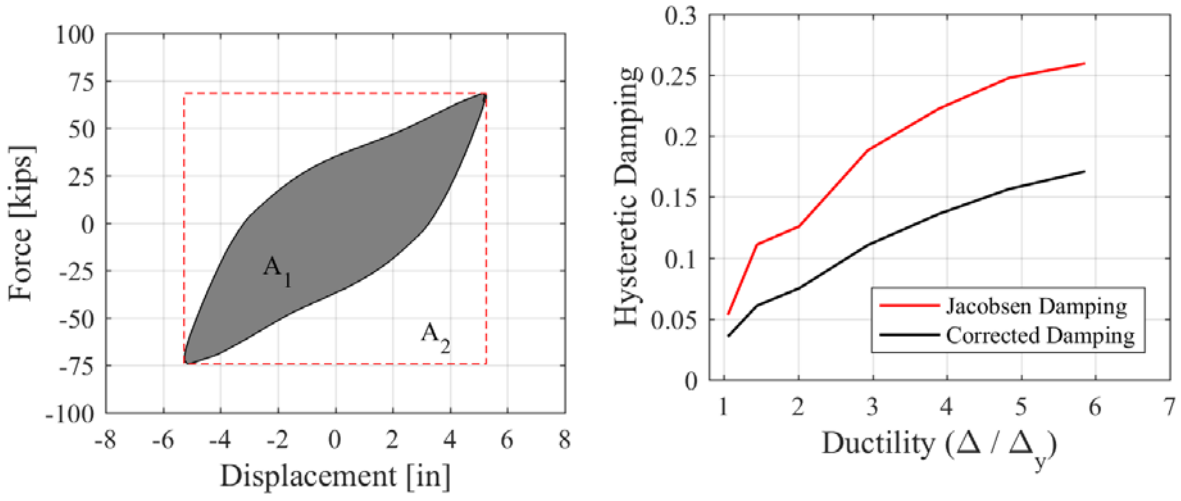

(a) **(b)**

Figure 4-16. (a) Jacobsen damping calculation; (b) Hysteretic damping

4.1.5. Comparison to Grade 60 Reinforced Column

In series of tests performed at NCSU, 30 columns were constructed using A706-60 rebar and tested under quasi-static, three cycle-set loading histories (Goodnight et al, 2015). Two of the A706-60 columns were compared to A706-80 Column Test 1. One of the A706-60 columns had the same geometry, longitudinal reinforcing steel content, transverse reinforcing steel content, and axial load ratio (Test 9, as numbered in the Goodnight et al., 2015 report). The other had all the same variables except longitudinal reinforcing steel content (Test 25). The longitudinal reinforcing steel content of the A706-60 Test 25 column was ρ = 2.1% (16 #7 bars), which theoretically matched the moment capacity of the column with 16 #6 Grade 80 bars. The load history for the Grade 80 column and the Grade 60 column with matched strength (Test 25) used displacement ductility increments of 1, 1.5, 2, 3, 4, 5, 6, 7, while the Grade 60 column with the same reinforcement content (Test 9) used displacement ductility increments of 1, 1.5, 2, 3, 4, 6, 8.

Figure 4-17 shows the force-displacement response of each column test. While Grade 60 Test 25 theoretically had a similar moment capacity as the Grade 80 test, the test day concrete strength was much higher for the Grade 60 test. In order to achieve the same axial load ratio (5%), a higher axial load was applied to the Grade 60 columns, resulting in a higher lateral force capacity.

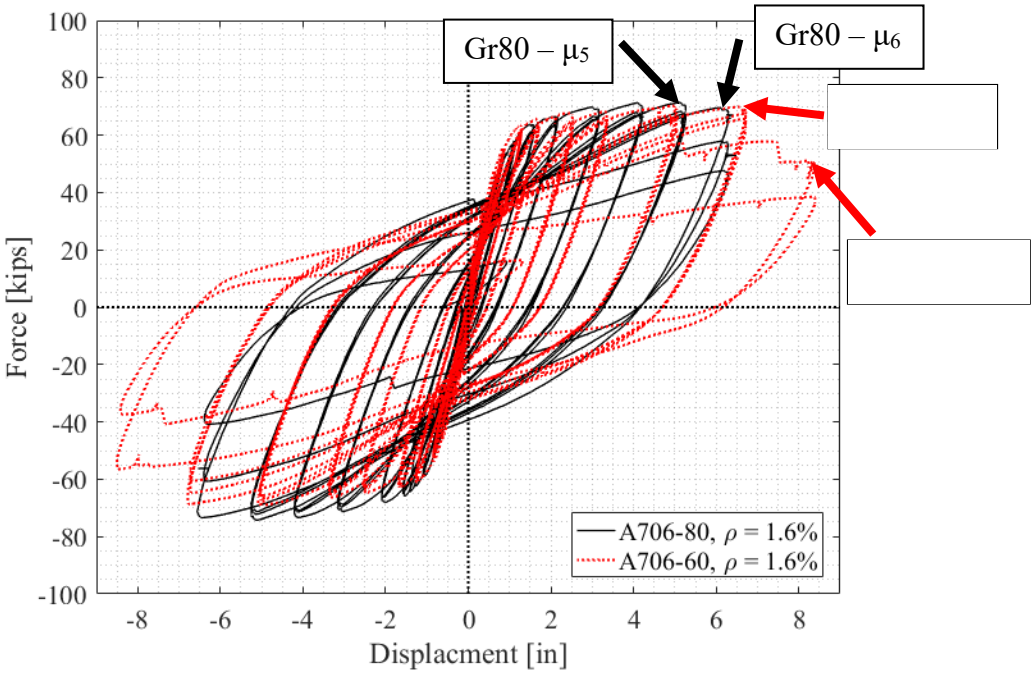

(a)

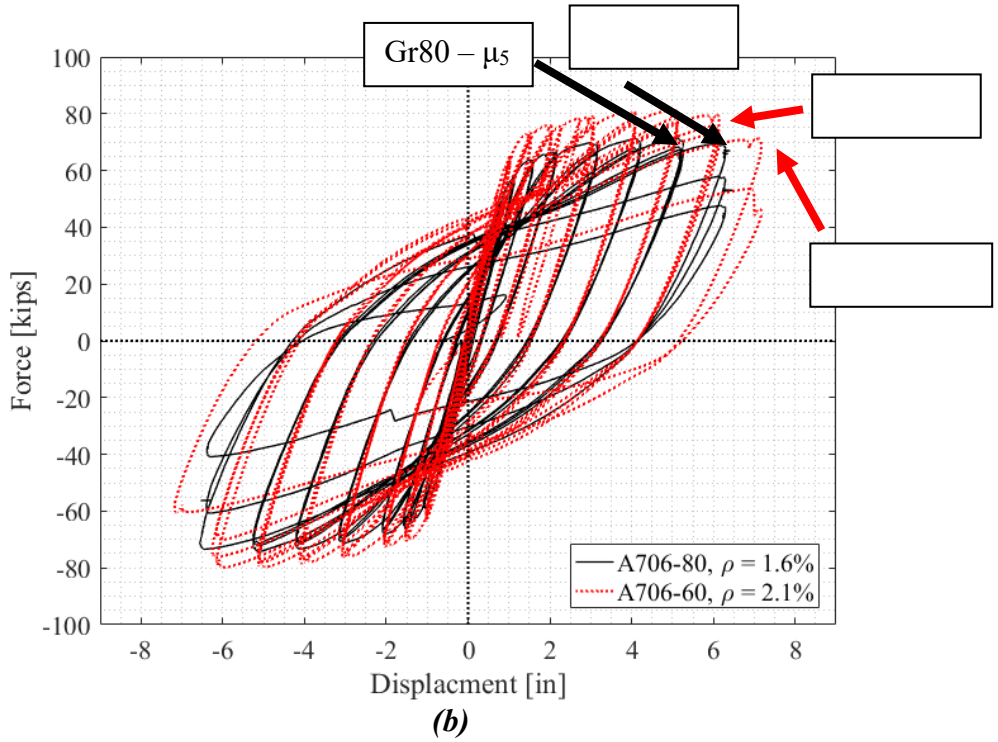

(b)

Figure 4-17. Hysteretic response of Grade 80 Test 1 and comparison Grade 60 columns with: (a) similar steel content; (b) similar strength

While the Grade 60 columns have higher displacement capacities than the Grade 80 column, the longitudinal bars buckle upon reversals from similar levels of lateral displacement and peak tensile strain prior to buckling, as shown in Table 4-6. Ductility measures are not directly comparable as the yield displacement of the Grade 80 columns is higher than Grade 60 columns due to the increased yield strength.

Table 4-6. Summary of damage limit states for column test 1

Column Test	Column Side	Longitudinal Bar Buckling			Bar Fracture	
		μ_D	Displacement	Strain (+)	μ_D	Displacement
A706-80 ρ_l = 1.6% ρ_t = 1.0%	South North	6 -6	6.30” -6.50”	0.049 N/A	6 -6	6.30” -6.30”
A706-60 ρ_l = 1.6% ρ_t = 1.0%	South North	8 -8	6.72” -6.72”	0.053 0.051	10 -10	8.42” -8.38”
A706-60 ρ_l = 2.1% ρ_t = 1.0%	South North	6 -5	6.14” -5.12”	0.042 0.035	7 -7	7.17” -7.17”

The Grade 60 columns had a similar instrumentation system, so the longitudinal rebar bond slip could be measured, as described in Section 4.1.3. The bond slip for the pull and push cycles of each column test were plotted versus the corresponding column displacement in Figure 4-18. The Grade 80 longitudinal reinforcement appears to slip slightly more than the Grade 60 at high levels of displacement, but it is very similar for the majority of the test.

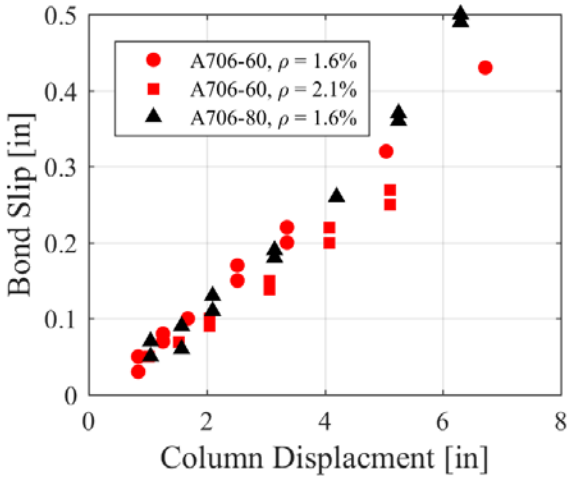

Figure 4-18. Comparison of bond slip for Grade 80 test 1 with Grade 60 columns

In addition to comparing the bond slip behavior, a comparison of the corrected hysteretic damping (described in Section 4.1.4) was also performed. Figure 4-19 shows that the hysteretic damping of the Grade 80 column and the comparison Grade 60 columns is very similar.

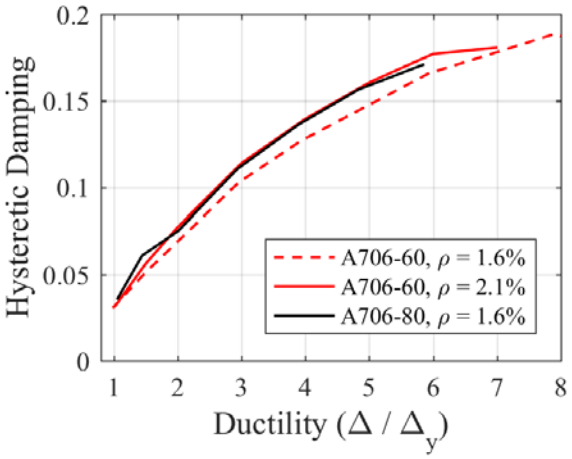

Figure 4-19. Comparison of damping vs. ductility for Grade 80 test 1

4.1.6. Analytical Model

In order to examine how the experimental force-displacement results compared to current modeling practice, Figure 4-20 shows the experimental force-displacement response along with a fiber model from OpenSees (Open System for Earthquake Engineering Simulation, McKenna et al., 2010) and a pushover analysis performed in Cumbia (Montejo and Kowalsky, 2007).

Montejo and Kowalsky (2007) developed a Matlab script called Cumbia in order to return the monotonic moment curvature (M-φ) relationship of various cross-section geometries through sectional analysis. The program uses confined and unconfined concrete models proposed by Mander (1988), and the reinforcing steel model proposed by King et al. (1986). Cumbia then uses the plastic hinge method presented in Priestley, et al. (2007) to calculate the member force-displacement response from the monotonic M-φ relationship. As shown in Figure 5-1, the elastic flexural deformation is determined using a triangular yield curvature distribution. The plastic flexural deformation is determined using a uniform curvature distribution with a constant height (the plastic hinge length). To account for the strain penetration, the curvature distribution extends into the footing by a certain depth (the strain penetration length).

OpenSees (McKenna et al., 2010) was used to model the cyclic behavior of the columns. Two elements modeled the column behavior: (1) a beam with hinges element for flexural deformation and (2) a zero-length strain penetration element for deformations from strain penetration. The beam with hinges element (recently simplified into the forceBeamColumn element) uses plastic hinge integration with modified Gauss-Radau quadrature, as described in Scott and Fenves (2006). The zero length element (Bond SP01, developed by Zhao and Sritharan, 2007), models the column base rotation due to strain penetration of the longitudinal reinforcement of the footing. Figure 4-20 shows that the experimental results display a good comparison with the OpenSees fiber model as well as the force-displacement prediction from Cumbia.

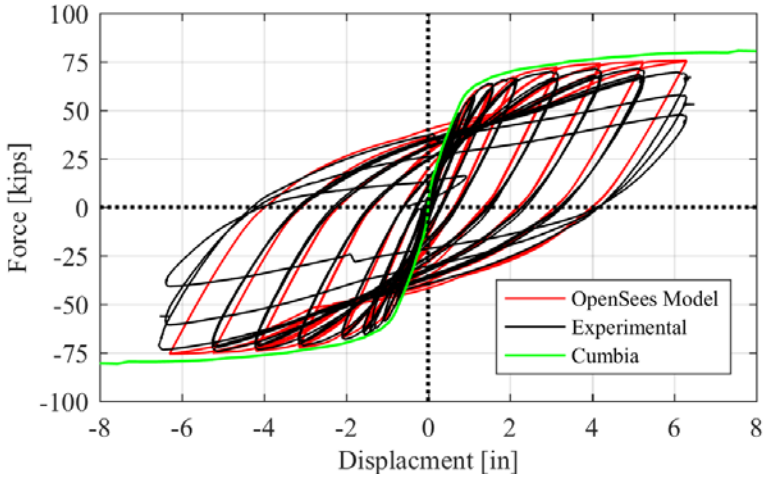

Figure 4-20. Actual and analytical force-displacement responses

4.2. Column Test 2 Summary

Column Test 2 was conducted at the CFL on the campus of NCSU on Thursday, June 29, 2017, as part of the project to evaluate the seismic performance of A706-80 rebar in RC members. The 8' specimen was subjected to a quasi-static three-cycle set loading and a constant 10% axial load ratio.

Table 4-7. Column test 2 summary information

COLUMN PARAMETERS	
Longitudinal Steel:	(16) #6 A706-80 Bars (ρ_l = 1.6%)
Transverse Steel:	#3 Spirals @ 2" Pitch (ρ_t = 1.0%)
Longitudinal Steel Yield Strength:	83 ksi
Transverse Steel Yield Strength:	79 ksi
Concrete Strength:	6.6 ksi
Axial Load:	300 kips
Axial Load Ratio:	10%
Experimental First Yield Displacement:	0.84"
Analytical Nominal Moment Capacity	644.6 kip*ft
Equivalent Yield Displacement	1.08"
Maximum Lateral Force	85.2 kips
Failure Mode	Rupture of previously buckled reinforcement
DAMAGE OBSERVATIONS	
First Cracking North	-¼ Fy' = -0.2"
First Cracking South	½ Fy' = 0.3"
Core Concrete Crushing North:	$\mu_{1.5}^{1+}$ = 1.62"
Core Concrete Crushing South:	$\mu_{1.5}^{1-}$ = -1.62"
Transverse Steel Yielding North:	At 2.67" during push to μ_3^{1+} = 3.24"
Transverse Steel Yielding South:	At -2.1" during pull to μ_2^{1-} = -2.16"
Longitudinal Bar Buckling North	During reversal from μ_4^{1-} = -4.32"
Longitudinal Bar Buckling South	During reversal from μ_4^{1+} = 4.32"
Longitudinal Bar Fracture North	At -1.4" during pull to μ_5^{1-} = -5.40"
Longitudinal Bar Fracture South	At 1.45" during push to μ_5^{1+} = 5.40"
Note: μ_4^{1-} signifies the first pull cycle of displacement ductility 4	

Table 4-8. Column test 2 strain limit states

MATERIAL STRAINS	
Core Concrete Crushing North:	$\varepsilon_s = 0.0071$ *(rebar compressive strain)*
Core Concrete Crushing South:	$\varepsilon_s = 0.0050$ *(rebar compressive strain)*
Transverse Steel Yielding North:	$\varepsilon_s = 0.0138$ *(rebar compressive strain)*
Transverse Steel Yielding South:	$\varepsilon_s = 0.0081$ *(rebar compressive strain)*
Longitudinal Bar Buckling North	$\varepsilon_s = 0.0306$ *(peak tensile strain prior to BB)* $\varepsilon_s = 0.0132$ *(rebar comp. strain prior to BB)*
Longitudinal Bar Buckling South	$\varepsilon_s = 0.0311$ *(peak tensile strain prior to BB)* $\varepsilon_s = 0.0130$ *(rebar comp. strain prior to BB)*

The column was subjected to three-cycle set loading. This load history consisted of single positive and negative cycles until the first yield of the reinforcement. The average first yield displacement was 0.85", which was multiplied by the ratio of the analytical first yield and nominal moments (1.28), as seen in Equation 4-1. The equivalent yield displacement of 1.08" was used for the rest of the test, performing three positive and negative cycles at displacement ductility (μ) 1, 1.5, 2, 3, 4, and 5.

On the day of the test, compressive tests were performed on 4" x 8" concrete cylinders that were tested according to ASTM C39. Table 4-9 contains the test day results.

Table 4-9. Test day concrete strength for column test 2

Column			**Footing**	
Cylinder	**Stress (ksi)**		**Cylinder**	**Stress (ksi)**
1	6.74		1	7.48
2	6.69		2	7.97
3	6.42		3	7.74
4	6.65		4	7.71
Average	**6.63**		**Average**	**7.73**

Figure 4-21 displays a plot of the force-displacement response along with a progression of longitudinal reinforcement fractures. Figure 4-22(a) shows the load history for this test, along with

similar markings for rebar fracture and two other damage limit states (core crushing and longitudinal bar buckling). Figure 4-22(b) displays the bar labeling scheme. As seen below, the column experiences failure when the longitudinal bars fracture, significantly reducing the lateral load carrying capacity.

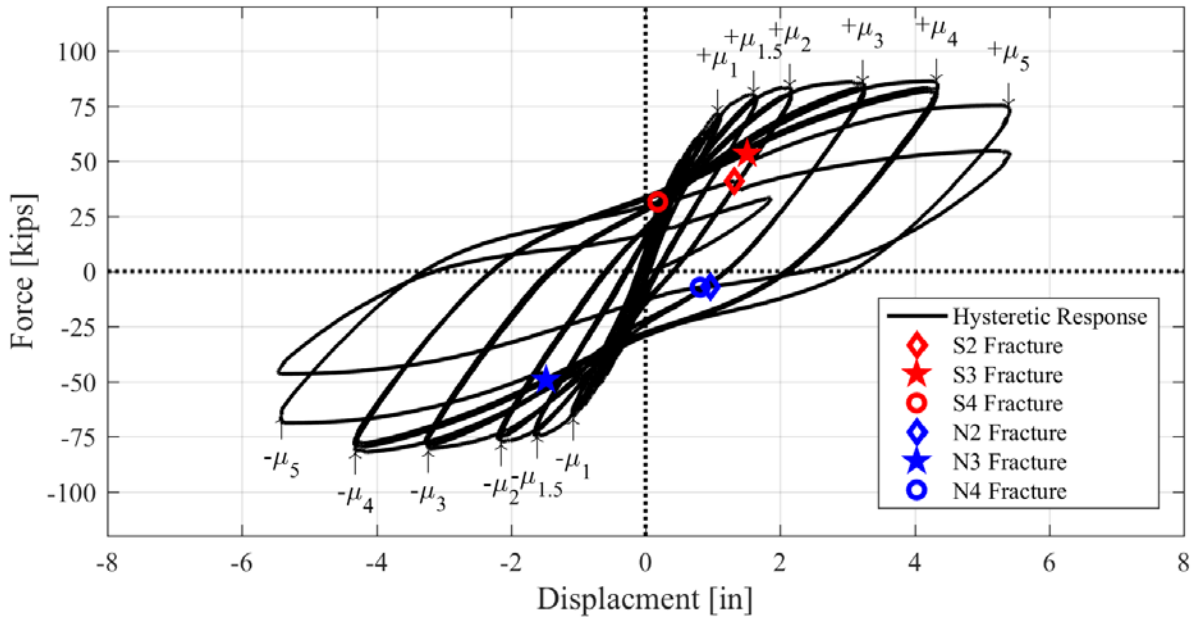

Figure 4-21. Column test 2 force-displacement response with rebar fracture locations

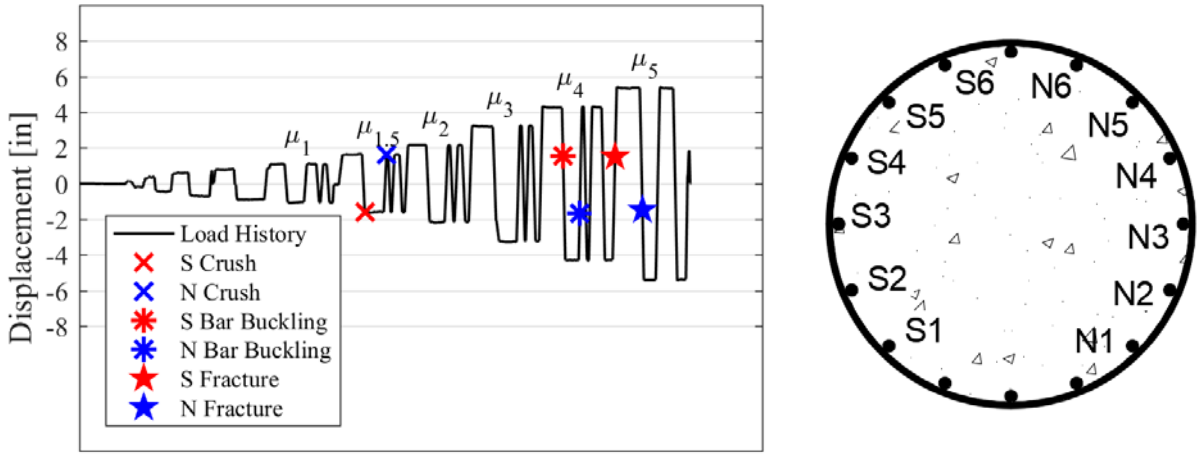

(a) **(b)**

Figure 4-22. (a) Column test 2 load history. (b) Column test 2 bar labels

4.2.1. Damage Progression

Damage occurred in a relatively uniform manner on the North and South sides of the column. Horizontal hairline cracks developed on the extreme faces of the column in the initial pre-yield cycles of the loading history. At half of the yield force, the largest crack widths measured 0.005 inches. At ¾*F_y, diagonal cracks began to develop on the non-extreme face. These diagonal cracks began at roughly 30" above the footing-column interface. In additional to diagonal cracking, cracks on the footing-column interface began to form at this level, also. At the first cycle at equivalent yield displacement (μ_1), the maximum crack widths measured on the column were 0.01 inches wide. By the third cycle at ductility 1 (μ_1^{3+}), crack widths had grown to 0.016 inches. During $\mu_{1.5}^{1+}$, column concrete began to scale off the column, which was taken to be an indication of the beginning of core concrete crushing. In addition, a crack was observed in the footing perpendicular to the footing-column interface. Maximum crack widths at $\mu_{1.5}$ measured 0.025 inches. In μ_2, maximum crack widths in the exposed core region of concrete grew to 0.04 inches. Horizontal cracks continued to develop on both of the extreme faces of the column. More diagonal cracks developed on the non-extreme faces and existing cracks spread down the sides of the column. By μ_3, more cracks had developed in the column, concentrating in the lower third of the column. Cracking of the footing also became more significant, and observations showed the possibility of base rotation of the column. At μ_4, cracks were concentrated in the bottom portion of the column; maximum crack widths exceeded 0.06 inches. In addition, visual evidence of longitudinal bar buckling was observed, which was examined further in the strain data available from the optical measuring system (Optotrak). Following bar buckling, bar fracture was observed in the extreme fiber bars on each side. These bars did not experience necking and their fracture surface was flat (Figure 4-28) similar to the fracture surface of bar S4 in the first column test (as seen in Figure 4-5(a)). Below are some of the pictures at different stages of damage throughout the test.

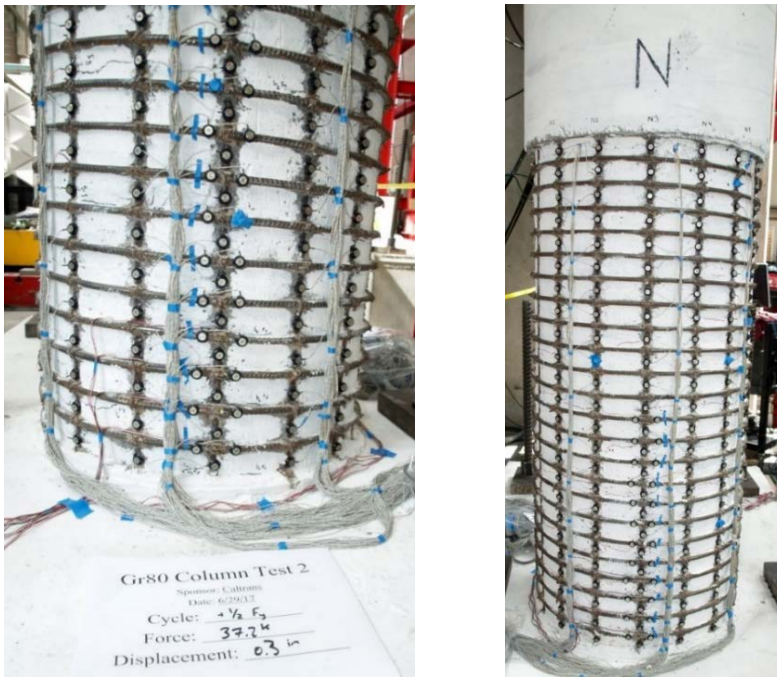

(a) **(b)**

Figure 4-23. (a) First cracking on South, ½ F_y; (b) First cracking on North, -¼ F_y

(a) **(b)** **(c)**

Figure 4-24. First Yield: (a) South; (b) West; (c) North

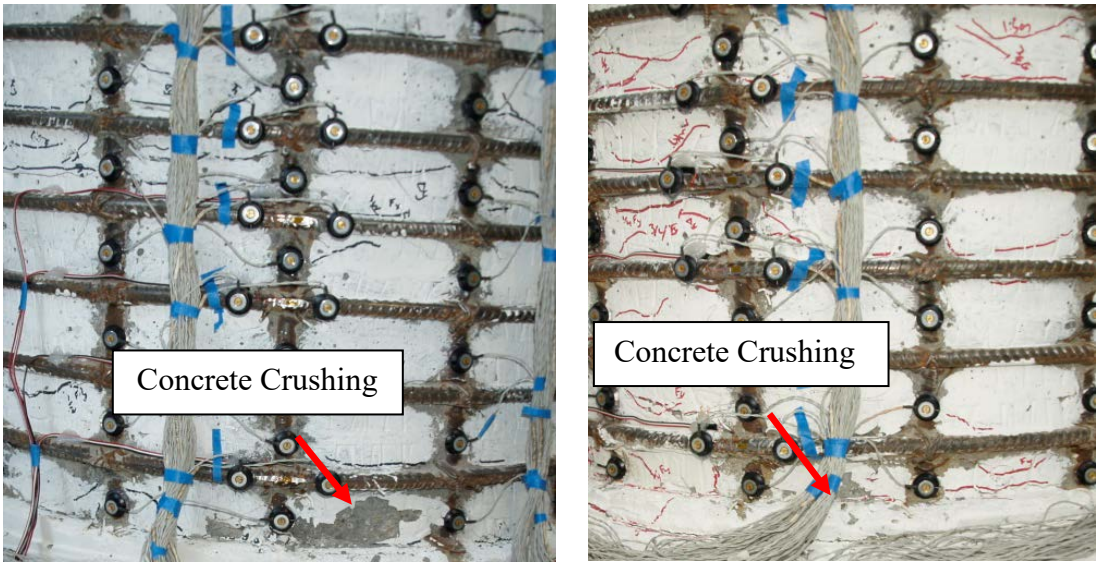

(a) (b)

Figure 4-25. (a) Concrete crushing on South, $\mu_{1.5}$; (b) Concrete crushing on North, $\mu_{1.5}$

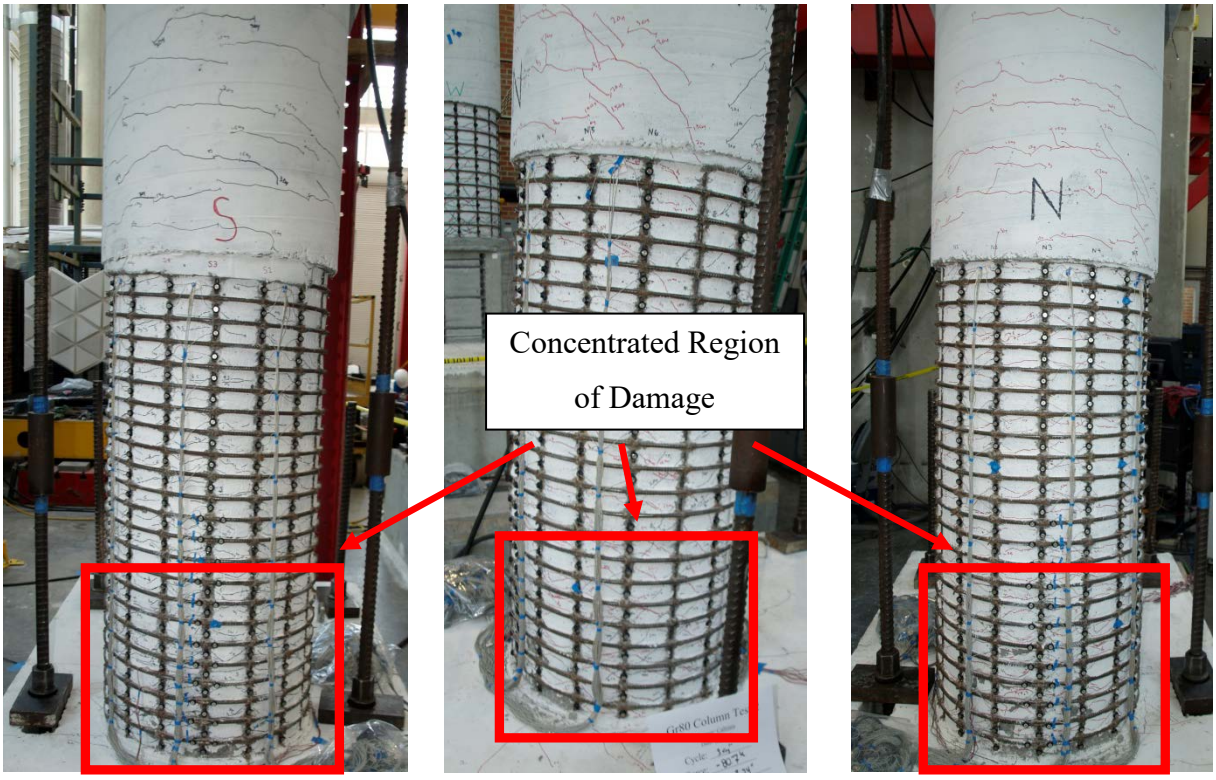

(a) (b) (c)

Figure 4-26. μ_3: (a) First push cycle, South; (b) Diagonal cracking on West; (c) First pull cycle, North

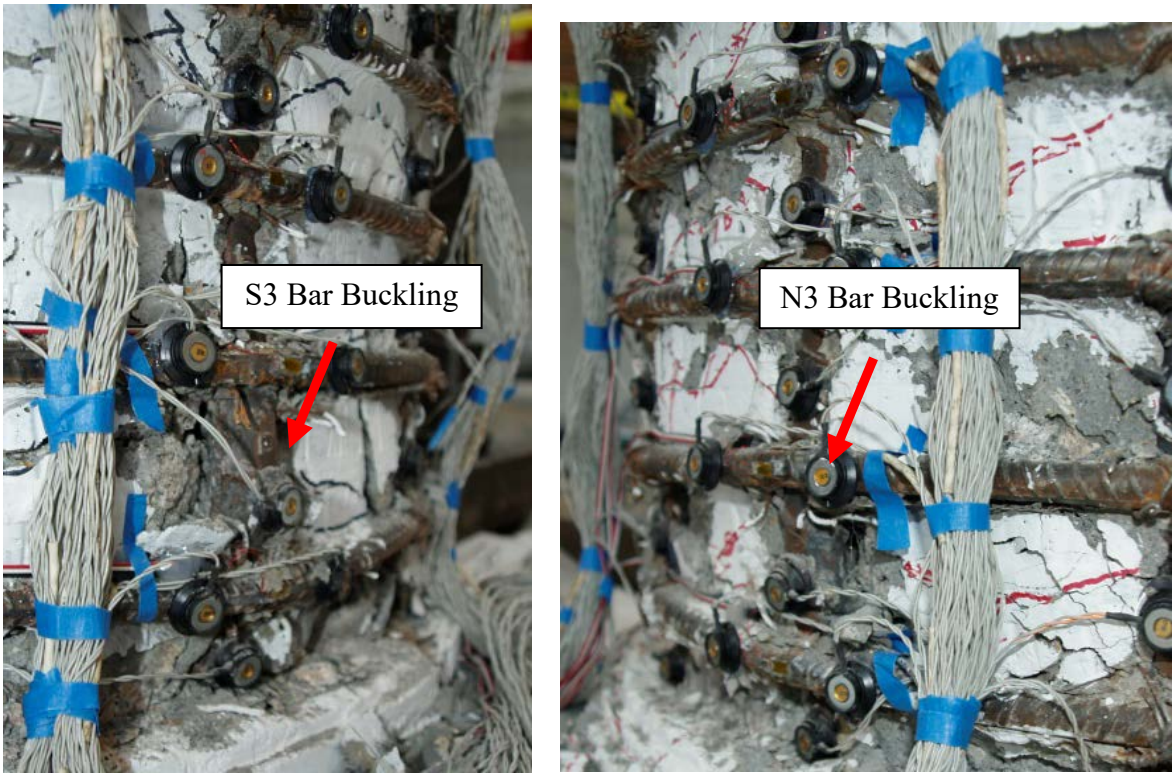

(a) **(b)**

Figure 4-27. (a) S3 buckled, μ_4^{3-}; (b) N3 buckled μ_4^{3+}

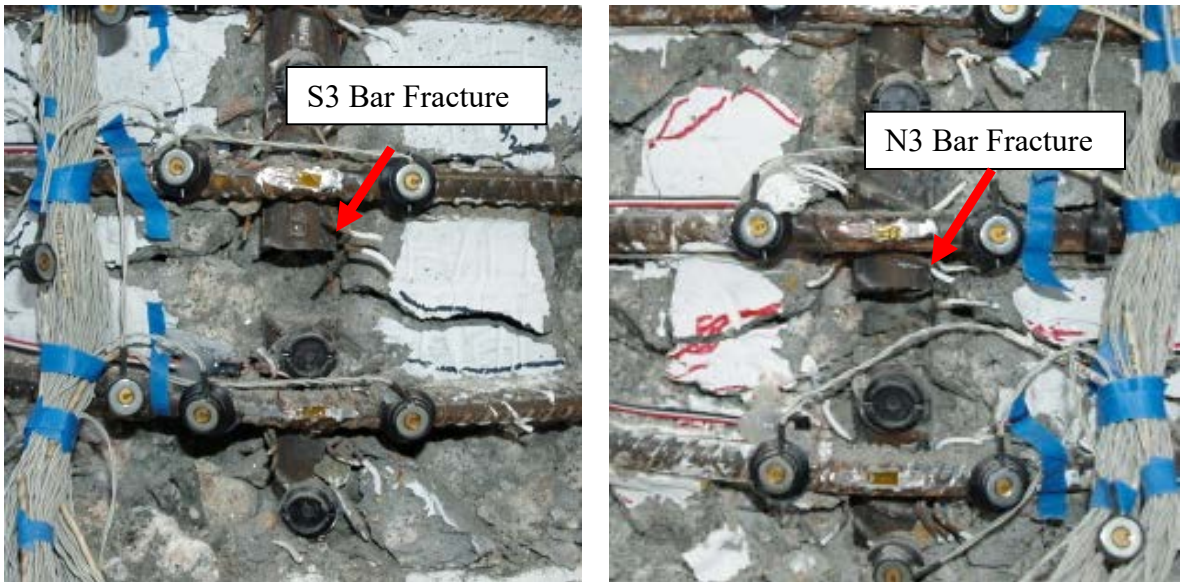

(a) **(b)**

Figure 4-28. (a) South bar fracture (S3), μ_5^{1+}; (b) North bar fracture (N3), μ_5^{1-}

4.2.2. Strain Analysis

By examining the 3D position of each LED marker throughout the duration of the test, strain levels in each of the instrumented longitudinal bars and transverse spirals was available until failure, as seen in Figure 3-11. Longitudinal bar strains on the North extreme face of the column reached 0.031 before buckling was observed. Bar N3 experienced the maximum tensile strain during the first pull cycle of ductility 4 (μ_4^{1-}), which is seen in Figure 4-29(b), and on the reversal to μ_4^{2+}, the first sign of buckling was observed, shown in Figure 4-29(a). Through visual observation, buckling was difficult to detect because much of the core concrete was still intact, but bucking was observed by examining the strain vs. displacement data of different locations along the longitudinal bar, as shown in Figure 4-8(b).

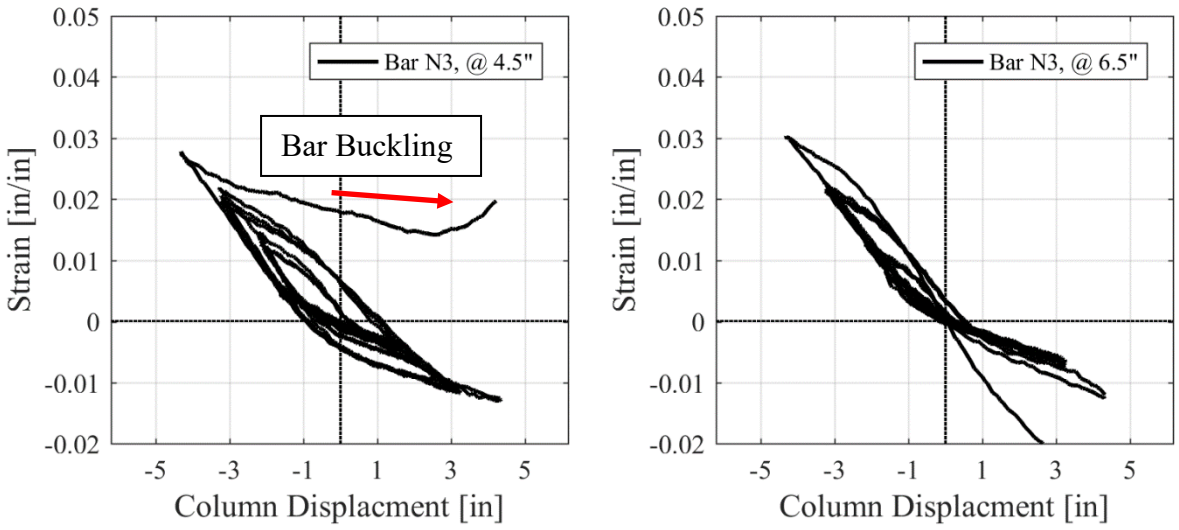

(a) **(b)**

Figure 4-29. Bar N3 strain vs displacement: (a) at 4.5", (b) at 6.5" above footing

As the extreme fiber bar (N3) buckled and fractured, the bars on either side (N2 & N4) experienced similar buckling at the third cycle of ductility 4 (N2) and the first cycle of ductility 5 (N4), as shown in Figure 4-30. As the extreme fiber longitudinal reinforcing bar buckles, the bar experiences a significant loss in stiffness. Thus, the compressive demands are transferred to the adjacent extreme fiber bars. Once the extreme fiber bar fractures, these bars experience a greater increase in compressive force and buckle more significantly.

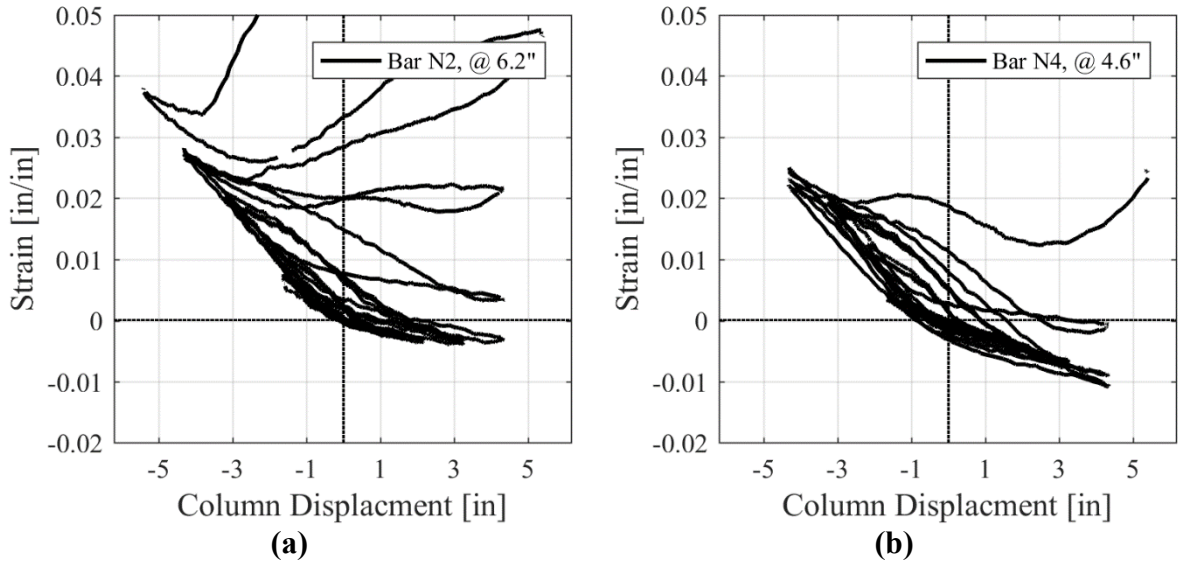

(a) **(b)**

Figure 4-30. Strain vs displacement of (a) bar N2; (b) bar N4

Similar behavior was seen on the South side. Maximum strains in the extreme fiber bar reached 0.031 before bar buckling was observed. Again, the point at which bar buckling was observed in the test was confirmed by the graph of the strain vs. peak column displacement as shown in Figure 4-31. Buckling was first seen at 4.8 inches above the footing in Figure 4-31(a). Maximum strain was observed at 8.8 inches above the footing in Figure 4-31(b). Similar

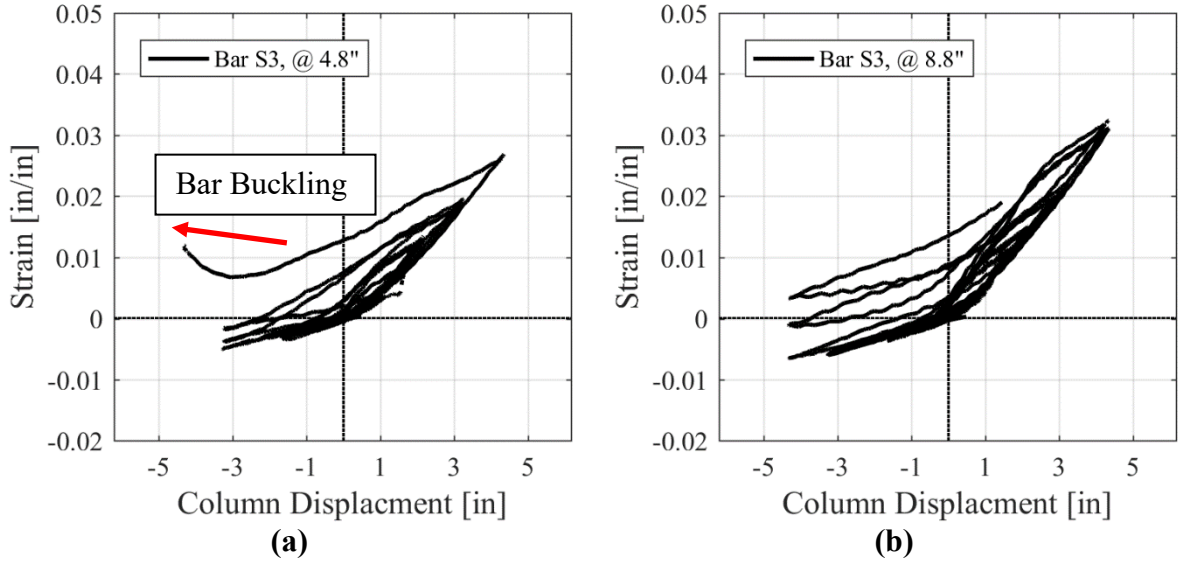

(a) **(b)**

Figure 4-31. Bar S3 strain vs displacement: (a) 4.8" above footing; (b) 8.8" above footing

Similar to the North side, as the extreme fiber bar (S3) buckled and fractured, the bars on either side (S2 & S4) experienced similar buckling during the first pull cycle of ductility 5, as shown in Figure 4-32.

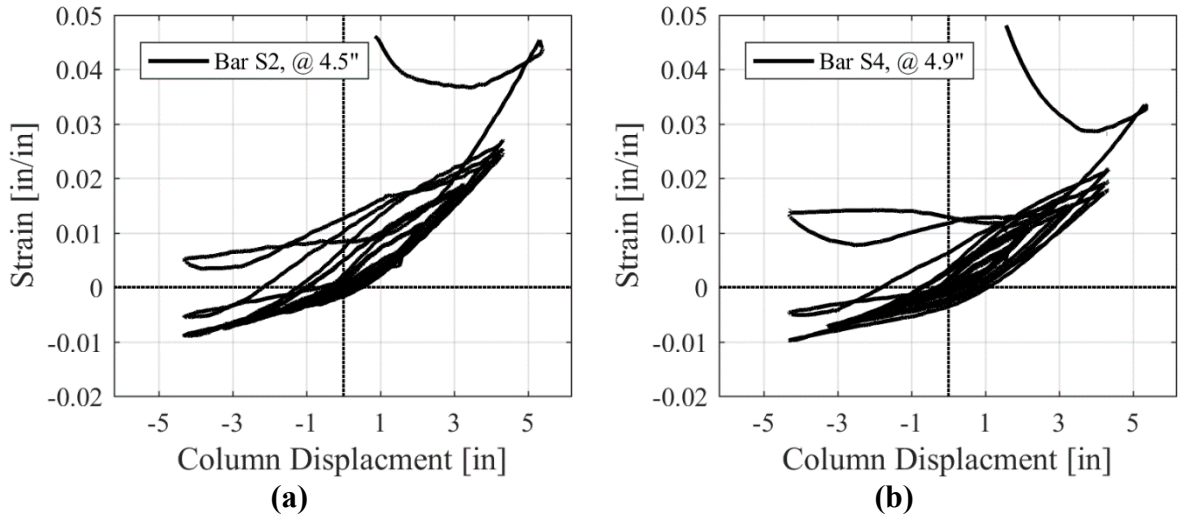

(a) **(b)**

Figure 4-32. Strain vs displacement of (a) bar S2; (b) bar S4

Figure 4-33 shows the strains in the spiral that confines the plastic hinge region. These spirals were instrumented with a strain gage and Optotrak LED markers. The strain gages on both sides de-bond around tensile strains of 0.017. As the spiral yields, it provides less confinement to the longitudinal rebar, which causes the longitudinal bars to buckle.

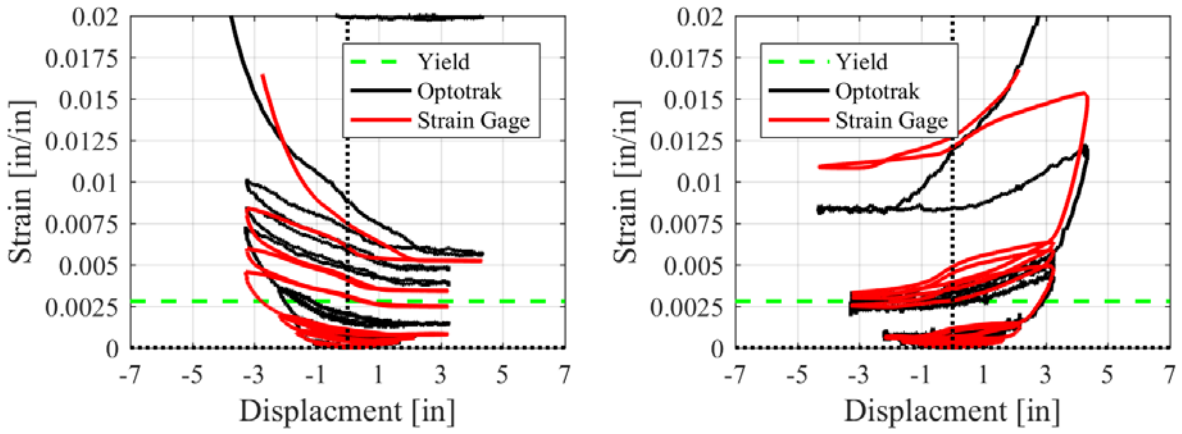

(a) **(b)**

Figure 4-33. (a) Lowest south spiral strain vs. displacement; (b) North spiral (2nd) strain vs. displacement

In addition, the data can also be formatted to plot the strain profile over the height of the column. This information shows the extent of longitudinal bar yielding or the spread of plasticity over the height of the plastic hinge region. Figure 4-34 shows the graphs of the strain vs. height for bars S3 and N3. Solid lines represent the maximum tensile strains for each gage at the specified cycle, while dashed lines depict the maximum compressive strains for the same bar. The spread of plasticity is approximately 30 inches on the South side and 30 inches on the North side.

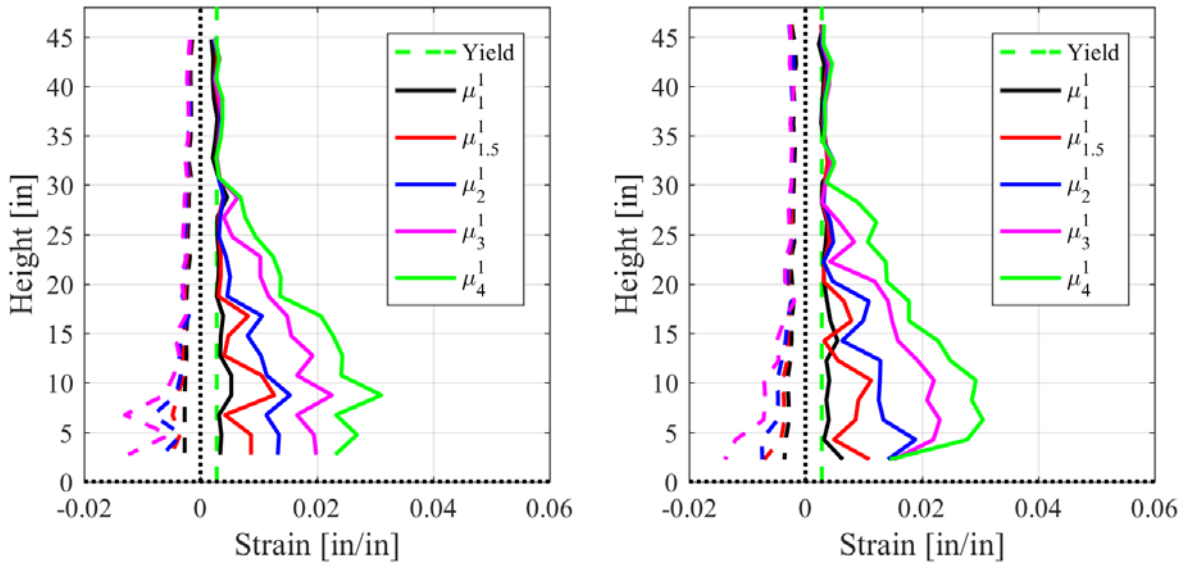

Figure 4-34. (a) Bar S3 strain profile; (b) Bar N3 strain profile

In addition to strain profiles for the longitudinal bars, Figure 4-35 shows the strain profiles for the spirals over the height of the column. Figure 4-35(a) shows that the spirals on the South side first yielded during μ_2, and spirals on the North side yielded during μ_3, Figure 4-35(b). This is much earlier than the first column test. As mentioned above, as the spirals yield, they provide less confinement to the longitudinal bars causing bar buckling to occur earlier. The only design variable that changed between the first and second column test was the axial load ratio.

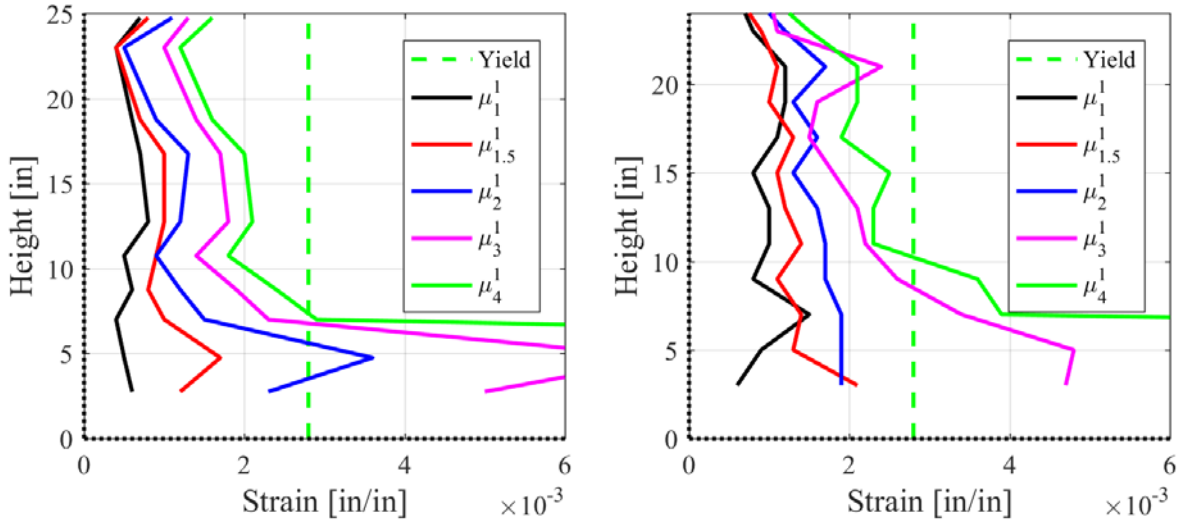

Figure 4-35. (a) South spiral strain profile; (b) North spiral strain profile

4.2.3. Components of Displacement

One component of displacement under a seismic event occurs from the bond slip of the longitudinal reinforcement, or strain penetration. Figure 4-36 includes the bond slip data for both sides of the column with the method described in Section 4.1.3.

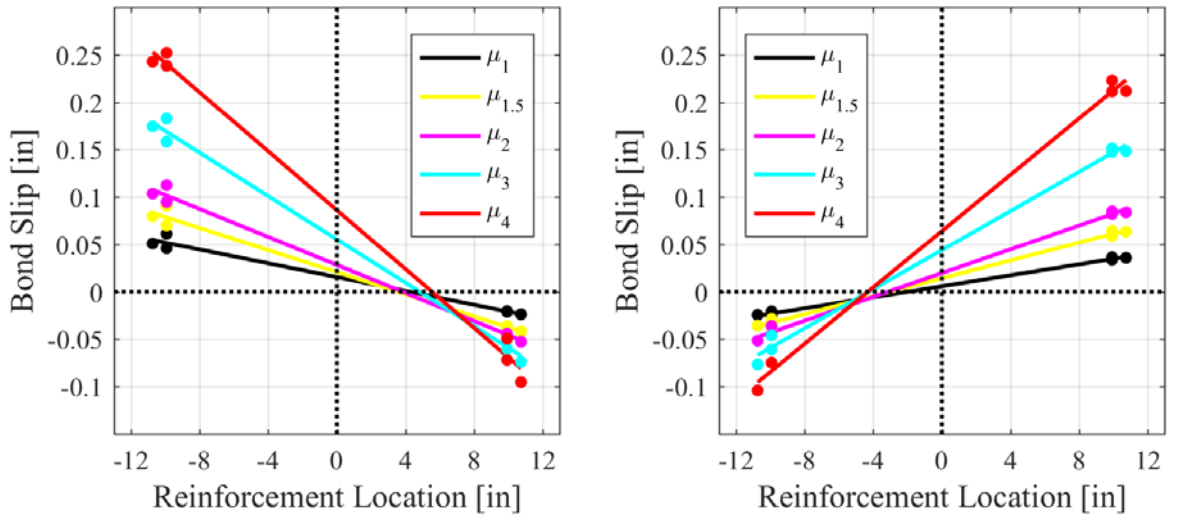

Figure 4-36. (a) Bond slip of south extreme fiber bar under push cycles; (b) Bond slip of north extreme fiber bar under pull cycles

As mentioned in Section 4.1.3, flexural deformation is calculated by integrating the curvature of the column over its height. The optical measurement system provides strain at discrete locations over the height of each longitudinal bar. The strains are used to estimate the curvature at discrete locations over the height of the column by taking the slope of linear fit through the strain at each height. This estimate of the curvature profile can then be integrated to calculate the component of displacement from flexural deformation of the plastic hinge. Figure 4-37(a) shows the curvature profile from this method at the first cycle of each level of ductility.

Figure 4-37(b) shows the combination of the components of displacement from base rotation due to strain penetration and the flexural deformation from integration of the curvature profile for the first cycle of each level of ductility. These two components of displacement combine to equal the column displacement at each ductility cycle. The small difference in displacement is attributed to errors in the calculation of each displacement component. This column had a lower displacement capacity than the first column, and also had less displacement due to bond slip, possibly due to the increased axial load.

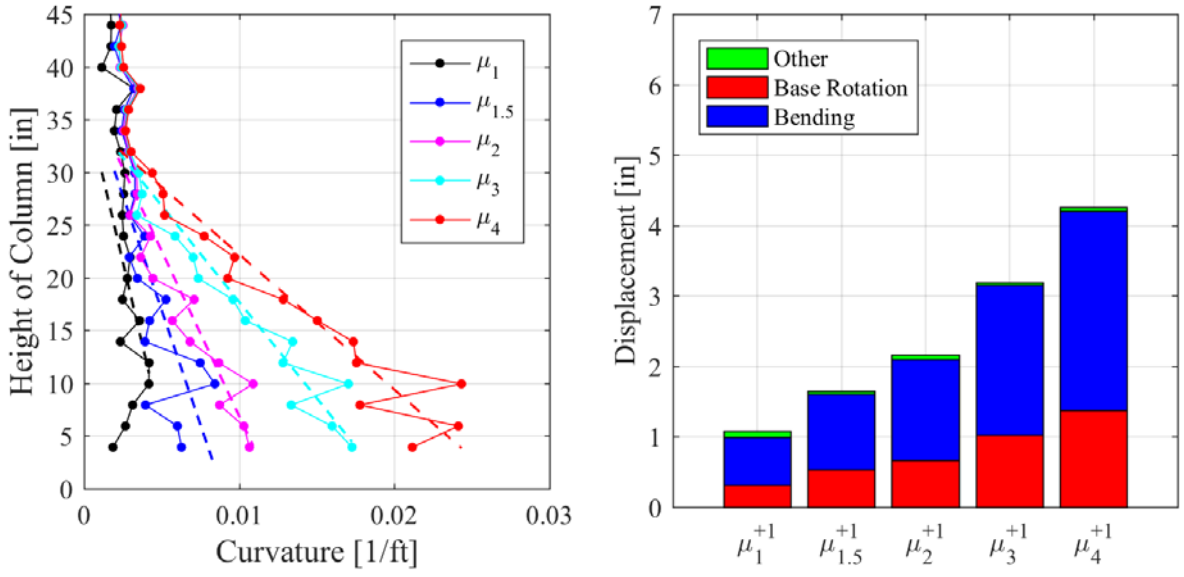

(a) **(b)**

Figure 4-37. (a) Curvature profile from strain interpolation; (b) Components of column displacement

4.2.4. Hysteretic Energy Dissipation

In order to determine the hysteretic damping of the RC column, the area-based hysteretic damping was calculated for the first cycle of each level of ductility. As described in Section 4.1.4, the Jacobsen hysteretic damping (Equation 4-2) was corrected by Equation 4-3. Thus, Figure 4-38 includes the Jacobsen hysteretic damping as well as the corrected hysteretic damping. The hysteretic damping is directly proportional to the energy dissipated by the column.

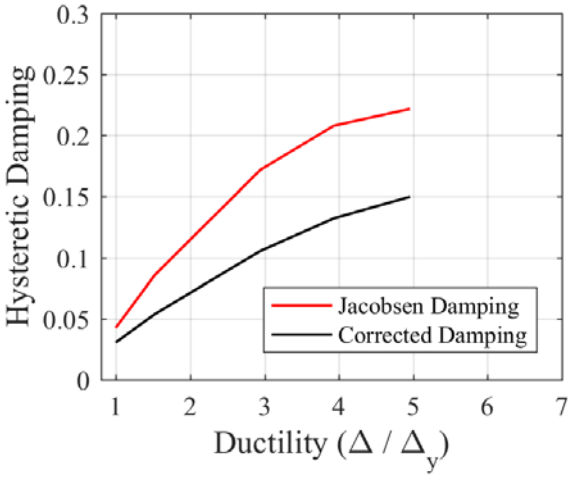

Figure 4-38. Hysteretic damping

4.2.5. Comparison to Grade 60 Columns

As mentioned in Section 4.1.5, Goodnight et al. (2015) performed 30 test on columns reinforced with A706-60 rebar under quasi-static, three cycle-set loading histories. Two of the columns tested in the previous test matrix are similar to this column test. One of the tests had the same geometry, longitudinal rebar content, transverse rebar content, and axial load ratio (Test 27, as numbered in the Goodnight et al., 2015 report). The other had all the same variables except longitudinal rebar content (Test 26). The rebar content of this comparison column was $\rho = 2.1\%$ (16 #7 bars), which theoretically matched the strength of the column with 16 #6 Grade 80 bars. The load history for all three columns followed displacement ductility increments of 1, 1.5, 2, 3, 4, 5, 6 (although the grade 80 column test ended at displacement ductility 5).

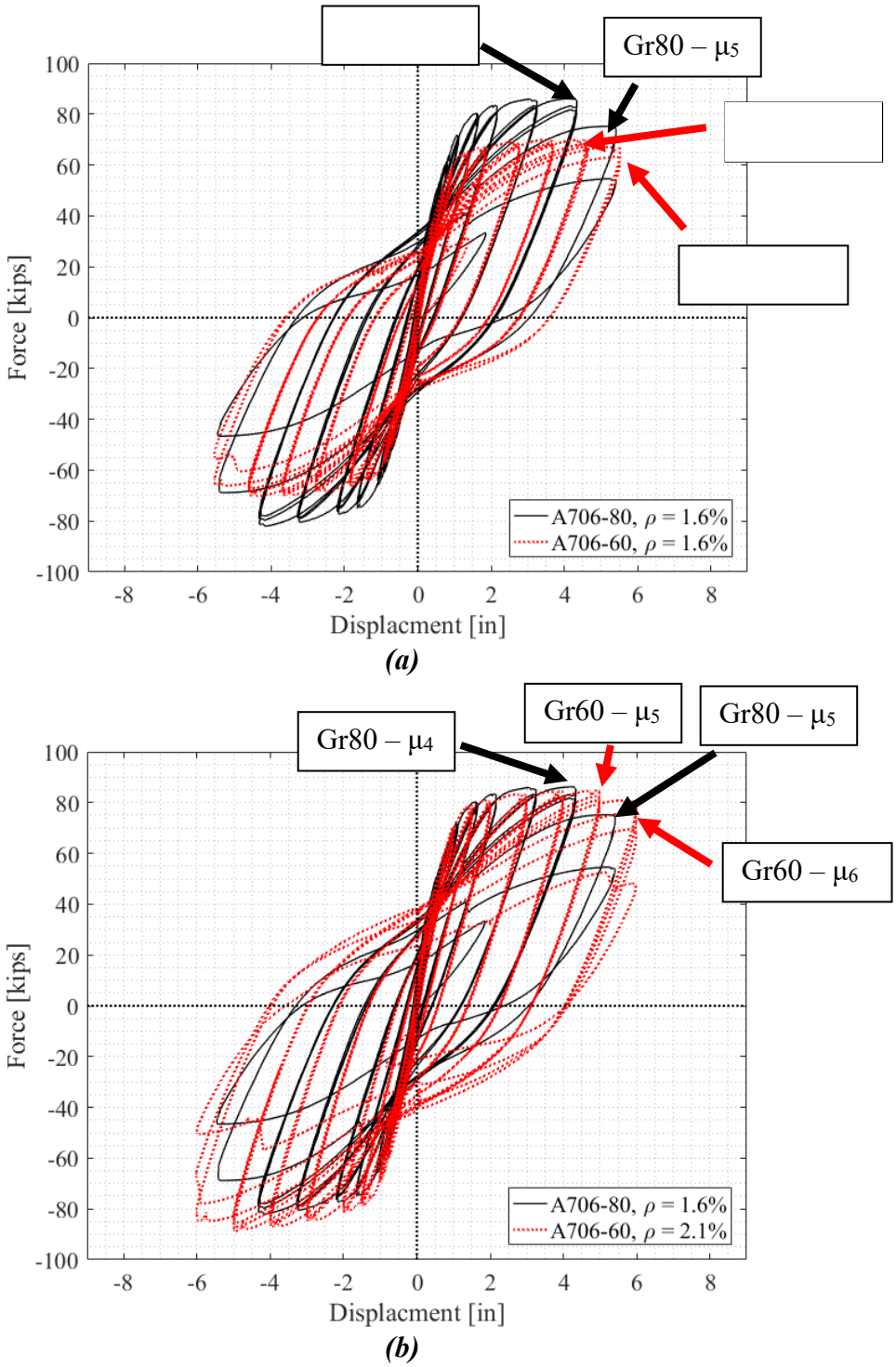

Figure 4-39. Hysteretic response of Grade 80 Test 2 and comparison Grade 60 columns with: (a) similar steel content; (b) similar strength

The Grade 60 columns have similar displacement capacities to the Grade 80 reinforced column, and the longitudinal bars buckle upon reversals from similar levels of lateral displacement and have similar peak tensile strains prior to buckling, as shown in Table 4-10. As mentioned previously, displacement ductility cannot be directly compared, as the yield displacement of the Grade 80 columns is higher than the comparison Grade 60 columns.

Table 4-10. Summary of damage limit states for column test 2

Column Test	Column Side	Longitudinal Bar Buckling			Bar Fracture	
		μ_D	Displacement	Strain (+)	μ_D	Displacement
A706-80 ρ_l = 1.6% ρ_t = 1.0%	South North	4 -4	4.32” -4.32”	0.031 0.031	5 -5	5.40” -5.40”
A706-60 ρ_l = 1.6% ρ_t = 1.0%	South North	5 -4	4.60” -3.67	0.036 0.024	6 -6	5.53” -5.53”
A706-60 ρ_l = 2.1% ρ_t = 1.0%	South North	5 -4	4.98” -3.98”	0.032 0.024	6 -6	5.98” -5.97”

As described in Section 4.1.3, the longitudinal rebar bond slip of the Grade 60 columns was measured and compared to the Grade 80 test column. The bond slip for the pull and push cycles of each column test were plotted versus the corresponding column displacement in Figure 4-40. As was the case with the first A706-80 column test, columns reinforced with Grade 80 rebar have slightly more bond slip than the Grade 60 rebar at high levels of displacement, but the bond slip behavior is very similar for the majority of the test.

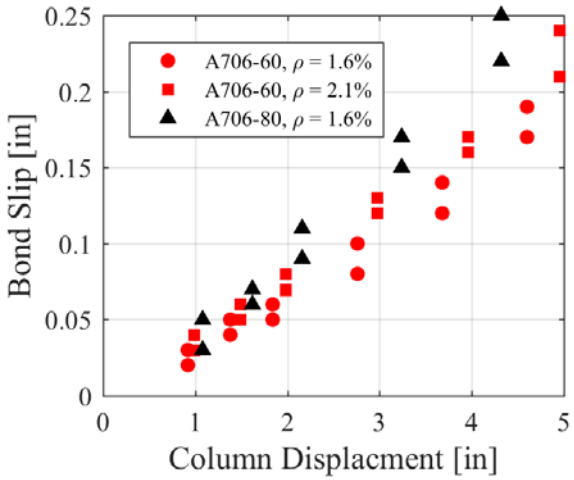

Figure 4-40. Compare bond slip for Grade 80 test 2 with Grade 60 columns

Figure 4-41 shows a comparison of the corrected hysteretic damping (as described in Section 4.1.4) and Grade 80 column and comparison Grade 60 columns had similar damping.

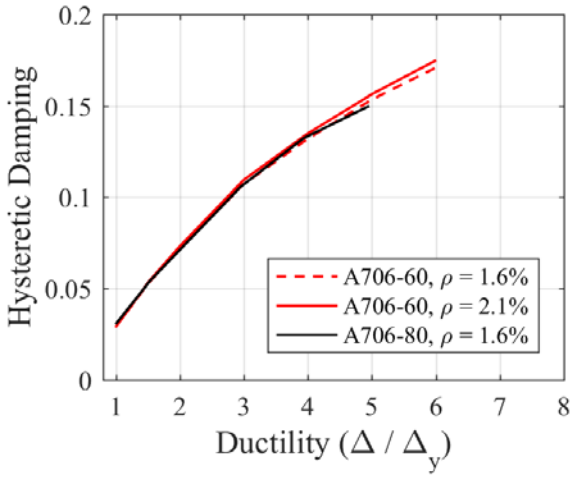

Figure 4-41. Comparison of damping vs. ductility for Grade 80 test 2

4.2.6. Analytical Model

In order to examine how the experimental force-displacement results compared to current modeling practice, the experimental force-displacement response was compared to the cyclic response of an OpenSees fiber model and a pushover analysis performed in Cumbia. Section 4.1.6 describes the development of each model. Figure 4-42 shows the comparison of the force-displacement response for each method. Similar to the first Grade 80 column test, the hysteretic response matches the modeling approach of each method.

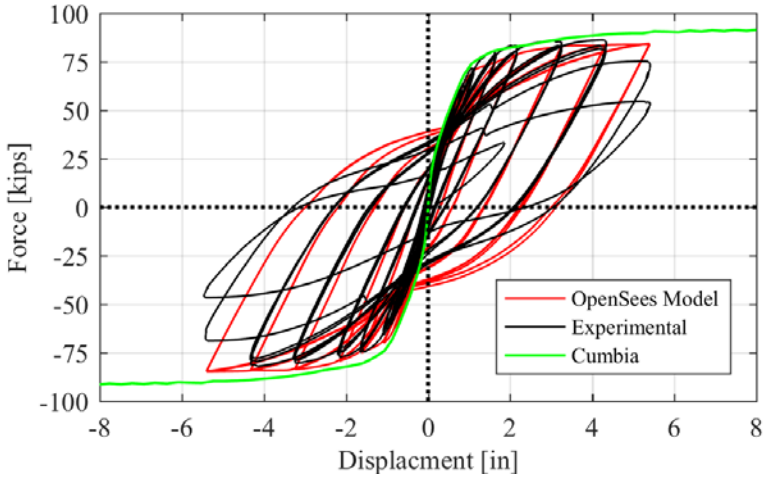

Figure 4-42. Actual and analytical force-displacement responses

4.3. Column Test 3 Summary

Column Test 3 was conducted at the CFL on the campus of NCSU on Wednesday, July 19, 2017, as part of the project to study the seismic performance of A706-80 rebar in reinforced concrete members. The 8' specimen was subjected to a quasi-static three-cycle set loading and a constant 5% axial load ratio.

Table 4-11. Column test 3 summary information

COLUMN PARAMETERS	
Longitudinal Steel:	(16) #6 A706-80 Bars (ρ_l = 1.6%)
Transverse Steel:	#3 Spirals @ 2.75" Pitch (ρ_t = 0.7%)
Longitudinal Steel Yield Strength:	83 ksi
Transverse Steel Yield Strength:	79 ksi
Concrete Strength:	6.8 ksi
Axial Load:	154 kips
Axial Load Ratio:	5%
Experimental First Yield Displacement:	0.80"
Analytical Nominal Moment Capacity	570.7 kip*ft
Equivalent Yield Displacement	1.07"
Maximum Lateral Force	74.0 kips
Failure Mode	Rupture of previously buckled reinforcement
DAMAGE OBSERVATIONS	
First Cracking North	-¼ F_y' = -0.18"
First Cracking South	¼ F_y' = 0.20"
Core Concrete Crushing North:	$\mu_{1.5}^{1+}$ = 1.61"
Core Concrete Crushing South:	$\mu_{1.5}^{1-}$ = -1.61"
Transverse Steel Yielding North:	At 2.91" during push to μ_3^{1+} = 3.21"
Transverse Steel Yielding South:	At -3.01" during pull to μ_3^{1-} = -3.21"
Longitudinal Bar Buckling North	During reversal from μ_4^{1-} = -4.28"
Longitudinal Bar Buckling South	During reversal from μ_4^{2+} = 4.28"
Longitudinal Bar Fracture North	At -3.49" during pull to μ_4^{3-} = -4.28"
Longitudinal Bar Fracture South	At 2.48" during push to μ_5^{1+} = 5.35"
Note: μ_4^{1-} signifies the first pull cycle of displacement ductility 4	

Table 4-12. Column test 3 strain limit states

MATERIAL STRAINS	
Core Concrete Crushing North:	ε_s = 0.0049 *(rebar compressive strain)*
Core Concrete Crushing South:	ε_s = 0.0057 *(rebar compressive strain)*
Transverse Steel Yielding North:	ε_s = 0.0112 *(rebar compressive strain)*
Transverse Steel Yielding South:	ε_s = 0.0119 *(rebar compressive strain)*
Longitudinal Bar Buckling North	** ε_s = 0.0284 *(peak tensile strain prior to BB)* ε_s = 0.0112 *(rebar comp. strain prior to BB)*
Longitudinal Bar Buckling South	ε_s = 0.0308 *(peak tensile strain prior to BB)* ε_s = 0.0124 *(rebar comp. strain prior to BB)*
** *Inaccurate, see explanation in Section 4.3.2*	

The column was subjected to three-cycle set loading. This load history consisted of single positive and negative cycles until the first yield of the reinforcement. The average first yield displacement was 0.80", which was multiplied by the ratio of the analytical first yield and nominal moments (1.34), as seen in Equation 4-1. The equivalent yield displacement was 1.07" and was used for the rest of the test, performing three positive and negative cycles at ductility (μ) 1, 1.5, 2, 3, 4, and 5.

On the day of the test, compressive tests were performed on 4" x 8" concrete cylinders that were tested according to ASTM C39. Table 4-13 contains the test day results.

Table 4-13. Test day concrete strength for column test 3

Column			**Footing**	
Cylinder	**Stress (ksi)**		**Cylinder**	**Stress (ksi)**
1	6.80		1	7.88
2	7.25		2	8.38
3	6.70		3	8.27
4	6.54		4	8.25
Average	**6.82**		**Average**	**8.20**

Figure 4-43 displays a plot of the force-displacement response along with a progression of longitudinal reinforcement fractures. Figure 4-44(a) shows the load history for this test, along with

similar markings for rebar fracture and two other damage limit states. Figure 4-44(b) displays the bar labeling scheme. As seen below, the column experiences failure when the longitudinal bars fracture, which significantly reduces the lateral load capacity. Extreme fiber tensile reinforcement on the North side of the column fractures in the last cycle of μ_4, but the lateral force capacity of the column does not drop below 80% of peak lateral force capacity, signifying that the column does not technically fail until μ_5.

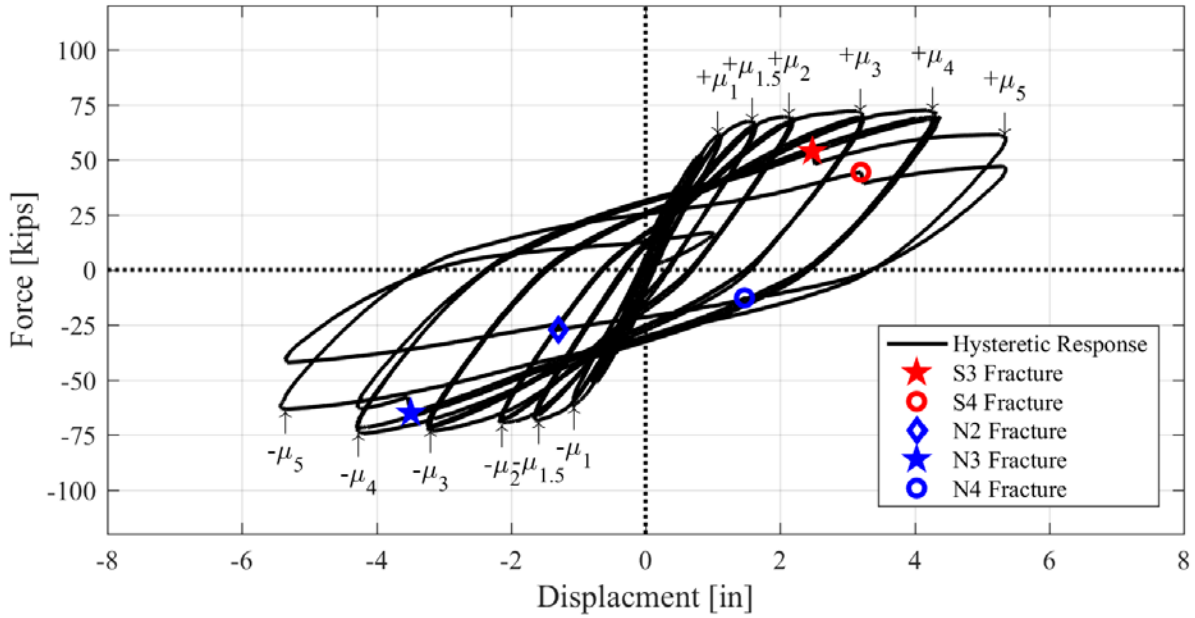

Figure 4-43. Column test 3 force-displacement response with rebar fracture locations

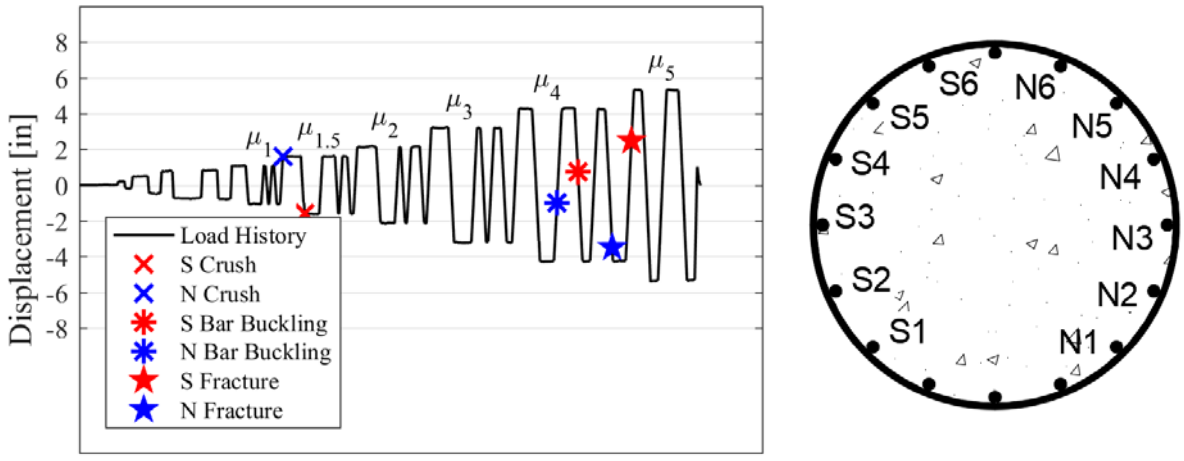

(a) **(b)**

Figure 4-44. (a) Column test 3 load history. (b) Column test 3 bar labels

4.3.1. Damage Progression

Damage occurred in a relatively uniform manner on the North and South sides of the column. Horizontal hairline cracks developed on the extreme faces of the column in the initial pre-yield cycles of the loading history. The first cracks were visible after the first push cycle to ¼*F_y. At ½*F_y, diagonal cracks began to develop on the non-extreme faces (East and West). These diagonal cracks began at roughly 20 inches above the footing-column interface. During the pull cycle to -¾ F_y, a crack on the top of the footing perpendicular to the column was observed on the North side. Similar footing cracking was observed on the South during the first push to F_y. At the first analytical first yield force (F_y), the maximum crack widths measured on the column were 0.01 inches wide. During $\mu_{1.5}^{1+}$, column concrete began to scale off the column, which was taken to be an indication of the beginning of core concrete crushing. Maximum crack widths at $\mu_{1.5}$ measured 0.04 inches. In μ_2, maximum crack widths in the exposed core region of concrete grew to 0.05 inches. By μ_3, cracks were concentrated in the bottom portion of the column; maximum crack widths exceeded 0.06 inches. Bar buckling was first visibly observed on the second cycle of μ_4, but this will be examined further in the strain data available from the optical measuring system (Optotrak). Below are some of the pictures at different stages of damage throughout the test.

(a) **(b)**

Figure 4-45. First cracking: (a) South face, ¼ F'$_y$; (b) North face, -¼ F'$_y$

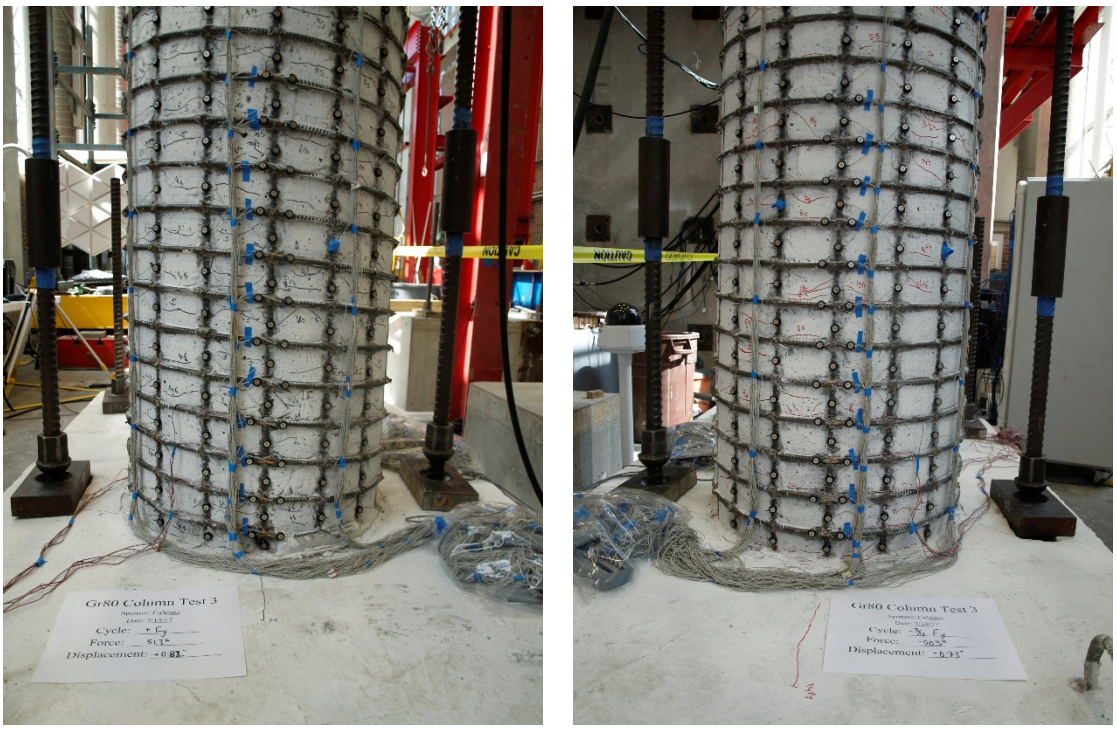

(a) **(b)**

Figure 4-46. Footing Cracking: (a) F'$_y$ on South; (b) -¾ F'$_y$ on North

(a) **(b)** **(c)**

Figure 4-47. First Yield (F'$_y$): (a) South face; (b) West face ; (c) North face

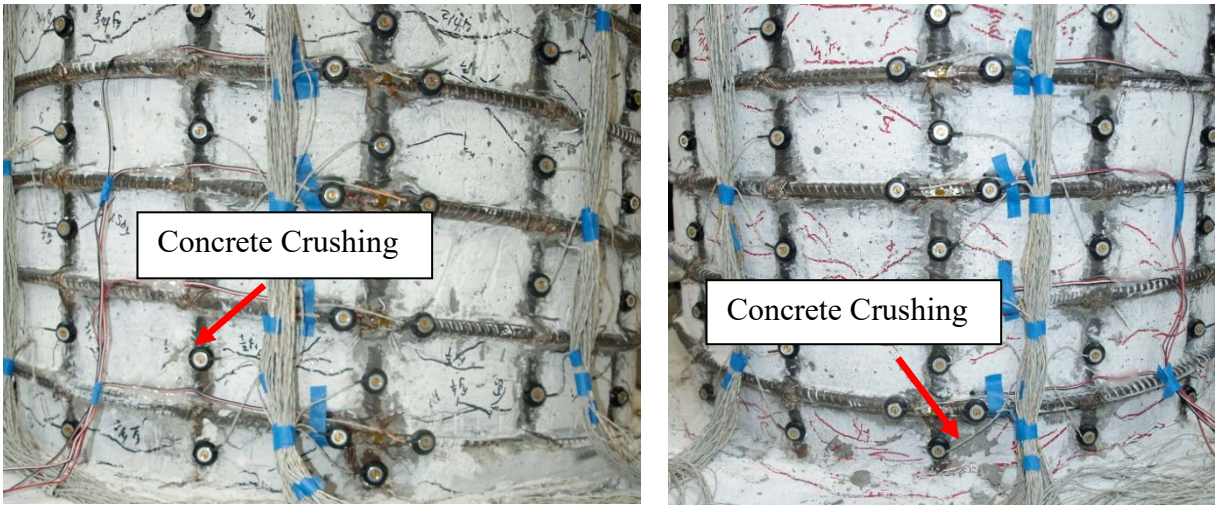

(a) **(b)**

Figure 4-48. Concrete crushing ($\mu_{1.5}$): (a) South; (b) North

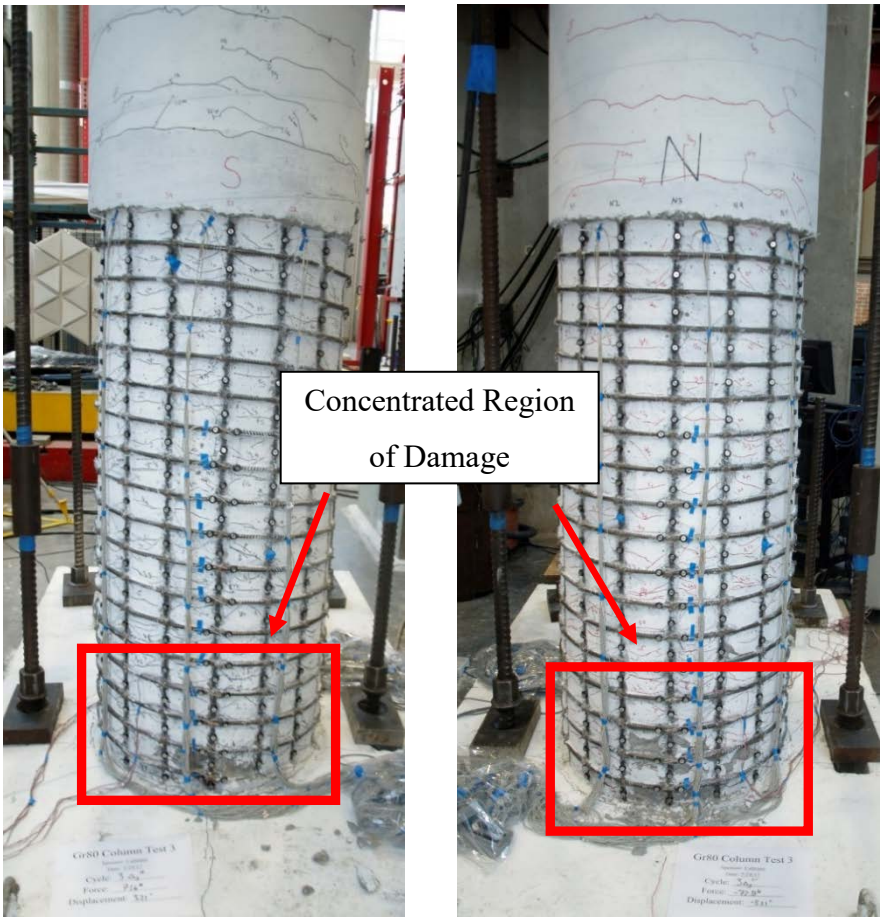

(a) **(b)**

Figure 4-49. Ductility 3: (a) South, μ_3^{1+} (b) North, μ_3^{1-}

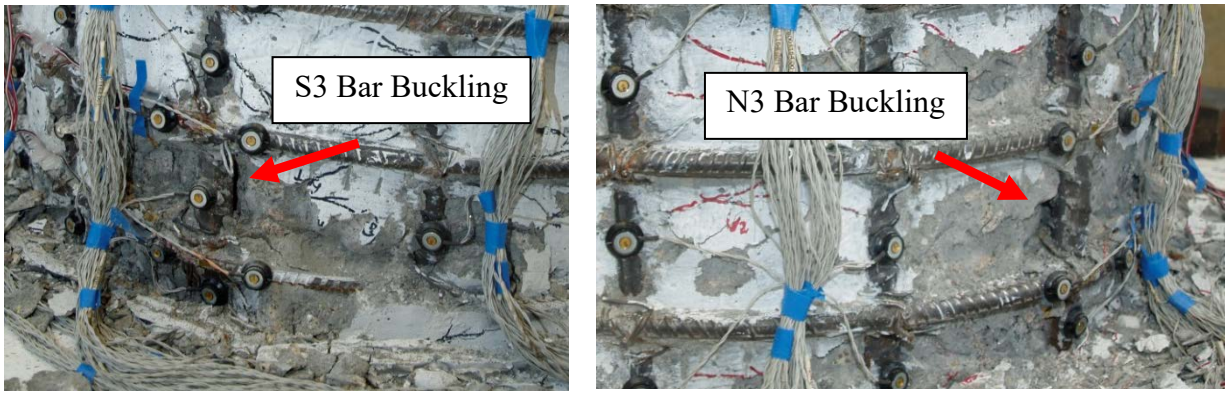

(a) **(b)**

Figure 4-50. (a) S3 buckled μ_4^{2-}; (b) N3 buckled, μ_4^{2+}

(a) **(b)**

Figure 4-51. (a) South bar fracture (S3), μ_5^{1+}; (b) North bar fracture (N3), μ_4^{3-}

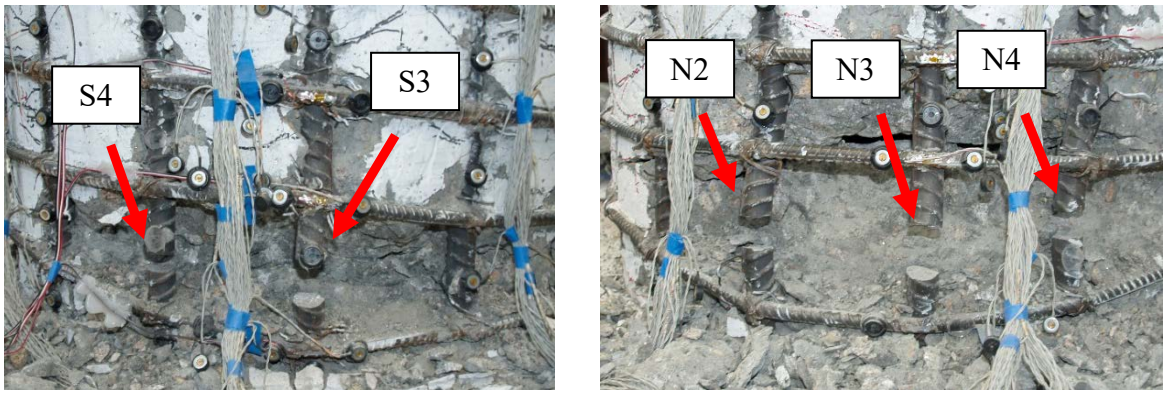

(a) **(b)**

Figure 4-52. Final Damage State: (a) South side, μ_5^{2+}; (b) North side, μ_5^{2-}

4.3.2. Strain Analysis

By examining the 3D position of each LED marker throughout the duration of the test, strain levels in each of the instrumented longitudinal bars and transverse spirals was available until failure. See Figure 3-11 for a picture of the cover concrete block-out and optical position instrumentation.

The highest level of strain in the longitudinal bars on the North extreme face of the column was 0.0284 on the first pull cycle of ductility 4 (μ_4^{1-}). Visible bar buckling was observed on the reversal from the second pull cycle of ductility 4. However, at the end of the first pull cycle of ductility 4, the 17th LED marker (second from the bottom) on bar N3 was observed as detached from the bar, as seen in Figure 4-53.

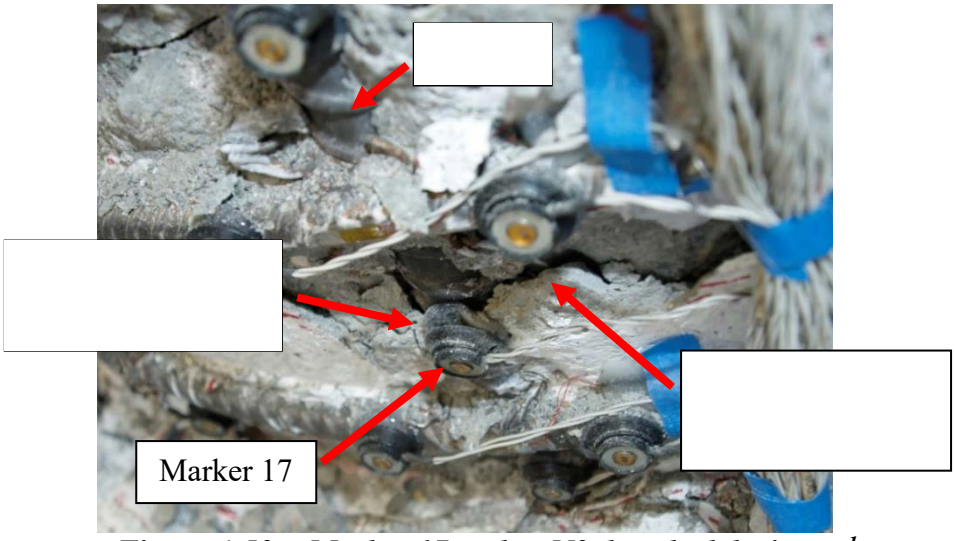

Figure 4-53. Marker 17 on bar N3 detached during μ_4^{1-}

As core concrete crushes, the crushed concrete begins to scale away from the column. In this case, as the core concrete crushed on the North side of the column, the concrete became wedged in between the glue used to attach the LED marker cap and the rebar. As this core concrete was loaded in compression, the core expands from the column. As the core concrete expanded, it moved the LED marker away from the bar and the position of the marker appeared to be lower than the original position. For this reason, when calculating the change of length of the two adjacent gage lengths (gage 17 & 16), the value of gage 17 appeared to be uncharacteristically lower than normal, while gage 16 appeared longer. Figure 4-54 shows this behavior in the strain

vs. displacement plots for each gage length. During the pull to a displacement of -4.3", gage 17 (centered at 2.5" above the footing) appears to experience inexplicably lower compressive strains, while gage 16 appears to have experience higher tensile strain.

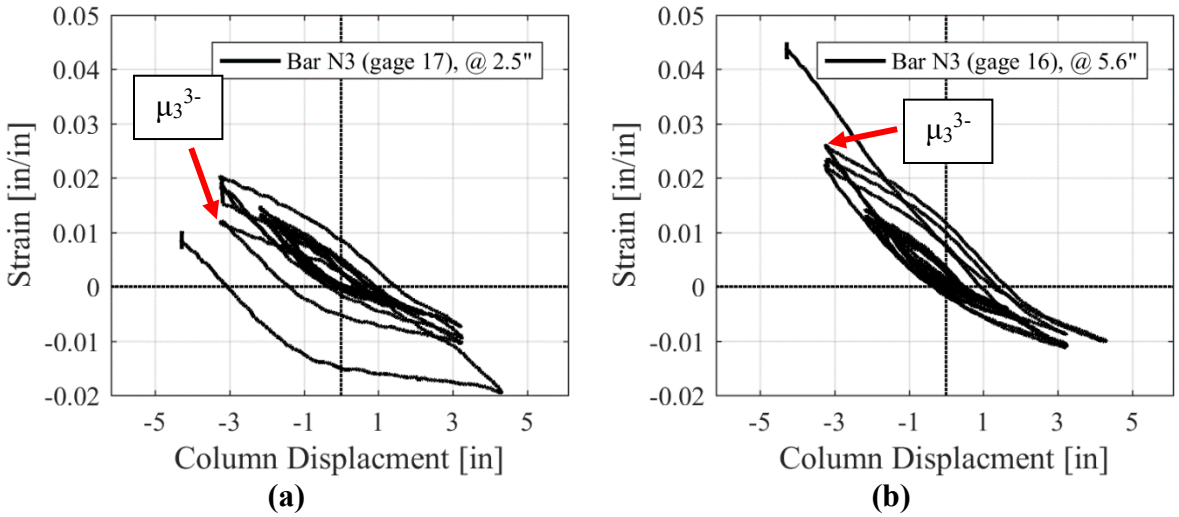

Figure 4-54. Bar N3: (a) Gage 17 @ 2.5" above footing; (b) Gage 16 @ 5.6" above footing

Figure 4-54 shows that marker 17 began to be affected by the expanding concrete during the last cycle of ductility 3 (μ_3^{3-}). During this cycle, levels of strain did not match the levels of strain during the first two cycles of μ_3. The only other explanation for this discontinuity in strain measurements is bar buckling, but the bar does not appear to buckle until μ_4. Thus, the strains of gages 16 and 17 could not be calculated correctly during μ_4. The maximum tensile strain prior to buckling was recorded at gage 15, centered at 8.4" above the footing, as shown in Figure 4-55. In previous column tests, maximum tensile strain has typically been observed at the height of gage 16. Thus, this peak measured tensile strain prior to bar buckling measured at gage 15 was likely lower than the actual peak tensile strain experienced by the bar. The maximum strain at gage 16 was inaccurate for the aforementioned reason that one of the LED markers detached from the rebar while measuring strain. Strain on the North side was not used for comparison to existing prediction models.

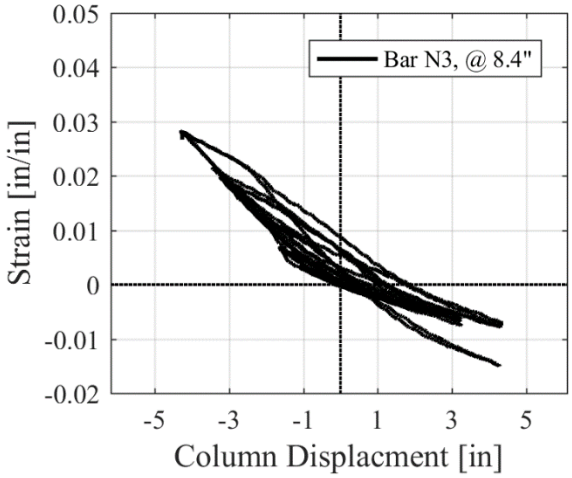

Figure 4-55. Peak tensile strain prior to bar buckling in bar N3

As the extreme fiber bar (N3) buckled and fractured, the bars on either side (N2 & N4) experienced buckling also. Bar N2 buckled upon reversal from the first pull cycle of μ_5, and the maximum tensile strain that this bar experienced prior to buckling was 0.0492, as shown in Figure 4-56(a). Bar N4 also buckled upon reversal from the first pull cycle of μ_5, but the maximum strain in this bar is unknown because two LED markers were detached from bar N4 during the N3 fracture. Figure 4-56(b) shows the onset of bar buckling.

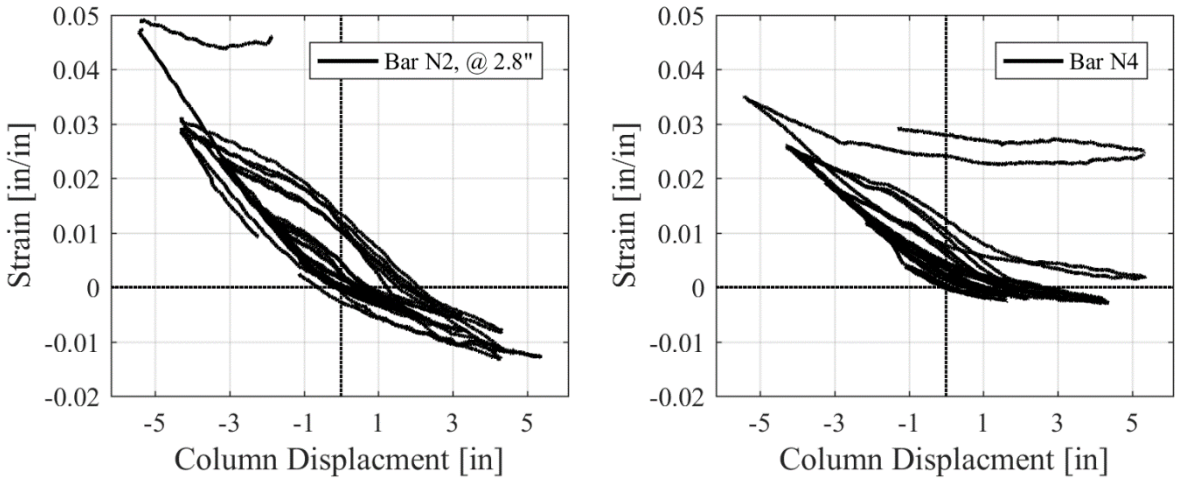

Figure 4-56. Strain vs. displacement: (a) bar N2; (b) bar N4

Maximum strains in the South extreme fiber bar reached 0.0319 before bar buckling was observed. Bar buckling was visually observed and confirmed by the graph of the strain vs. peak column displacement during the second pull cycle of ductility 4 (μ_4^{2-}). Figure 4-57 shows at gage

17, which was centered approximately 2.4 inches above the footing. Bar S3 later fractures during the first push cycle of ductility 5 (μ_5^{1+}).

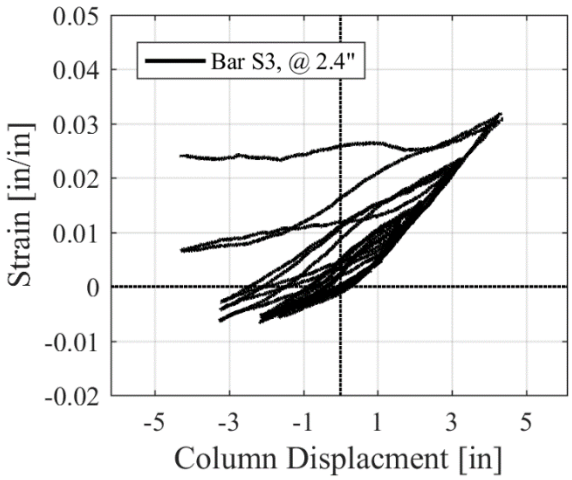

Figure 4-57. Bar S3 strain vs. displacement

Once the extreme longitudinal bar (S3) buckled, adjacent bars buckled on subsequent cycles, as shown in Figure 4-58.

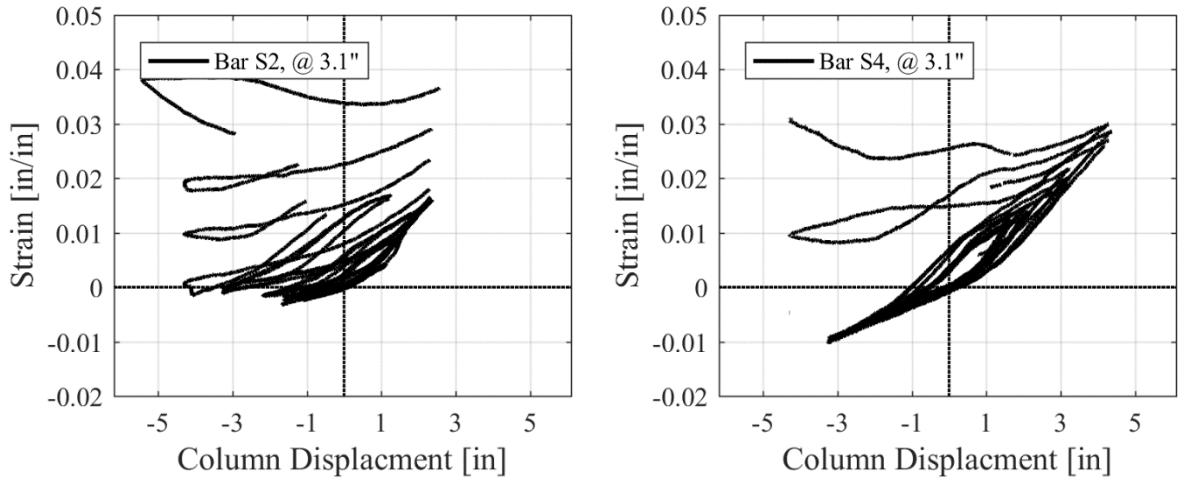

(a) **(b)**

Figure 4-58. (a) Bar S2 buckling; (b) bar S4 buckling

An error occurred with the optical position data on bar S2. As the bar was loaded in tension, the optical position data was unavailable, leaving gaps in the strain data for column displacements greater than 3 inches. Compressive strain data was still available, however, which indicates the onset of bar buckling.

Figure 4-59 shows the strains in the second lowest spiral that confines the plastic hinge region. These spirals were instrumented with a strain gage and Optotrak LED markers. The strain gages on both sides de-bond around tensile strains of 0.017. As the spiral yields, it provides less confinement to the longitudinal rebar, which causes the longitudinal bars to buckle. The spirals on both sides yield when loaded in compression during μ_3. During μ_4, the spirals experience significant plastic deformation, which corresponds to when the extreme fiber longitudinal bars begin to buckle. More investigation should be performed on the relationship between transverse steel stiffness and longitudinal bar buckling.

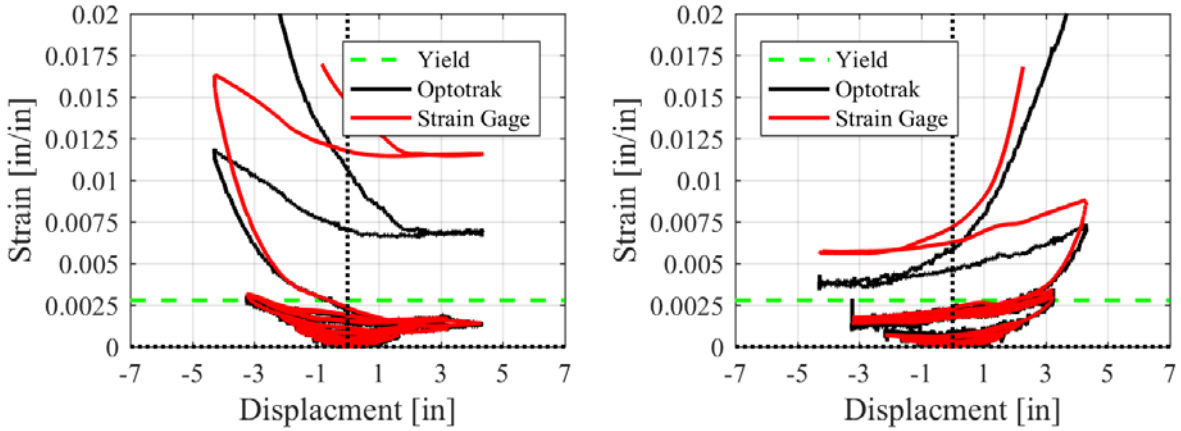

Figure 4-59. Strain vs. displacement: (a) 2nd South spiral; (b) 2nd North spiral

In addition, the data can also be formatted to plot the strain profile over the height of the column. This information shows the extent of longitudinal bar yielding, or the spread of plasticity, over the height of the plastic hinge region. Figure 4-60 shows the graphs of the strain vs. height for bars S3 and N3. Solid lines represent the maximum tensile strains for each gage at the specified cycle, while dashed lines depict the maximum compressive strains for the same bar. The spread of plasticity is approximately 30 inches on the South side and 27 inches on the North side.

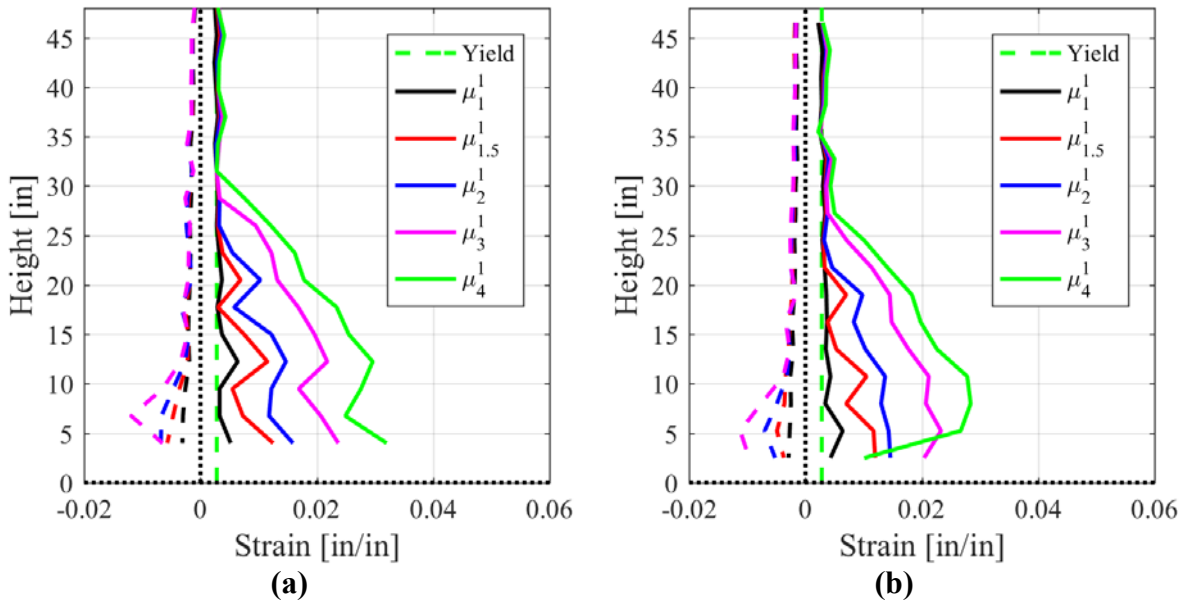

Figure 4-60. (a) Bar S3 strain profile; (b) Bar N3 strain profile

In addition to strain profiles for the longitudinal bars, Figure 4-61 shows the strain profiles for the spirals over the height of the column. As the spirals yield, they provide less confinement to the longitudinal bars causing bar buckling to occur earlier. This behavior is similar to the second column test.

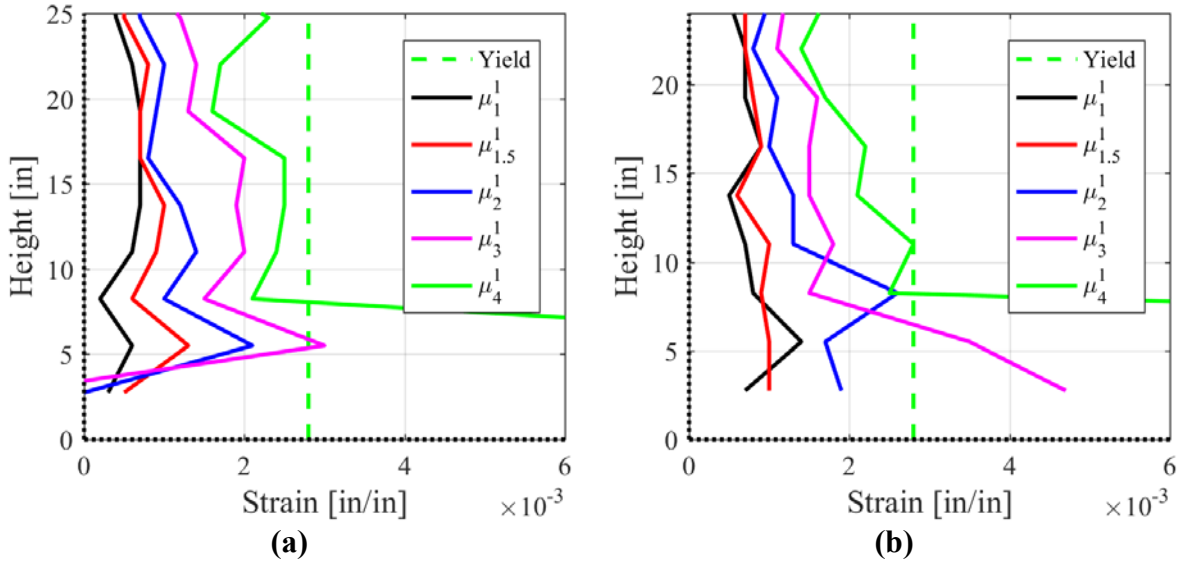

Figure 4-61. (a) South spiral strain profile; (b) North spiral strain profile

4.3.3. Components of Displacement

The component of displacement from longitudinal bond slip of the reinforcement is calculated using the process described in Section 4.1.3. Figure 4-36 includes the bond slip data under push and pull cycles prior to buckling of the reinforcement.

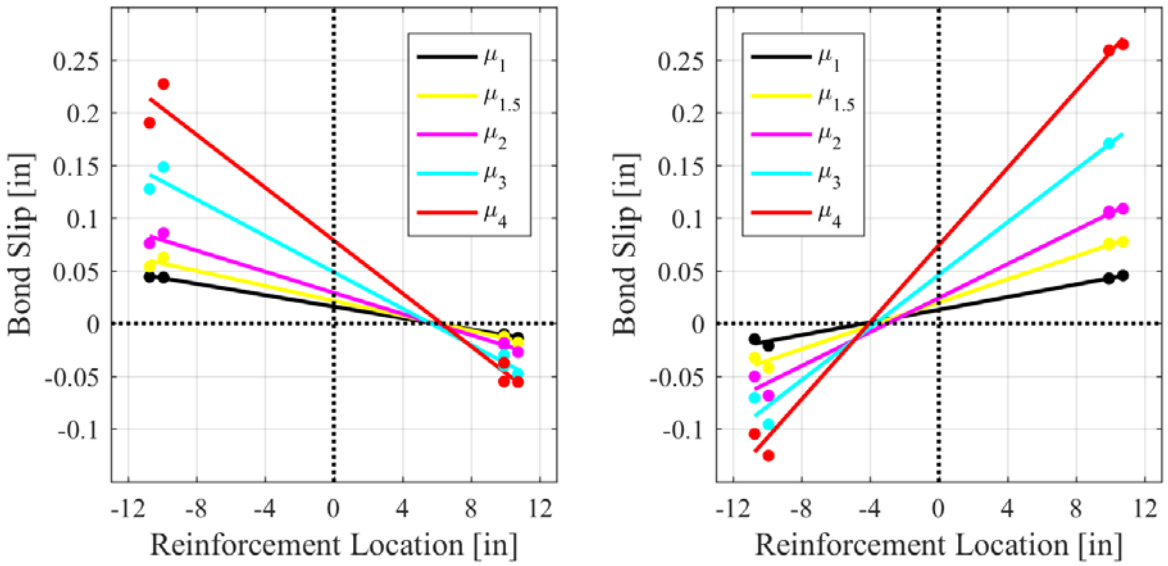

Figure 4-62. (a) Bond slip of south extreme fiber bar under push cycles; (b) Bond slip of north extreme fiber bar under pull cycles

As mentioned in Section 4.1.3, flexural deformation in the plastic hinge region is calculated by integrating the curvature of the column over its height. The optical measurement system provides strain profiles in each longitudinal bar that can be used to estimate the curvature over the height of the column. This estimate of the curvature profile can then be integrated to calculate the component of displacement from flexural deformation of the plastic hinge. Figure 4-63(a) shows the curvature profile from this method at the first cycle of each level of ductility.

Figure 4-63(b) shows the combination of the components of displacement from base rotation due to strain penetration and the flexural deformation from integration of the curvature profile for the first cycle of each level of ductility. These two components of displacement combine to equal the column displacement at each ductility cycle. The small difference in displacement is attributed to errors in the calculation of each displacement component.

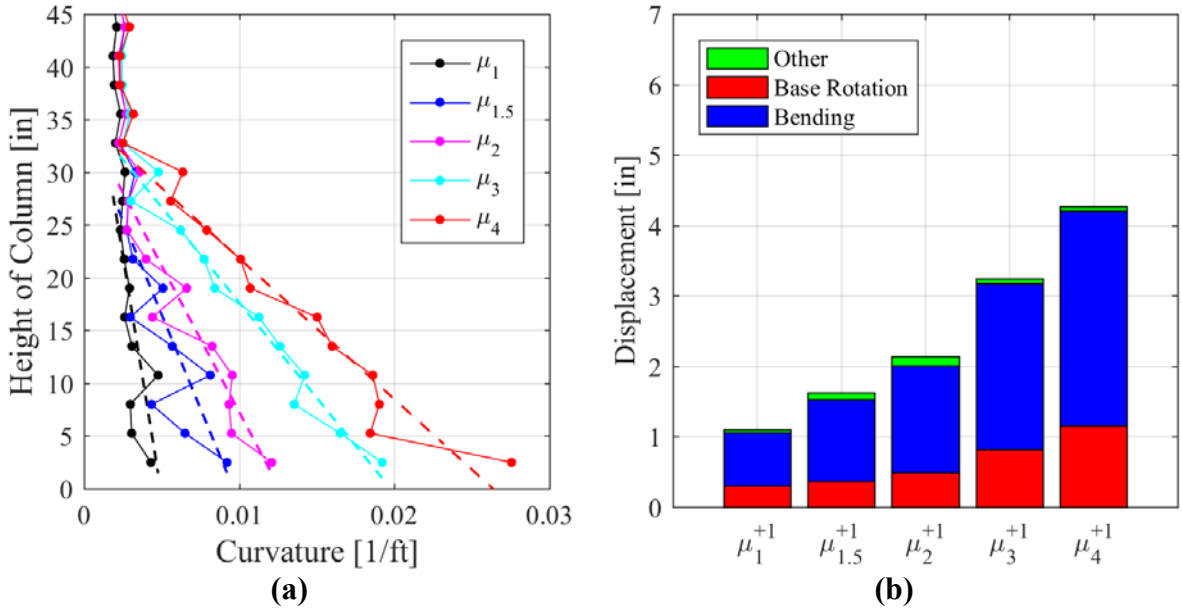

(a) **(b)**

Figure 4-63. (a) Curvature profile from strain interpolation; (b) Components of column displacement

4.3.4. Hysteretic Energy Dissipation

As described in Section 4.1.4, the corrected Jacobsen hysteretic damping was calculated for the first cycle of each ductility. Figure 4-64 shows the Jacobsen hysteretic damping as well as the corrected hysteretic damping.

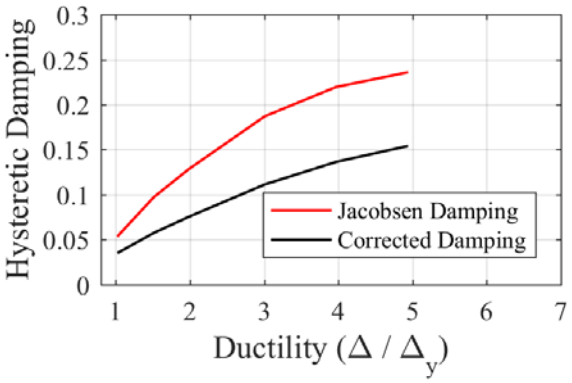

Figure 4-64. Hysteretic damping

4.3.5. Comparison to Grade 60 Columns

As mentioned in Section 4.1.5, Goodnight et al. (2015) performed thirty A706-60 column tests under quasi-static, three cycle-set loading histories. Test 15 (as numbered in the Goodnight

et al., 2015 report) had the same geometry, longitudinal rebar content, transverse rebar content, and axial load ratio. The load history for the Grade 80 column used displacement ductility increments of 1, 1.5, 2, 3, 4, 5, 6, 7, while the Grade 60 column used displacement ductility increments of 1, 1.5, 2, 3, 4, 6, 8. Figure 4-65 shows the two hysteretic responses.

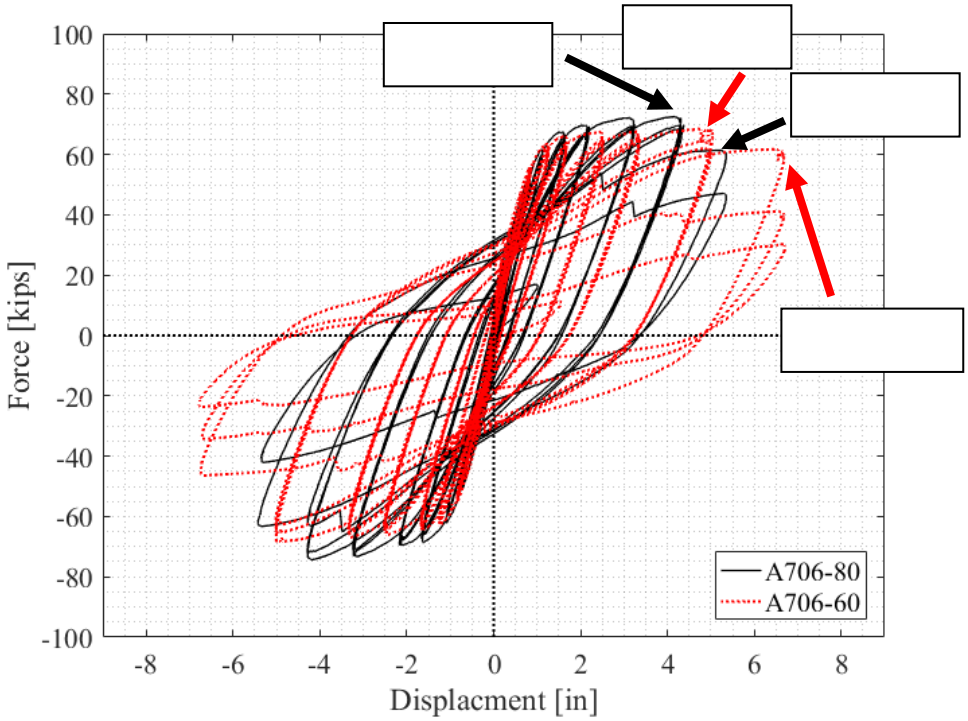

Figure 4-65. Hysteretic response of Grade 80 Test 3 and comparison Grade 60 column

The Grade 60 column has similar displacement capacity to the Grade 80 reinforced column, and the longitudinal bars buckle upon reversals from similar levels of lateral displacement and have similar peak tensile strains prior to buckling, as shown in Table 4-14. While the extreme fiber bar on the North fractured at μ_4, the column did not fail until μ_5 (strength drop by 20%)

Table 4-14. Summary of damage limit states for column test 3

Column Test	Column Side	Longitudinal Bar Buckling			Bar Fracture	
		μ_D	Displacement	Strain (+)	μ_D	Displacement
A706-80 $\rho_l = 1.6\%$ $\rho_t = 0.7\%$	South North	4 -4	4.28 -4.28	0.032 N/A	5 -4	5.35” -4.28”
A706-60 $\rho_l = 1.6\%$ $\rho_t = 0.7\%$	South North	6 -6	5.00” -5.00”	0.037 0.038	8 -8	6.69” -6.67”

As described in Section 4.1.3, the longitudinal rebar bond slip of the Grade 60 columns was measured and compared to the Grade 80 test column. The bond slip for the pull and push cycles of each column test were plotted versus the corresponding column displacement in Figure 4-66. Grade 80 columns have slightly more bond slip than the Grade 60 rebar at high levels of displacement, but the bond slip behavior is very similar for the majority of the test.

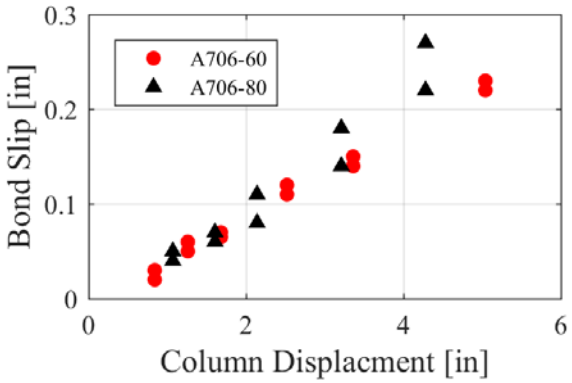

Figure 4-66. Compare bond slip for Grade 80 test 3 with Grade 60 column

Figure 4-67 shows a comparison of the corrected hysteretic damping (as described in Section 4.1.4). The Grade 80 column and comparison Grade 60 columns have very similar damping versus ductility curves. As mentioned previously, ductility does not necessarily correlate to column displacement because of the difference in yield displacement.

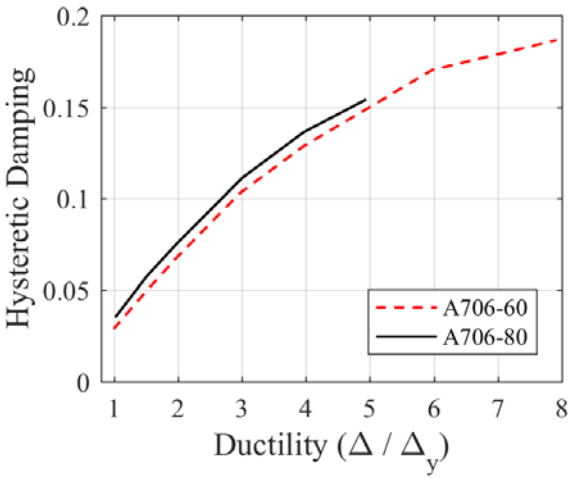

Figure 4-67. Comparison of damping vs. ductility for Grade 80 test 3

4.3.6. Analytical Model

In order to examine how the experimental force-displacement results compared to current modeling practice, the experimental force-displacement response was compared to the cyclic response of an OpenSees fiber model and a pushover analysis performed in Cumbia. Section 4.1.6 describes the development of each model. Figure 4-68 shows the comparison of the force-displacement response for each method. Similar to the other Grade 80 tests, the hysteretic response matches the modeling approach of each method.

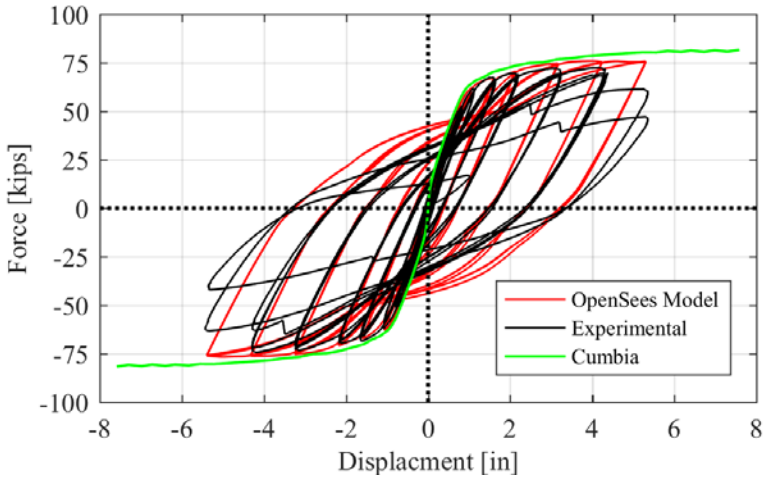

Figure 4-68. Actual and analytical force-displacement responses

4.4. Column Test 4 Summary

Column Test 4 was conducted at the CFL on the campus of NCSU on Friday, August 4, 2017, as part of the project to study the seismic performance of A706-80 rebar in reinforced concrete members. The 8' specimen was subjected to a quasi-static three-cycle set loading and a constant 5% axial load ratio.

Table 4-15. Column test 4 summary information

COLUMN PARAMETERS	
Longitudinal Steel:	(16) #6 A706-80 Bars (ρ_l = 1.6%)
Transverse Steel:	#3 Spirals @ 1.5" Pitch (ρ_t = 1.3%)
Longitudinal Steel Yield Strength:	83 ksi
Transverse Steel Yield Strength:	79 ksi
Concrete Strength:	6.9 ksi
Axial Load:	157 kips
Axial Load Ratio:	5%
Experimental First Yield Displacement:	0.76"
Analytical Nominal Moment Capacity	577.6 kip*ft
Equivalent Yield Displacement	1.03"
Maximum Lateral Force	77.2 kips
Failure Mode	Rupture of previously buckled reinforcement
DAMAGE OBSERVATIONS	
First Cracking North	- ½ F_y' = -0.34"
First Cracking South	½ F_y' = 0.29"
Core Concrete Crushing North:	$\mu_{1.5}^{1+}$ = 1.55"
Core Concrete Crushing South:	$\mu_{1.5}^{2-}$ = -1.57"
Transverse Steel Yielding North:	At 3.24" during push to μ_4^{1+} = 4.12"
Transverse Steel Yielding South:	At -3.79" during pull to μ_4^{1-} = -4.12"
Longitudinal Bar Buckling North	** During reversal from μ_6^{1-} = -6.18"
Longitudinal Bar Buckling South	During reversal from μ_6^{2+} = 6.18"
Longitudinal Bar Fracture North	**At 2.59" during pull to μ_6^{3-} = -6.19"
Longitudinal Bar Fracture South	At -2.74" during push to μ_7^{2+} = 7.22"
Note: μ_4^{1-} signifies the first pull cycle of displacement ductility 4 *** See Section 4.4.2 for information about North side buckling and fracture*	

Table 4-16. Column test 4 strain limit states

MATERIAL STRAINS	
Core Concrete Crushing North:	ε_s = 0.0051 *(rebar compressive strain)*
Core Concrete Crushing South:	ε_s = 0.0048 *(rebar compressive strain)*
Transverse Steel Yielding North:	ε_s = 0.0191 *(rebar compressive strain)*
Transverse Steel Yielding South:	ε_s = 0.0162 *(rebar compressive strain)*
Longitudinal Bar Buckling North	** ε_s = 0.0460 *(peak tensile strain prior to BB)* ** ε_s = 0.0232 *(rebar comp. strain prior to BB)*
Longitudinal Bar Buckling South	ε_s = 0.0463 *(peak tensile strain prior to BB)* ε_s = 0.0201 *(rebar comp. strain prior to BB)*
*** See Section 4.4.2 for information about North side buckling and fracture*	

The column was subjected to three-cycle set loading. This load history consisted of single positive and negative cycles until the first yield of the reinforcement. The average first yield displacement was 0.76", which was multiplied by the ratio of the analytical first yield and nominal moments (1.35), as seen in Equation 4-1. The equivalent yield displacement was 1.03 inches and was used for the rest of the test, performing three positive and negative cycles at displacement ductility (μ) 1, 1.5, 2, 3, 4, 5, 6, and 7.

On the day of the test, compressive tests were performed on 4" x 8" concrete cylinders that were tested according to ASTM C39. Table 4-17 contains the test day results.

Table 4-17. Test day concrete strength for column test 4

Column			**Footing**	
Cylinder	**Stress (ksi)**		**Cylinder**	**Stress (ksi)**
1	7.19		1	8.41
2	7.20		2	7.52
3	6.56		3	8.32
4	6.78		4	8.14
Average	**6.93**		**Average**	**8.10**

Figure 4-69 displays a plot of the force-displacement response along with a progression of longitudinal reinforcement fractures. Figure 4-70(a) shows the load history for this test, along with

similar markings for rebar fracture and two other damage limit states. Figure 4-70(b) displays the bar labeling scheme. As seen below, the column experiences failure when the longitudinal bars fracture, significantly reducing the lateral load-carrying capacity.

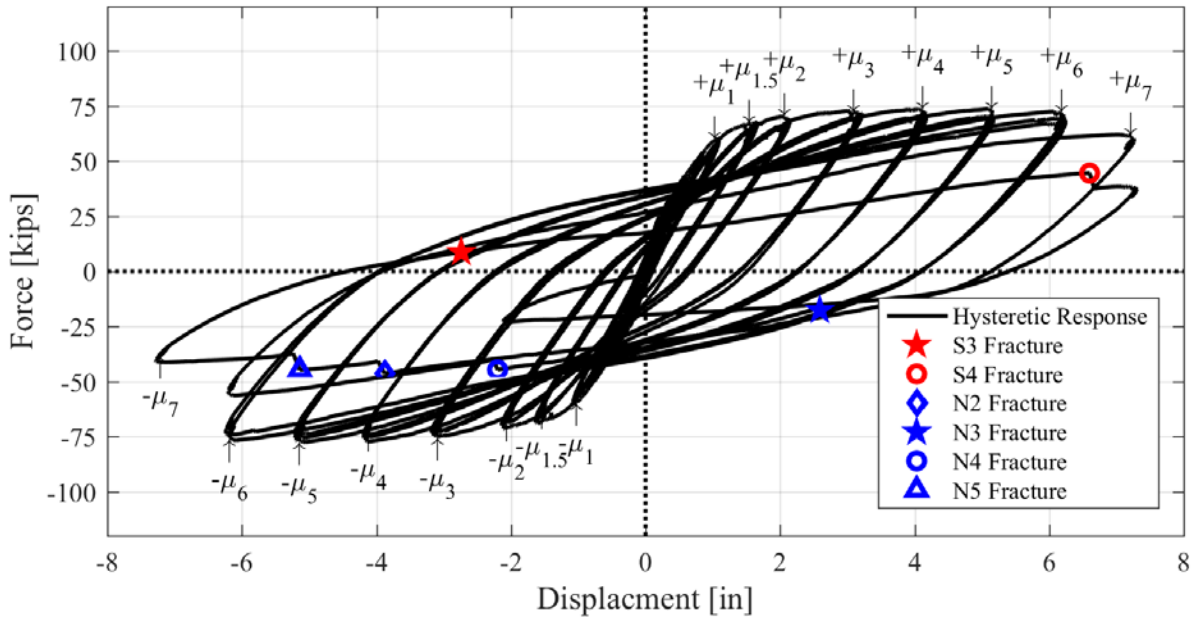

Figure 4-69. Column test 4 force-displacement response with rebar fracture locations

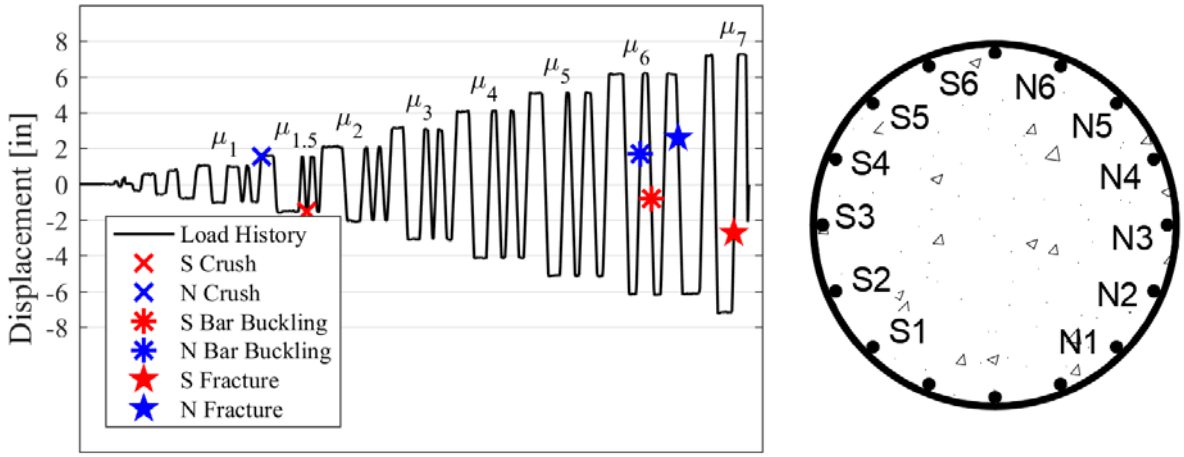

(a) **(b)**

Figure 4-70. (a) Column test 4 load history. (b) Column test 4 bar labels

4.4.1. Damage Progression

Damage in the column proceeded in the following manner. Hairline cracks began to form on both North and South sides of the column at the cycle in which half of the analytical yield force was applied to the column (½ F_y). At ¾ F_y, diagonal cracks began to form on the East and West faces of the column. In addition, cracks began to form on the footing of the column, parallel to the spirals and running towards the holes allow the post-tension bars to run through the footing to apply the axial load. At this level, the maximum crack widths measure 0.01". Cracks continued to develop over the height of the column throughout the test. Maximum crack widths grew to 0.016" at first equivalent yield. By $\mu_{1.5}$, crack widths had grown to 0.025", and the first signs of core concrete crushing were observed. At μ_2, a 0.04" crack was observed at the base of the North side of the column, in the footing-column interface. At ductility 3, a large portion of the footing cover concrete was observed to have cracked in a radial pattern on the surface. This indicates the beginning of "uplift" of the footing cover concrete. The same "uplift" happened on the South side of the column in the cycles of μ_4. This crushing of the footing cover concrete continued to become more evident in subsequent cycles. By ductility 4, crack formation was concentrated to the base of the column on the extreme faces, and diagonal cracks extended across the non-extreme faces. Upon the reversal from μ_6^{3+}, two loud pops and a strength drop indicated the fracture of longitudinal bars N3 and N4. Visible bar buckling was not observed on the North side of the column before these fractures occurred. These fractures did not occur within the blocked out region of the column, but within the footing. After fracture, crushed concrete was removed in order to view the fractured bars. A more detailed explanation of the reason why will follow in Section 4.4.2. Visible bar buckling was observed on the South side of the column at μ_7^{1-}, and the first fracture on the South side of the column did not come until the first reversal from μ_7^{1-}. Bar fractures occurred in the following order: N3-N4-N2-N5-S3-S4 (see Figure 65). Below are some of the pictures at different stages of damage throughout the test.

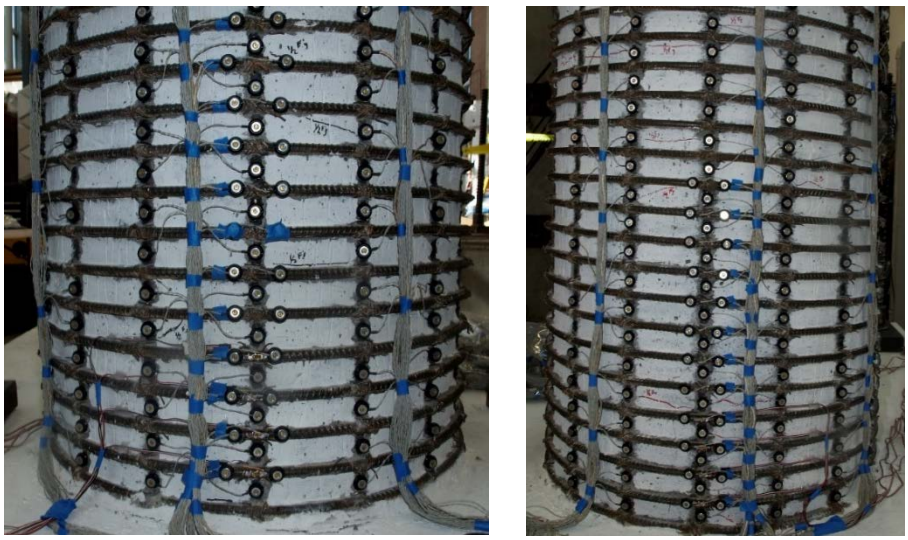

(a) **(b)**

Figure 4-71. First cracking: (a) South face, ½ F'y; (b) North face, -½ F'y

(a) **(b)**

Figure 4-72. Footing Cracking: (a) F'y on South; (b) ¾ F'y on North

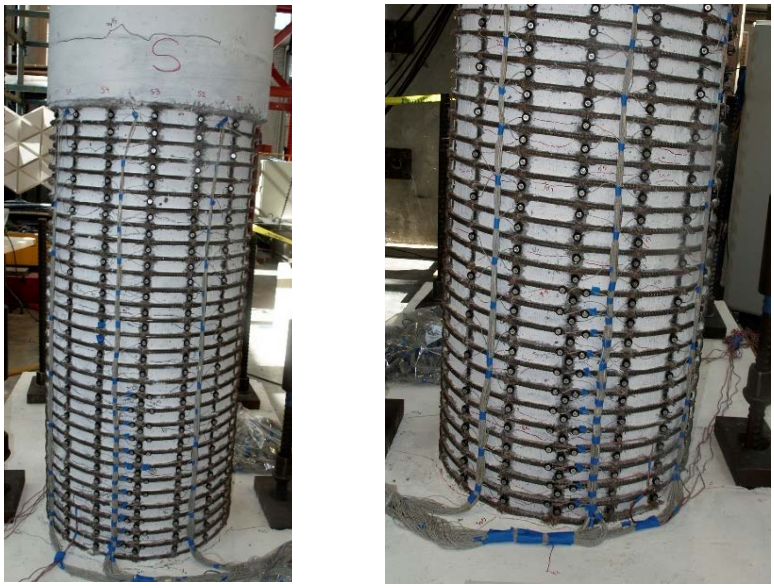

(a) **(b)**

Figure 4-73. First Yield (F'y): (a) South face; (b) North face

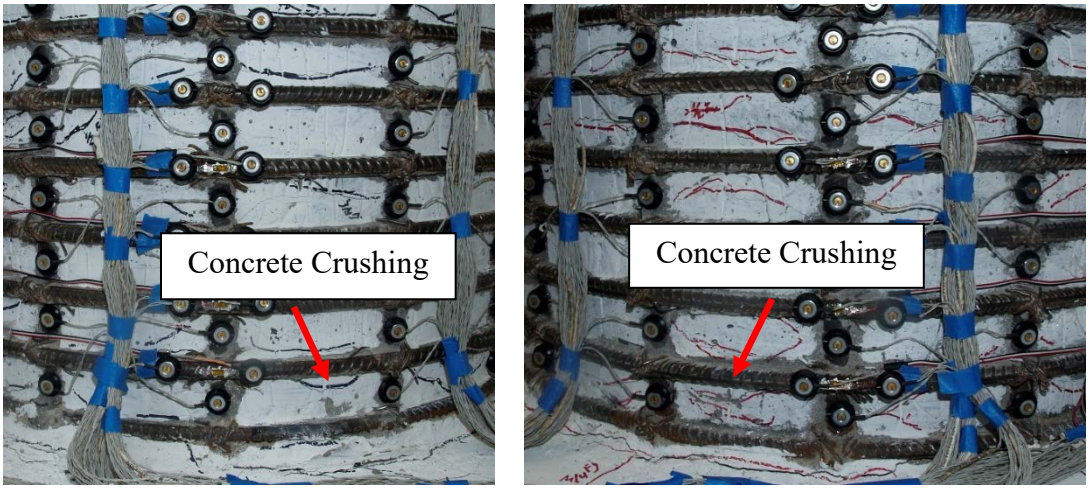

(a) **(b)**

Figure 4-74. Concrete Crushing: (a) South, $\mu_{1.5}^{3+}$; (b) North, $\mu_{1.5}^{1-}$

(a) **(b)**

Figure 4-75. Onset of footing concrete "uplift": (a) South, μ_4^{1+}; (b) North, μ_3^{1-}

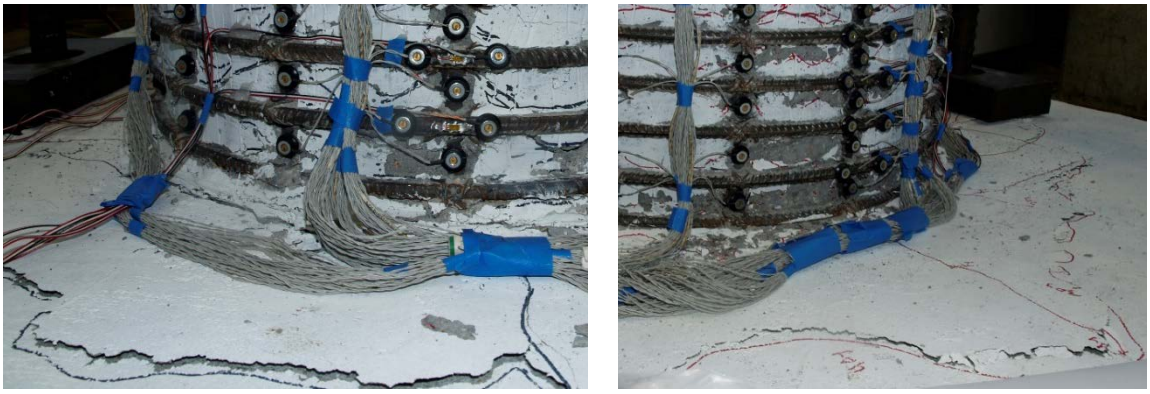

(a) **(b)**

Figure 4-76. Significant footing cover "uplift": (a) South, μ_4^{2+}; (b) North, μ_4^{1-}

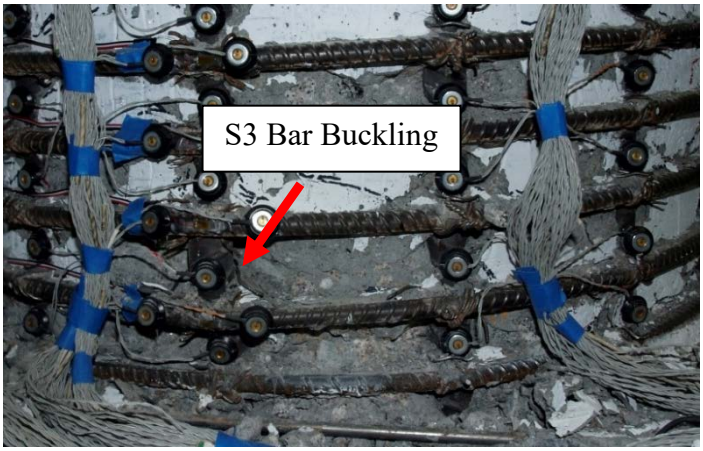

Figure 4-77. S3 buckled at μ_7^{1-}

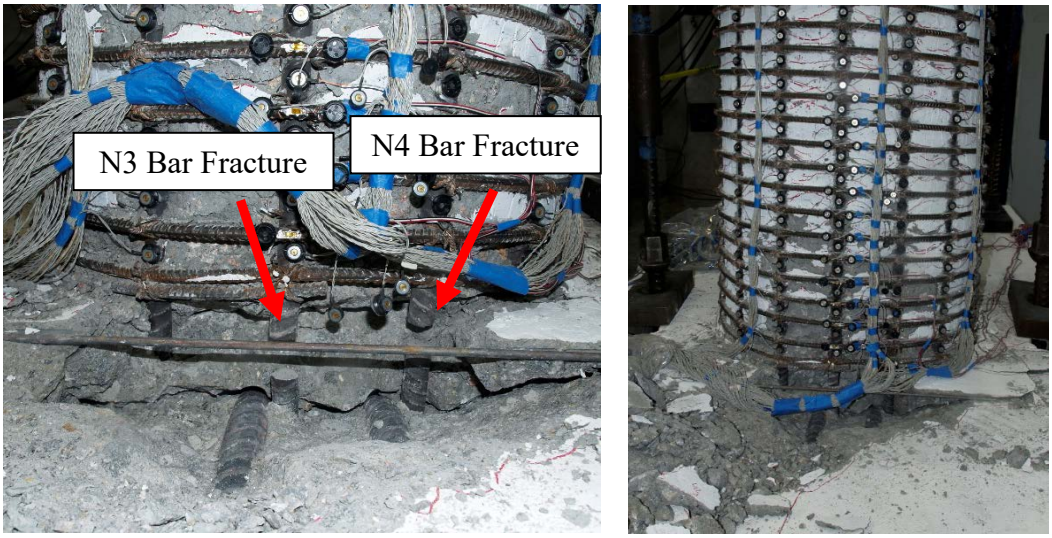

(a) **(b)**

Figure 4-78. (a) North bar fractures (N3 & N4), μ_6^{3-}; (b) Overall picture of North side

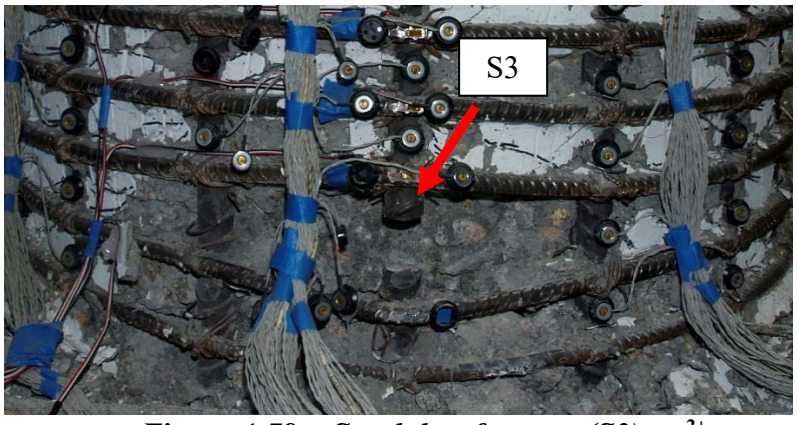

Figure 4-79. South bar fracture (S3), μ_7^{2+}

4.4.2. Explanation of Early Bar Fracture on North Side

As mentioned in the test summary, the first drop in strength of the column occurred when the longitudinal bars on the North side fractured. This is the desired failure mode of the reinforced concrete column with modern detailing requirements, and has been the failure mode for the four tests in this data sequence. In the previous three columns, bar buckling and subsequent fracture have occurred in the lower region of the column where the cover concrete has been blocked out. With Test 4, however, longitudinal bar buckling and fracture first occurred below the surface of the footing-column interface. This is seen in Figure 4-80. All loose concrete had been removed.

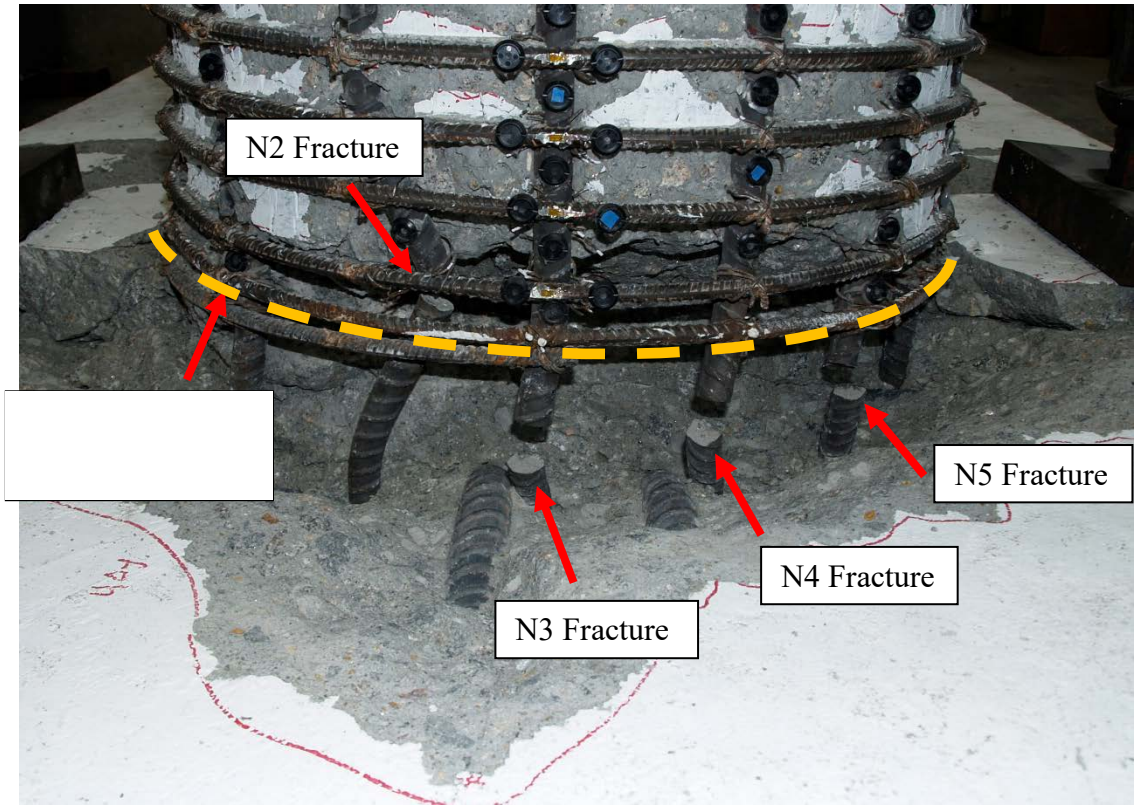

Figure 4-80. Rebar fracture locations on North side of Test 4 and original footing-column interface

As seen in the figure above, only half of one spiral of the transverse reinforcement extended into the footing. Transverse reinforcement provides confinement to core concrete, but also restricts longitudinal bar buckling. As longitudinal bar buckling is prevented, the cyclic displacement capacity of the column is increased. Concrete at the footing column interface began to crush at

ductility 4. As this concrete crushed, the longitudinal bars that extended into the footing did not have similar confinement against bar buckling as the rest of the column. In addition, the lower spirals appear to have shifted up, which typically occurs as the buckling reinforcing bar pushes them.

This column was designed with a volumetric transverse steel ratio of 1.3% (spiral pitch of 1.5"). However, the portion of the longitudinal bar that buckled and eventually fractured occurred in the footing where the spacing of transverse reinforcement was greater than 1.5". The distance from the lowest spiral (as measured after the test) to the top of the footing longitudinal steel was 2". This was due to an error in construction. Because the column longitudinal steel fractured in a region that did not conform to the specified column design, the authors suggest that the capacity of the column (peak displacement and maximum reinforcement strains) in the pull direction be ignored. The South side of the column experienced bar buckling and fracture above the footing, so the authors suggest that the push cycles be used to quantify strain and displacement capacities.

Additionally, when reinforcing bars on the North side fractured, large portions of damaged concrete were removed to observe the fracture locations at the base of the column on the North side. On the first push to ductility 7 (μ_7^{1+}), the lateral force capacity dropped from 67.0 kips to 61.8 kips. The maximum lateral force in the push direction was 72.5 kips, so this indicated a 15% strength reduction. Such a significant drop in force had not been observed in other tests without longitudinal bar fracture. It was not until the push to μ_7^{2+}, however, that reinforcing bars S3 and S4 fractured, marking a more significant reduction of force capacity. Therefore, the authors believe that this drop in strength is attributed to removing concrete from the North side of the column in order to view fractured reinforcement and thus decreasing the size of the compression block. While this concrete was severely damaged, portions could have still provided compressive strength. A smaller compressive block signifies a lower capacity of the cross-section, thus explaining this decrease in strength.

4.4.3. Strain Analysis

By examining the 3D position of each LED marker throughout the duration of the test, strain levels in each of the instrumented longitudinal bars and transverse spirals were available until failure. See Figure 3-11 for a picture of the instrumentation setup.

On the extreme tensile reinforcement on the North side of the column, the optical measuring system shows evidence of bar buckling occurring on the second push cycle of ductility 6 (μ_6^{2+}). The highest level of strain recorded by the Optotrak system in the longitudinal bars on the North extreme face of the column was 0.046 on the second pull cycle of ductility 6 (μ_6^{2-}) at 5.4" above the footing. This is probably not the maximum strain experienced by the bar, however, as buckling also occurred in a region of the column that did not have instrumentation (see Section 4.4.2). The bar fractured two cycles later during the pull to μ_6^{3-}. Figure 4-81(a) shows the plot of the longitudinal bar strain vs. peak column displacement in the location where buckling could be observed, and Figure 4-81(b) shows where maximum strain was recorded.

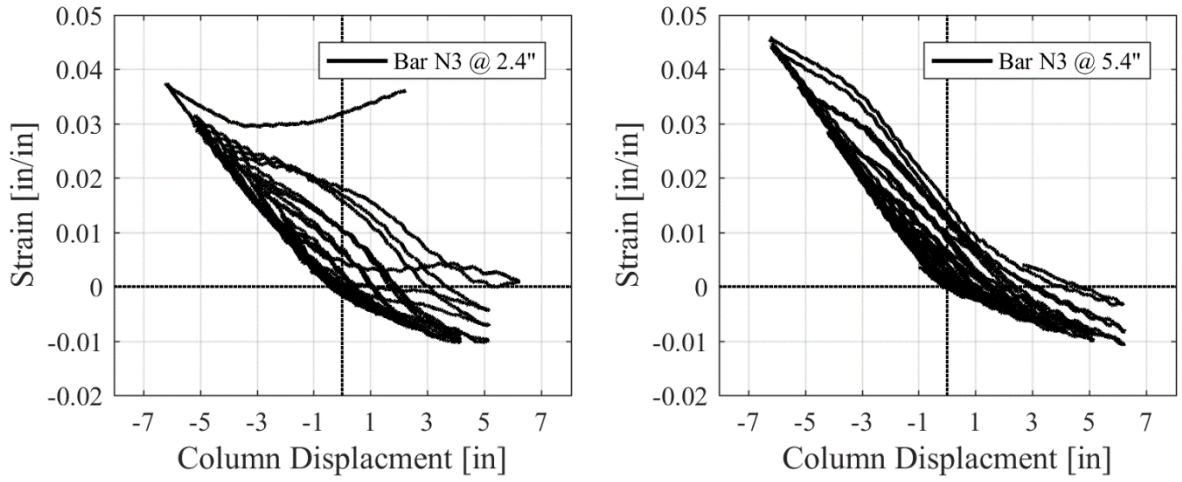

Figure 4-81. Strain vs. displacement of bar N3: (a) 2.4" above footing; (b) 5.4" above footing

As mentioned previously, bar N4 fractured during the same cycle as bar N3. This was more than likely due to the severity of the buckling of N4 in the footing due to the lack of transverse reinforcement. The maximum tensile strain in bar N4 was 0.0449 (seen in Figure 4-82(b)), which may not have been the true maximum tensile strain. Strain vs. displacement plot at 4.1" above the

footing show the bar to have buckled during the third push cycle of ductility 6, seen in Figure 4-82(a). On the subsequent cycle, the bar fractured.

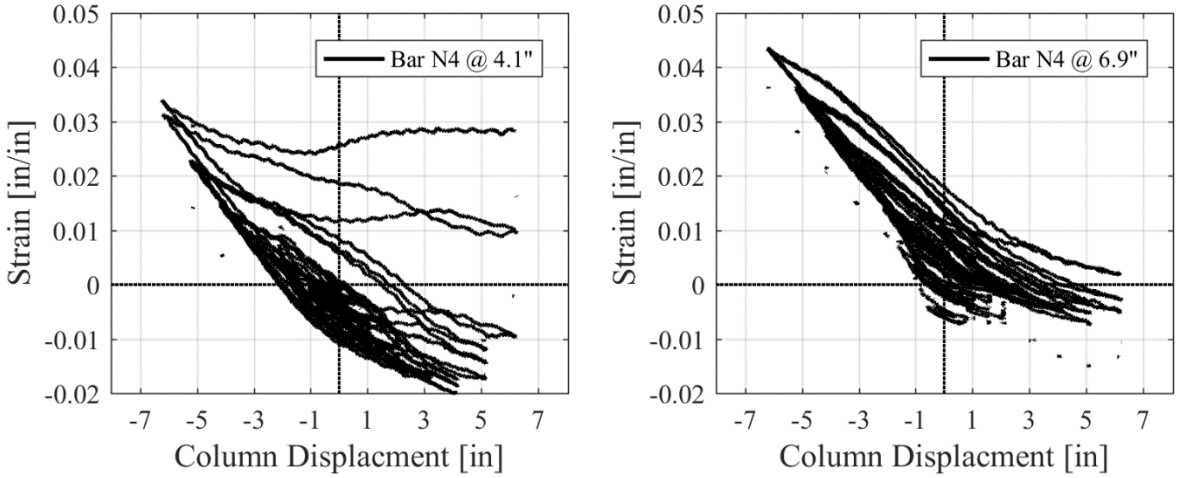

(a) **(b)**

Figure 4-82. Bar N4 strain vs. displacement at: (a) 4.1" above footing; (b) 6.9" above footing

Bar N2 buckled during the third push cycle of ductility 6 (μ_6^{3+}), the same cycle that N4 buckled, as seen in Figure 4-83, and fractured during the first pull cycle of ductility 7 (μ_7^{1-}).

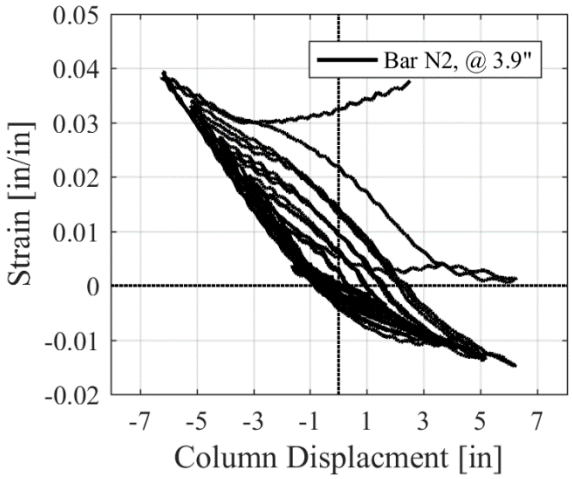

Figure 4-83. Strain vs. displacement of bar N2

Maximum strains in the extreme fiber bar on the South side of the column reached 0.0463 before bar buckling was observed. Visible bar buckling was not observed during the test until μ_7^{1-}, but through examination of the plot of strain vs. displacement, there is evidence of bar buckling

during the pull cycle to μ_6^{2-}, as seen in Figure 4-84 at 4.1" above the footing. Bar S3 eventually fractures during the second push cycle of ductility 7 (μ_7^{2+}).

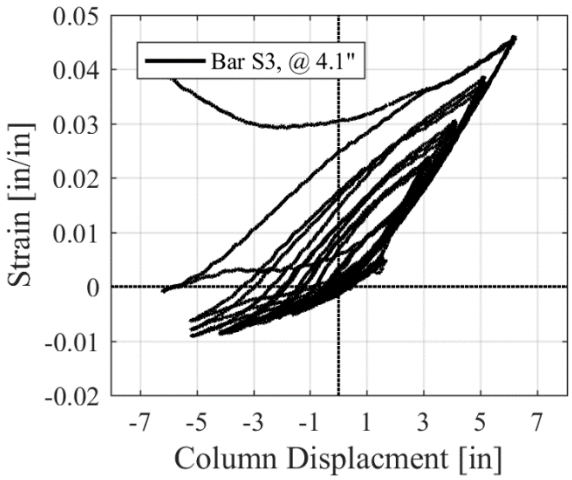

Figure 4-84. Bar S3 strain vs. displacement

Bar S4 fractured during the push cycle to μ_7^{2+}, and the maximum strain recorded in this bar was 0.0619 during the first push cycle to μ_7^{1+}. The fracture occurred right below the footing-column interface, such that bar buckling was not observed before fracture. Plots of the strain vs. displacement did not show evidence of bar buckling, but upon further investigation, it was found that this was because the bar buckled under the instrumented region of the column. The column had sufficient transverse reinforcement extend into the footing; the bar buckled under a portion of the spiral with 1.5" spacing. For future columns, transverse reinforcement spacing should be even tighter in the footing to ensure that buckling occurs within the instrumented region of the column. Figure 4-85(a) shows the strain vs. displacement for bar S4 at 4.3" above the footing. Figure 4-85(b) shows an image of the fractured bar after the crushed concrete was removed with an estimation of the location of the original footing-column interface. As the figure shows, bar S4 fractured below the instrumented region, but the spiral spacing stayed constant into the footing.

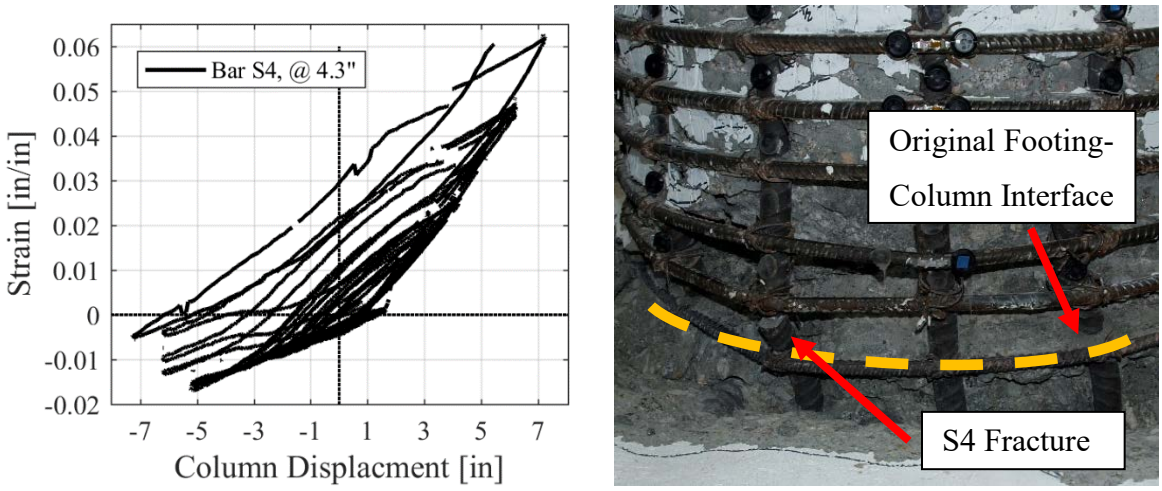

Figure 4-85. (a) Strain vs. displacement of bar S4; (b) Bar S4 after fracture

Bar S2 reached a peak tensile strain of 0.058 at the first push cycle to ductility 7, and evidence of slight buckling was seen during the reversal to μ_7^{1-}. This bar did not fracture, however, on the subsequent push cycle (μ_7^{2+}), but from pictures after the test, it has sustained very severe buckling. Figure 4-86 shows the plot of strain vs. displacement.

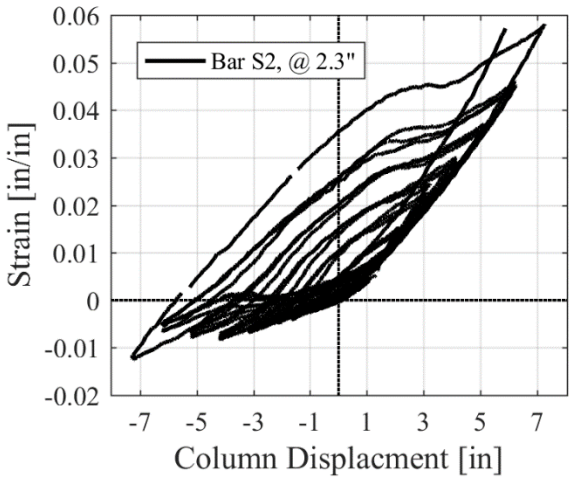

Figure 4-86. Bar S2 strain vs. displacement at 2.3" above footing

Figure 4-87 shows the strains in the second lowest spiral that confines the plastic hinge region. These spirals were instrumented with a strain gage and Optotrak LED markers. The strain gages on both sides de-bond around tensile strains of 0.017. As the spiral yields, it provides less confinement to the longitudinal steel, which causes the longitudinal bars to buckle. The spirals on

both sides yield when loaded in compression during μ_4. When the spirals experience significant plastic deformation, this corresponds to when the extreme fiber longitudinal bars begin to buckle.

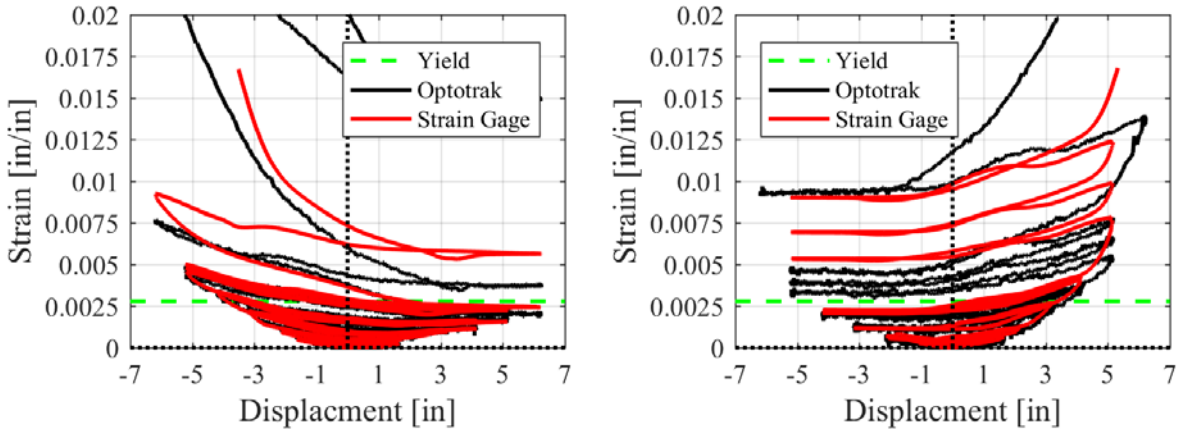

Figure 4-87. Strain vs. displacement: (a) 2nd South spiral; (b) 2nd North spiral

Figure 4-88 shows the plot of the strain profiles over the height of the column, as described in Section 4.1.2. The spread of plasticity is approximately 35 inches on the South side and 34 inches on the North side.

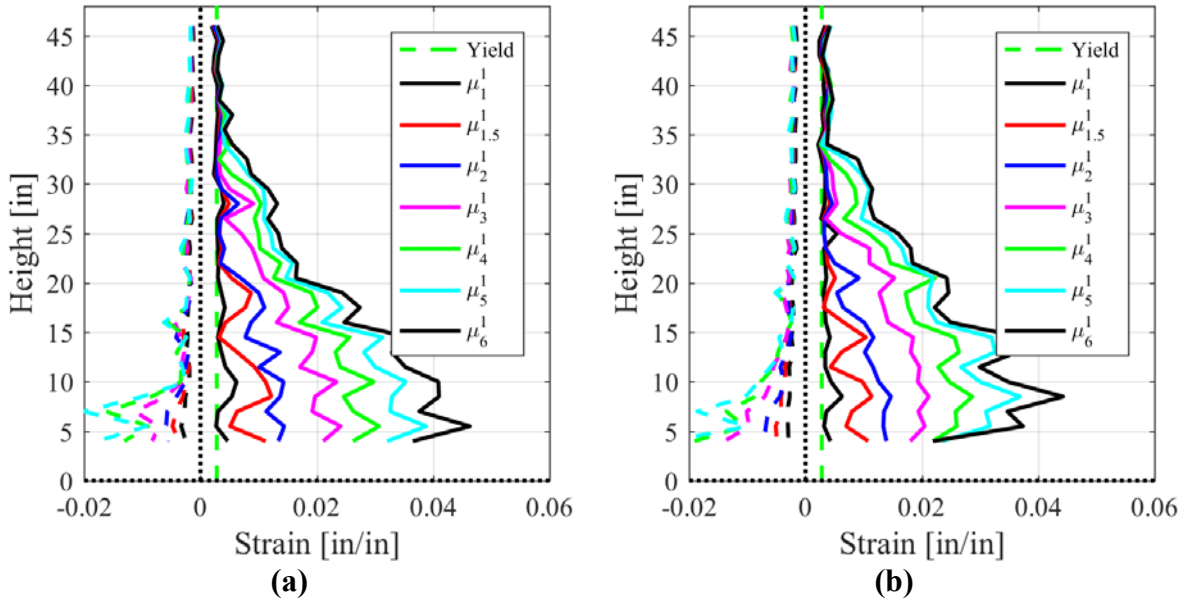

Figure 4-88. (a) Bar S3 strain profile; (b) Bar N3 strain profile

In addition to strain profiles for the longitudinal bars, Figure 4-89 shows the strain profiles for the spirals over the height of the column. As the spirals yield, they provide less confinement to

the longitudinal bars causing bar buckling to occur earlier. Transverse steel on the either side of the column begins to yield during μ_4.

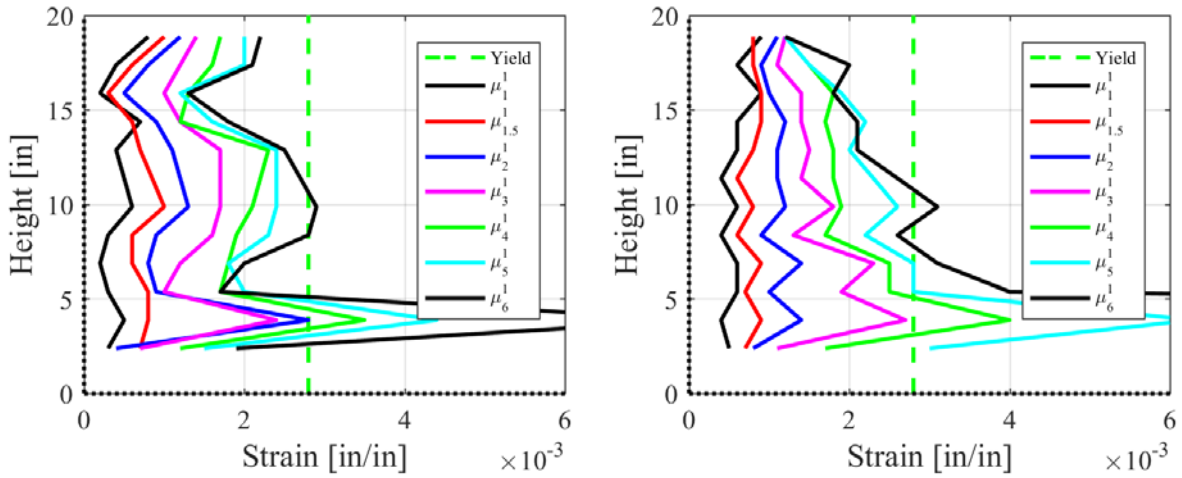

Figure 4-89. (a) South spiral strain profile; (b) North spiral strain profile

4.4.4. Components of Displacement

The component of displacement from longitudinal bond slip of the reinforcement is calculated using the process described in Section 4.1.3 and included in Figure 4-90.

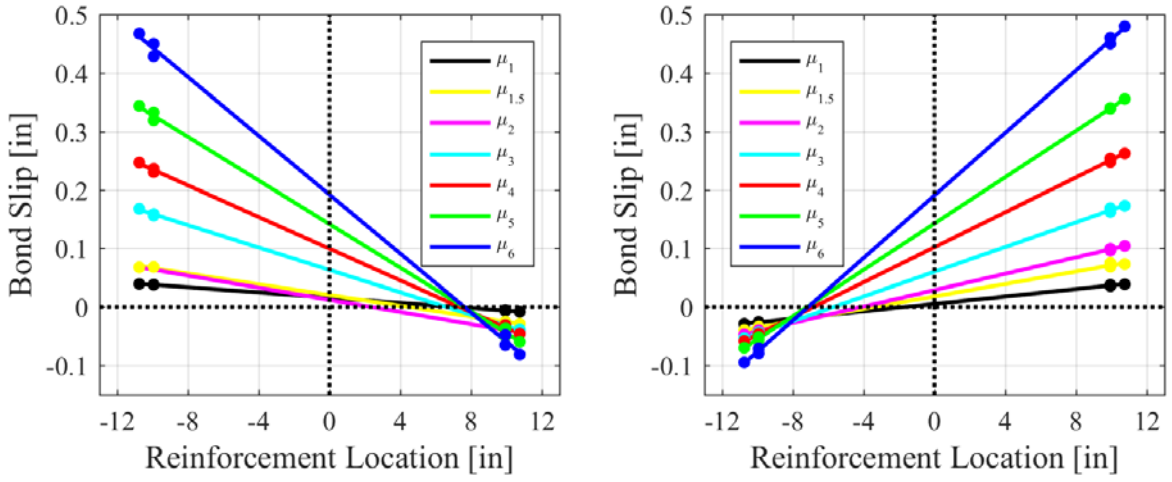

Figure 4-90. Bond slip of: (a) S3 under push cycles; (b) N3 under pull cycles

As mentioned in Section 4.1.3, flexural deformation in the plastic hinge region is calculated by integrating the curvature of the column over its height. The optical measurement system

provides strain profiles in each longitudinal bar that can be used to estimate the curvature over the height of the column. This estimate of the curvature profile can then be integrated to calculate the component of displacement from flexural deformation of the plastic hinge. Figure 4-91(a) shows the curvature profile from this method at the first cycle of each level of ductility.

Figure 4-91(b) shows the combination of the components of displacement from base rotation due to strain penetration and the flexural deformation from integration of the curvature profile for the first cycle of each level of ductility. These two components of displacement combine to equal the column displacement at each ductility cycle. The small difference in displacement is attributed to errors in the calculation of each displacement component.

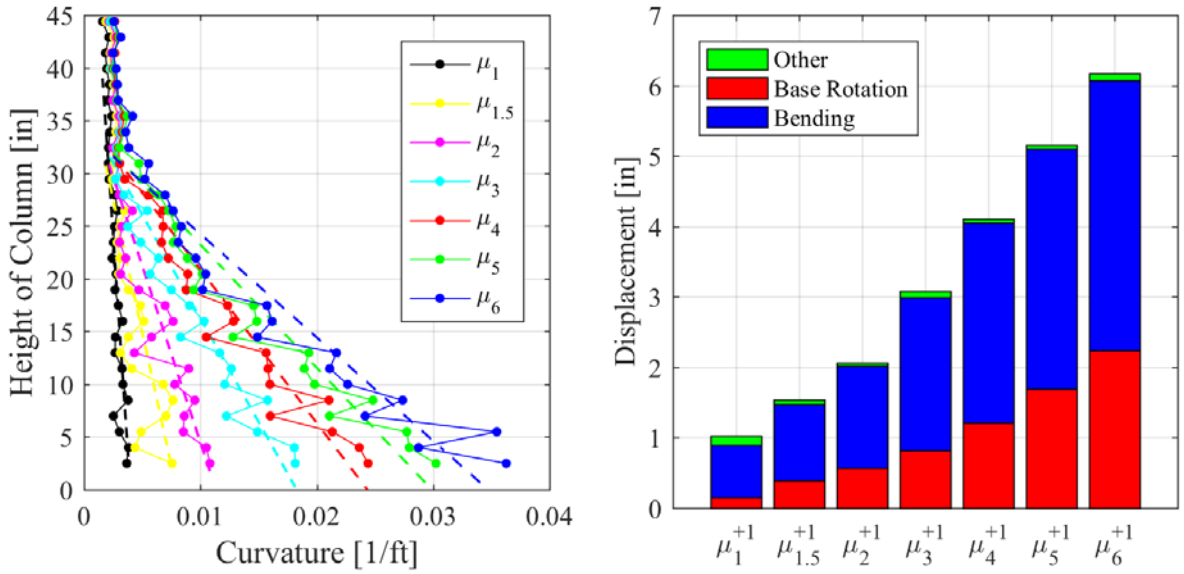

Figure 4-91. (a) Curvature profile from strain interpolation; (b) Components of column displacement

4.4.5. Hysteretic Energy Dissipation

As described in Section 4.1.4, the corrected Jacobsen hysteretic damping was calculated for the first cycle of each ductility. Figure 4-92 shows the Jacobsen hysteretic damping as well as the corrected hysteretic damping.

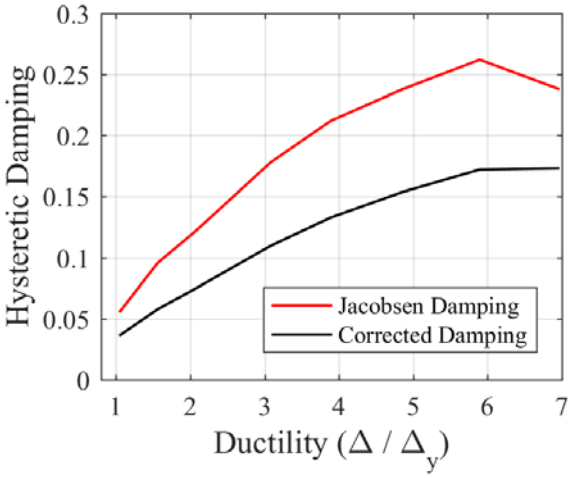

Figure 4-92. Hysteretic damping

4.4.6. Comparison to Grade 60 Columns

As mentioned in Section 4.1.5, Goodnight et al. (2015) performed thirty A706-60 column tests under quasi-static, three cycle-set loading histories. Test 16 (as numbered in the Goodnight et al., 2015 report) had the same geometry, longitudinal steel content, transverse steel content, and axial load ratio. Test 13 (Goodnight et al., 2015) had similar details except that the transverse steel was #4 spirals spaced at 2.75”. While this produced a similar volumetric steel ratio, the detailing was slightly different in order to identify the differences in detailing.

Figure 4-93 shows the force-displacement response of each. The A706-60 columns have similar displacement capacities to the A706-80 reinforced column. The load history for the Grade 80 column used displacement ductility increments of 1, 1.5, 2, 3, 4, 5, 6, 7, while the Grade 60 columns used displacement ductility increments of 1, 1.5, 2, 3, 4, 6, 8, 10.

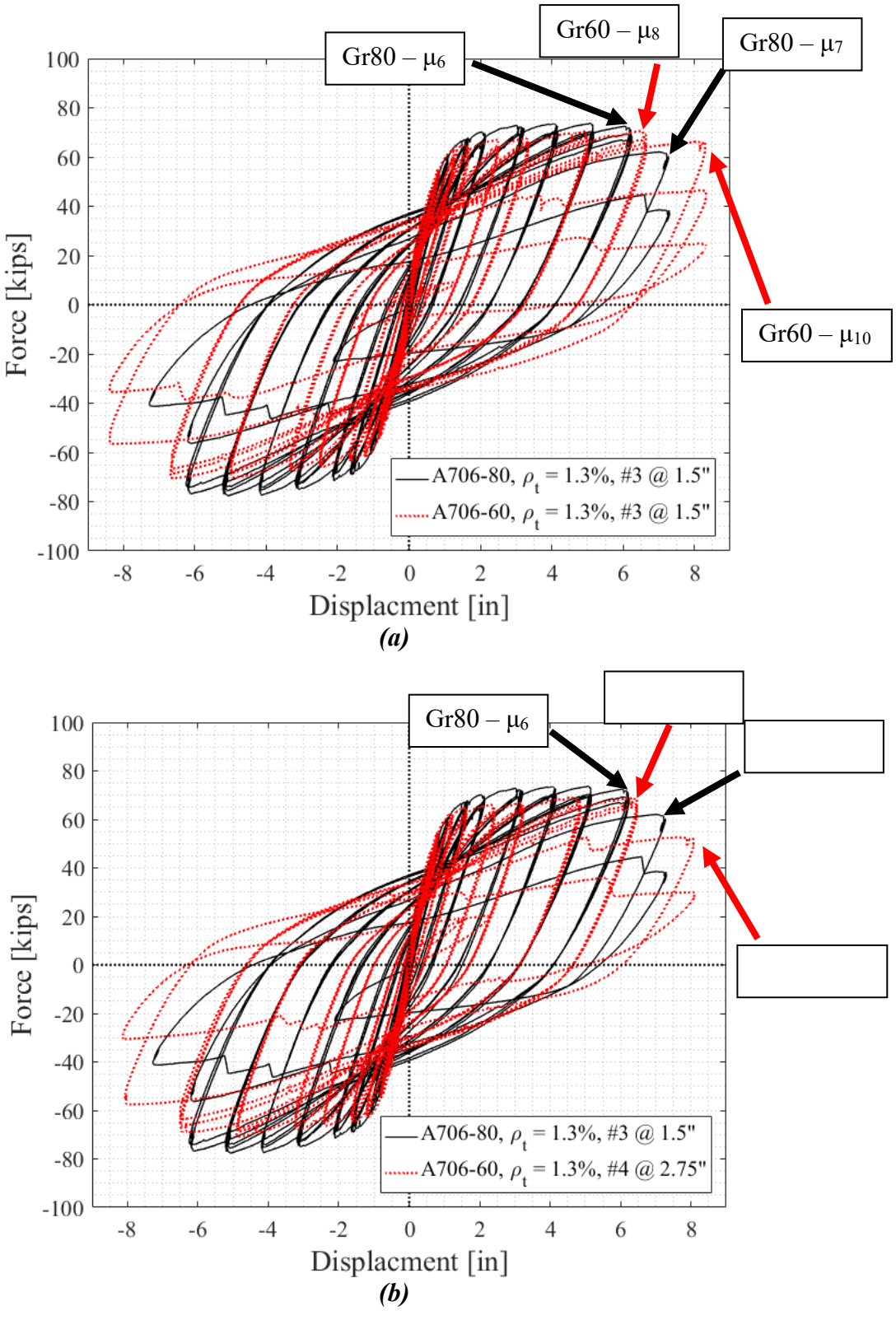

Figure 4-93. Grade 80 column test 4 vs comparison Grade 60 column tests

Table 4-18 shows the displacement and ductility for two damage limit states, as described in Section 4.1.5. As mentioned in Section 4.4.2, the bar fracture on the North side does not represent a true representation of the detailing and will not be counted for the true displacement capacity of the column.

Table 4-18. Summary of damage limit states for column test 4

Column Test	Column Side	Longitudinal Bar Buckling			Bar Fracture	
		μ_D	Displacement	Strain (+)	μ_D	Displacement
A706-80 ρ_l = 1.6% ρ_t = 1.3%	South North	6 -6	6.18” -6.18”	0.046 0.046	7 -6 *	7.22” -6.19” *
A706-60 (Test 16) ρ_t = 1.3%	South North	8 -8	6.65 -6.68	0.056 0.052	10 -10	8.34” -8.32”
A706-60 (Test 13) ρ_t = 1.3%	South North	8 -8	6.46” -6.50”	0.047 0.047	10 -10	8.12” -8.06”

As described in Section 4.1.3, the longitudinal rebar bond slip of the Grade 60 columns was measured and compared to the Grade 80 test column. The bond slip for the pull and push cycles of each column test were plotted versus the corresponding column displacement in Figure 4-94. The Grade 80 columns have slightly more bond slip than the Grade 60 rebar at high levels of displacement, but the bond slip behavior versus column displacement was very similar for the majority of the test.

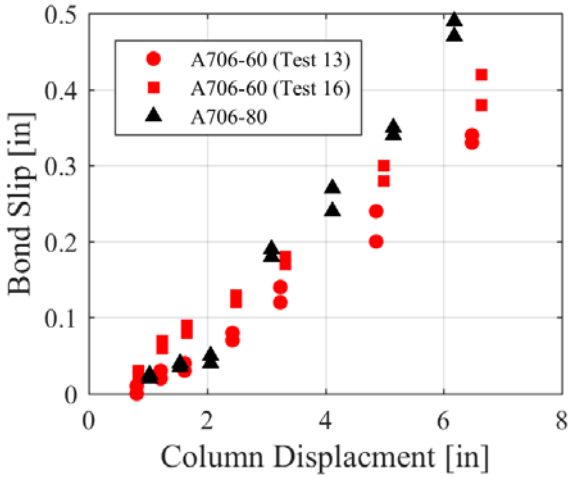

Figure 4-94. Compare bond slip for Grade 80 test 4 with Grade 60 column

Figure 4-95 shows a comparison of the corrected hysteretic damping (as described in Section 4.1.4). The Grade 80 column and comparison Grade 60 columns had very similar damping versus ductility curves. As mentioned previously, ductility does not necessarily correlate to column displacement because of the difference in yield displacement.

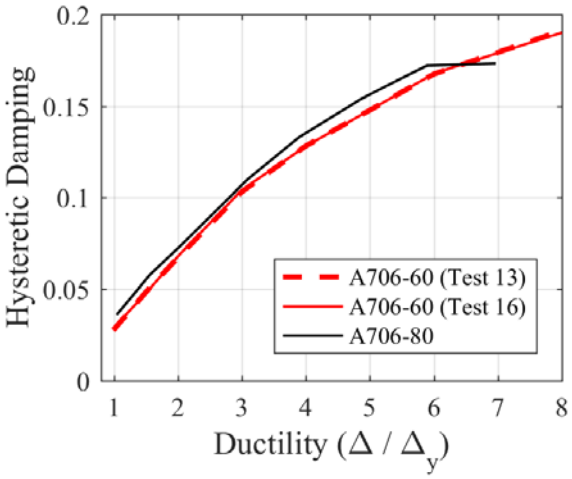

Figure 4-95. Hysteretic damping comparison for Grade 80 and 60 columns

4.4.7. Analytical Model

In order to examine how the experimental force-displacement results compared to current modeling practice, the experimental force-displacement response was compared to the cyclic response of an OpenSees fiber model and a pushover analysis performed in Cumbia. Section 4.1.6 describes the development of each model. Figure 4-68 shows the comparison of the force-

displacement response for each method. Similar to the other Grade 80 tests, the hysteretic response matches the modeling approach of each method.

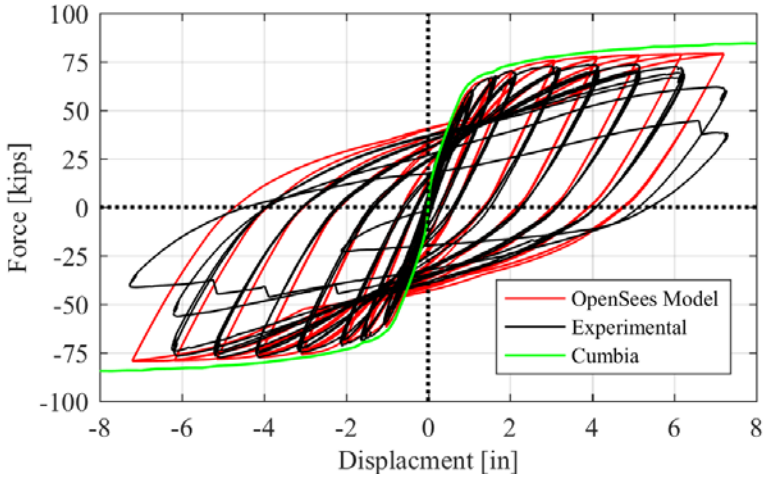

Figure 4-96. Actual and analytical force-displacement responses

CHAPTER 5. DESIGN VARIABLE COMPARISON

In order to use A706 Grade 80 rebar in plastic hinge forming concrete members, structural engineers must know certain design variables. Variables of particular interest are: (1) plastic hinge lengths, (2) rebar strain limit states, (3) equivalent viscous damping, and (4) bond slip (also referred to as strain penetration). The following chapter compares each of these to current design practice, but a larger dataset of Grade 80 columns should be tested in order to characterize the seismic behavior of the rebar more comprehensively.

5.1. Plastic Hinge Length

In modern seismic design, certain members of a structure are designed as ductile elements, which will form plastic hinges in the case of a seismic event. These plastic hinges will dissipate energy and prevent damage from spreading to other parts of the structure. Members designed to form plastic hinges must have a large displacement capacity and be designed to experience large levels of elastic loading. Engineers characterize different levels of damage as key limit states and use curvatures or strains to quantify these limit states. In order to convert curvatures to target displacements, engineers integrate simplified curvature distributions in a method known as the plastic hinge method.

The plastic hinge method presented in this section follows the model outlined in Priestly et al. (2007). This method simplifies the elastic and plastic curvature distributions into simple shapes for ease of use. A triangular curvature distribution characterizes the elastic curvature, while plastic flexural displacements are obtained by integrating a constant curvature distribution at the base of the column. The height of this plastic curvature distribution is the plastic hinge length. Goodnight et al. (2015) saw that this uniform distribution of curvature did not correctly characterize the distribution of curvature from physical tests. They proposed a new plastic hinge method, which utilized a triangular curvature distribution. Figure 5-1 shows an illustration of the Priestley et al. (2007), or PCK, plastic hinge method.

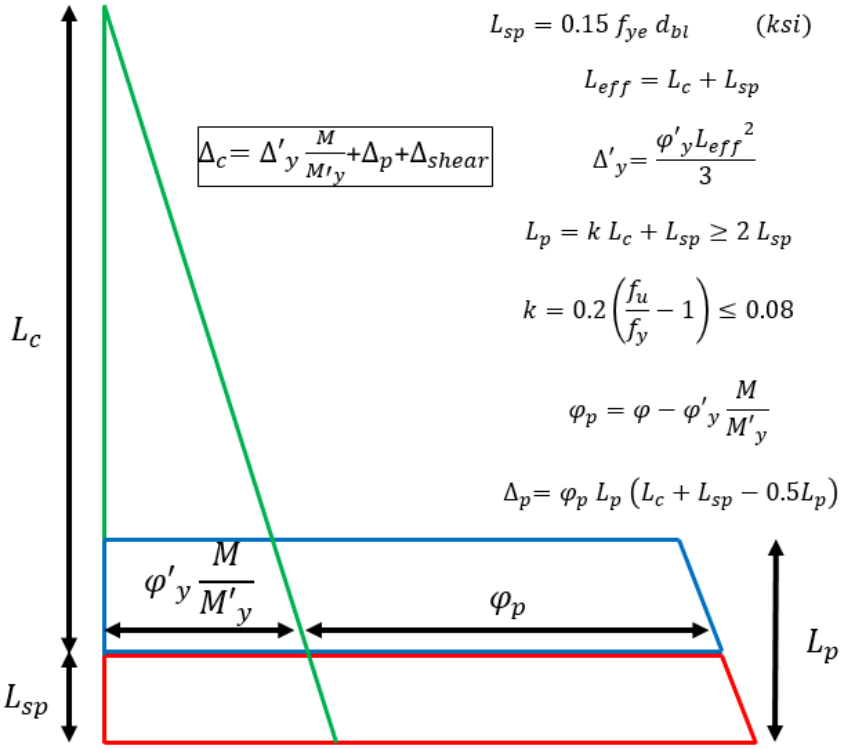

Figure 5-1. PCK plastic hinge method (Priestley, Calvi, and Kowalsky, 2007)

The Caltrans Seismic Design Criteria (Caltrans, 2013) uses the PCK plastic hinge model, as shown in Equation 5-1.

$$L_p = 0.08L + 0.15 f_{ye} d_{bl} \geq 0.3 f_{ye} d_{bl} \qquad \text{Equation 5-1}$$

The plastic hinge method is a simplified approach to relate plastic curvatures to plastic displacements. Thus, in order to test the accuracy of the current plastic hinge method for A706-80 rebar, the maximum curvature and peak column displacement at each level of ductility was used to calculate the equivalent plastic hinge length from each of the Grade 80 column tests. This length was compared to the current models for plastic hinge length.

In order to calculate the equivalent plastic hinge length from the column tests, the experimental equivalent yield displacement was used to calculate the equivalent yield curvature, as seen in Equation 5-2. The effective length was the clear column length plus the length of strain penetration, as seen in Equation 5-3. Following this, the plastic displacement and plastic curvatures were calculated by subtracting the experimental equivalent yield displacement and yield curvature,

respectively. The experimental plastic hinge length was calculated at each cycle of ductility by dividing the plastic displacement by the plastic curvature time's column length, as seen in Equation 5-4.

$$\phi_y = \frac{3\Delta_y}{L_{eff}^{\ 2}} \qquad \text{Equation 5-2}$$

$$L_{eff} = L + 0.15 f_{ye} d_{bl} \qquad \text{Equation 5-3}$$

$$L_p = \frac{\Delta_p}{\phi_p L} = \frac{\Delta - \Delta_y}{\left(\phi - \phi_y\right) L} \qquad \text{Equation 5-4}$$

Figure 5-2 shows the experimental plastic hinge length compared to the PCK plastic hinge length. This figure shows good agreement between the back calculation of the plastic hinge length from the column test and the analytical model for plastic hinge length, which is currently used in design. This suggests that the current plastic hinge method could be used for A706-80 rebar without changes to design procedure.

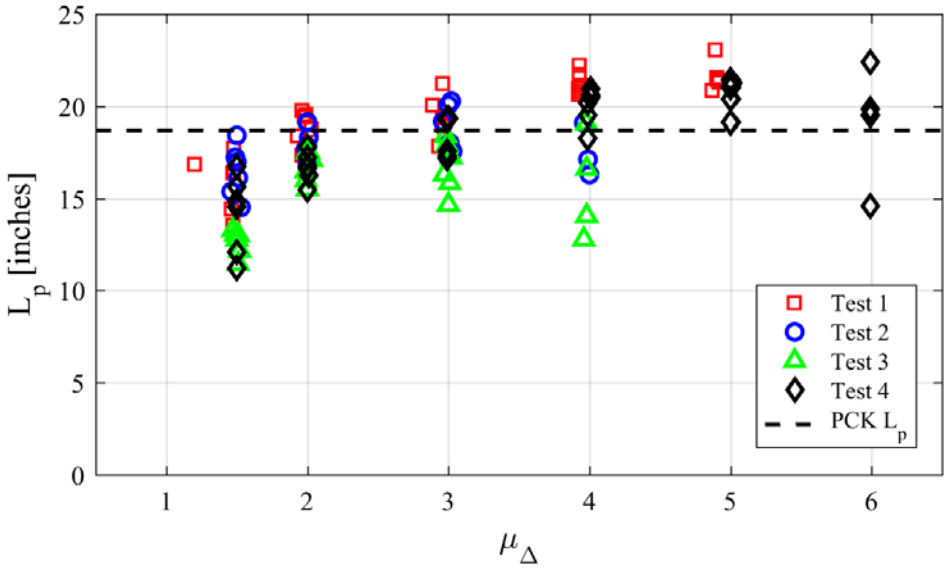

Figure 5-2. Experimental vs. PCK plastic hinge length

5.2. Strain Limit States

As mentioned previously, structural engineers use measurements of either curvature or strain to characterize damage limit states. In performance-based design, structural engineers can check the likelihood of exceeding different limit states for various levels of hazard. This enables engineers to quantify more accurately the performance of a structure over its lifetime. Typical limit states include serviceability, damage control, and collapse. Kowalsky (2000) summarized typical values of current performance limit states, shown in Table 5-1.

Table 5-1. Performance strain limits (Kowalsky, 2000)

Limit State	Concrete Compressive Strain Limit	Steel Tensile Strain Limit
Serviceability	0.004 (cover concrete crushing)	0.015 (residual cracks exceed 1mm)
Damage Control	0.018 (limit of concrete repair)	0.060 (tensile-based bar buckling)

5.2.1. Serviceability

Priestley et al. (1996) quantifies the serviceability limit state as the onset of cover concrete crushing or residual crack widths exceeding one millimeter. Exceeding the serviceability limit state does not pose a safety concern, but it does mark the point when repair is needed. These repairs include repairs to cover concrete and other non-invasive procedures to prevent reinforcing steel from corroding.

The cover concrete of the Grade 80 columns was blocked out for the optical measurement system, so cover concrete crack widths and crushing could not be observed. However, during the experiments, the onset of core concrete was observed and assumed as an approximation of the damage control limit state. This happened at ductility 1.5 or 2 for each column. The table below lists the maximum compressive strains in the rebar prior to concrete crushing. These strains have been recorded by the optical measurement system on the longitudinal steel, and due to strain compatibility, they reflect the compressive strain demands on the core concrete.

Table 5-2. Concrete compressive strains at core concrete crushing

Test Number	Column Side	Concrete Compressive Strain
1	North	N/A
	South	0.0058
2	North	0.0071
	South	0.0050
3	North	0.0049
	South	0.0057
4	North	0.0051
	South	0.0048

Table 5-2 shows that the strain limit state proposed by Kowalsky (2000) of 0.004 is slightly conservative according to the Grade 80 column tests, but is a good approximation of the serviceability limit state.

5.2.2. Damage Control 1

Engineers typically quantify the damage control limit state as the onset of longitudinal bar buckling or core concrete crushing. This limit state marks the point at which conventional repair techniques cannot be applied to the column and the structure will likely need to be replaced. Goodnight et al. (2015), however, proposed an intermediate damage control limit state for yielding of the transverse steel. As the core concrete is placed in compression under lateral loads, the dilation of the core places high tensile demands on the transverse reinforcement. As transverse steel yields, it experiences a reduction in stiffness. A reduction in transverse steel stiffness corresponds to an inability to confine the dilation of the core concrete. In addition, this changes the boundary conditions for longitudinal reinforcing steel, which becomes more susceptible to bar buckling. This limit state signifies a change in repair strategy from repair of cover concrete to the need for additional transverse reinforcement, in the form of steel jacketing or FRP wraps. They proposed Equation 5-5 as the intermediate damage control strain in compression. This equation was calibrated entirely off the Grade 60 column tests performed by Goodnight et al. (2015) due to a lack of sufficient strain data for other columns in the literature.

$$\varepsilon_{c\,yield}^{spiral} = 0.009 - 0.3\frac{A_{st}}{A_g} + 3.9\frac{f_{yhe}}{E_s} \qquad \text{Equation 5-5}$$

The peak compressive strain in the longitudinal steel (and corresponding concrete) prior to transverse steel yielding was observed during the Grade 80 column tests. Table 5-3 shows the strain limit states for the intermediate damage control limit state.

Table 5-3. Concrete compressive strain at yielding of transverse steel

Test Number	Column Side	Peak Compressive Strain	Goodnight (2015) Prediction
1	North South	N/A 0.0129	0.015
2	North South	0.0138 0.0081	0.015
3	North South	0.0112 0.0113	0.015
4	North South	0.0191 0.0162	0.015

The results in Table 5-3 indicate that the limit state proposed by Goodnight et al. (2015) slightly over-predicts the intermediate damage control limit state. Further analysis of Equation 5-5 shows that the last parameter, the yield strain of the transverse steel, causes an increase in the prediction. Goodnight et al. (2015) calibrated this model using Grade 60 rebar, but these columns were constructed with Grade 80 rebar. If the expected yield strain of Grade 60 rebar is used in the equation, the result is 0.012, which more closely corresponds to the experimental results. If this intermediate damage control limit state is to be used for columns with high strength rebar, further adjustments may be needed.

5.2.3. Damage Control 2

Longitudinal bar buckling and significant core damage mark the typical damage control limit state (Priestley et al., 1996). Previous researchers have observed a reduction in column performance following bar buckling, which signifies the imminence of bar fracture and rapid

lateral strength loss. Moyer and Kowalsky (2003) have observed that the onset of bar buckling is based on the peak tensile strain in the bar on the previous cycle.

In this section, the peak tensile strain and column drift ratio prior to the onset of bar buckling will be compared to models proposed by Goodnight et al. (2015) as well as Berry and Eberhard (2005). These models represent current standards in predicting the bar buckling limit state. The Goodnight et al. (2015) model predicts the peak tensile strain prior to bar buckling, as seen in Equation 5-6. The Berry and Eberhard (2005) model uses similar column parameters to predict the column drift ratio at bar buckling, as seen in Equation 5-7. Table 5-4 shows the peak longitudinal tensile strain prior to bar buckling and the column drift ratio at bar buckling as well as values from the two prediction models.

$$\varepsilon_{s\,buckling}^{bar} = 0.03 + 700\rho_v \frac{f_{yhe}}{E_s} - \frac{P}{f'_{ce} A_g} \qquad \text{Equation 5-6}$$

$$\frac{\Delta}{L} = 3.25\left(1 + 150\frac{\rho_s d_{bl}}{D}\right)\left(1 - \frac{P}{f'_{ce} A_g}\right)\left(1 + \frac{L}{10D}\right) \qquad \text{Equation 5-7}$$

Table 5-4. Bar buckling strain and displacements

Test Number	Column Side	Peak Tensile Strain	Goodnight Strain Prediction	Column Drift Ratio	Berry Drift Prediction
1	North South	N/A 0.0490	0.044	6.6%	4.6%
2	North South	0.0306 0.0311	0.039	4.5%	4.4%
3	North South	N/A 0.0308	0.038	4.5%	4.4%
4	North South	N/A 0.0463	0.050	6.4%	4.4%

The results in Table 5-4 show similar behavior between the predictions from the Goodnight and Berry models and the Grade 80 column tests. These models were calibrated with test data from Grade 60 reinforced columns. Since the predictions are similar to the results from the Grade 80 columns, this implies that the Grade 80 columns will perform similarly to comparison Grade 60 columns. However, the authors suggest that more Grade 80 column tests be performed to validate

this result and more fully investigate the influence of other design variables on bar buckling behavior.

5.2.4. Bar Fracture

Although longitudinal bar fracture typically results in a rapid decline of lateral force carrying capacity, current models do not exist to predict this ultimate limit state. The bar buckling limit state has been interpreted as the point that should not be exceeded for new design, with the understanding that columns typically have higher displacement capacity than the displacement at bar buckling. This includes an inherent factor of safety in the design as the post-buckling displacement capacity can be seen as a "reserve" capacity. However, the Grade 80 reinforcement in the previously discussed column tests fractured soon after bar buckling, eliminating this inherent factor of safety. The cause of this early fracture will be examined and a solution will be proposed in later chapters.

5.3. Equivalent Viscous Damping

Equivalent viscous damping contributes to the amount of energy dissipation a structure will provide. Past researchers (Trejo et al., 2014 and Sokoli and Ghannoum, 2016) have suggested that the use of Grade 80 reinforcement decreases the equivalent viscous damping of the structure compared to Grade 60 columns. They suggest that this reduction in equivalent viscous damping will lead to a reduction in energy dissipation. Dissipation of seismic energy is a key role that plastic hinge members play in how a structure resists seismic forces. Structural engineers also need accurate knowledge of the equivalent viscous damping for the development of structural models, particularly frame-based structural models. Typically, a member is assigned a certain damping versus ductility relationship. These relationships vary based on the materials used and the type of hysteretic response. A standard damping vs. ductility relationship for the hysteretic response of a reinforced concrete bridge column (Thin Takeda) appears in Priestly et al. (2007) as seen in Equation 5-8.

$$\xi_{eq} = 0.05 + 0.444\frac{\mu - 1}{\mu\pi} \qquad \text{Equation 5-8}$$

Section 4.1.4 described how to obtain the corrected hysteretic damping for each of the four Grade 80 column tests. In order to obtain the total equivalent viscous damping, the component of elastic viscous damping must be added to the total hysteretic damping for each ductility. Priestley et al. (2007) proposes Equation 5-9 to combine elastic and hysteretic components of damping.

$$\xi_{eq} = \kappa\xi_{el} + \xi_{hyst} \qquad \text{Equation 5-9}$$

Priestley and Grant (2005) suggest that elastic viscous damping should be calculated through tangent stiffness proportional damping at a value of typically 0.05. Priestley et al. (2007) also apply a correction factor, κ, to the elastic damping depending on the type of hysteretic response, seen in the parameter λ in Equation 5-10. As mentioned above, the hysteretic response of a reinforced concrete bridge column is characterized by the Thin Takeda hysteretic rule for which the value of λ is -0.378.

$$\kappa = \mu^{\lambda} \qquad \text{Equation 5-10}$$

Thus, the total equivalent viscous damping of the Grade 80 columns can be calculated for each level of ductility using Equation 5-11.

$$\xi_{eq} = (0.05)\,\mu^{-0.378} + \left(\frac{2}{\pi}\frac{A_1}{A_2}\right)\left(\left[(0.53\mu + 0.8)\left(\frac{2}{\pi}\frac{A_1}{A_2}\right)\right]^{-\left(\frac{\mu}{40}+40\right)}\right) \qquad \text{Equation 5-11}$$

Using Equation 5-11, the equivalent viscous damping was calculated for each level of ductility of the Grade 80 column tests and compared to the results of a typical damping vs. ductility relationship (PCK), as seen in Equation 5-8, shown in Figure 5-3(a). The equivalent viscous damping was calculated using the same method for the comparison columns with Grade 60 rebar and compared to the PCK model in Figure 5-3(b). While the equivalent viscous damping does not match the PCK model, these figures show good comparison between the equivalent viscous damping for the Grade 80 and Grade 60 column tests.

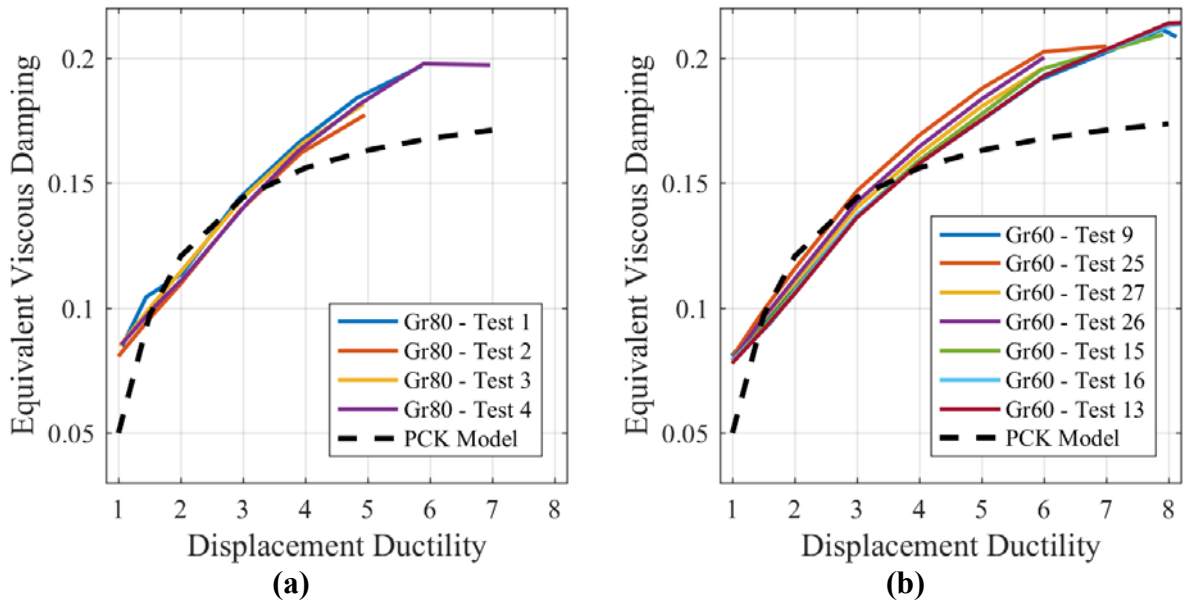

Figure 5-3. (a) Equivalent viscous damping of Grade 80 columns; (b) EVD of Grade 60 comparison columns

5.4. Cumulative Dissipation of Energy

As a measure of performance, total dissipated energy is only useful as a comparative tool if the columns for which the comparison is conducted share the same displacement load history. Consider the difference between a shake table test and a 3-cycle set load history for two identical columns. In the case of the shake table test, the number of cycles to failure is far fewer than that observed in the 3 cycle set test, thus leading to much lower levels of dissipated energy during the shake table test. This is simply a reflection of the load history differences between the two loading protocols. Taken further, two identical columns could be subjected to a 3 cycle set to failure (bar fracture), while the other could be subjected to just one cycle to failure (also bar fracture). An example of such a test is shown below (Moyer and Kowalsky, 2003). Clearly, the hystreretic response in Figure 5-4(a) (single cycle to failure) has a much lower level of total dissipated energy (orders of magnitude) compared to Figure 5-4(b) (3 cycle set to failure).

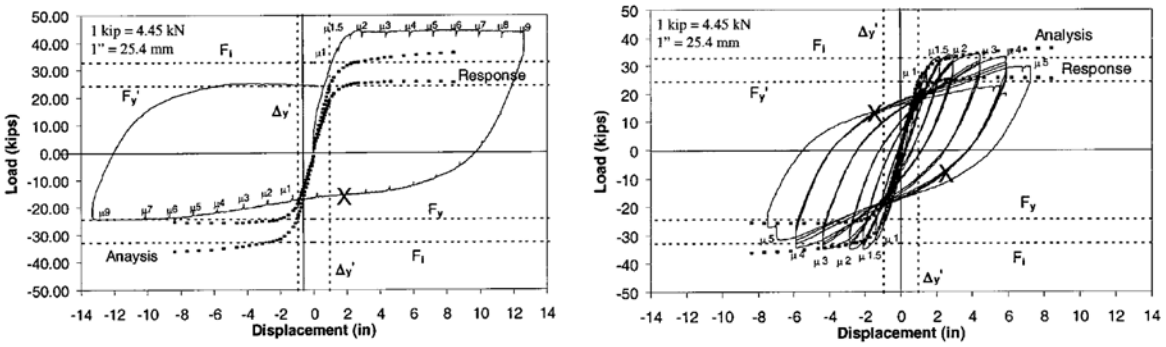

(a) Single cycle *(b) Multiple cycles*

Figure 5-4. Differences between single and multiple cycle loading (Moyer and Kowalsky, 2003)

If two columns are subjected to identical load histories (in terms of displacements at each cycle), then the comparison of energy dissipation becomes more meaningful. However, when comparing the Grade 80 columns tested as part of this research to their grade 60 counterparts, there are two differences with regards to loading history that must be noted. First, the grade 80 columns have a higher yield point, and as a consequence, a higher ductility one displacement. As a result, the amplitude of the cycles that the grade 80 columns are subjected to do not exactly match the cycles that the grade 60 columns are subjected to (since the loading is defined by increments of ductility one, which is unique for each column). Second, while all grade 80 columns were subjected to a loading history that consisted of 3 cycles at ductility 1, 1.5, 2, 3, 4, 5, 6, 7, 8 (increasing in single ductility increments to failure), some of the grade 60 columns were subjected to 3 cycles at ductility 1, 1.5, 2, 3, 4, 6, 8, 10 (increments of 2 ductility levels beyond ductility 4). As a consequence, comparing total dissipated energy will result in differences that are partially attributed to the difference in load history.

As an alternative to cumulative dissipated energy, the energy dissipated at each ductility level may also be calculated. That data is shown in Figure 5-5 through Figure 5-8 for each of the test columns. Each 'x' represents the total dissipated energy for the cycles at the respective displacement ductility level shown. The number of cycles sustained at each ductility level for each of the columns is shown in Table 5-5. Based on these graphs, the dissipated energy per ductility level is comparable for the grade 80 and grade 60 columns. However, it is important to note that the displacement level at a given ductility is higher for the grade 80 columns than the grade 60

columns due to the higher yield point. This will result in higher dissipated energy for a given ductility. Also, these columns have consistent axial load ratios, however, as the concrete strengths vary between the grade 80 and grade 60 columns, the magnitudes of the axial loads are different. Differences in axial load result in differences in lateral force capacity, which in turn impact the dissipated energy. Throughout Figure 5-5 through Figure 5-8, note that at the highest ductility levels, once bars start to fracture, the energy dissipated per ductility level decreases as expected due to the lower lateral force capacity once bars have fractured.

Table 5-5. Number of cycles at each ductility level for Grade 80 and Grade 60 Columns

Test	μ_Δ=1	μ_Δ=1.5	μ_Δ=2	μ_Δ=3	μ_Δ=4	μ_Δ=5	μ_Δ=6	μ_Δ=7	μ_Δ=8	μ_Δ=10
1 Gr80	3	3	3	3	3	3	3	0	0	0
9 Gr60	3	3	3	3	3	0	3	0	3	2
25 Gr60	3	3	3	3	3	3	3	2	0	0
2 Gr80	3	3	3	3	3	2	0	0	0	0
27 Gr60	3	3	3	3	3	3	2	0	0	0
26 Gr60	3	3	3	3	3	3	4	0	0	0
3 Gr80	3	3	3	3	3	2	0	0	0	0
15 Gr60	3	3	3	3	3	0	3	0	3	0
4 Gr80	3	3	3	3	3	3	3	2	0	0
16 Gr60	3	3	3	3	3	0	3	0	3	3
13 Gr60	3	3	3	3	3	0	3	0	3	2

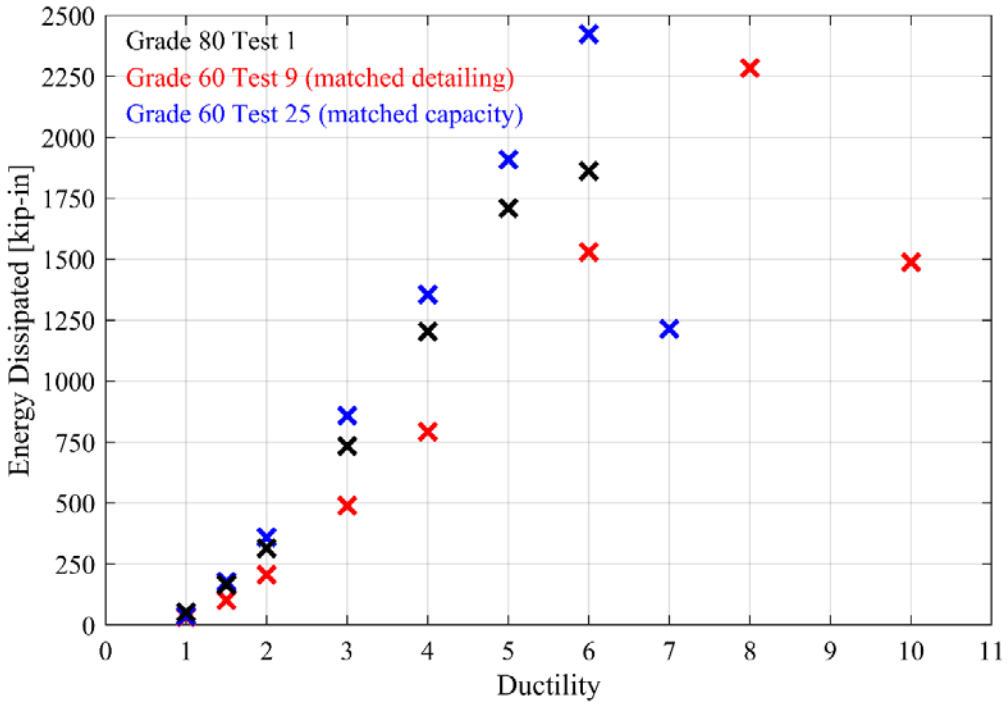

Figure 5-5. Test 1 (and comparison columns) per-ductility level energy dissipation

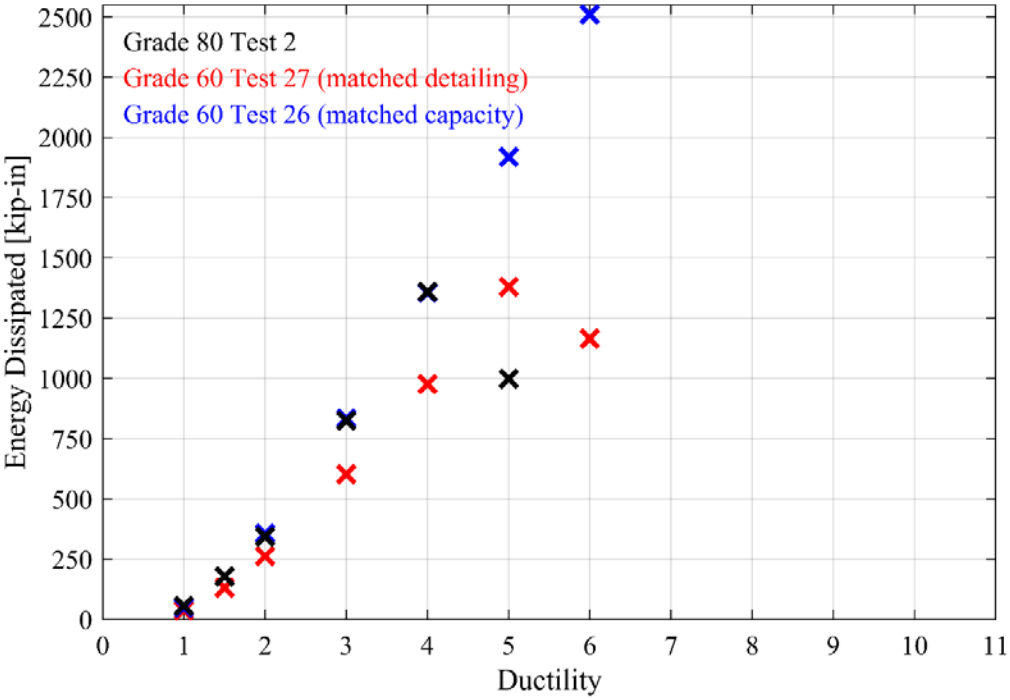

Figure 5-6. Test 2 (and comparison columns) per-ductility level energy dissipation

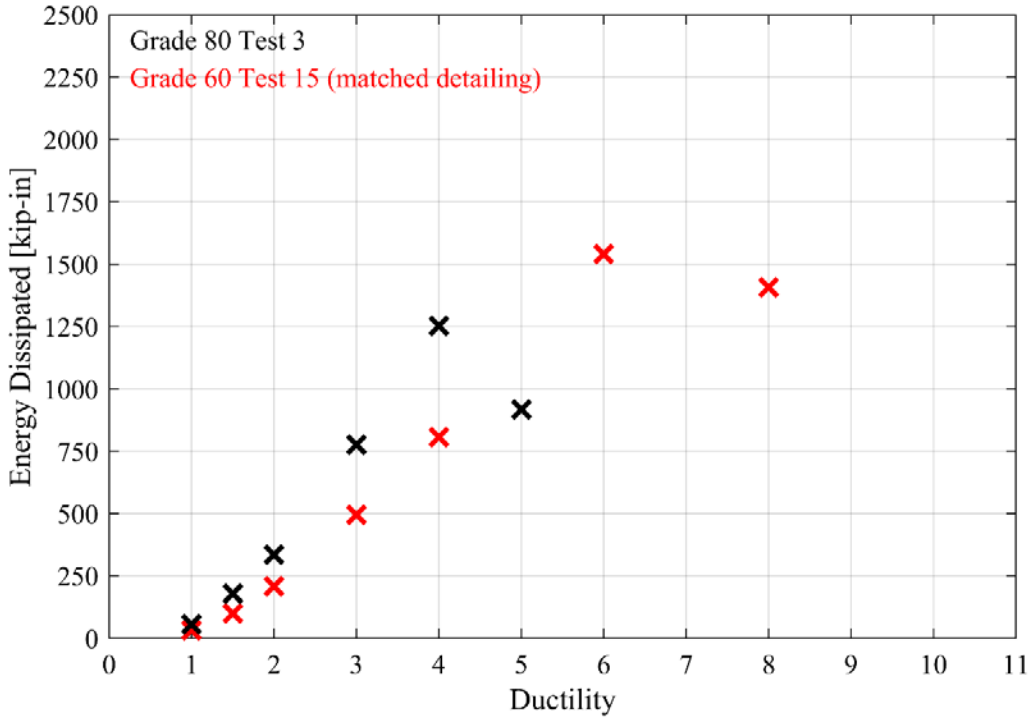

Figure 5-7. Test 3 (and comparison columns) per-ductility level energy dissipation

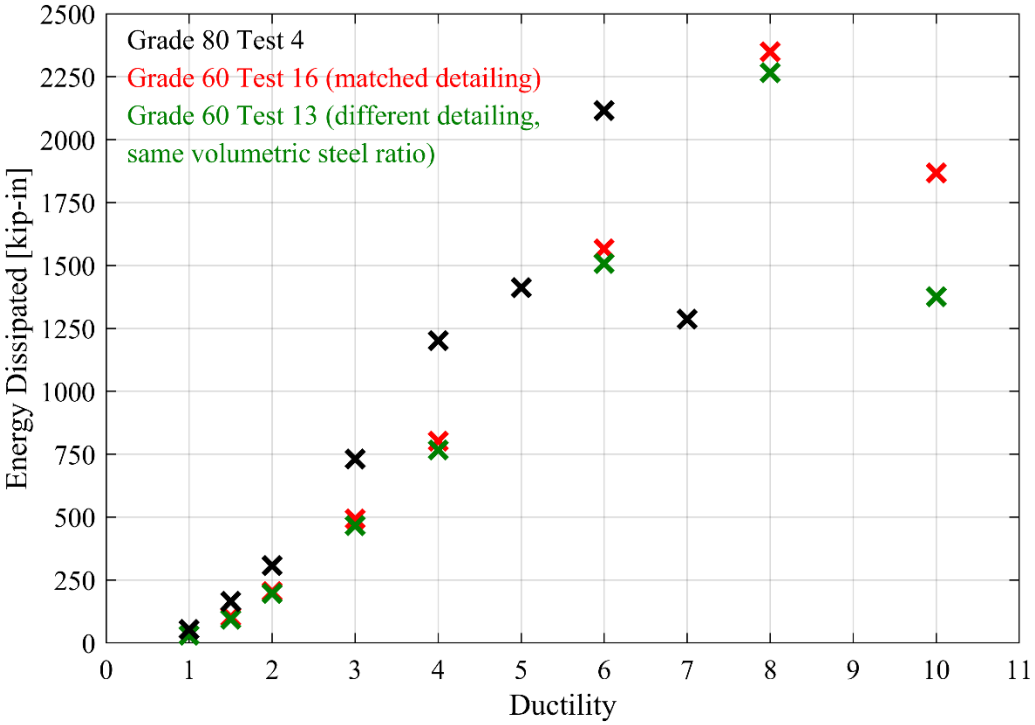

Figure 5-8. Test 4 (and comparison columns) per-ductility level energy dissipation

Figure 5-9 represents the cumulative dissipated energy for the grade 80 and grade 60 columns through the end of the test. Some tests were stopped after one bar fracture on each side (such as Test 27 of the grade 60 columns), others went further. As a result, a dashed line is provided which signifies the first bar fracture for each of the tests, which provides a more meaningful comparison. Also a second dashed line shows the total dissipated energy through displacement ductility 4 (all columns followed the same load history through at least that level of ductility).

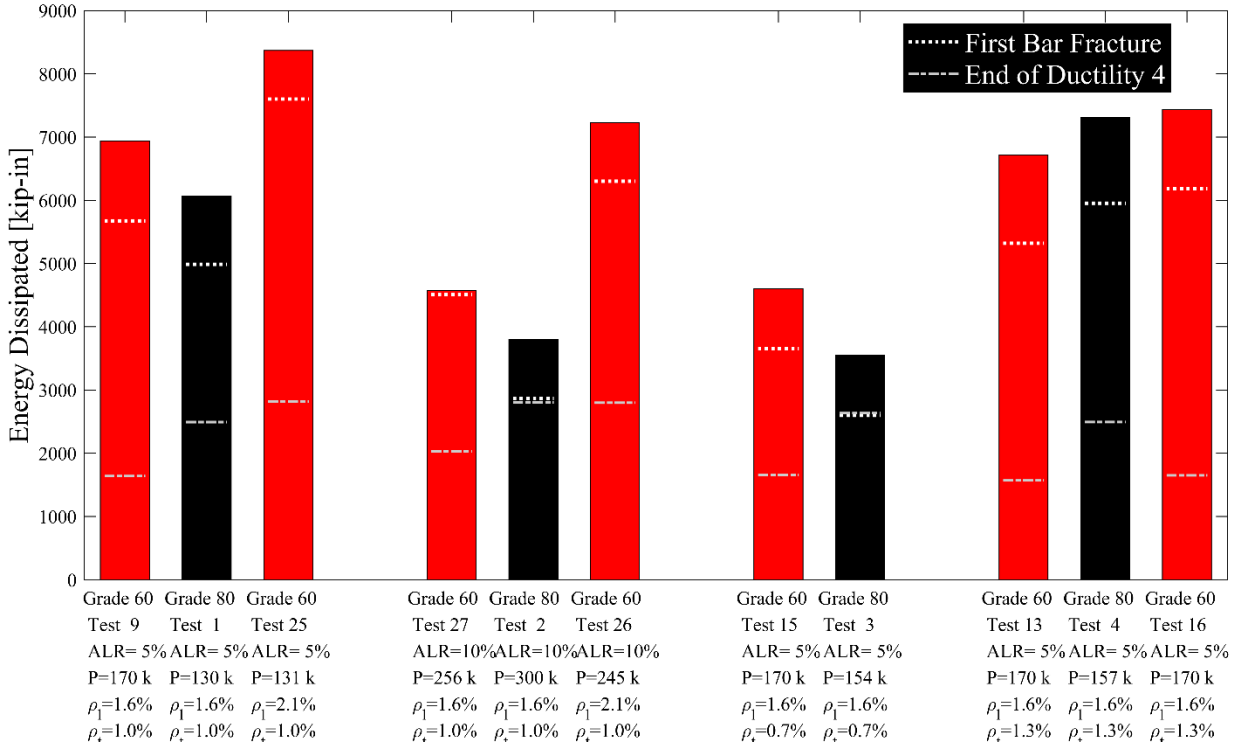

Figure 5-9. Comparison of total dissipated energy

For grade 80 test 1, the column sustained the lowest total dissipated energy to the point of bar fracture when compared to the companion grade 60 columns. Grade 60 test 9 represents the column with the same amount of steel as the grade 80 column (1.6%), while grade 60 test 25 represents the column with the matched strength (i.e., higher amount of grade 60 steel (2.1%), which is the more meaningful comparison). Also, grade 60 test 25 followed the same load history as test 1 of the grade 80 columns, and also maintained nearly the same axial load (130 vs 131 kips). The only difference between these columns is the displacement that defines ductility 1. Even with these differences, the grade 60 column sustains substantially more energy to first bar fracture than

the grade 80 column. The comparison to grade 60 test 9 is less meaningful as the grade 60 column was not subjected to ductility 5 or 7 cycles, and also had a higher axial load (170 vs 130). Despite missing the ductility 5 and 7 cycles, as well as having a lower yield strength (which results in lower force capacity) the grade 60 column with the same reinforcement content dissipated somewhat higher energy to first bar fracture.

For grade 80 test 2 the column followed a similar behavior exhibiting substantially less total dissipated energy when compared to the column with matched strength (grade 60 test 26). These columns were subjected to the same load history (aside from the difference in ductility 1 definition). The axial load for the grade 60 column was 245 kips, while the axial load for the grade 80 column was 300 kips. Test 27 of the grade 60 column had the same amount of reinforcement as the grade 80 column, and still exhibited higher levels of dissipation of energy at first bar fracture.

For grade 80 test 3, there was only one comparison column and it contained the same amount of longitudinal steel. The axial load was slightly less in the grade 80 column (154k vs 170k). Although the load history for the grade 60 column contained 2 ductility increments past ductility 4, bar fracture occurred at ductility 4 for the grade 80 column, thus allowing a direct comparison in terms of dissipated energy. As was the case for tests 1 and 2, the grade 60 column dissipated higher energy prior to first bar fracture. These columns also contained the lightest level of transverse steel, explaining the earlier onset of bar fracture compared to tests 1, 2, and 4.

Grade 80 test 4 contained the highest level of transverse steel (1.3%). Companion grade 60 columns both had the same longitudinal and transverse steel ratios. The grade 60 comparison columns were subjected to loading cycles with a 2 ductility increment beyond ductility 4, which would lead to lower levels of dissipated energy when compared to the grade 80 column. Since these three columns sustained the highest ductility levels (due to the tighter spacing of transverse steel), the differences in load history become more pronounced which may explain why these columns exhibited similar levels of total dissipated energy. I.e., if the ductility 5 and 7 cycles are removed from the grade 80 column, the total dissipated energy would of course reduce, resulting in behavior similar to tests 1, 2, and 3. Because of these issues, comparisons for dissipated energy for the test 4 column and its grade 60 counterparts is more difficult.

In conclusion, for a given ductility level, the dissipated energy is similar for grade 60 and 80 steel. When examining the total dissipated energy at first bar fracture, the grade 80 columns consistently exhibited lower levels of dissipated energy. This is a function of bar fracture occurring earlier after the onset of bar buckling for grade 80 columns. As discussed later in this report, the earlier onset of bar fracture is a consequence of the lower critical compressive strain of the grade 80 steel. Also, it should be noted that the results shown here should be evaluated on a qualitative basis since there are differences in loading histories between test specimens. It is felt that bar fracture is connected to exceedance of a strain threshold as opposed to accumulation of energy through cyclic loading. I.e., repeated cycles at lower levels of ductility would result in higher levels of dissipated energy while the strain amplitude to cause bar fracture would remain essentially the same.

5.5. Bond Slip (Strain Penetration)

As seen in Chapter 4, the component of column displacement attributed to base rotation from bond slip is comparable to that of flexure above the base (see Figure 4-14(b)). Several past researchers have suggested that using high strength rebar leads to higher levels of bond slip, or strain penetration (Restrepo et al., 2006; Hassan et al., 2008; Sokoli and Ghannoum, 2016). This increase in strain penetration would increase the expected column displacement. Bond slip for the tests described in this report were calculated and compared to the values from Grade 60 columns (see Figure 4-18). Figure 5-10 shows the bond slip versus column displacement for each Grade 80 column compared to the Grade 60 column. This figure shows that the Grade 80 reinforcement has slightly higher amounts of bond slip for higher displacements; however, this difference is not likely enough to significantly change column displacements.

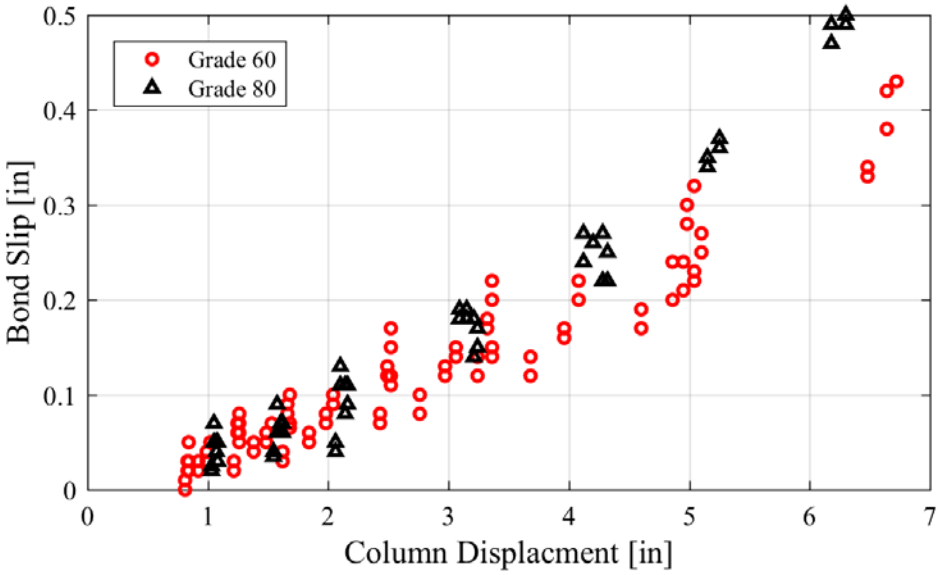

Figure 5-10. Bond slip comparison for Grade 60 vs. Grade 80 columns

5.6. Conclusions

Analysis of the results of the four Grade 80 column tests suggest that current models for plastic hinge lengths, strain limit states, equivalent viscous damping, and bond slip of Grade 60 columns are accurate for Grade 80 columns. More column tests should be performed in order to make definitive conclusions, but these results suggest that A706 Grade 80 rebar could be used in the place of Grade 60 rebar without any adjustment to the design parameters.

CHAPTER 6. LONGITUDINAL BAR FRACTURE

6.1. Comparison of Column Limit States

While conducting the column tests described in this report, it was observed that A706-80 longitudinal reinforcement fractured within one or two load reversal cycles of clearly observable buckling. Comparison columns with A706 Grade 60 reinforcement (Goodnight et al., 2015) with similar geometry and detailing were able to sustain more cycles after visible buckling. Figure 6-1 shows a graphical representation of the load histories of each column. Each square marker represents a displacement to which the column was loaded. For simplicity, only the positive displacements have been included on this graph, but each column was also subjected to an equal displacement in the negative direction. There are four groupings of load histories corresponding to the positive displacements of the four Grade 80 column tests in black, and the comparison Grade 60 columns in red. Each set of points also contains markings for certain limit states. The equivalent yield displacement is marked on each load history with a horizontal dotted line. The first instance of visually observed longitudinal bar buckling is marked with a circle and the first longitudinal bar fracture is marked by an "x."

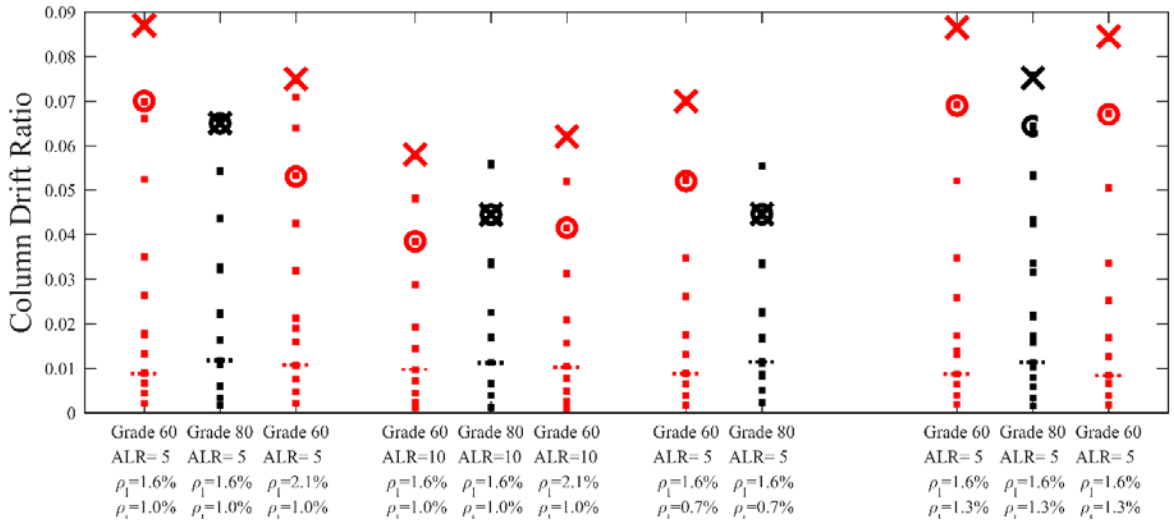

Figure 6-1. Column load histories with limit states

As the graph shows, although bar buckling tends to occur at similar levels of column displacement, bar fracture occurs later in the Grade 60 columns. In addition to being different grades of rebar, the rebar was also produced by different mills. For the sake of anonymity, this

report refers to Mill 1 as the producer of the Grade 80 column rebar and Mill 2 as the producer of the Grade 60 column rebar.

Figure 6-1 also shows that the drift ratio capacity of the Grade 80 columns is still well above 4%. However, the post-buckling drift capacity of the Grade 80 columns is worse than comparison Grade 60 columns. This chapter attempts to identify the cause and propose a solution for this issue, which would possibly increase the displacement capacity of columns.

6.2. Reasons for Early Fracture

When longitudinal bars fracture after buckling in reverse-cyclic column tests, researchers often have used the term low-cycle fatigue to describe failure (Mander, 1983; Chai, 1991, Haber et al., 2013). Cyclic fatigue tests have been performed on reinforcing steel for several decades. High-cycle fatigue refers to bars that are loaded in tension and compression cycles to stresses or strains below yielding, which causes fracture after cycles numbering in the thousands (Paul et al., 2014). Low-cycle fatigue testing subjects bars to stresses or strains higher than yield, and the number of cycles prior to fracture often depends on the strain amplitude. Zhou et al. (2010) suggested that the low-cycle fatigue behavior of A706 steel should perform according to Equation 6-1, where ε_{ap} is strain amplitude and N_f is number of cycles to fracture. The highest strain amplitude tested (4.66) resulted in 43 cycles to fracture.

$$\varepsilon_{ap} = 0.116\left(2N_f\right)^{-0.348} \qquad \text{Equation 6-1}$$

Ghannoum and Slavin (2016) show evidence that the low-cycle fatigue performance of Grade 80 rebar is worse than comparison Grade 60 rebar. This could explain why the A706-60 columns had a greater displacement capacity than the A706-80 columns.

However, buckled longitudinal reinforcing steel is under a much different state of strain than rebar subjected to low-cycle fatigue. Longitudinal bar buckling imposes a combination of axial and bending loads on the rebar cross-section, and low-cycle fatigue tests are inconsistent in addressing rebar buckling. Some low-cycle fatigue tests allow bars to buckle on compressive loading cycles (Brown and Kunnath, 2004), while others design test methods to prevent bar

buckling (Hawileh et al., 2010). If the bar is not allowed to buckle, strain demands on the cross-section remain constant from axial loading. However, if the bar buckles under compressive loads, the bar experiences axial and bending demands. The axial strain is constant across the cross-section, but the bending strain profile varies linearly across the cross-section. Buckling thus amplifies the compressive strain demand on the cross-section, as Figure 6-2 shows.

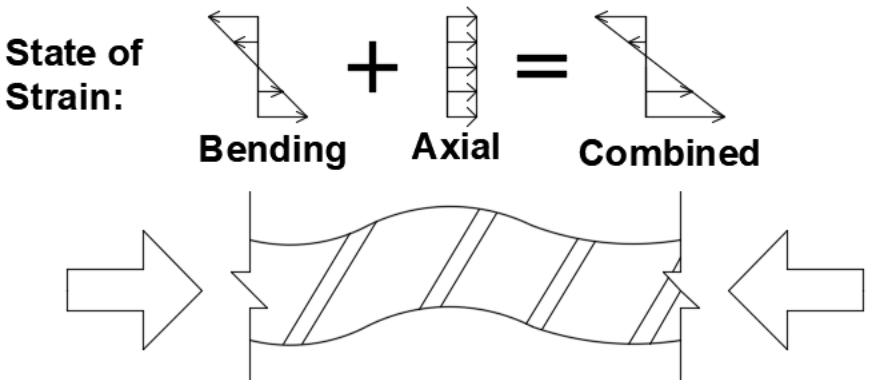

Figure 6-2. State of strain in buckled bar

The varying strain gradient on a buckled bar suggests that buckling will significantly affect fatigue performance, if not introduce another failure mode all together. As noted in Section 2.5, Restrepo-Posada (1992) suggested that if the compressive capacity of the material were "used up," compressive cracks would form at the base of the rebar ribs. He proposed that a "critical buckle" existed: if the rebar were buckled past this level, the compressive cracks that formed at the base of the rebar ribs would be so great that the bar would fracture on the subsequent tensile cycle. This failure theory attributes failure to the absolute magnitude of imposed strain from bending due to buckling, rather than low-cycle fatigue. The authors of this report support this theory, and in order to test its validity, strain demands on the longitudinal bar cross-section due to buckling were quantified based on tests described in this report to determine if a critical bending strain existed.

6.3. Calculating Curvature from Bar Profile

As noted in Section 3.3, the longitudinal and transverse steel in these columns was instrumented with a 3D optical positioning system. Cover concrete on the bottom half of the column was blocked out to attached the optical markers. This block-out did not affect column

performance at high levels of displacement as was demonstrated by Goodnight et al. (2015) and Brown et al. (2008). Figure 3-11 shows a photo of the cover block-out.

Using the optical measurement system, the position of the bar can be captured throughout the test. Equation 6-2 shows the relationship between curvature, φ_{bl}, and position function, $w(x)$, from the principles of solid mechanics. If one assumes the slopes of the position function are small, then $dw / dx << 1$ and the curvature of the bar is equal to the second derivative of the position function as seen in Equation 6-3.

$$\phi_{bl} = \frac{\frac{d^2}{dx^2} w(x)}{\left[1 + \left(\frac{d}{dx} w(x)\right)^2\right]^{\frac{3}{2}}} \quad \text{Equation 6-2}$$

$$\phi_{bl} \approx \frac{d^2}{dx^2} w(x) \quad \text{Equation 6-3}$$

Furthermore, for a uniform cross-section such as steel reinforcement, the maximum strain demand on the section is equal to the curvature times half of the diameter, d_{bl}, as seen in Equation 6-4.

$$\varepsilon_b = \phi_{bl} \frac{d_{bl}}{2} \quad \text{Equation 6-4}$$

Combining each of these equations, the bending strain demand is directly proportional to the second derivative of the curvature, as seen in Equation 6-5.

$$\varepsilon_b = \frac{d^2}{dx^2} w(x) \frac{d_{bl}}{2} \quad \text{Equation 6-5}$$

Throughout the test, the optical measurement system captures the 3D coordinates of each longitudinal bar. Figure 6-3 shows the position of longitudinal bar S4 during the first Grade 80 column test at the first pull cycle of displacement ductility 1, 3, and 6.

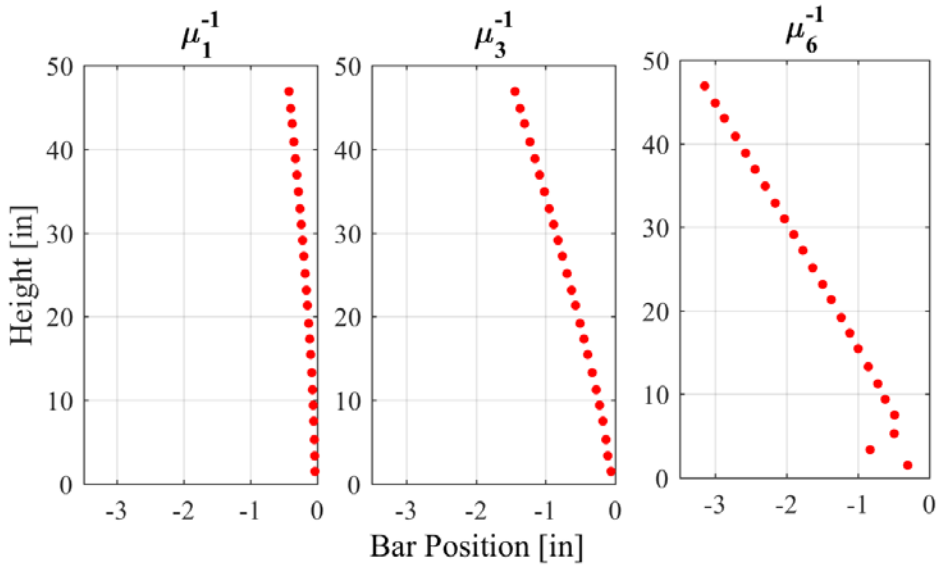

Figure 6-3. Longitudinal bar position throughout test

During the first pull cycle of ductility 1 (μ_1^{-1}), the bottom half of bar S4 is almost vertical as the column is experiencing approximately 1" of displacement. Bar S4 shows more displacement and bending during μ_3^{-1}, but the bar does not show visual evidence of buckling. More investigation was performed to assess the degree of buckling based on strain from bending. As mentioned in Section 4.1.2, bar S4 experienced the most significant level of buckling during μ_6^{-1}, as seen in the far right of Figure 6-3. Three Optotrak markers were located on the position of maximum buckling, and fourth order polynomial function was fit to the position of these markers on the buckled bar in order to estimate the shape function of the bar, as seen in Figure 6-4(a). The second derivative of this polynomial fit is the curvature, as seen in Figure 6-4(b).

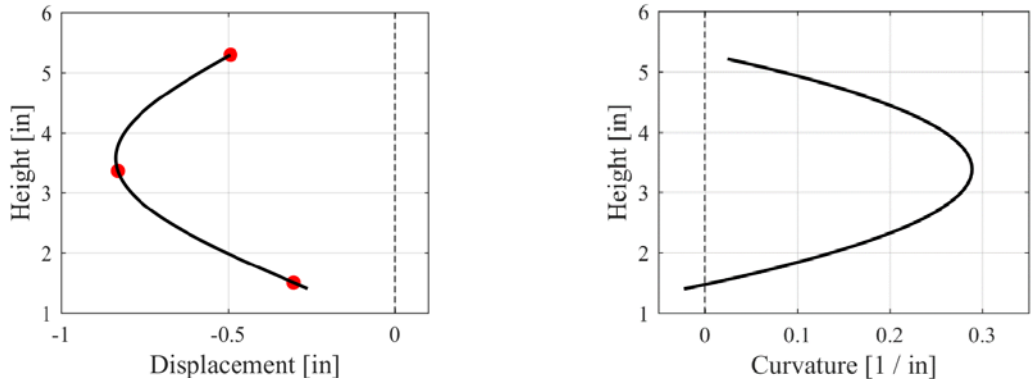

Figure 6-4. (a) Buckled shape of bar; (b) Curvature of buckled bar.

However, the optical measurement system reads the position of each optical marker at approximately the center of the marker. Each optical marker is inserted into a plastic cap that is glued to the surface of the longitudinal bar. Due to the way the optical marker is attached to the rebar, the center of the marker is approximately 0.18” from the surface of each bar. Each longitudinal bar has a nominal diameter of 0.75”, so the optical measurement system is reading the position of the bar approximately 0.55” from the neutral axis of the bar. Equation 6-5 is only accurate if the position, $w(x)$, is taken at the neutral axis. The offset introduces error into the calculation of the curvature of the bar.

In order to find the displaced shape of the bar at the neutral axis from the recorded data, the position of the neutral axis must be calculated from the position of the optical marker. As stated previously, a fourth order polynomial was fit to the position of each optical marker on the buckled bar. The first derivative of this polynomial fit is its slope. The slope of the polynomial was found at the location of each marker. In order to offset the position of the marker to the neutral axis of the bar, the line perpendicular to the slope was found. The slope of the line perpendicular to the tangent line is the negative reciprocal of the slope of the tangent line. Using this slope, the line perpendicular to the tangent line at the location of each optical marker was determined. Knowing that the marker is approximately 0.55” from the neutral axis of the rebar, the line perpendicular to the polynomial fit was used to estimate the position of the neutral axis corresponding to each optical marker. Figure 6-5(a) shows the position of the bar estimated by the position of the optical markers (LED) and the approximate position of the neutral axis. Each group of points includes a fourth order polynomial fit to estimate the bar position.

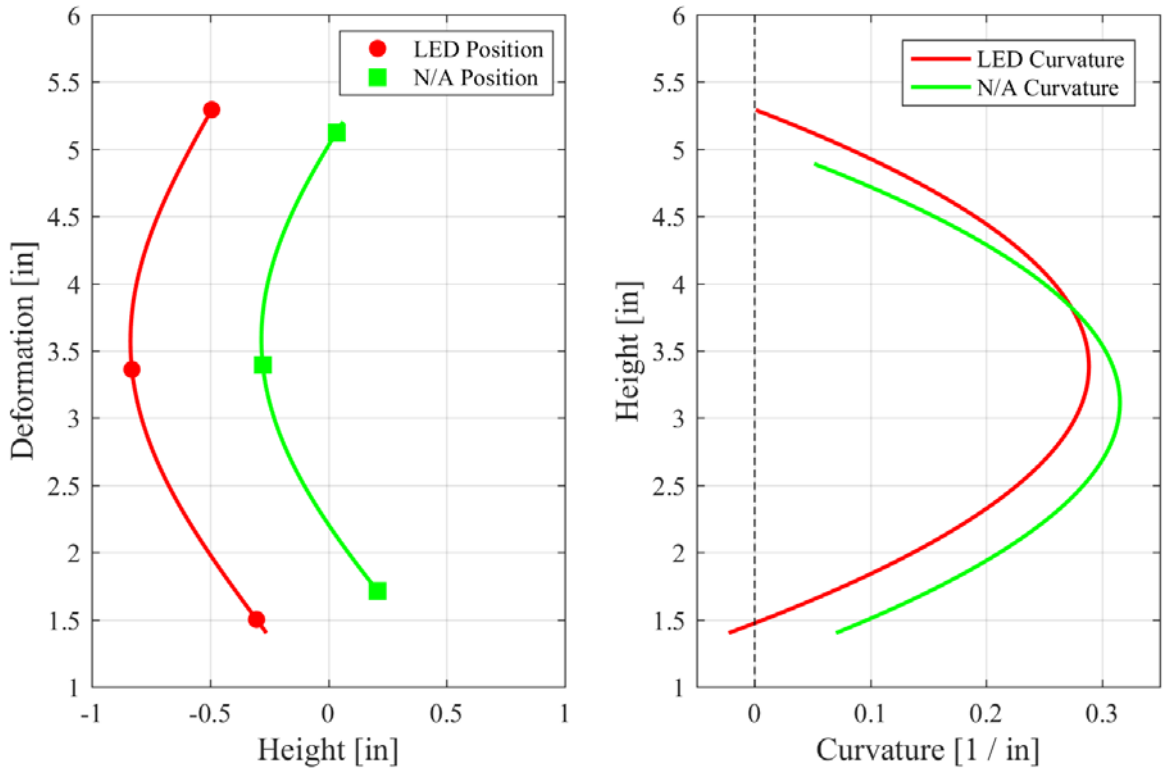

Figure 6-5. (a) Position of optical marker and neutral axis; (b) Curvature of position function for optical markers vs. neutral axis

Figure 6-5(b) shows that the curvature demand on the bar is underestimated by taking the second derivative of the polynomial fit to the position of the optical markers. Correcting the position of the optical markers to the approximate location of the neutral axis provides a more accurate estimation of the curvature and bending strain demands on the bar.

The bending strain demands were obtained using nominal calculations and represent the best approximation of the global state of strain in the bar. The observed state of strain does not likely represent the actual local strain demands on the bar, but is a good estimation for comparison with the results of material tests, as seen in the following section. Since a buckled bar is in a state of axial compression, the actual compressive strain demand will be slightly under-predicted using this method. The true state of stress includes components of axial and bending stresses. However, the demands from bending are much higher than the axial demands.

As a proof of this, take bar S4 from the first Grade 80 column test. Figure 6-5(b) shows that the maximum curvature demand on the section is 0.315 1/in., which corresponds to a maximum strain along the cross-section of 0.12. The maximum axial compressive strain in the bar is approximately 0.01, as seen in Figure 4-8(a). Bar S4 experiences ten times the amount of bending strain than axial strain. Thus, it was assumed that the state of strain from bending was a good approximation of the overall strain in the bar.

Other researchers have tried to quantify the effect of combined axial and bending forces on a buckled rebar. Mau and El-Mabsout (1989) developed a finite element model for bar buckling which included the effect of bending strains with the same method proposed in Equation 6-5. Bae et al. (2005) also acknowledged the "second order effects," referring to the strain from bending as "axial strain from transverse deformation." They developed an equation to predict the bending strain from the transverse deformation. In order to include these second order effects in a model, transverse deformation must be assumed from the geometry and detailing. While the equations present by Bae et al. (2005) seem to show a decent level of agreement with the analysis performed on the column longitudinal bars, they are also very complex and seem difficult to implement in a material model. The strain from bending in a buckled reinforcing bar has been acknowledged by others in the past, but to the author's knowledge, no one has been able to correctly quantify this strain from bending in a column longitudinal bar.

6.4. Critical Bending Strain

In each of the column tests, the bending strain demand at each loading cycle was examined for the longitudinal bars where the data was available. Figure 6-6 shows strain from bending versus column drift ratio for bar S3 in Grade 80 Column Test 2.

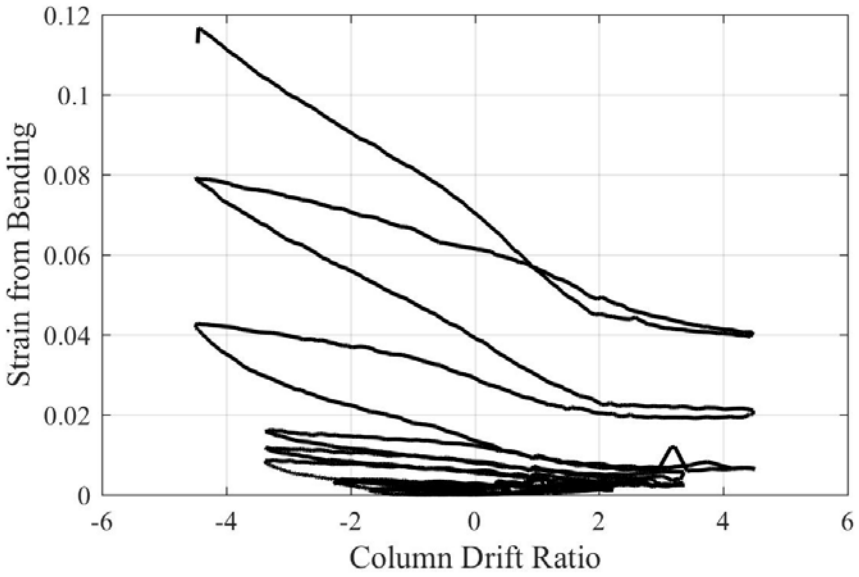

Figure 6-6. Bending strains at different levels of column displacement

Figure 6-6 shows the bending strain demand on the longitudinal bar increases as the column displacement increases. The bending strain was close to zero until the column was loaded to a drift ratio of approximately -4.5%. This corresponds to μ_4, which is when the longitudinal bar (S3) begins to buckle, as mentioned in Section 4.2.2. This graph of the column displacement versus strain due to bending is another way to identify longitudinal bar buckling, in addition to the method described in Section 4.1.2. At small levels of column drift ratio, the strain from bending is zero. The strain from bending rises above zero at a drift ratio of approximately 3.5%. Visible bar buckling, however, is not observed until a bending strain of approximately 4.2%. While the longitudinal bar is not visibly buckled in the lower levels of column displacement, small levels of bending are present. **This is an important distinction, as it presents bar buckling as a continuum, rather than binary process (i.e. buckled, or not). Identification of visible bar buckling is dependent on the observer, whereas, examination of the data from Figure 6-6 leads to a quantitative assessment of buckling that is a function of imposed lateral deformation demand.** Upon investigation of the bending strain history from the longitudinal bars from other column tests, longitudinal bar buckling was visible after the reinforcement had experienced approximately 4% strain from bending.

This analysis was performed on each longitudinal bar that buckled and later fractured during the Grade 80 column tests for which data was available. In some tests, the optical markers

detached from the bar or malfunctioned during the test such that the strain demands from bar buckling could not be calculated. Figure 6-7 shows the bending strain history that each longitudinal bar experienced during the test. The red "x" shows bars that fractured on the subsequent pull cycle. Some longitudinal reinforcing bars showed very small levels of strain from bending prior to significant buckling, such as the first column of data points. Other bars behaved such that the amount of buckling, and corresponding bending strain, gradually increased over the course of the test. This variant behavior explains the granularity in this figure.

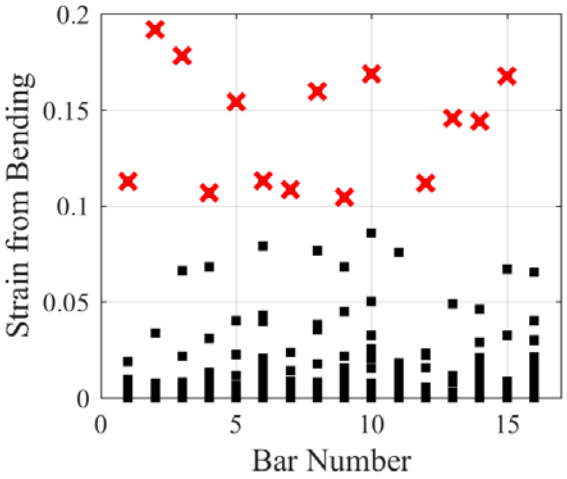

Figure 6-7. Strain history from Grade 80 bars in column test

Figure 6-7 displays a trend that when the bending strain demand on the column bars exceeded a value between 0.09 and 0.10, bars fractured on the subsequent cycle. Some data points exist with bending strains much higher than 0.10 that fracture on the subsequent cycle, but as explained earlier, the progression of bending strain varies for each rebar. The observable trend is that if the strain from bending in a longitudinal rebar exceeds 0.10, the rebar will fracture on the subsequent cycle. This indicates that 0.10 may be the "critical bending strain" of the A706-80 rebar used to construct the columns. Similar analysis was performed on the longitudinal bars from the Grade 60 column tests from Goodnight et al. (2015). Figure 6-8 shows the strain history from each of the bars in the Grade 60 tests.

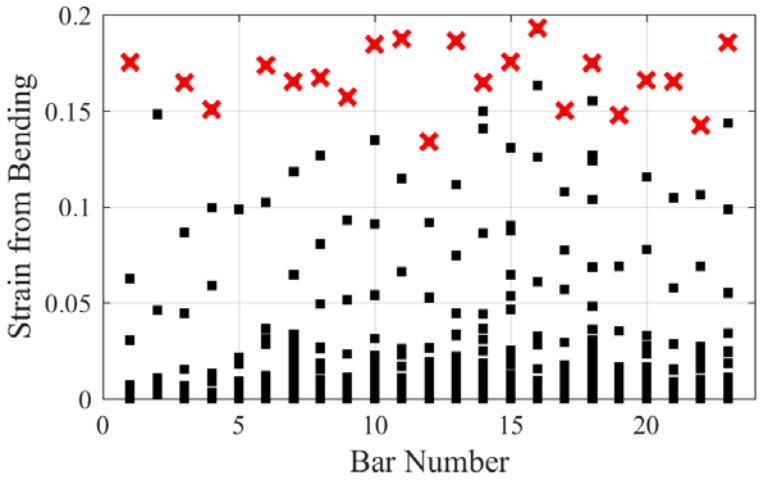

Figure 6-8. Strain history from Grade 60 bars in column test

Figure 6-8 shows that the critical bending strain for the Grade 60 longitudinal bars may be 0.14 to 0.16, with 0.14 as a lower-bound estimate of this critical strain. Figure 6-9 shows the two strain histories with approximate critical strain values.

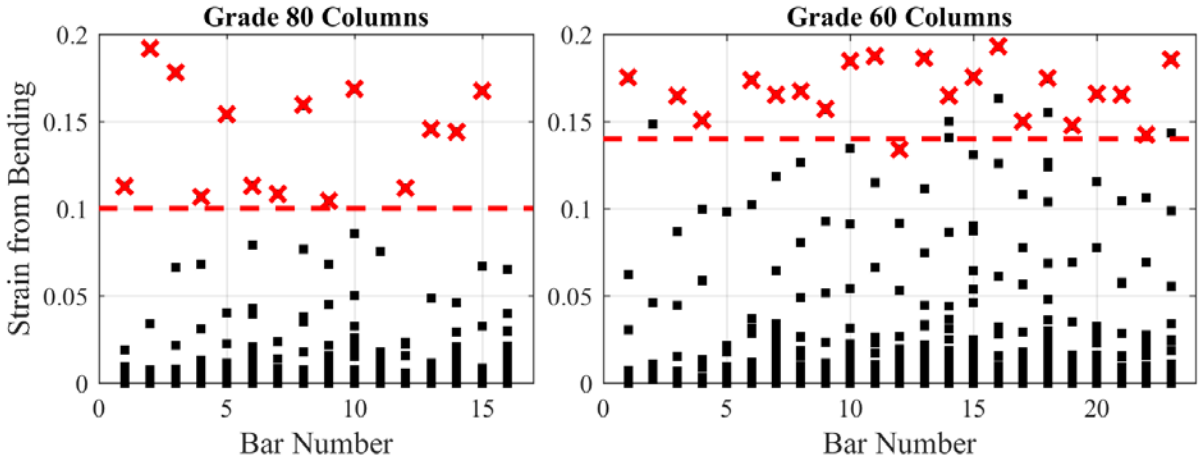

Figure 6-9. Comparison of strain histories and critical strains for Grade 80 and 60 column tests

This analysis suggests that the displacement capacity of the Grade 80 columns was lower than the Grade 60 comparison columns because the critical bending strain of the Grade 80 longitudinal bars was lower than the critical bending strain of the Grade 60 bars. The value of critical bending strain influences how the bars perform after buckling. The authors believe that if the critical bending strain of the reinforcing bars is increased, the displacement capacity of the columns will correspondingly increase.

Rebar producers were contacted to explore the possibility of increasing the critical bending strain capacity. In order to assess the impacts of changes implemented by producers, a simple test to quantify the critical bending strain was developed, which is described in the following chapter.

6.5. Previous Tensile Strain vs. Bending Strain

In the previous section, the strain from bending in longitudinal reinforcement is presented as a measurement of the extent of longitudinal bar buckling, as seen in Figure 6-6. Design variables such as spacing of transverse steel and axial load influence the column displacement at the first occurrence of longitudinal bar buckling (Goodnight et al., 2015). Moyer and Kowalsky (2003) have shown that the magnitude of tension strain during the previous load cycle also influences bar buckling. These three variables (transverse steel spacing, axial load, and maximum tension strain from the previous cycle) affect how quickly a longitudinal bar will buckle under cyclic loading, or the rate of buckling.

In order to analyze the rate of buckling for different column designs, the maximum bending strain in the longitudinal bar can be compared to the maximum tension strain on the previous cycle for each column longitudinal bar. Figure 6-10(a) shows the accumulation of strain from bending over the course of the column test for bar S3 from the second Grade 80 column test. Figure 6-10(b) shows the uniaxial tension and compression strain in the same bar as measured by the change in length between the Optotrak markers (described in Section 3.4) and axial strain history. As mentioned previously, the uniaxial strain data was measured between multiple gage lengths over the height of the column. For the comparison of strain from bending to uniaxial tension strain, the gage length with the maximum tensile strain was chosen. For bar S3 from the second column test, the maximum tensile strain occurred at a gage centered 8.8” above the footing, shown in Figure 6-10(b).

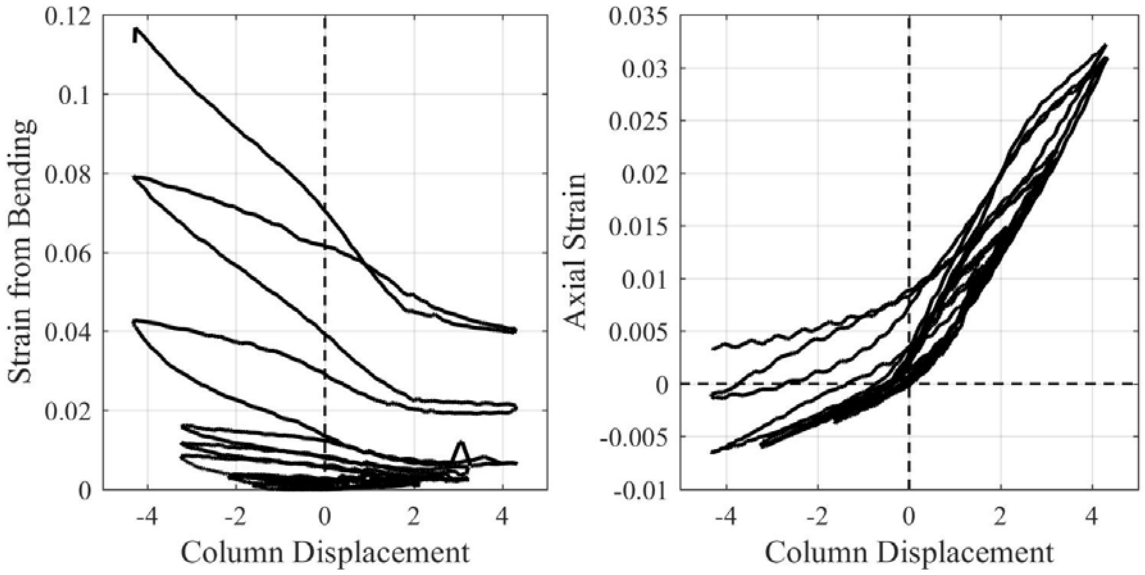

Figure 6-10. (a) Bending strain vs. column displacement; (b) Axial strain vs. column displacement

In order to compare the uniaxial load (tension strain) to the amount of buckling (strain from bending), the maximum tension strain from the previous cycle, or "previous tension strain", was compared to the bending strain of the current cycle. Figure 6-11 shows the relationship between the uniaxial demand and amount of buckling of the reinforcement.

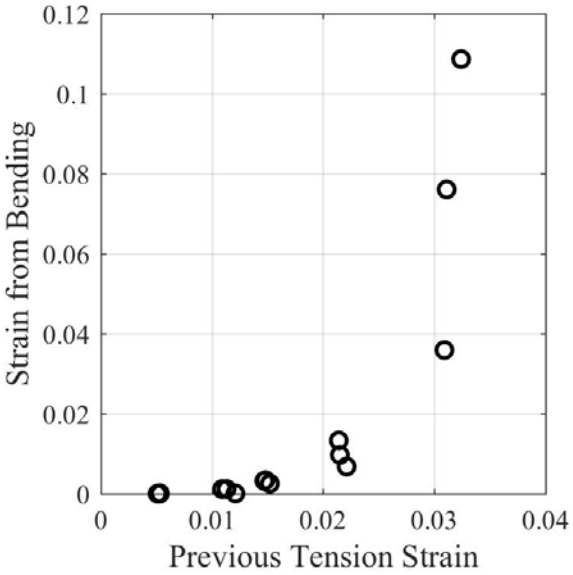

Figure 6-11. Previous tension strain vs. strain from bending

Figure 6-11 shows the rate of buckling for the second Grade 80 column test. This data could be utilized to create relationships between uniaxial demand and buckling in longitudinal reinforcement. Using this data, analytical bar buckling and fracture models could be compared to experimental results.

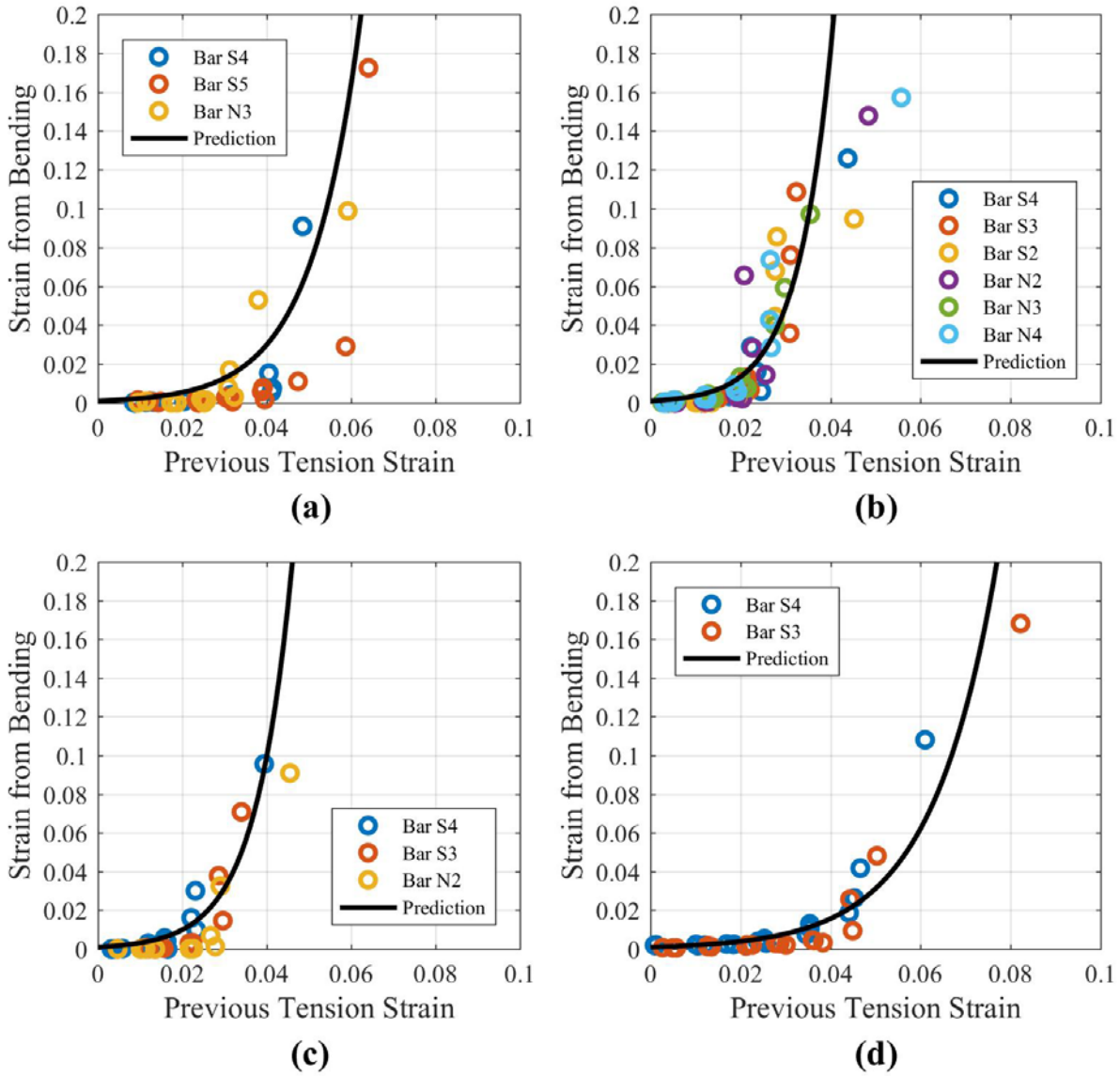

Figure 6-12. Uniaxial vs. bending strain for (a) Gr80 column test 1, ρ_l = 1.6%, ρ_t = 1.0%, ALR = 5%; (b) Gr80 column test 2, ρ_l = 1.6%, ρ_t = 1.0%, ALR = 10%; (c) Gr80 column test 3, ρ_l = 1.6%, ρ_t = 0.7%, ALR = 5%; (d) Gr80 column test 4, ρ_l = 1.6%, ρ_t = 1.3%, ALR = 5%

The uniaxial and bending strain relationship was calculated for each of the Grade 80 column longitudinal bars for which bending strain data was available. Figure 6-12 shows uniaxial

versus bending strain demand for each column test, along with a prediction that was fit to these results. This relationship between uniaxial and bending strain demand is impacted by the level of transverse steel and axial load ratio, as expected. The longitudinal reinforcement labels are available at the beginning of each column test summary in Chapter 4.

As more tests are performed, an exponential function could fit to the data and calibrated by varying multiple parameters. A form of this equation could be used in order to predict the tensile strain resulting in bar fracture for columns under cyclic loading. Currently, models exist to predict the maximum tensile strain prior to buckling (Equation 5-6), but with this method, the tensile strain prior to bar fracture could be calculated. Using moment curvature analysis, the tensile strain could be used to calculate a curvature, which then can be used to calculate a column displacement with the plastic hinge method. Longitudinal bar buckling is often used as the ultimate limit state in column design with the knowledge that the column will have slightly more capacity than the bar buckling limit state, thus adding an inherent factor of safety to the design. Another reason that bar buckling is used as the ultimate limit state, however, is that current models do not exist to predict bar fracture.

More columns should be analyzed to verify the relationship between uniaxial tension strain demand and strain from bending. Additionally, the authors hypothesize that by increasing the critical bending strain of the column longitudinal reinforcement, the displacement capacity of the column will increase. In order to verify this hypothesis, more RC columns will be tested at NCSU using Grade 80 longitudinal reinforcement with critical bending strains of 0.14 or higher.

It should be noted that mechanistic models for the behavior noted in Figure 6-12 are possible and should be pursued to develop analytical solutions. Such models could be compared with data from Figure 6-12 for both the onset of buckling and fracture. The data presented in Figure 6-12 is preliminary, but nonetheless promising as it transitions the thought process of bar buckling from a binary to continuum.

CHAPTER 7. BUCKLED BAR TENSION TEST

7.1. Development of the Test

As mentioned in the previous chapter, the critical bending strain, ε_{cr}, of the A706-80 rebar used to construct the Grade 80 columns was lower than the A706-60 ε_{cr}. This difference in ε_{cr} may explain the different displacement capacities of the Grade 60 and Grade 80 column tests. In the previous chapter, the critical bending strain was calculated using the optical measurement data from large-scale column tests.

However, a simplified material test was developed to quantify ε_{cr} of a given rebar. This test, called the "Buckled Bar Tension Test" (BBT Test), attempted to simulate the loading conditions of a buckled rebar by applying tensile and compressive loads on a rebar specimen in an MTS Universal Testing Machine. Figure 7-1(a) shows the test setup with the Universal Testing Machine and the Optotrak camera, and Figure 7-1(b) shows a rebar specimen with the optical markers.

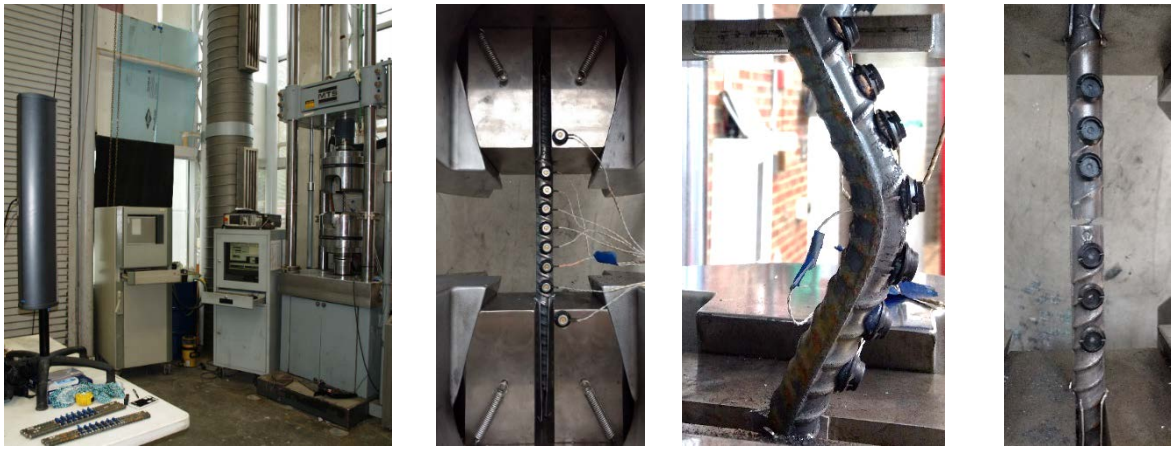

(a) **(b)** **(c)** **(d)**

Figure 7-1. (a) BBT test setup; (b) Rebar specimen with optical markers; (c) Buckled specimen; (d) Fractured specimen

Multiple rebar specimens from the same batch of rebar were cut, prepared, and subjected each to a single compressive and tensile load cycle. Each specimen was loaded in compression until buckling, as seen in Figure 7-1(c). Once the bar buckled to a prescribed curvature, the bar was loaded in tension until fracture, as seen in Figure 7-1(d). The curvature was monitored during

the test on each bar throughout the compressive loading using the optical measurement system. As mentioned in Section 6.3, the position of each optical marker was used to find the position of the neutral axis. A fourth order polynomial was then fit to the position of the neutral axis of the bar recorded by the optical measurement system, as seen in Figure 7-2(b). The second derivative of this polynomial is the curvature. The maximum strain demand is found at the point of maximum curvature. As mentioned previously, this is a nominal calculation of the global state of strain in the rebar. Figure 7-2(c) shows the difference between the curvatures calculated using the position of each optical marker (or LED) and by using the position of the neutral axis. This correction also proved useful if the rebar buckled backwards. If the rebar sample buckled toward the camera, as seen in Figure 7-2(a), taking the second derivative of the fit of the optical markers underestimated the actual curvature on the bar. However, if the bar buckled backwards, the curvature from the fit of the optical markers was overestimated.

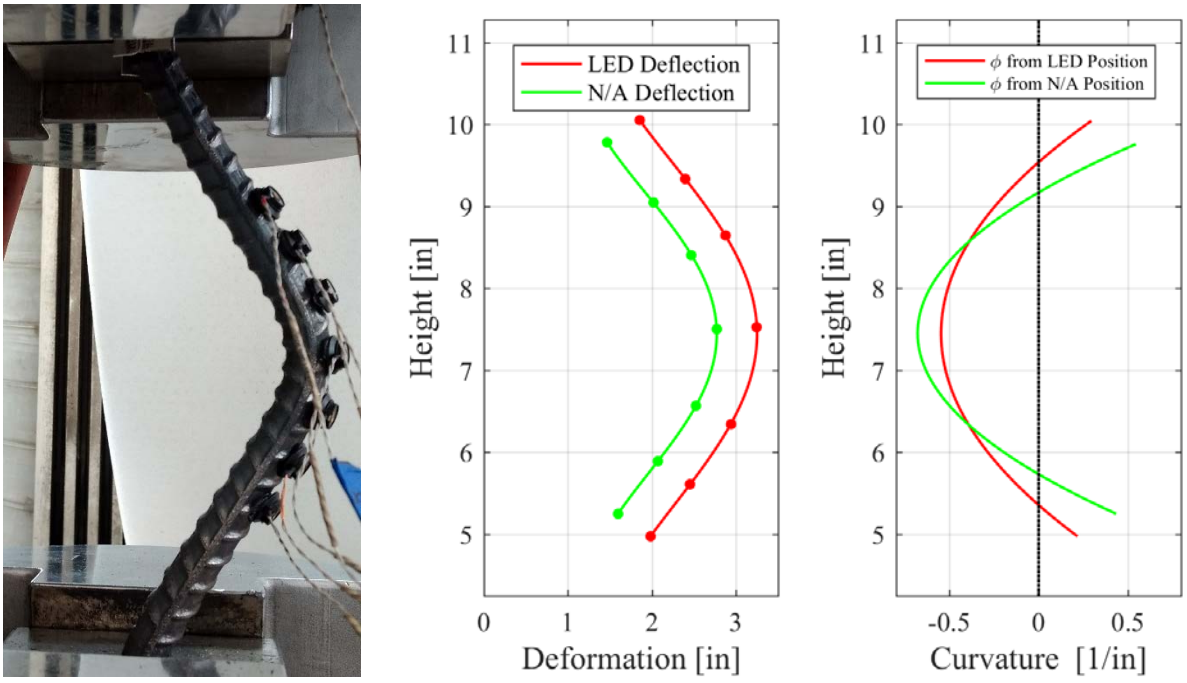

Figure 7-2. (a) Picture of buckled bar; (b) Position of optical markers and adjustment to neutral axis; (c) Calculation of curvature

By performing the buckled bar tension test on multiple rebar from the same heat, two different failure modes were observed. When bars buckled to a relatively small curvature, the rebar was able to straighten and developed the full strain capacity. This was quantified as a ductile

failure. The elongation at fracture was similar to those measured in a simple tension test, as seen in Figure 7-3. Moreover, the failure surface of these bars was similar to results from a tension test, shown in Figure 7-4(a), with necking prior to fracture. When bars were then pulled into tension after buckling to larger curvatures, their elongation at fracture was much lower than results from a typical pull test. This type of failure was classified as brittle. The cross-section failure surface was also flat, with fracture propagating from the rebar face that underwent compressive loading, as seen in Figure 7-4(b). The type of failure seen in Figure 7-4(b) are similar to failures from low-cycle fatigue tests, as seen in Helgason et al. (1976). While low-cycle fatigue testing causes crack propagation and brittle failures, this test shows that brittle failure will also occur in a rebar buckled to a sufficiently large curvature. This result suggests that similar failure modes can be induced through low-cycle fatigue and the buckled bar tension test.

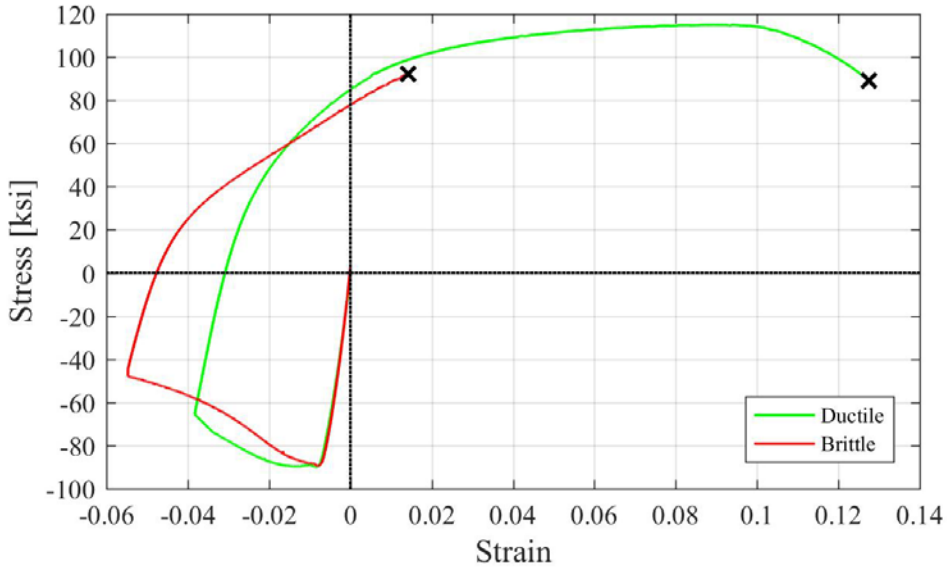

Figure 7-3. Ductile vs. brittle stress-strain curves

(a) **(b)**

Figure 7-4. (a) "Ductile" rebar fracture; (b) "Brittle" rebar fracture

In addition, the fracture surface seen in Figure 7-4(b) resembles the fracture surface seen in the bars that failed during the column test. Figure 7-5 shows pictures of the fracture surfaces of the longitudinal bars from the Grade 80 column tests. These bars had no necking and the failure surface was flat, as in Figure 7-5(a), or flat on the side of global compression and jagged on the tensile side, as in Figure 7-5(b). The failure surface was flat if the bar experienced a lower level of bending strain and jagged with higher levels of strain from bending. All the ruptured column bars had similar failure surfaces; none of the column bars experienced necking prior to fracture, signifying a similar failure mode for each bar.

(a) **(b)**

Figure 7-5. Column test bar fracture surfaces

In addition to identifying the critical bending strain of the steel reinforcement, the mechanism that initiates this brittle fracture in the rebar was examined. As mentioned previously, Restrepo-Posada (1992) suggested that a "critical buckle" existed that would subject the bar to extreme compressive strain demands. These compressive demands would then weaken the material such that is would be susceptible to cracks on the following tensile cycle. Figure 2-4(a) shows a rebar that has been loaded in compression until it buckled significantly and then unloaded. The bar was then cut in half, and Restrepo-Posada used an electron microscope to identify cracks at the base of the rebar ribs, as seen in Figure 2-4(b). These cracks were identified after compressive loading and relaxation of the compressive load. It is still unclear whether these cracks formed during the compressive loading or as the bar was unloaded. However, it is clear that compressive loading of the rebar resulted in the onset of cracks as the base of the rebar ribs. During unloading or subsequent tensile loading, these cracks open to cause premature, or brittle, bar fracture. Figure 7-6 shows evidence that bar fracture initiates on the face of the rebar which experienced compressive loading and that the crack initiates at the base of the rebar rib. This figure shows a rebar that had been subjected to a high bending strain and did not straighten prior to fracture.

Figure 7-6. Onset of bar fracture after buckled bar tension test

7.2. Critical Bending Strain from the BBT Test

In order to identify the critical bending strain of each reinforcing bar, multiple bar specimens were cut from the same bar and subjected to different levels of buckling (and strain demand from bending). Using the optical measurement system, the curvature of the bar was

monitored throughout the test. By subjecting each rebar to an incrementally larger curvature from buckling (and strain demand from bending), the test indicated what the level of bending strain demand on the bar cross-section resulted in brittle fracture after subsequent loading to tension. This point would mark the "critical bending strain." Figure 7-7 shows a group of rebar specimens that have been fractured after buckling in the buckled bar tension test. They are arranged from the lowest curvature (or strain demand) on the left to the greatest on the right. The first five bars show evidence of necking, an indication of ductile failure. The four bars on the right, however, have flat fracture surfaces, and the last two bars did not fully straighten before fracture.

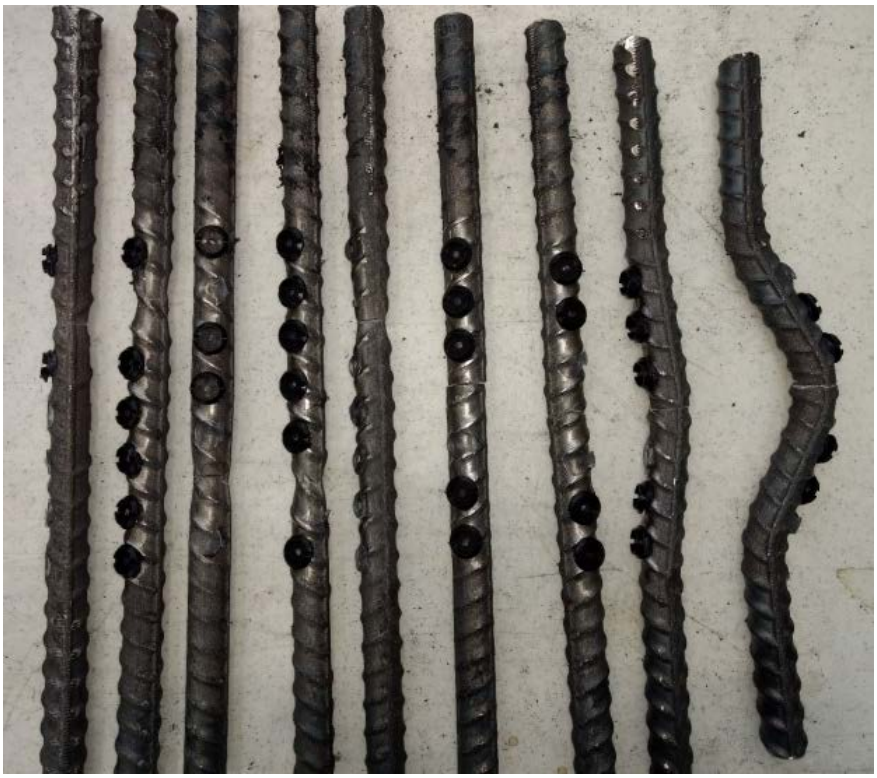

Figure 7-7. BBT test specimens after fracture

7.2.1. Column Rebar Critical Bending Strain

In order to find the critical bending strain of the reinforcing steel used in the column tests, multiple samples were cut from each bar. While extra rebar used to construct the Grade 80 columns was available for material tests, sample bars from the rebar used in the Grade 60 columns were not available. The reinforcing steel producer of the original Grade 60 column bars (Mill 2) was contacted and samples were obtained to use in material tests. It was assumed that these sample

bars obtained from Mill 2 matched the average material properties as the rebar used in the Grade 60 column tests. The Grade 60 columns were constructed from multiple heats of Grade 60 rebar from the same producer.

Multiple one-cycle tests were conducted on matching reinforcing bars from the Grade 60 and Grade 80 columns. The rebar specimens were buckled to varying levels of curvature and then pulled to fracture. The results were examined to find a trend between bending strain demand and the beginning of the brittle behavior seen in Figure 7-4(b). Figure 7-8 shows the results of all the BBT tests performed on the column bars. As mentioned above, the producer of the Grade 60 column bars is Mill 2, while Mill 1 produced the Grade 80 column bars. The y-axis of Figure 7-8 is elongation under load (EUL), or the axial strain at fracture. Typical values of EUL range from 0.10 to 0.18.

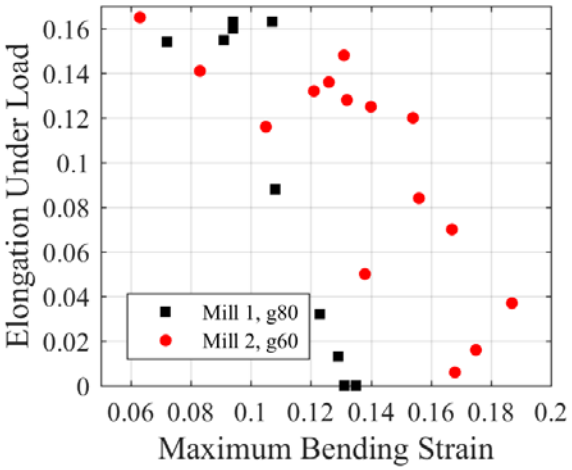

Figure 7-8. BBT results for rebar used in column tests

Figure 7-8 shows that when the bending strain on the Grade 80 column bars exceeds 0.1, the EUL starts to decrease. This drop in EUL corresponds to the onset of brittle behavior, indicating that the BBT quantifies the critical bending strain of the Grade 80 reinforcement is approximately 0.10. The results of the BBT match the results of the analysis of the buckled longitudinal bars from the column tests, shown in Figure 6-9. In addition, analysis on the Grade 60 column bars indicated the critical bending strain was about 0.14 from Figure 6-9, which corresponds to the results of the BBT shown in Figure 7-8.

As mentioned previously, it is believed that the Grade 80 reinforced columns had a lower displacement capacity than the Grade 60 columns because the Grade 80 bars fractured earlier than comparison Grade 60 bars even though both buckled at approximately the same displacement. The authors of this report propose that this early fracture is due to a difference in the critical bending strain capacity of the Grade 60 and 80 bars. Figure 7-8 suggests that the BBT test can simulate the loads placed on a buckled longitudinal reinforcing bar during a cyclic column test and estimate the critical bending strain without conducting reverse cyclic tests on scaled columns.

In order to examine the factors that affect the critical bending strain of steel reinforcement, multiple BBT Tests were performed on rebar with varying yield strength, chemical composition, and rib geometry. The aspect ratio of the specimens and bending strain rate were also examined. The following sections show the results of these tests.

7.2.2. Effect of Rebar Yield Strength

Figure 7-8 shows that the critical bending strain of the Grade 80 reinforcement was lower than that of the Grade 60 rebar. As mentioned previously, the two different mills had produced the two grades of rebar. In order to examine the impact of yield strength on the critical bending strain, samples of both Grade 60 and 80 from Mills one and two were obtained. Figure 7-9 shows the buckled bar tension test results for the Grade 60 and 80 rebar from Mills 1 and 2.

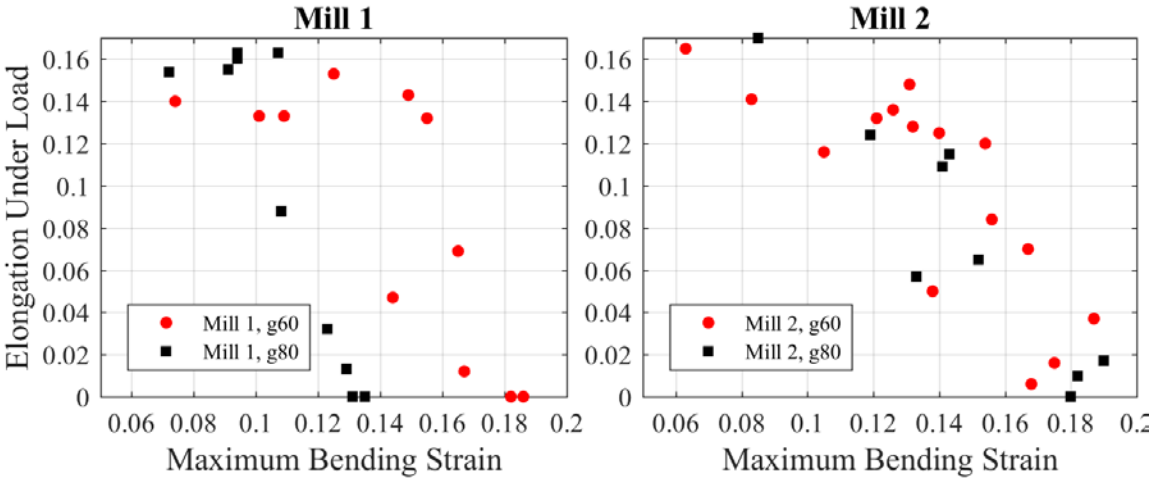

Figure 7-9. BBT test results from Grade 60 and 80 from Mills 1 and 2

Figure 7-9 shows that Mill 1 Grade 60 rebar has similar performance to the Mill 2 Grade 60 rebar, but the Mill 1 Grade 80 rebar had worse performance than the Mill 2 Grade 80 rebar. Rebar of Grade 60 and 80 from Mill 2 showed no difference in performance. These results indicated that yield strength is likely not the primary influence on the critical bending strain. The authors hypothesize that columns constructed with Grade 80 rebar from Mill 2 would have similar displacement capacity to the Grade 60 columns due to the similarity in the critical bending strain.

7.2.3. Effect of Bar Details and Chemical Composition

Since rebar yield strength was not seen to influence critical bending strain, further investigation was performed to identify why Grade 80 rebar from Mill 1 performed worse than rebar with similar strength from Mill 2. After observing the details of the rebar from Mills 1 and 2, a pronounced difference in the rebar profile, specifically the geometry of the ribs (also known as deformations or lugs), was observed. Figure 7-10 shows pictures of the profiles of the rebar from each mill.

(a) **(b)**

Figure 7-10. (a) Mill 1 bar profile; (b) Mill 2 bar profile

As seen in Figure 7-10, the radius at the base of the ribs, where the rib joins to the shaft of the rebar, is much larger for the rebar from Mill 2 than Mill 1. A study by Helgason et al. (1976) showed that rib radius was the most critical factor for causing stress concentrations. This has been collaborated by another study by Zheng and Abel (1998) showing that as the rib radius increases, the stress concentration decreases. As the bar buckles and compressive force demand increases, these stresses will concentrate at the base of the rebar ribs. If the stress concentration factor is higher, these stresses will weaken the material and cause the onset of cracks under tensile load, as seen in Figure 2-4. Helgason et al. (1976) and Zheng and Abel (1998) studied the impacts of stress

concentrations on fatigue loading. However, the stress concentrations will have a greater impact when the rebar is bent due to buckling.

Furthermore, studies by Ghannoum and Slavin (2016) showed that the ratio of the minimum radius at the base of the rebar ribs to the deformation height (R_{min}/H) affected the low-cycle fatigue performance of the reinforcing bars. Smaller rib radii resulted in fracture propagation along the base of the rib. They suggested that increasing R_{min}/H might improve low-cycle fatigue performance. While the authors of this report are not studying low-cycle fatigue, it is interesting that rib radius seems to influence both behaviors.

In order to examine the effect of stress concentrations under compressive loads, a digital image correlation (DIC) software was used. This software takes pictures of a specimen throughout the test. Prior to the test, the specimen was painted white and a hatch pattern of black dots applied to the area of interest. The software calculates the size of each dot and the original distance between dots. As the specimen deforms during the test, the dots move and deform, and the software calculates this relative movement as strain. Thus, the DIC software can show the strain field on a specimen under load.

Figure 7-11 shows the strain field of the compressive face of buckled reinforcing bars from Mill 1 and 2. The figure shows the maximum compressive strains forming on the shaft of the rebar, not the ribs, at the middle of the buckled shape. In Figure 7-11(a), the region of higher compressive strain appears wider than the region of higher compressive strain in Figure 7-11(b). This corresponds to the bar rib geometry as seen in Figure 7-10 where the rib of the rebar from Mill 1 is sharply joined to the shaft, while the rebar rib from Mill 2 has a much softer transition.

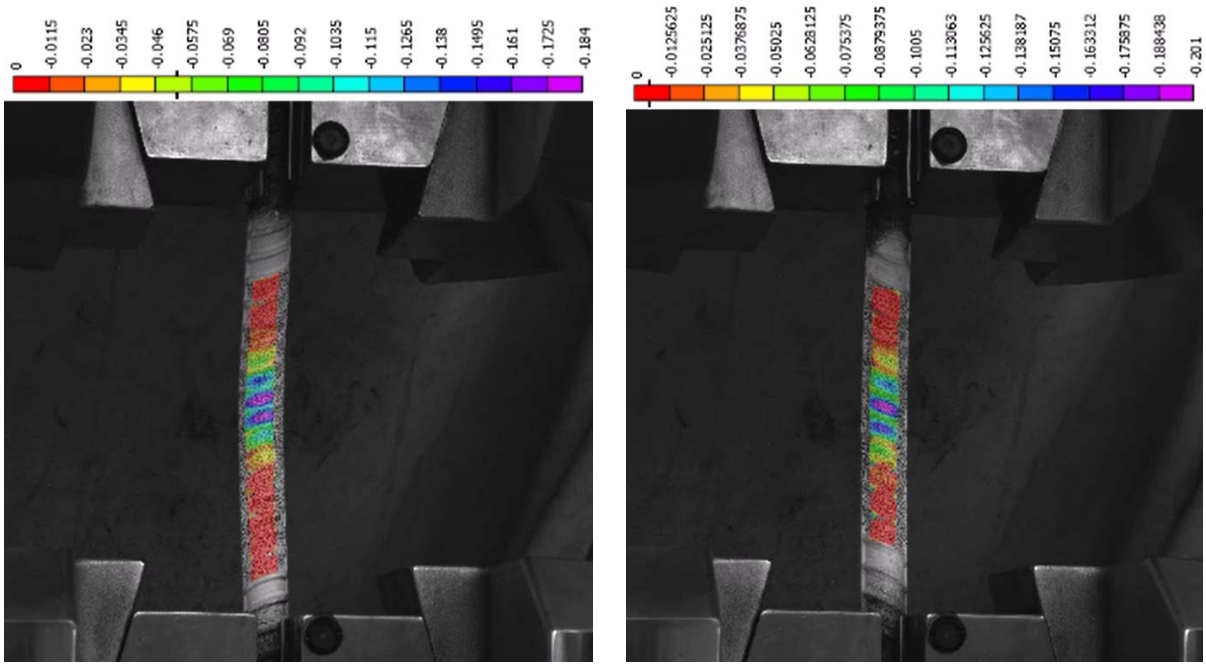

(a) **(b)**

Figure 7-11. (a) DIC results of Mill 1 rebar; (b) DIC results of Mill 2 rebar

Figure 7-11 shows the mechanism through which the compressive strains concentrate on the rebar shaft on the compressive face of the rebar. As mentioned previously, the transition between rebar shaft and rib will cause stress concentrations. Numerical analysis performed by Helgason et al. (1976) indicated that the ratio of strain at the base of the radius to the bar surface could be as high as 1.82. In addition, residual stress will be present at the rebar ribs due to the varying cooling rate (Fleck et al., 1985). These factors indicate that rib radius has a significant impact on critical bending strain.

In addition, the surface of the rebar from Mill 2 was much rougher than the rebar from Mill 1. Helgason et al. (1976) saw that bars from the same mill had increased fatigue performance as the surface roughness increased. They suggested that as the rolls approached the end of their service life, they wore out and produced rougher rebar surfaces. This rough surface seems to improve fatigue performance as well as critical bending strain capacity, although the dataset is not large enough to identify this variable as truly influential.

The impact of chemical composition on the critical bending strain was also studied. Mill 1 adjusted their chemical composition in an effort to increase the critical bending strain. In order to

increase the strain capacity of the rebar, Mill 1 increased the amount of vanadium in the microalloying. Vanadium has been shown to increase the strength of the reinforcing bar, while still maintaining a high ductility. As the rebar yields, nitrogen atoms are dislocated from their bonds and are pinned to the free vanadium atoms, which increases strain capacity and negates the effects of strain aging (Overby et al., 2016).

Initial results showed very little difference in tensile behavior for the new heat of Grade 80 rebar from Mill 1, labeled Grade 80-v2, as seen in Figure 7-12. The increased amount of vanadium seemed to increase the strength of the rebar.

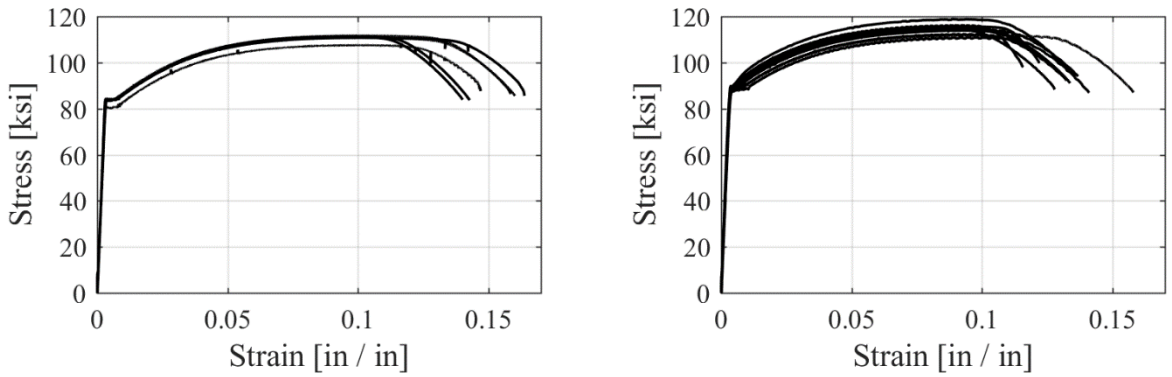

Figure 7-12. (a) Mill 1 Grade 80-v1 stress vs. strain; (b) Grade 80-v2 stress vs. strain

The buckled bar tension test was performed on the Grade 80-v2 rebar. Figure 7-13(a) shows that brittle failure did not occur bending strain of approximately 0.13, with many bars bending to even higher strains before the onset of brittle behavior. In order to verify these results, Mill 1 produced a new batch of rebar with the same chemical composition (Grade 80-v2b), and the Figure 7-13(b) shows the results of this test. Figure 7-13(b) shows that the critical bending strain for Grade 80-v2b is similar to Grade 80-v1, the original Mill 1 rebar.

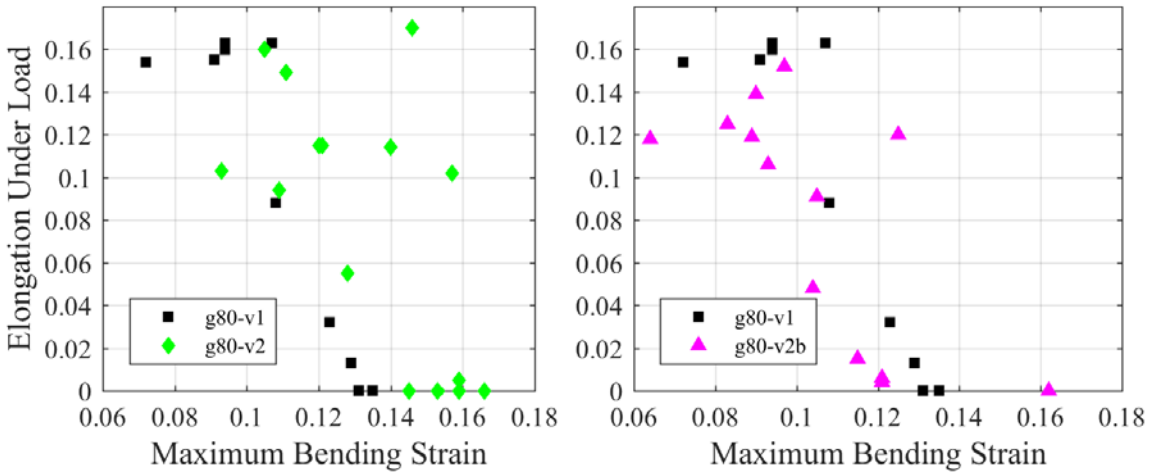

Figure 7-13. BBT test results for (a) Grade 80-v2; (b) Grade 80-v2b

These results suggest than altering the chemical composition may not increase the critical bending strain of the reinforcement. The bar geometry for each heat was then examined in an effort to understand other differences in the bar specimens which may influence the results of the BBT tests.

Figure 7-14 shows pictures of the ribs of each bar. There are two observations that are not clear from this picture. First, the bars from v1 had the least amount of surface roughness, v2 bars had slightly rougher surfaces, and bars from v2b were the most rough. In addition, the rib height of bars from v1 and v2 were similar and the height of the rib from v2b was slightly less. Figure 7-14 does show a difference in the transition from rib material to rebar shaft: Grade 80-v2 bars have a slightly smoother transition from rebar shaft to rebar rib material. This smooth transition appears to minimize the effect of the stress concentrations forming at the base of the rebar ribs and increase the critical bending strain.

Figure 7-14. Mill 1, Grade 80 rebar bar profiles: (a) v1; (b) v2; (c) v2b

The results of these tests suggested that rebar rib radius was the critical factor affecting the critical bending strain. Chemical composition, rib height, and surface roughness may affect the critical bending strain, but other studies are needed to show the effect of each variable.

In order to test the effect of chemical composition and see the magnitude of the rebar rib stress concentration, the ribs of several bars were machined off, so that only the inner core remained. Without the ribs, the results of the buckled bar tension test would show the impact of the different chemical compositions on the critical bending strain, assuming the same brittle fracture would occur due to the compressive strain demands on the cross section. A local machine shop machined the ribs off the bars from Grade 80-v1 and Grade 80-v2 to a diameter of 5/8”, as seen in Figure 7-15.

Machining the ribs off the bar also removes the outer layer of steel that has experienced carburization. The composition of the inner portion of the rebar may be slightly different from the outer portion. However, a study by Paul et al. (2014) indicated that the hardness of a rebar produced

by microalloying is relatively uniform across the rebar cross-section, indicating that removing the rebar ribs will not drastically alter performance.

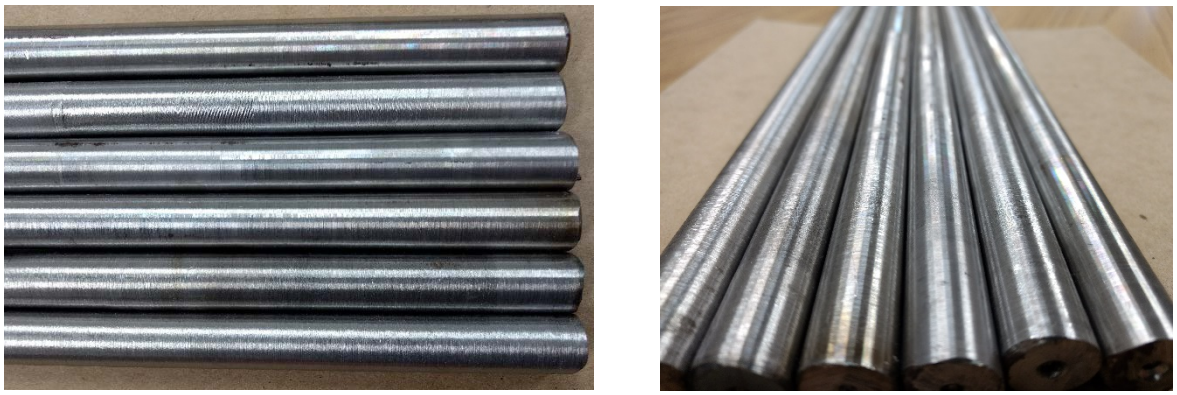

(a) **(b)**

Figure 7-15. Turned down rebar: (a) Plan view; (b) View along length

After examining the results of the BBT test on the turned down bars, several observations were made. First, the failure mode seen in Figure 7-4 did occur in the bars without ribs. Figure 7-16 shows the ductile (with necking and high elongation at fracture) and brittle (with no necking and low elongation at fracture) failure modes.

(a) **(b)**

Figure 7-16. (a) Ductile failure mode for turned down bar; (b) Brittle failure

However, it was also noticed that the precision to which the rebar ribs were removed affected the performance. Each bar was turned down in a lathe, but at some regions, the bars had small grooves due to the machining process. These small grooves caused the bar to fail in a brittle

manner in the locations of the groove, rather than in the location of maximum compressive strain, as seen in Figure 7-17. When this failure mode was observed, machine rebar for future tests were smoothed even more with wire brushes and sandpaper. Even small grooves may cause stress concentrations, so it is uncertain whether the roughness of each bar affects the bar performance. However, for the majority of the bars, a trend was observed in the critical bending strain, indicating that this likely did not significantly affect the results.

Figure 7-17. Brittle failure of turned down bar in undesired location

Figure 7-18 shows plot of the bending strain demand for each of the machined rebar specimens versus the elongation at fracture, along with the rebar with ribs. There does not appear to be a difference in the critical bending strain of the turned down bars from the Grade 80-v1 batch and the Grade 80-v2 batch from Mill 1. As mentioned previously, these two batches had very different chemical compositions: v2 had twice the amount of Vanadium than v1. However, the critical bending strain did not change significantly. This indicates that chemical composition does not have a significant impact on the critical bending strain of reinforcing bars. More research will be performed to determine whether other chemical compositions have different effects.

Figure 7-18 also shows that when the ribs are removed from the rebar, the critical bending strain of the reinforcement increases dramatically (from 0.1 to 0.23). This indicates the

significance of the stress concentrations from rebar ribs on the critical bending strain in the reinforcement. The increase in critical bending strain from the machined rebar specimens suggest that the stresses experienced at the base of the rebar ribs are more than double the stresses on the rest of the bar. This corresponds well to analytical studies, which have examined finite-element models to determine that rib stress concentration factors can exceed two in rebar subjected to fatigue loads (Zheng and Abel, 1998). Since rebar ribs have a negative impact on the capacity of rebar after buckling, one idea would be to remove the rebar ribs in the plastic hinge region. This would possibly increase the displacement capacity of the member, but would also likely be impractical for actual implementation.

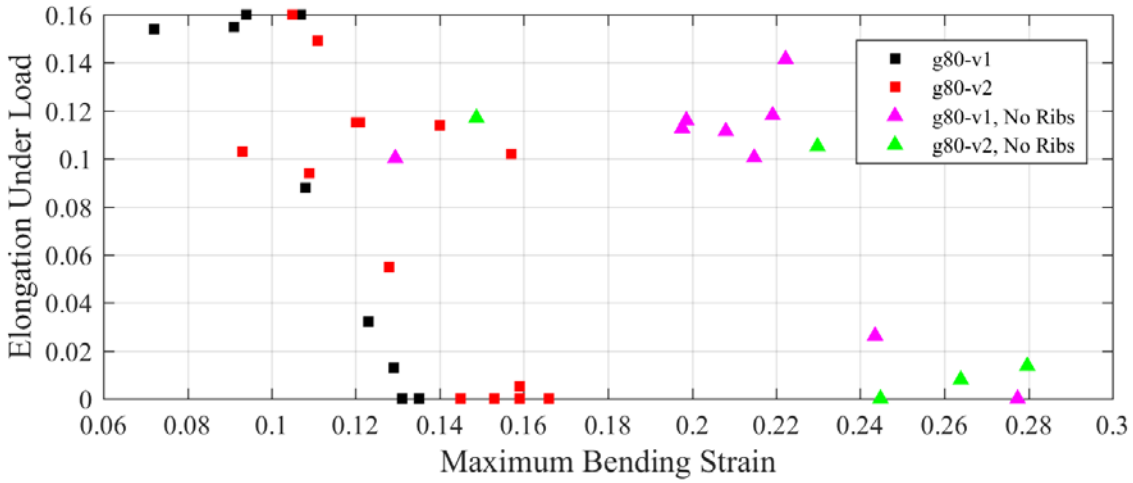

Figure 7-18. BBT results for rebar with and without ribs

Increasing the rebar rib radii appears to be the best solution for increasing the critical bending strain. These results correspond with results of fatigue tests that show improved performance for larger rib radii as this reduces the amount of stress concentration at the base of the rebar rib. Cracks due to exceeding critical bending strain, as well as fatigue cracks, form at the base of the rebar rib. However, if the rib radius is too large, the development length will be affected. Currently, the ASTM A706 standard has minimum height and spacing requirements for rebar ribs. More investigation should be performed to see the impact of increased rib radius on development length

Additionally, other Grade 80 rebar from Mill 1 was available from a past research project (Grade 80-v0). The buckled bar tension test was conducted on samples of this rebar, and the results

shown in Figure 7-19(a). As seen in this figure, the critical bending strain for the Grade 80-v0 rebar is approximately 0.14, which corresponds to the critical bending strain of the Grade 60 rebar. In order to understand this difference, the profile of the rebar was examined as shown in Figure 7-19(b). The rib radius on this rebar was not significantly different from the other rebar from Mill 1, although the transition from rebar shaft to rib does resemble the ribs of the Grade 80-v2 rebar from Mill 1, which had improved behavior. The surface of this rebar was also much rougher than the other rebar from Mill 1, suggesting that surface roughness could result in improved performance.

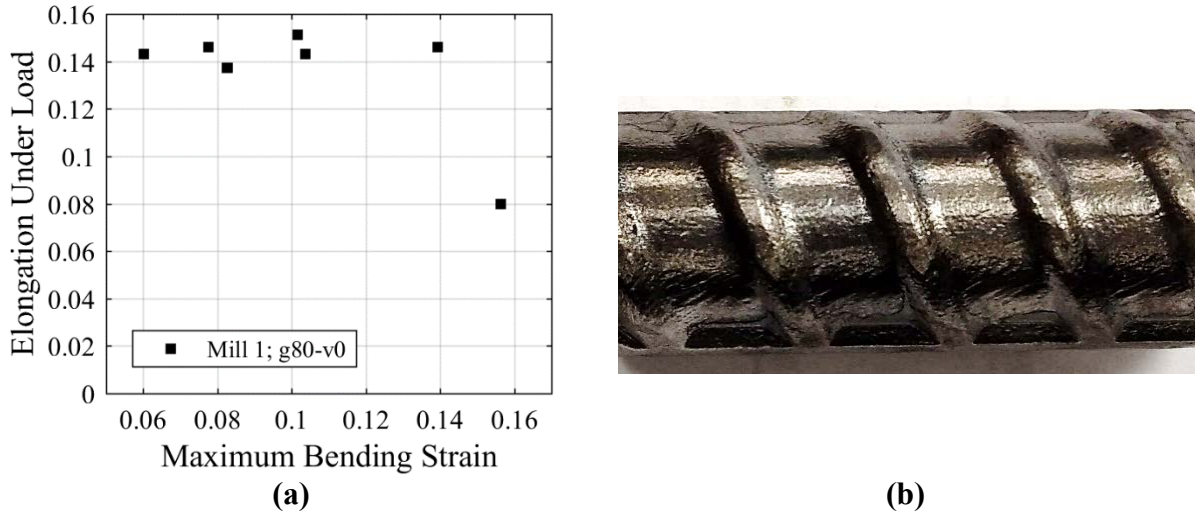

Figure 7-19. (a) BBT on Mill 1, Grade 80-v0 rebar; (b) Bar profile for Grade 80-v0 rebar

Based on the positive results of the BBT test on the Grade 80 rebar from Mill 2, the next logical step is to construct columns from this rebar to confirm that the observed BBT behavior translates into improved column behavior. However, before doing so, an additional set of samples were obtained. Figure 7-20 shows the results of these tests. As Figure 7-20 shows, the new Grade 80 rebar from Mill 2 had very similar if not improved performance to the original Grade 80 rebar from Mill 2. The chemical compositions for each heat of rebar did not change dramatically, and the rib profile remained similar for each heat as well.

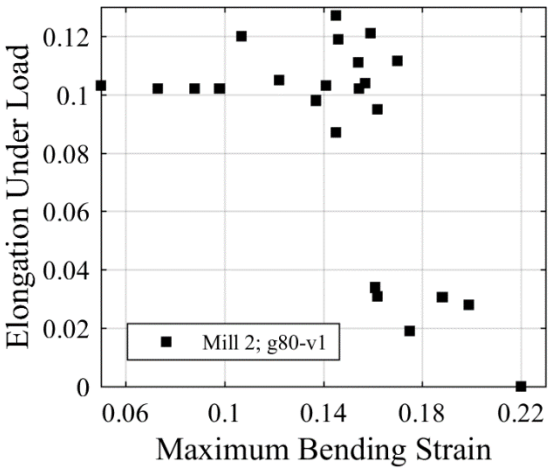

Figure 7-20. BBT tension test results for Mill 2, Grade 80-v1 rebar

Figure 7-21 shows the rib profile as well as a photo of the surface of each side of the bar. Side A has a similar rib profile and surface roughness to the Mill 2, Grade 80-v0 rebar, which is shown in Figure 7-10(b). However, the rib radius of side B is sharper than on side A, but the surface of B is much rougher than the surface of A. This also suggests that the rib radius as well as surface roughness influences the critical bending strain.

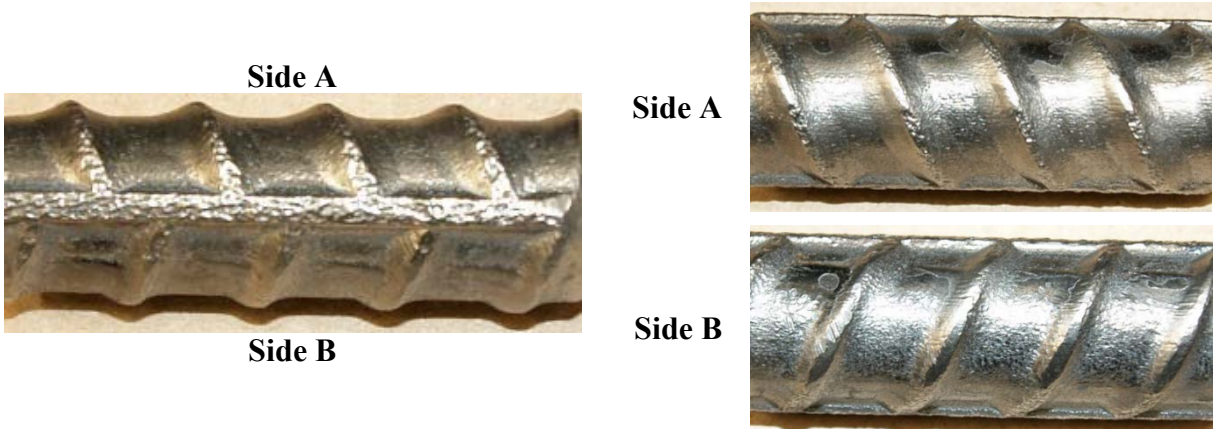

Figure 7-21. Mill 2, Grade 80-v1 rebar profile and surface

After examining the results of the buckled bar tension test on various batches of Grade 80 rebar, it was hypothesized that a larger rib radius and increased rebar surface roughness will increase the critical bending strain of rebar. It is yet to be confirmed if chemical composition influences this behavior.

7.2.4. Effect of Bar Manufacture Process

Rebar production Mills 1 and 2 used microalloying alone to achieve the increase in rebar strength. However, some mills use the process of quenching and self-tempering (QST), or thermo-mechanically treated (TMT) to achieve this increase in strength. Countries outside the United States often use this type rebar for reinforcement in members subjected to plastic strain demands, such as plastic hinge members. However, the tensile to yield strength ratio (T/Y) for QST bars typically ranges from 1.2 to 1.25. Currently, the ASTM standard requires a T/Y ratio of 1.25 for the A706 designation, which disqualifies much of the QST for the A706 standard. Currently, researchers at NCSU are performing analysis and experiments to see if a lower T/Y could be permissible for reinforcement in plastic hinge members.

Modi el al. (2014) describes the quench and self-temper process for reinforcing steel. As the hot rolled bar leaves the final mill stand, the rebar is rapidly quenched, or cooled, by a special water spray system. This quenching leaves a hard layer of steel on the surface of the rebar in the martensitic phase, while the inner core remains hot and in the austenite phase. The heat from the core flows to the cooler surface of the bar, which tempers the surface into “tempered martensite.” The austenitic core later transforms into a ductile ferrite-pearlite structure. Steel in the martensite phase is very hard, but also very brittle. Tempering the layer of martensitic steel through a slow diffusion of heat leaves a finished product that is almost as hard and strong as martensite, but with much improved ductility and toughness. The ferrite-pearlite phase of steel is not as hard as the martensitic phase, but it is much more ductile (Callister and Rethwisch, 2010). Figure 7-22 shows an example of a typical QST rebar cross-section. The varying hardness across the cross-section of a QST rebar has been verified in Paul et al. (2014). Certain alloys are still added to QST rebar similar to the microalloying process, but the QST process allows for less expensive alloys to be used.

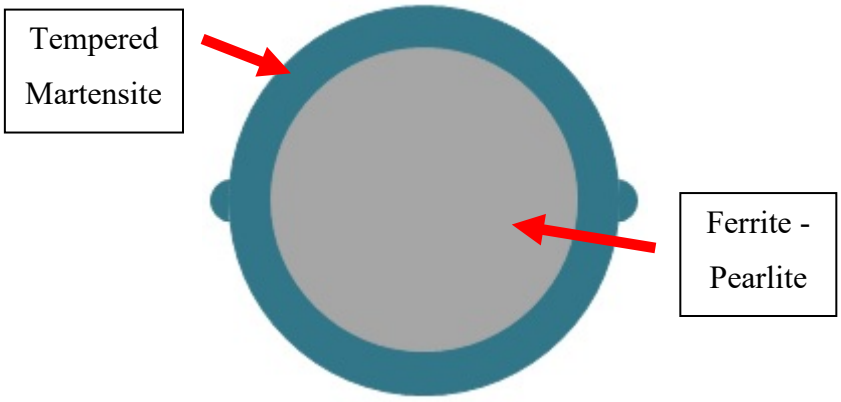

Figure 7-22. Cross-section of a QST rebar

Some research has indicated that QST bars provide better fatigue life than bars produced by microalloying (Ghannoum and Slavin, 2016), but other research has concluded that QST produces rebar with worse fatigue life than rebar produced by microalloying (Paul et al., 2014). Nevertheless, several bar samples were obtained from a reinforcing steel producer using the QST method, which will be referred to as Mill 3. Figure 7-23 includes sample stress vs. strain results of pull tests for various size QST bars. Typically, QST bars are not used in seismic regions in the United States due to the limit on the ratio of tensile strength to yield strength (T/Y) in the ASTM A706 standard. As seen in Figure 7-23, the T/Y ratio for both of these bars is 1.26, which meets the 1.25 limit for A706, but the variance in T/Y ratio would disqualify a large number of these bars. Studies are currently underway at NCSU to quantify the effect of T/Y ratio on spread of plasticity and member performance.

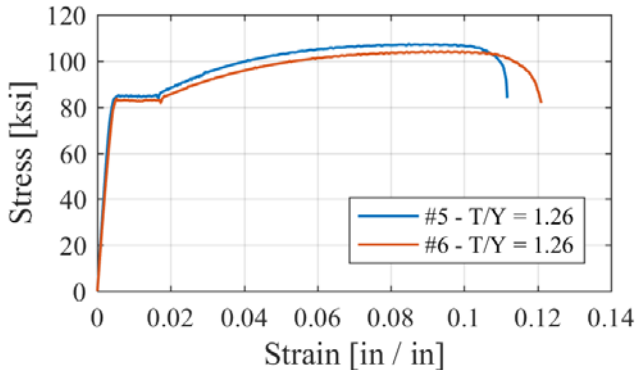

Figure 7-23. Stress vs. strain for #5 and #6 Mill 3 rebar

The different manufacture process led to different fracture surfaces. The ductile fracture surface of the bars produced by microalloying were conical with an angled shear lip and a flat face on the interior of the bar, as seen in Figure 7-24(c) and (d). The QST bar, however, had a much more jagged fracture surface as seen in Figure 7-24(a) and (b). Each bar experiences necking prior to fracture and have similar values of elongation under load, or axial strain at fracture, but the failure surfaces are much different. This is likely due to the different chemical compositions across the cross-section of the QST rebar.

(a) **(b)** **(c)** **(d)**

Figure 7-24. (a), (b) Ductile fracture surface of Mill 3 rebar; (c), (d) Ductile fracture surface of Mill 1 rebar

Despite often not meeting the requirements for the A706 designation, the buckled bar tension test was performed on various bar sizes of QST rebar. Figure 7-25 shows the results of the BBT Test on rebar produced by the QST process.

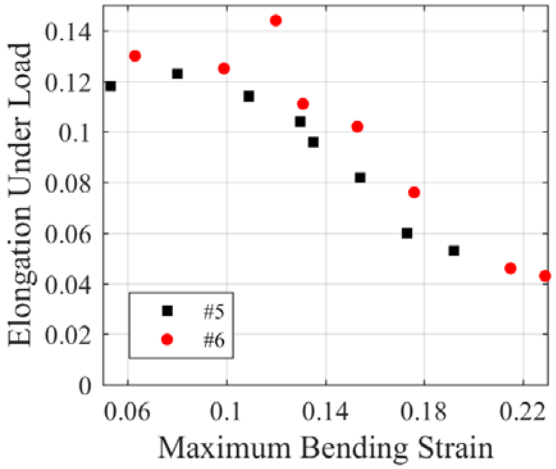

Figure 7-25. BBT test results for Mill 3 rebar

As seen in Figure 7-25, the axial strain at fracture does not decrease drastically as the bending strain increases. Rebar produced by microalloying tends to experience a sudden drop in tensile strain capacity after the bending demands exceed a certain threshold. In addition, the failure surface of the QST bars which experienced brittle failure was different from the rebar produced by microalloying. When rebar produced by microalloying buckled so that the strain demand exceeded the critical bending strain, the elongation under load significantly reduced, and the failure surface changed from conical to flat, as seen in Figure 7-4. However, when the bending strain on the QST bar exceeded 0.13 for the #5 and 0.1 for the #6 rebar, the fracture surface changed from the surface seen in Figure 7-24(a) to the surface seen in Figure 7-26(a). Fracture propagated along the base of the rib. However, the onset of this type of fracture did not result in an immediate drop in tensile strain capacity. It was only when the bending strain exceeded 0.14 when the elongation at fracture started to decrease. Rebar that fractured at a lower tensile strain capacity still had the same fracture surface, as seen in Figure 7-26(b). This delay in the decline of tensile strain capacity could beneficially affect the behavior of the rebar in column tests, as the post-buckling strain capacity would be higher than typical rebar. The improvement in performance is likely due to the harder surface of the QST rebar. If the surface is harder, cracks will not propagate through the cross-section as in rebar produced by microalloying. Future column tests are planned at NCSU with QST rebar to see if improved critical bending strain will correspond to improved column performance.

(a) **(b)**

Figure 7-26. QST rebar failure surface after (a) bending strain of 0.1, (b) bending strain of 0.23

7.2.5. Effect of Strain Rate and Aspect Ratio

Previous tests have shown that cracks resulting from compressive loading may increase as the load rate increases (Nemat-Nasser and Chang, 1990). In order to test whether the bending strain rate is fast enough to show the effects of strain rate, a group of rebar specimens with a high aspect ratio (L/D = 16) that were loaded in compression at 0.2 inches/minute were tested. This corresponded to an average bending strain rate of 0.4 με/second. Figure 7-27(a) shows a sample plot of bending strain rate versus time to see the calculation of bending strain rate. Another group of specimens from the same heat of rebar and an aspect ratio of 10 were tested at load rates varying from 0.2 inches/minute to 0.5 inches/minute in compression, which corresponds to an average bending strain rate of 0.8 με/second. The critical bending strain of each dataset did not change significantly (0.01 at most), as seen in Figure 7-27(b). This suggests that the bending strain rate of the buckled bar tension test does not significantly influence the results. For each of the specimens tested with the buckled bar tension test, the strain rate bending strain rate varied from 0.2 to 1.2 με/second.

In addition, varying the aspect ratio, or ratio of clear span to diameter, did not influence the critical bending strain. By testing bars with multiple aspect ratios, the assumption that bending strain affects rebar tensile capacity, regardless of aspect ratio, was verified. The typical spacing of transverse steel in an RC column is no greater than $5d_{bl}$ to restrict the possibility of longitudinal

bar buckling. Transverse steel will often yield and the total length over which the rebar will buckle will often be greater than $5d_{bl}$, but the aspect ratio of the buckled bar likely will not be greater than 10. However, since aspect ratio and bending strain rate do not affect the critical buckling strain, any rebar specimens with any aspect ratio can be used in the buckled bar tension test, despite not matching aspect ratios of actual column longitudinal rebar. Using rebar specimens with higher aspect ratios will place less lateral load on the crosshead of the testing apparatus when the rebar buckles, which is more desirable for safe testing.

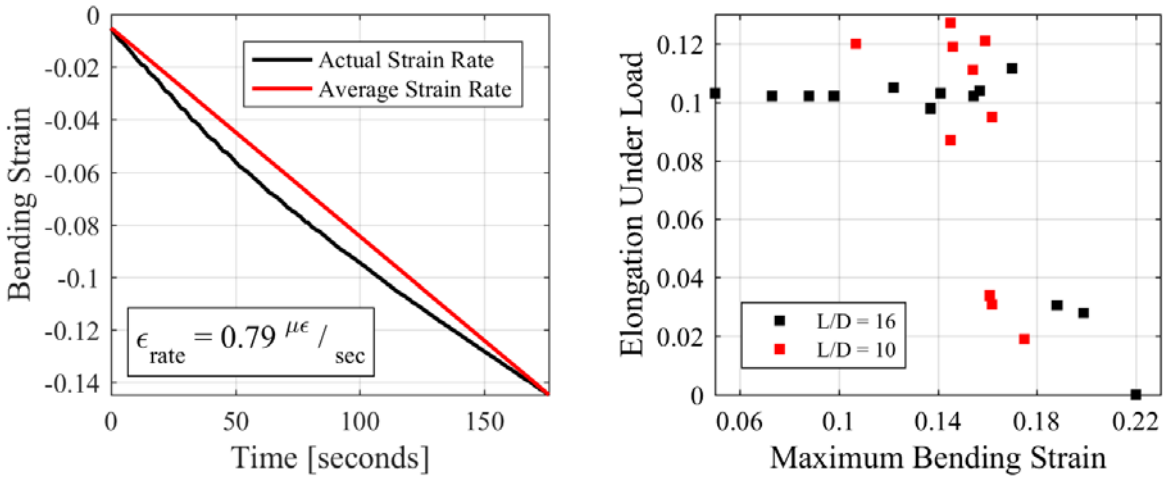

Figure 7-27. (a) Bending strain rate calculation for BBT; (b) BBT for varying strain rate

As mentioned in Section 7.2.1, the critical bending strain measured in the longitudinal reinforcement of the column tests matches the critical bending strain measured using the results of the BBT test reasonably well. The strain rate in the column longitudinal steel prior to the peak strain from bending was calculated, as seen in the highlighted region of strain in Figure 7-28(a) and calculated in Figure 7-28(b).

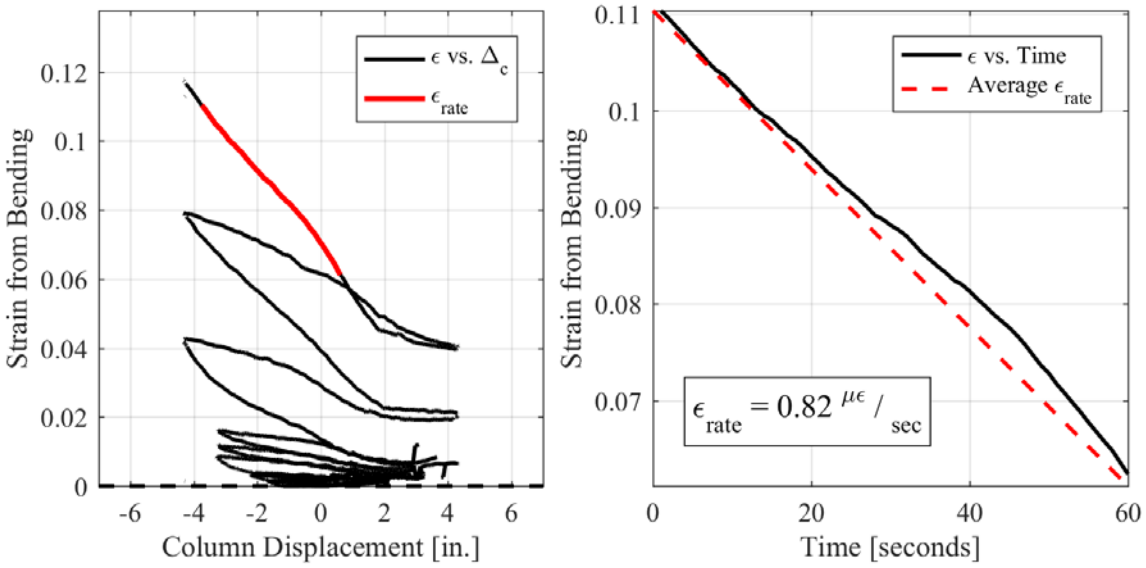

Figure 7-28. (a) Bending strain vs. column displacement; (b) Bending strain vs. time with bending strain rate

The bending strain rate of the column longitudinal bars ranged from 0.32 to 1.94 με/second, which is similar to the strain rates used in the BBT test. The slight variation in strain rate does not affect the results since the strain rate is likely lower than the threshold of the strain rate effect. Mander et al (1988) performed a regression analysis of the results of dynamic tests and proposed Equation 7-1 to express the increase of yield stress as a function of strain rate for axial loading.

$$\frac{f_{yd}}{f_y} = 0.953\left(1+\left|\frac{\varepsilon_{rate}}{700}\right|^{\frac{1}{6}}\right) \qquad \text{Equation 7-1}$$

Bending strain rate likely has the opposite effect, however, as Nemat-Nasser and Chang (1990) indicated that an increase in the strain rate of compressive loading would amplify the propagation of cracks. During the quasi-static cyclic tests on Grade 60 and 80 columns, the effect of strain rate on the critical bending strain of longitudinal reinforcement is negligible. However, dynamic loading would likely increase in strength of the rebar decrease the critical compressive strain. Dynamic tests are needed to evaluate the impact of strain rate.

7.3. Bending Strain vs. Axial Displacement

After 133 buckled bar tension tests were performed on various rebar specimens, the relationship between axial compression and bending strain was also examined. A correlation between axial compression and bending strain could be used for multiple applications.

First, this type of relationship could be incorporated into a uniaxial material model. Following bar buckling, the axial compressive strain could be related to compressive strain demands from bending. The designer could specify a certain critical bending strain resulting in bar fracture. Current uniaxial models define the bar fracture limit state as the exceedance of the tensile strain capacity or the low-cycle fatigue capacity. This type of addition to a uniaxial material model would incorporate this failure mode into design and possibly add a bar fracture limit state.

Secondly, practitioners could use this type of relationship to develop a buckled bar tension test that would be easy to implement. The current buckled bar tension test, as proposed in this report, requires an expensive optical measurement system to measure bar profile and corresponding bending strain demand. However, a clearly defined axial deformation vs. bending strain relationship would eliminate the need for an optical measurement system. This would allow for anyone with a simple universal testing machine (UTM) to perform the BBT test to evaluate the critical bending strain of steel reinforcement.

This report presents the hypothesis that an increase in the critical bending strain will correspond to an increase in column displacement capacity. Therefore, testing the critical compressive strain of a certain rebar before specifying it for use in a plastic hinge-forming member could measure the predicted capacity of the member. The buckled bar tension test could be used to evaluate seismic performance. Additionally, the “bend/re-bend” rebar test as seen in Zhao and Ghannoum (2016) could be used to identify critical bending strain. This test shows promise for evaluating seismic performance, but the bend process may not replicate the buckling of an actual rebar. When the rebar is bent about pins of a certain diameter, the ribs are placed in compression. This could reduce cracking from compressive loads. Future studies should be performed to see if the results of the bend/re-bend test correspond to the results of the buckled bar tension test to predict critical compressive strain.

Figure 7-29 shows the relationship between bending strain (ε_{max}) times the ratio of clear length to bar diameter ($^{L}/_{D}$) to axial deformation (Δ_{axial}). A second order polynomial fit the data very accurately, having a coefficient of determination (R^2) of 0.96. This relationship can be used for the development of future uniaxial material models or for a simpler BBT test to evaluate the suitability for reinforcement in seismic applications.

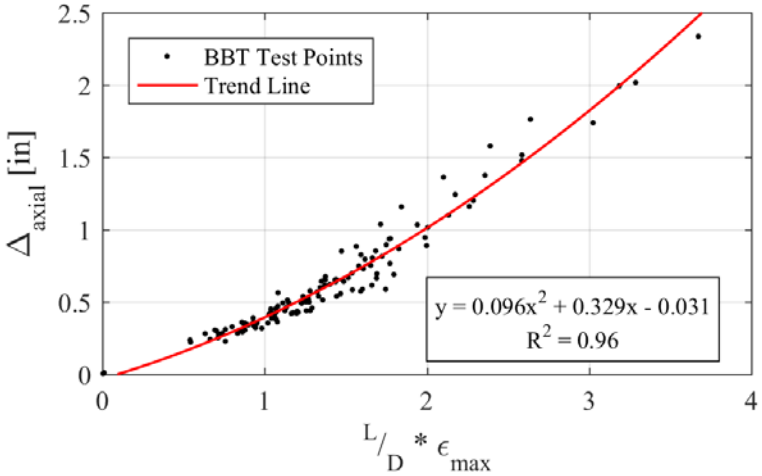

Figure 7-29. Bending strain vs. axial deformation

7.4. Summary of BBT Test Results

The buckled bar tension (BBT) test enabled an experimental evaluation of the critical bending strain of rebar without performing column tests. The results of the four Grade 80 column tests suggested that the decrease in displacement capacity after bar buckling was due to a decreased critical bending strain in the reinforcement. The authors hypothesize that if the rebar critical bending strain was increased, corresponding columns may have a higher displacement capacity.

Initial analysis of the results of the BBT data indicate that the radius at the base of the rebar rib is the prime factor that influences the critical bending strain due to its effect on the stress concentration factor under compressive loading. Surface roughness and manufacture process also appear to affect this value. More investigation should be performed to examine the impact of chemical composition and strain rate. If an increase in strain rate has a negative impact on critical bending strain, columns subjected to dynamic loading such as shake table tests and earthquake

loads would have lower displacement capacities after buckling. However, this lower capacity may be negated by the dynamic strain rate effect that increases the axial capacity.

Table 7-1 displays a summary of the critical bending strain from the BBT test. As mentioned previously, the Grade 80 columns (constructed with Mill 1, Grade 80-v1 rebar) had lower displacement capacities than the comparison Grade 60 columns (constructed with Mill 2, Grade 60 rebar). These different rebar also had different values of critical bending strain. The authors hypothesize that increasing the critical bending strain will increase the displacement capacity of the column. To test this, more columns will be constructed at NCSU with rebar having higher critical bending strain values to see if the displacement capacity of the column increases.

Table 7-1. Summary of BBT Test Results

Mill	Manufacture Process	Designation	Critical Bending Strain
1	Micro-alloying	Grade 60	0.14
		Grade 80 – v0	0.14
		Grade 80 – v1	0.10
		Grade 80 – v2	0.13
		Grade 80 – v2b	0.10
2	Micro-alloying	Grade 60	0.14
		Grade 80 – v0	0.14
		Grade 80 – v1	0.16
3	Quench and Self-Tempered	Grade 80 – #5	0.14
		Grade 80 – #6	0.14

A correlation between axial displacement and bending strain was observed from the results of the BBT test. These results could be used by future researchers for the development of a uniaxial material model which takes into account the bar fracture limit state using a design value of critical bending strain. Current reinforcing steel material models account for bar fracture with an exceedance of the tensile strain capacity or the low-cycle fatigue capacity. These models tend to

overestimate the fracture capacity of reinforcing steel that experiences bar buckling under cyclic loads. In addition, practitioners could use the axial displacement vs. bending strain relationship to develop a uniaxial test for new reinforcing steel to measure the critical bending strain and the corresponding suitability of the reinforcing steel for use in plastic hinge members. However, more column tests should be performed to validate the assumption that increased compressive strain capacity corresponds to an increase in the post-buckling displacement capacity of a column.

CHAPTER 8. CONCLUSIONS AND FUTURE WORK

8.1. Summary of Column Test Results

Four circular reinforced concrete columns were constructed at the CFL at NCSU. The longitudinal and transverse reinforcing steel for each column was ASTM A706 Grade 80 rebar. Column geometry and reinforcement detailing were scaled to match standard details used in design. The detailing also matched previous columns tested at NCSU that had been constructed with A706 Grade 60 rebar. The initial goals of the research were to characterize the seismic performance of A706 Grade 80 rebar and identify plastic hinge lengths, bond slip, performance limit states, and equivalent viscous damping, comparing these parameters to those used in the design of Grade 60 columns.

A unique optical measurement system enabled measurement of the strains in the longitudinal reinforcing steel and the strain profile over the plastic hinge length. Using this information, the experimental plastic hinge length was calculated and the amount of strain penetration, or bond slip, was measured in each Grade 80 column test. The plastic hinge length of the Grade 80 columns matched the current model for Grade 60 columns. The Grade 80 columns also had comparable amounts of bond slip to the Grade 60 columns. The equivalent viscous damping was calculated for each column and the damping versus ductility curves were similar for Grade 60 and Grade 80 columns. With regards to energy dissipation, for a given ductility level, the dissipated energy is similar for grade 60 and 80 steel reinforced columns. When examining the total dissipated energy at first bar fracture, the grade 80 columns consistently exhibited lower levels of dissipated energy. This is a function of bar fracture occurring earlier after the onset of bar buckling for grade 80 columns. The only difference in behavior observed between the Grade 60 and Grade 80 columns was the displacement capacity.

While columns reinforced with either grade of rebar experienced bar buckling at approximately the same column drift ratio and tensile strain, the longitudinal rebar in the Grade 80 columns fractured much sooner than the comparison Grade 60 columns. The lateral force capacity of the columns dropped significantly after longitudinal bar fracture. The authors believe that the

difference in the post-buckling capacity of the reinforcing steel is due to differences in the critical bending strain of the rebar and developed the buckled bar tension test to identify this parameter.

The bending strain demand on the longitudinal reinforcement was quantified and a relationship between uniaxial tension strain and strain from bending was proposed. This equation used axial load ratio and transverse volumetric steel ratio along with the longitudinal bar critical bending strain to predict the uniaxial tension strain that would result in bar fracture under cyclic loading. While this equation accurately predicted the column displacement of bar fracture, more experimental results are needed to analyze the effect of each parameter.

8.2. Summary of BBT Test Results

In order to characterize the critical bending strain capacity of various rebar, the buckled bar tension test was developed. This test subjected a rebar specimen to one compressive load cycle that buckled the rebar followed by a tensile load cycle until the bar fractured. This load protocol was chosen in order to simulate the bending strain demand that a rebar experiences when the longitudinal bars in the plastic hinge region buckle.

The quantity of strain due to bending in a buckled rebar was observed to influence the tensile strain capacity of the rebar. The value of strain from bending strain that caused brittle fracture in the longitudinal reinforcement of the columns corresponded to the bending strain in the material test that resulted in a brittle failure. This strain was referred to as the critical bending strain. The correlation indicated that material test (buckled bar tension test) correctly simulated the loading conditions of a buckled longitudinal reinforcing bar.

Through performing a large number of tests on various types of rebar, several parameters were identified that influenced the critical bending strain. A larger radius at the intersection of the rebar rib (deformation) and shaft was observed to increase the critical bending strain. Some evidence also suggested that a rougher surface of the rebar would result in a higher critical bending strain. Most of the rebar samples were produced by mills that strengthened their bars by microalloying, but rebar produced by the quench and self-temper (QST) manufacture process were

also tested. The QST bars had an improved critical bending strain. The results of the tests suggested that chemical composition did not influence the critical bending strain.

The Grade 60 columns had a higher displacement capacity as well as rebar with a higher critical bending strain than the Grade 80 columns. Therefore, the authors hypothesize that if columns were constructed with Grade 80 rebar with a higher critical bending strain, these columns would have higher displacement capacities. In order to test this hypothesis, more Grade 80 columns are currently under construction at NCSU with Grade 80 rebar from three different reinforcing steel mills that each have critical bending strains similar to Grade 60 rebar. These tests will show whether critical bending strain has a direct correlation to column displacement capacity.

If critical bending strain has a direct correlation to column displacement capacity, the buckled bar tension test could be used to test the suitability of different reinforcing steels for use in plastic hinge members. This test currently uses a unique optical measurement system to calculate the bending strain demand on rebar specimens. However, this report proposes a relationship between axial displacement, aspect ratio of the rebar specimen, and bending strain that would enable others to perform this test. The buckled bar tension test would serve as a quality control test for rebar designed for seismic applications.

8.3. Future Work

As mentioned previously, more column tests should be performed on Grade 80 rebar to characterize plastic hinge lengths, equivalent viscous damping, and performance limit states. These columns should vary different design variables such as longitudinal steel, transverse steel, axial load, and aspect ratios. In addition, more column tests are needed in order to test the hypothesis that critical bending strain corresponds to column displacement capacity. More buckled bar tension tests can be performed in order to better identify the influence of rib radius, surface roughness, and chemical composition on the critical bending strain as well as to look for other factors that influence this parameter. Lastly, the investigation of bar buckling as a continuum process should be continued, and other mechanistic models for bar fracture should be developed.

REFERENCES

ASTM A370-16. “Standard Test Methods and Definitions for Mechanical Testing of Steel Products.” ASTM International. West Conshohocken, PA. 2016. pp. 49.

ASTM A706/A706M-16. “Standard Specification for Deformed and Plain Low-Alloy Steel Bars for Concrete Reinforcement.” ASTM International. West Conshohocken, PA. 2016. pp. 7.

ASTM C39-17a. “Standard Test Method for Compressive Strength of Cylindrical Concrete Specimens.” ASTM International. West Conshohocken, PA. 2016. pp. 8.

ASTM E606-12. “Standard Test Method for Strain-Controlled Fatigue Testing.” ASTM International. West Conshohocken, PA. 2012. pp. 16.

Bae, S., Mieses, A. M., and Bayrak, O. (2005) “Inelastic buckling of reinforcing bars.” *Journal of Structural Engineering* 131(2). pp. 314-321.

Barbosa, A. R., Link, T., and Trejo, D. (2015) "Seismic Performance of High-Strength Steel RC Bridge Columns." *Journal of Bridge Engineering* 21(2).

Berry, M. P. and Eberhard, M. O. (2005) “Practical performance model for bar buckling.” *Journal of Structural Engineering* 131(7). pp. 1060-1070.

Brown, J. and Kunnath, S. K. (2004) “Low-cycle fatigue failure of reinforcing steel bars.” *ACI Materials Journal* 101(6). pp. 457-466.

Brown, W. A., Lehman, D. E., and Stanton, J. F. (2008) “Bar buckling in reinforced concrete bridge columns.” PEER Report 2007/11. Pacific Earthquake Engineering Research Center. pp. 138.

Brooke, N. J., Megget, L. M., and Ingham, J. M. (2006) “Bond performance of interior beam-column joist with high-strength reinforcement.” *ACI Structural Journal* 103(4). pp. 596-603.

Callister, W.D., Jr., and Rethwisch, D.G. (2010) “Material Science and Engineering: An Introduction.” Eighth Edition. John Wiley & Sons. New York

Caltrans (2013) “Caltrans Seismic Design Criteria.” Version 1.7. Caltrans. pp. 180.

Chai, Y. H. (1991) “Steel jacketing of circular reinforced concrete bridge columns for enhanced flexural performance.” PhD Dissertation. University of California, San Diego. pp. 297.

Chang, B., Hutchinson, T., Wang, X., and Englekirk, R. (2014). “Seismic performance of beam-column subassemblies with high-strength steel reinforcement.” *ACI Structural Journal* 111(6). pp. 1329-1338.

Erickson, S. D. and Heeringa, R. (2016) "Tall Building Concrete Shear Wall Design Using High Strength Grade 80 Longitudinal Reinforcing in San Francisco." *Proceedings of the 2-16 Annual Meeting of the Los Angeles Tall Buildings Structural Design Council*. pp. 65-74.

FEMA 356. (2000). "Prestandard and Commentary for the Seismic Rehabilitation of Buildings." Prepared by the American Society of Civil Engineers. Reston, VA. pp. 518.

Feng, Y, Kowalsky, M. J., and Nau, J. M. (2014). "Fiber-Based Modeling of Circular Reinforced Concrete Bridge Columns" *Journal of Earthquake Engineering*, 18. pp. 714-734.

Fleck, N. A., Shin, C. S., and Smith, R. A. (1985) "Fatigue crack growth under compressive loading." *Engineering Fracture Mechanics* 21(1). pp. 173-185.

Gerber, T. L. and Fuchs, H. O. (1968) "Analysis of nonpropagating fatigue cracks in notched parts with compressive mean stress." *Journal of Materials* 3(2). JMLSA. pp. 359-374.

Ghannoum, W. M. and Slavin, C. M. (2016) "Low-cycle fatigue performance of high-strength steel reinforcing bars." *ACI Materials Journal* 113(6). pp. 803-814.

Goodnight, J. C., Kowalsky, M. J., and Nau J. M. (2015). "The effects of load history and design variables on Performance Limit States of Circular Bridge Columns." Vol. 1-3. Final report to Alaska Department of Transportation and Public Facilities. January. pp. 1258.

Haber, Z. B., Saiidi, M. S., and Sanders, D. H. (2013) "Precast column-footing connections for accelerated bridge construction in seismic zones." Caltrans Report No. CA13-2290. pp. 546.

Hassan, T. K., Seliem, H. M., Dwairi, H., Rizkalla, S. H., and Zia, P. (2008). "Shear Behavior of Large Concrete Beams Reinforced with High-Strength Steel." *ACI Structural Journal* 105 (2). pp. 173-179.

Hawileh, R. A., Abdalla, J. A., Oudah, F., and Abdelrahman, K. (2010) "Low-cycle fatigue life behaviour of BS 460B and BS 500B steel reinforcing bars." *Fatigue & Fracture of Engineering Materials & Structures* 33. Blackwell Publishing Ltd. pp. 397-407.

Helgason, T., Hanson, J. M., Somes, N. F., Corley, W. G., and Hognestad, E. (1976) "Fatigue strength of high-yield reinforcing bars." *National Cooperative Highway Research Program Report 164*. Transportation Research Board National Research Council, Washington, DC. pp. 103.

Jacobsen, L. S. (1930). "Steady forced vibrations as influenced by damping." *ASME Transactions* 52(1). pp. 169–181.

Jhamb, I. C. and MacGregor, J. G. (1974) "Effect of surface characteristics on fatigue strength of reinforcing steel." *ACI Special Publication 41-7*. SP 41-7. pp. 139-167.

King, D. J., Priestly, M. J. N., and Park R., "Computer programs for concrete column design." Research report 86/12, Department of Civil Engineering, University of Canterbury, New Zealand. May 1986.

Kowalsky, M. J. (2000). "Deformation limit states for circular reinforced concrete bridge columns." *Journal of Structural Engineering* 126(8). pp. 869-878.

Kunnath, S. K., Kanvinde, A., Xiao, Y., and Zhang, G. (2009) "Effects of buckling and low cycle fatigue on seismic performance of reinforcing bars and mechanical couplers for critical structural members." Caltrans Report No. CA/UCD-SESM-08-01. pp. 77.

Lepage, A., Tavallai, H., Pujol, S., and Rautenberg, J. M. (2012). "High-Performance Steel Bars and Fibers as Concrete Reinforcement for Seismic-Resistant Frames." *Advances in Civil Engineering*. DOI: 10.1155/2012/450981.

Mander, J. B. (1983). "Seismic design of bridge piers." PhD Thesis. University of Canterbury. Christchurch, New Zealand. pp. 503.

Mander, J. B., Priestly, M. J. N., and Park R. (1988) "Theoretical stress-strain model for confined concrete.' *Journal of the Structural Division ASCE*. 114(8). pp. 1804-1826.

Mau, S. T. and El-Mabsout, M. (1989) "Inelastic buckling of reinforcing bars." *Journal of Engineering Mechanics* 115(1). pp. 1-17.

Modi, A., Hindolia, D. A., and Sharma, R. (2014) "Sequential improvement of quenching-self-tempering-thermal-treatment rolling process for a modern manufacturing system – a case study." *International Journal of Innovations in Engineering and Technology* 4(4). pp. 100-111.

Montejo, L. A. and Kowalsky, M. J. (2007). "CUMBIA – Set of Codes for the Analysis of Reinforced Concrete Members." Technical Report No. IS-07-01, North Carolina State University, Raleigh, NC.

Montejo, L. A., Kowalsky, M. J., and Hassan, T. (2009) "Seismic behavior of flexural dominated reinforced concrete bridge columns at low temperatures." *Journal of Cold Regions Engineering* 23(1). DOI: 10.1061/(ASCE)0887-381X(2009)23:1(18). pp. 18-42.

Moyer, M. J. and Kowalsky, M. J. (2003) "Influence of tension strain on buckling of reinforcement in concrete columns." *ACI Structural Journal* 100(1). pp. 75-85.

McKenna, F., Fenves, G. L., Scott, M. H., and Jeremi´c, B. (2010) "Open system for earthquake engineering simulation" (available online at: http://opensees.berkeley.edu).

Nemat-Nasser, S. and Chang, S. (1990) "Compression-induced high strain rate void collapse, tensile cracking, and recrystallization in ductile single polycrystals." *Mechanics of Materials* 10. pp. 1-17.

Northern Digital Inc. (2011). "OPTOTRAK Certus HD dynamic measuring machine." <https://www.ndigital.com/msci/products/certus-hd/> (Aug. 20, 2016).

Okamoto, M., Sato, T., Tanimura, Y., and Kuroiwa, T. (2004). "Experimental study on seismic performance verification method for RC members using high-strength materials." *Journal of Advanced Concrete Technology* 2(2). pp. 223-231.

Overby, D. T., M. Kowalsky, and R. Seracino. (2015). "A706 Grade 80 Reinforcement for Seismic Applications." Caltrans-funded Research Project. Research Report No. RD-15-15. pp. 113.

Paul, S. K., Rana, P. K., Das, D., Chandra, S., and Kundu, S. (2014) "High and low cycle fatigue performance comparison between micro-alloyed and TMT rebar." *Construction and Building Materials* 54. pp. 170-179.

Pauley, T. and Priestley, M. J. N. (1992). *Seismic Design of Reinforced Concrete and Masonry Buidlings*. John Wiley and Sons. New York. pp. 744.

Priestley, M. J. N., Calvi, G. M., and Kowalsky, M. J. (2007). *Displacement-Based Seismic Design of Structures*. IUSS Press, Pavia, Italy. pp. 721.

Priestley, M. J. N. and Grant, D. N. (2005) "Viscous damping in seismic design and analysis." *Journal of Earthquake Engineering* 9(2). pp. 229-255.

Priestley, M. J. N., Seible, F., and Calvi, G. M. (1996). *Seismic Design and Retrofit of Bridges*. John Wiley and Sons. New York. pp. 704.

Rautenberg, J. M., Pujol, S., Tavallali, H., and Lepage, A. (2013). "Drift Capacity of Concrete Columns Reinforced with High-Strength Steel." *ACI Structural Journal* 110 (2). pp. 307-317.

Restrepo, J. I., Seible, F., Stephan, B., and Schoettler, M. J. (2006). "Seismic Testing of Bridge Columns Incorporating High-Performance Materials." *ACI Structural Journal* 103 (4). pp. 496-504.

Restrepo-Posada, J. I. (1992) "Seismic behaviour of connections between precast concrete elements." PhD Thesis. University of Canterbury. Christchurch, New Zealand. pp. 412.

Scott, M.H. and Fenves, G.L. (2006) "Plastic hinge integration methods for force-based beam-column elements." *Journal of Structural Engineering*. 132(2), pp. 244-252.

Shahrooz, B.M., Reis, J.M., Wells, E.L., Miller, R.A., Harries, K.A., and Russell, H.G. (2014). "Flexural Members with High-Strength Reinforcement: Behavior and Code Implications." *Journal of Bridge Engineering*. *ASCE.* 04014003. pp. 1-7.

Slavin, C. M. and Ghannoum, W. M. (2015). "Defining Structurally Acceptable Properties of High-Strength Steel Bars through Material and Column Testing, Part 1: Material Testing Report." *CPF Research Grant Agreement #05-14*. Charles Pankow Foundation. pp. 135.

Sokoli, D. (2014). "Seismic Performance of Concrete Columns Reinforced with High Strength Steel." Master's Thesis. University of Texas at Austin.

Sokoli, D. and Ghannoum, W. M. (2016). "High-Strength Reinforcement in Columns under High Shear Stresses." *ACI Structural Journal* 113 (3). pp. 605-614.

Sun, Y., Cai, G., and Takeshi, T. (2013). "Seismic Behavior and Performance-based Design of Resilient Concrete Columns." *Applied Mechanics and Materials* 438-439. pp. 1453-1460.

Trejo, D., Barbosa, A.R., and Link, T. (2014). "Seismic Performance of Circular Reinforced Concrete Bridge Columns Constructed with Grade 80 Reinforcement." Research Project SRS 500-610.

Wang, T., Liu, X., Zhao, H. (2014). "Experimental Research on Seismic Behavior of +-shaped Columns Reinforced with High-strength Steel Bars under Cyclic Loading." *Journal of Civil Engineering* 19 (4). pp. 982-993.

Xiao, X. Guan, F.L., Yan, S. (2008). "Use of ultra-high-strength bars for seismic performance of rectangular high-strength concrete frame columns." *Magazine of Concrete Research* 60(4). pp. 253-259.

Zhao, J. and Sritharan, S. (2007) "Modeling of strain penetration effects in fiber-based analysis of reinforced concrete structures." *ACI Structural Journal* 104(2). pp. 133-141.

Zheng, H. and Abel, A. (1998) "Stress concentration and fatigue of profiled reinforcing steels." *International Journal of Fatigue* 20(10). pp. 767-773.

Zhou, Y., Ou, Y., Lee, G. C., and O'Connor, J. S. (2010) "Mechanical and low-cycle fatigue behavior of stainless reinforcing steel for earthquake engineering applications." *Earthquake Engineering and Engineering Vibration* 9(3). pp. 449-457.